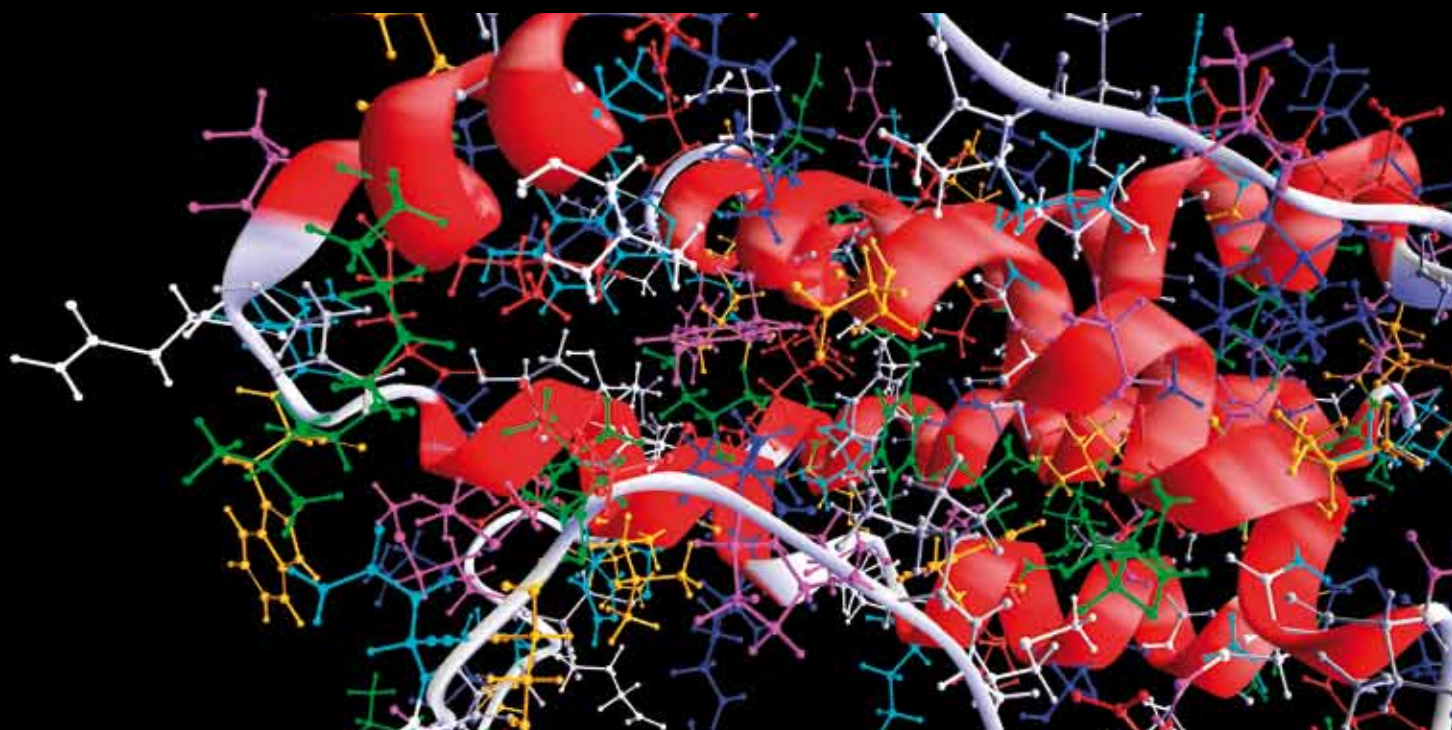


ELECTROMAGNETIC TISSUE PROPERTIES IMAGING FOR BIOMEDICAL APPLICATIONS

GUEST EDITORS: JIN KEUN SEO, WILLIAM LIONHEART, ULRICH KATSCHER, AND EUNG JE WOO





Electromagnetic Tissue Properties Imaging for Biomedical Applications

Computational and Mathematical Methods in Medicine

Electromagnetic Tissue Properties Imaging for Biomedical Applications

Guest Editors: Jin Keun Seo, William Lionheart, Ulrich Katscher,
and Eung Je Woo



Copyright © 2013 Hindawi Publishing Corporation. All rights reserved.

This is a special issue published in “Computational and Mathematical Methods in Medicine.” All articles are open access articles distributed under the Creative Commons Attribution License, which permits unrestricted use, distribution, and reproduction in any medium, provided the original work is properly cited.

Editorial Board

Emil Alexov, USA

Georgios Archontis, Cyprus

Dimos Baltas, Germany

Chris Bauch, Canada

Maxim Bazhenov, USA

Thierry Busso, France

Carlo Cattani, Italy

Sheng-yong Chen, China

William Crum, UK

Ricardo Femat, Mexico

Alfonso T. García-Sosa, Estonia

Damien Hall, Australia

Volkhard Helms, Germany

Seiya Imoto, Japan

Lev Klebanov, Czech Republic

Quan Long, UK

C-M Charlie Ma, USA

Reinoud Maex, France

Simeone Marino, USA

Michele Migliore, Italy

Karol Miller, Australia

Ernst Niebur, USA

Kazuhisa Nishizawa, Japan

Hugo Palmans, UK

David James Sherman, France

Sivabal Sivaloganathan, Canada

Nestor V. Torres, Spain

Nelson J. Trujillo-Barreto, Cuba

Gabriel Turinici, France

Kutlu O. Ulgen, Turkey

Edelmira Valero, Spain

Jacek Waniewski, Poland

Guang Wu, China

Henggui Zhang, United Kingdom

Contents

Electromagnetic Tissue Properties Imaging for Biomedical Applications, Jin Keun Seo, William Lionheart, Ulrich Katscher, and EungJe Woo
Volume 2013, Article ID 461846, 1 page

Recent Progress on the Factorization Method for Electrical Impedance Tomography, Bastian Harrach
Volume 2013, Article ID 425184, 8 pages

A Local Region of Interest Imaging Method for Electrical Impedance Tomography with Internal Electrodes, Hyeuknam Kwon, Alistair L. McEwan, Tong In Oh, Adnan Farooq, Eung Je Woo, and Jin Keun Seo
Volume 2013, Article ID 964918, 9 pages

Numerical Simulations of MREIT Conductivity Imaging for Brain Tumor Detection, Zi Jun Meng, Saurav Z. K. Sajib, Munish Chauhan, Rosalind J. Sadleir, Hyung Joong Kim, Oh In Kwon, and Eung Je Woo
Volume 2013, Article ID 704829, 10 pages

Effective Admittivity of Biological Tissues as a Coefficient of Elliptic PDE, Jin Keun Seo, Tushar Kanti Bera, Hyeuknam Kwon, and Rosalind Sadleir
Volume 2013, Article ID 353849, 10 pages

Model Independent MRE Data Analysis, Kogo Yoshikawa and Gen Nakamura
Volume 2013, Article ID 912920, 11 pages

Current Density Imaging Using Directly Measured Harmonic B_z Data in MREIT, Chunjae Park and Oh In Kwon
Volume 2013, Article ID 381507, 9 pages

Robust Myocardial Motion Tracking for Echocardiography: Variational Framework Integrating Local-to-Global Deformation, Chi Young Ahn
Volume 2013, Article ID 974027, 14 pages

Noninvasive Measurement of Conductivity Anisotropy at Larmor Frequency Using MRI, Joonsung Lee, Yizhuang Song, Narae Choi, Sungmin Cho, Jin Keun Seo, and Dong-Hyun Kim
Volume 2013, Article ID 421619, 12 pages

Recent Progress and Future Challenges in MR Electric Properties Tomography, Ulrich Katscher, Dong-Hyun Kim, and Jin Keun Seo
Volume 2013, Article ID 546562, 11 pages

EIT-Based Fabric Pressure Sensing, A. Yao, C. L. Yang, J. K. Seo, and M. Soleimani
Volume 2013, Article ID 405325, 9 pages

CoReHA 2.0: A Software Package for *In Vivo* MREIT Experiments, Kiwan Jeon and Chang-Ock Lee
Volume 2013, Article ID 941745, 8 pages

An Iterative Method for Problems with Multiscale Conductivity, Hyea Hyun Kim, Atul S. Minhas, and Eung Je Woo
Volume 2012, Article ID 893040, 12 pages

Editorial

Electromagnetic Tissue Properties Imaging for Biomedical Applications

Jin Keun Seo,¹ William Lionheart,² Ulrich Katscher,³ and EungJe Woo⁴

¹ *Department of Computational Science & Engineering/Mathematics, Yonsei University, Seoul 120-749, Republic of Korea*

² *School of Mathematics, University of Manchester, Alan Turing Building, Oxford Road, Manchester M13 9PL, UK*

³ *Philips Technologie GmbH, Roentgenstraße 24-26, Hamburg, Germany*

⁴ *Department of Biomedical Engineering, Kyung Hee University, Gyeonggi-do 446-701, Republic of Korea*

Correspondence should be addressed to Jin Keun Seo; seoj@yonsei.ac.kr

Received 22 October 2013; Accepted 22 October 2013

Copyright © 2013 Jin Keun Seo et al. This is an open access article distributed under the Creative Commons Attribution License, which permits unrestricted use, distribution, and reproduction in any medium, provided the original work is properly cited.

Recently, imaging techniques in science, engineering, and medicine have evolved to expand our ability to visualize a property of an object such as the human body. In particular, there has been marked progress in electromagnetic property imaging techniques, where cross sectional image reconstructions of electric conductivity, permittivity, and magnetic susceptibility distributions inside the human body are pursued. These techniques also have wider application to imaging methods in medicine, biotechnology, nondestructive testing, monitoring of industrial process, and others.

This special issue focuses on imaging methodologies, mathematical models, and computational algorithms for imaging electrical tissue properties for biomedical applications. The imaging problems in this topic can be formulated as inverse problems that are intrinsically nonlinear. Finding solutions with practical significance and value requires in-depth understanding of the underlying physical phenomena and data acquisition systems as well as implementation details of image reconstruction algorithms. Experience over the last three decades has shown that the symbiotic interplay between theoretical mathematics, computational mathematics, and experiments is crucial for understanding and solving these nonlinear problems in practice.

With this special issue, we hope to give an opportunity for this scientific community to consolidate knowledge in

the field and to identify the new challenges and the most promising directions for future progress.

*Jin Keun Seo
William Lionheart
Ulrich Katscher
EungJe Woo*

Research Article

Recent Progress on the Factorization Method for Electrical Impedance Tomography

Bastian Harrach

Department of Mathematics, University of Würzburg, 97074 Würzburg, Germany

Correspondence should be addressed to Bastian Harrach; bastian.harrach@uni-wuerzburg.de

Received 12 November 2012; Accepted 15 March 2013

Academic Editor: Bill Lionheart

Copyright © 2013 Bastian Harrach. This is an open access article distributed under the Creative Commons Attribution License, which permits unrestricted use, distribution, and reproduction in any medium, provided the original work is properly cited.

The Factorization Method is a noniterative method to detect the shape and position of conductivity anomalies inside an object. The method was introduced by Kirsch for inverse scattering problems and extended to electrical impedance tomography (EIT) by Brühl and Hanke. Since these pioneering works, substantial progress has been made on the theoretical foundations of the method. The necessary assumptions have been weakened, and the proofs have been considerably simplified. In this work, we aim to summarize this progress and present a state-of-the-art formulation of the Factorization Method for EIT with continuous data. In particular, we formulate the method for general piecewise analytic conductivities and give short and self-contained proofs.

1. Introduction

Electrical impedance tomography (EIT) aims to reconstruct the spatial conductivity distribution inside an imaging subject $\Omega \subseteq \mathbb{R}^n$ from current-voltage measurements on a part of its surface $\Sigma \subseteq \partial\Omega$. Mathematically, this leads to the problem of recovering the coefficient $\sigma(x)$ in the elliptic partial differential equation

$$\nabla \cdot \sigma \nabla u_\sigma^g = 0 \quad \text{in } \Omega, \quad \sigma \partial_\nu u_\sigma^g|_{\partial\Omega} = \begin{cases} g & \text{on } \Sigma, \\ 0 & \text{else} \end{cases} \quad (1)$$

from knowledge of the corresponding Neumann-to-Dirichlet operator (NtD)

$$\Lambda(\sigma) : g \mapsto u_\sigma^g|_\Sigma, \quad (2)$$

where u_σ^g is the solution of (1). We describe the precise mathematical setting in Section 2.1.

In several applications, EIT is used to determine the position of conductivity changes. This includes anomaly detection problems, where $\Lambda(\sigma)$ is compared to a reference NtD $\Lambda(\sigma_0)$ in order to determine, if and where σ differs from a known background conductivity σ_0 . This problem also appears in time-difference EIT, where measurements at different times are compared to monitor temporal conductivity changes.

These applications lead to the *shape reconstruction* problem of determining the support of $\sigma - \sigma_0$ from $\Lambda(\sigma)$ and $\Lambda(\sigma_0)$.

A prominent noniterative shape reconstruction method is the Factorization Method. It was introduced by Kirsch [1] for inverse scattering problems and extended to EIT by Brühl and Hanke [2–4]. In its original form (cf. [4]), the method assumes that

$$\sigma_0(x) = 1, \quad \sigma(x) = 1 + \kappa(x) \chi_D(x), \quad (3)$$

where $D \subseteq \Omega$ is a union of separated, smoothly bounded, and simply connected domains, on which there is a conductivity jump of at least $\epsilon > 0$; that is,

$$\kappa(x) \geq \epsilon \quad \forall x \in D, \quad \text{or } \kappa(x) \leq -\epsilon \quad \forall x \in D. \quad (4)$$

The method then characterizes the unknown shape D by a *range criterion*. For all unit vectors $d \in \mathbb{R}^n$, $\|d\| = 1$,

$$z \in D \quad \text{iff } \Phi_{z,d}|_\Sigma \in \mathcal{R}(|\Lambda(\sigma) - \Lambda(1)|^{1/2}), \quad (5)$$

where $\Phi_{z,d}$ is the so-called *dipole function*, that is, the solution of

$$\Delta \Phi_{z,d} = d \cdot \nabla \delta_z \quad \text{in } \Omega, \quad \partial_\nu \Phi_{z,d}|_{\partial\Omega} = 0. \quad (6)$$

The range criterion (5) can be implemented numerically, so that each point $z \in \Omega$ can be tested whether it belongs to the unknown inclusion or not.

Substantial progress has been made on the Factorization Method since the original works of Kirsch, Brühl, and Hanke. In the following, we restrict ourselves to progress in the context of EIT. Overviews on the FM for EIT have been given by Hanke and Brühl [5], in the book of Kirsch and Grinberg [6], and in a recent chapter of Hanke and Kirsch in Scherzer's Handbook of Mathematical Methods in Imaging [7]. The FM for EIT has been treated as a special case of more general elliptic problems by Kirsch [8], the author [9], and by Nachman, Päiväranta and Teirilä [10]. A half-space setting has been considered by Hanke and Schappel [11]. Electrode models have been covered in the works of Brühl, Lechleiter, Hakula, Hanke, Hyvönen and Pursiainen [5, 12–15]. The FM has been extended to the complex conductivity case arising in frequency-difference EIT by Seo, Woo and the author [16, 17]. A priori separated indefinite inclusions have been treated by Schmitt [18], and Schmitt and Kirsch discussed the determination of the contrast level in the context of the FM for EIT in [19]. Hyvönen and the author have removed the assumptions on the inclusion contrast and boundary regularity in [20], and [21] discusses the relation of the FM to localized potentials.

In this work, we aim to summarize the theoretical progress and present a state-of-the-art formulation of the Factorization Method for EIT with continuous data. In particular, we will formulate the method for general piecewise analytic conductivities and give short and self-contained proofs.

2. Setting and Auxiliary Results

2.1. The Setting. We start by making the mathematical setting precise. Let $\Omega \subseteq \mathbb{R}^n$, $n \geq 2$, denote a bounded domain with smooth boundary $\partial\Omega$ and outer normal vector ν . Let $\Sigma \subseteq \partial\Omega$ be an open part of the boundary. $L_+^\infty(\Omega)$ denotes the subspace of $L^\infty(\Omega)$ -functions with positive essential infima. $H_\diamond^1(\Omega)$ and $L_\diamond^2(\Sigma)$ denote the spaces of H^1 - and L^2 -functions with vanishing integral mean on $\partial\Omega$ (resp., Σ).

For $\sigma \in L_+^\infty(\Omega)$ and $g \in L_\diamond^2(\Sigma)$, there exists a unique solution $u_\sigma^g \in H_\diamond^1(\Omega)$ of the elliptic partial differential equation

$$\nabla \cdot \sigma \nabla u_\sigma^g = 0 \quad \text{in } \Omega, \quad \sigma \partial_\nu u_\sigma^g|_{\partial\Omega} = \begin{cases} g & \text{on } \Sigma, \\ 0 & \text{else,} \end{cases} \quad (7)$$

so that we can define the Neumann-to-Dirichlet operator (NtD)

$$\Lambda(\sigma) : L_\diamond^2(\Sigma) \longrightarrow L_\diamond^2(\Sigma), \quad g \longmapsto u_\sigma^g|_\Sigma, \quad (8)$$

where $u_\sigma^g \in H_\diamond^1(\Omega)$ solves (7). $\Lambda(\sigma)$ is a self-adjoint, compact linear operator.

Let $\sigma_0 \in L_+^\infty(\Omega)$ be piecewise analytic. For each point $z \in \Omega$ that has a neighborhood in which σ_0 is analytic, and each unit vector $d \in \mathbb{R}^n$, $\|d\| = 1$, let $\Phi_{z,d}$ be the solution of

$$\nabla \cdot \sigma_0 \nabla \Phi_{z,d} = d \cdot \nabla \delta_z \quad \text{in } \Omega, \quad \sigma_0 \partial_\nu \Phi_{z,d}|_{\partial\Omega} = 0. \quad (9)$$

$\Phi_{z,d}$ is called a *dipole function*.

2.2. Auxiliary Results. Our presentation of the Factorization Method in the next section relies on the following four lemmas. The first lemma is frequently called a *monotony lemma* since it shows that a larger conductivity leads to a smaller NtD. More precisely, it shows a relation between the difference of two NtDs and the difference of the corresponding conductivities and the interior energy of an electric potential. The second lemma shows that this energy term is the image of the adjoint of an auxiliary virtual measurement operator that is defined on a subregion of Ω . The third lemma is a functional analytic relation between the norm of an image of an operator and the range of its adjoint. Together with the first two lemmas, it implies that the range of the auxiliary virtual measurement operator can be calculated from the NtDs. Finally, using the previous dipole functions, the last lemma shows that the range of the auxiliary virtual measurement operator determines the region on which they are defined.

We start with the monotony lemma.

Lemma 1. *Let $\sigma_1, \sigma_0 \in L_+^\infty(\Omega)$. Then, for all $g \in L_\diamond^2(\partial\Omega)$,*

$$\int_\Omega (\sigma_0 - \sigma_1) |\nabla u_0|^2 dx \leq \int_\Sigma g (\Lambda_1 - \Lambda_0) g ds \leq \int_\Omega \frac{\sigma_0}{\sigma_1} (\sigma_0 - \sigma_1) |\nabla u_0|^2 dx, \quad (10)$$

where we abbreviated $\Lambda_j := \Lambda(\sigma_j)$, $j = 0, 1$, and $u_0 := u_{\sigma_0}^g$.

Proof. The lemma seems to go back to Ikehata, Kang, Seo, and Sheen [22, 23], cf. also the similar arguments in Kirsch [8], Ide et al. [24], and in the works of Seo and the author [16, 25]. For the sake of completeness, we copy the short proof from [25]. For all $g \in L_\diamond^2(\partial\Omega)$, we have that

$$\begin{aligned} \int_\Omega \sigma_1 \nabla u_1 \cdot \nabla u_0 dx &= \int_\Sigma g u_0 ds \\ &= \int_\Omega \sigma_0 \nabla u_0 \cdot \nabla u_0 dx = \int_\Sigma g \Lambda_0 g ds. \end{aligned} \quad (11)$$

Hence, from

$$\begin{aligned} \int_\Omega \sigma_1 \nabla (u_1 - u_0) \cdot \nabla (u_1 - u_0) dx &= \int_\Omega \sigma_1 |\nabla u_1|^2 dx - \int_\Omega \sigma_0 |\nabla u_0|^2 dx \\ &\quad + \int_\Omega (\sigma_1 - \sigma_0) |\nabla u_0|^2 dx, \end{aligned} \quad (12)$$

we obtain that

$$\begin{aligned} \int_\Sigma g (\Lambda_1 - \Lambda_0) g ds &= \int_\Omega (\sigma_0 - \sigma_1) |\nabla u_0|^2 dx \\ &\quad + \int_\Omega \sigma_1 |\nabla (u_1 - u_0)|^2 dx, \end{aligned} \quad (13)$$

which already yields the first asserted inequality.

By interchanging σ_1 and σ_0 , we conclude that

$$\begin{aligned} & \int_{\Sigma} g (\Lambda_0 - \Lambda_1) g ds \\ &= \int_{\Omega} (\sigma_1 - \sigma_0) |\nabla u_1|^2 dx + \int_{\Omega} \sigma_0 |\nabla (u_0 - u_1)|^2 dx \quad (14) \\ &= \int_{\Omega} \left(\sigma_1 \left| \nabla u_1 - \frac{\sigma_0}{\sigma_1} \nabla u_0 \right|^2 + \left(\sigma_0 - \frac{\sigma_0^2}{\sigma_1} \right) |\nabla u_0|^2 \right) dx \end{aligned}$$

and, hence, obtain the second inequality. \square

Given a reference conductivity $\sigma_0 \in L_+^{\infty}(\Omega)$ and a measurable subset $D \subseteq \Omega$, we define the *virtual measurement operator* L_D by

$$L_D : L^2(D)^n \longrightarrow L_{\diamond}^2(\Sigma), \quad F \longmapsto \nu|_{\Sigma}, \quad (15)$$

where $\nu \in H_{\diamond}^1(\Omega)$ solves

$$\int_{\Omega} \sigma_0 \nabla \nu \cdot \nabla w dx = \int_D F \cdot \nabla w dx \quad \forall w \in H_{\diamond}^1(\Omega). \quad (16)$$

The energy term $|\nabla u_0|^2$ in Lemma 1 can be identified with the norm of the adjoint of this virtual measurement operator.

Lemma 2. *The adjoint operator of L_D is given by*

$$L_D^* : L_{\diamond}^2(\Sigma) \longrightarrow L^2(D)^n, \quad g \longmapsto \nabla u_0|_D, \quad (17)$$

where $u_0 \in H_{\diamond}^1(\Omega)$ solves

$$\nabla \cdot \sigma_0 \nabla u_0 = 0 \quad \text{in } \Omega, \quad \sigma_0 \partial_{\nu} u_0|_{\partial\Omega} = \begin{cases} g & \text{on } \Sigma, \\ 0 & \text{else.} \end{cases} \quad (18)$$

Proof. For all $g \in L_{\diamond}^2(\Sigma)$ and $F \in L^2(D)^n$, we have that

$$\begin{aligned} \int_D (L_D^* g) \cdot F dx &= \int_{\Sigma} g (L_D F) dx = \int_{\Sigma} g \nu|_{\Sigma} dx \\ &= \int_{\Omega} \sigma_0 \nabla u_0 \cdot \nabla \nu dx = \int_D \nabla u_0 \cdot F dx, \end{aligned} \quad (19)$$

which shows the assertion. \square

The following functional analytic lemma uses bounds on the image of an operator to characterize the range of its dual operator.

Lemma 3. *Let X and Y be real Hilbert spaces with inner products $(\cdot, \cdot)_X$ and $(\cdot, \cdot)_Y$, respectively. Let $A \in \mathcal{L}(X; Y)$ and $x' \in X$. Then,*

$$x' \in \mathcal{R}(A^*) \quad \text{iff } \exists C > 0 : |(x', x)_X| \leq C \|Ax\| \quad \forall x \in X. \quad (20)$$

In particular, if X, Y_1 , and Y_2 are three real Hilbert spaces, $A_i \in \mathcal{L}(Y_i, X)$, $i = 1, 2$, and if there exists $C > 0$ with

$$\|A_1^* x\| \leq C \|A_2^* x\| \quad \forall x \in X, \quad (21)$$

then $\mathcal{R}(A_1) \subseteq \mathcal{R}(A_2)$.

Proof. The assertion can be generalized to Banach spaces, and, in that context, it is called the “14th important property of Banach spaces” in Bourbaki [26]. For the sake of completeness, we rewrite the proof from [27] to Hilbert spaces.

If $x' \in \mathcal{R}(A^*)$, then there exists $y' \in Y$ such that $x' = A^* y'$. Hence,

$$\begin{aligned} |(x', x)_X| &= |(A^* y', x)_X| \\ &= |(y', Ax)_Y| \leq \|y'\| \|Ax\| \quad \forall x \in X, \end{aligned} \quad (22)$$

so that the assertion holds with $C = \|y'\|$.

Now let $x' \in X$ be such that there exists $C > 0$ with $|(x', x)_X| \leq C \|Ax\|$ for all $x \in X$. We define

$$f(y) := (x', x)_X \quad \text{for every } y = Ax \in \mathcal{R}(A). \quad (23)$$

Then, f is a well-defined, continuous linear functional on $\mathcal{R}(A)$. By setting it to zero on $\mathcal{R}(A)^{\perp}$, we can extend f to a continuous linear functional on Y . Using the Riesz theorem, it follows that there exists $y' \in Y$ with

$$(y', y)_Y = f(y) \quad \forall y \in \mathcal{R}(A). \quad (24)$$

Hence, for all $x \in X$, we have

$$(A^* y', x)_X = (y', Ax)_Y = f(Ax) = (x', x)_X, \quad (25)$$

so that $x' = A^* y' \in \mathcal{R}(A^*)$. \square

The last lemma shows that the range of the virtual measurement operator L_D determines the region D on which it is defined. We state the lemma for a simple special case, a generalized version of the lemma will be formulated in Section 3.2.

Lemma 4. *Let $\sigma_0 = 1$, $D \subseteq \Omega$ be open, and $\overline{D} \subseteq \Omega$ have a connected complement $\Omega \setminus \overline{D}$.*

Then, for all unit vectors $d \in \mathbb{R}^n$, $\|d\| = 1$, and every point $z \in \Omega \setminus \partial D$, it holds that

$$z \in D \quad \text{iff } \Phi_{z,d}|_{\Sigma} \in \mathcal{R}(L_D). \quad (26)$$

Proof. The proof is similar to the one of [21, Lemma 2.9].

First, let $z \in D$ and $\epsilon > 0$ be such that $\overline{B_{\epsilon}(z)} \subseteq D$. We choose

$$\begin{aligned} f_1 &\in H^1(B_{\epsilon}(z)) \quad \text{with } f_1|_{\partial B_{\epsilon}(z)} = \Phi_{z,d}|_{\partial B_{\epsilon}(z)}, \\ f_2 &\in H^1(B_{\epsilon}(z)) \quad \text{with } \Delta f_2 = 0, \\ \partial_{\nu} f_2|_{\partial B_{\epsilon}(z)} &= \partial_{\nu} \Phi_{z,d}|_{\partial B_{\epsilon}(z)}, \end{aligned} \quad (27)$$

and let $F \in L^2(D)^n$ be the zero continuation of $\nabla(f_1 - f_2)$ to D .

Then, the function

$$\nu := \begin{cases} \Phi_{z,d} & \text{in } \Omega \setminus \overline{B_{\epsilon}(z)}, \\ f_1 & \text{in } B_{\epsilon}(z) \end{cases} \quad (28)$$

fulfills $v \in H_{\diamond}^1(\Omega)$, and, for all $w \in H_{\diamond}^1(\Omega)$,

$$\begin{aligned} & \int_{\Omega} \nabla v \cdot \nabla w dx \\ &= \int_{\Omega \setminus \overline{B_{\epsilon}(z)}} \nabla \Phi_{z,d} \cdot \nabla w dx + \int_{B_{\epsilon}(z)} \nabla f_1 \cdot \nabla w dx \\ &= - \int_{\partial B_{\epsilon}(z)} \partial_{\nu} \Phi_{z,d} w|_{\partial B_{\epsilon}(z)} ds + \int_{B_{\epsilon}(z)} \nabla f_1 \cdot \nabla w dx \\ &= \int_{B_{\epsilon}(z)} \nabla (f_1 - f_2) \cdot \nabla w dx = \int_D F \cdot \nabla w dx. \end{aligned} \quad (29)$$

This shows that $\Phi_{z,d}|_{\Sigma} = v|_{\Sigma} = L_D(F) \in \mathcal{R}(L_D)$.

Now let $\Phi_{z,d}|_{\Sigma} \in \mathcal{R}(L_D)$. Let $v \in H_{\diamond}^1(\Omega)$ be the function from the definition of L_D . Then,

$$v|_{\Sigma} = \Phi_{z,d}|_{\Sigma}, \quad \partial_{\nu} v|_{\Sigma} = 0 = \partial_{\nu} \Phi_{z,d}|_{\Sigma}, \quad (30)$$

so that it follows by unique continuation that $v = \Phi_{z,d}$ in the connected set $\Omega \setminus (\overline{D} \cup \{z\})$.

If $z \notin \overline{D}$, then $d \cdot \nabla \delta_z \notin H^{-2}(\Omega \setminus \overline{D})$, and thus $\Phi_{z,d} \notin L^2(\Omega \setminus \overline{D})$, which contradicts that $v = \Phi_{z,d}$ in $\Omega \setminus (\overline{D} \cup \{z\})$. Hence, $z \in \overline{D}$. \square

3. The Factorization Method

Now we will formulate the Factorization Method and characterize a region where a conductivity σ differs from a reference conductivity σ_0 by a range criterion. Before we turn to a new general formulation of the method, we first state it for a special case that is similar to the one that was treated in the original works of Brühl and Hanke [3, 4].

3.1. The Factorization Method for a Simple Special Case

Theorem 5. *Let $\sigma_0 = 1$ and $\sigma = 1 + \chi_D$, where $D \subseteq \Omega$ is an open set so that $\overline{D} \subseteq \Omega$ has a connected complement $\Omega \setminus \overline{D}$. Then, for all $z \in \Omega$, $z \notin \partial D$, and all dipole directions $d \in \mathbb{R}^n$, $\|d\| = 1$,*

$$z \in D \quad \text{iff} \quad \Phi_{z,d}|_{\Sigma} \in \mathcal{R}(|\Lambda(\sigma) - \Lambda(1)|^{1/2}). \quad (31)$$

Proof. The monotony Lemma 1 yields that for all $g \in L_{\diamond}^2(\partial\Omega)$,

$$\int_D |\nabla u_0|^2 dx \geq \int_{\Sigma} g (\Lambda(1) - \Lambda(\sigma)) g ds \geq \int_D \frac{1}{2} |\nabla u_0|^2 dx. \quad (32)$$

Hence, $|\Lambda(\sigma) - \Lambda(1)| = \Lambda(1) - \Lambda(\sigma)$, and, using Lemma 2, we can restate this in the form

$$\|L_{D,g}^*\|^2 \geq \|\Lambda(\sigma) - \Lambda(1)\|^{1/2} g\|^2 \geq \frac{1}{2} \|L_{D,g}^*\|^2. \quad (33)$$

Using the functional analytic Lemma 3, this implies that

$$\mathcal{R}(L_D) = \mathcal{R}(|\Lambda(\sigma) - \Lambda(1)|^{1/2}), \quad (34)$$

and thus the assertion follows from the relation between D and $\mathcal{R}(L_D)$ in Lemma 4. \square

Obviously, the same arguments can be used to treat the case $\sigma(x) = 1 + \kappa(x)\chi_D(x)$, when there exists a conductivity jump $\epsilon > 0$ so that either

$$\kappa(x) \geq \epsilon \quad \forall x \in D \quad \text{or} \quad \kappa(x) \leq -\epsilon \quad \forall x \in D. \quad (35)$$

3.2. The Factorization Method for the General Piecewise Analytic Case. Now we drop the assumptions that the background is constant, that there is a clear conductivity jump, and that the complement of the inclusions is connected. We will merely assume that the reference conductivity σ_0 is a piecewise analytic function and that either $\sigma - \sigma_0 \geq 0$ or $\sigma - \sigma_0 \leq 0$. Roughly speaking, under this general assumption, the Factorization Method then characterizes the support of $\sigma - \sigma_0$ up to holes in the support that have no connections to Σ . For a precise formulation, we use the concept of the inner and outer support from [28] that has been inspired by the use of the infinity support of Kusiak and Sylvester [29]; see also [25, 30].

Definition 6. A relatively open set $U \subseteq \overline{\Omega}$ is called *connected* to Σ if $U \cap \Omega$ is connected and $U \cap \Sigma \neq \emptyset$.

For a measurable function $\kappa : \Omega \rightarrow \mathbb{R}$, we define

- (a) the *support* $\text{supp}(\kappa)$ as the complement (in $\overline{\Omega}$) of the union of those relatively open $U \subseteq \overline{\Omega}$, for which $\kappa|_U \equiv 0$,
- (b) the *inner support* $\text{inn supp } \kappa$ as the union of those open sets $U \subseteq \Omega$, for which $\text{ess inf}_{x \in U} |\kappa(x)| > 0$,
- (c) the *outer support* $\text{out}_{\Sigma} \text{ supp } \kappa$ as the complement (in $\overline{\Omega}$) of the union of those relatively open $U \subseteq \overline{\Omega}$ that are connected to Σ and for which $\kappa|_U \equiv 0$.

The interior of a set $M \subseteq \Omega$ is denoted by $\text{int } M$ and its closure (with respect to \mathbb{R}^n) by \overline{M} . If M is measurable, we also define

- (d) $\text{out}_{\Sigma} M = \text{out}_{\Sigma} \text{ supp } \chi_M$.

It is easily checked that $\text{out}_{\Sigma}(\text{supp } \kappa) = \text{out}_{\Sigma} \text{ supp } \kappa$.

With this concept, we can extend the range characterization in Lemma 4 to a general setting (see also Remark 9 later).

Lemma 7. *Let $\sigma_0 \in L_+^{\infty}(\Omega)$ be piecewise analytic. Let $D \subseteq \Omega$ be measurable.*

Then, for all unit vectors $d \in \mathbb{R}^n$, $\|d\| = 1$, and every point $z \in \Omega$ that has a neighborhood in which σ_0 is analytic,

$$z \in \text{int } D \quad \text{implies} \quad \Phi_{z,d}|_{\Sigma} \in \mathcal{R}(L_D), \quad (36)$$

and

$$\Phi_{z,d}|_{\Sigma} \in \mathcal{R}(L_D) \quad \text{implies} \quad z \in \text{out}_{\Sigma} D. \quad (37)$$

Proof. If $z \in \text{int } D$, then there exists a small ball $\overline{B_{\epsilon}(z)} \subseteq D$, and the first assertion follows as in the proof of Lemma 4.

To show the second assertion, let $\Phi_{z,d}|_{\Sigma} \in \mathcal{R}(L_D)$, and let $v \in H_{\diamond}^1(\Omega)$ be the function from the definition of L_D , so that (as in the proof of Lemma 4)

$$v|_{\Sigma} = \Phi_{z,d}|_{\Sigma}, \quad \partial_{\nu} v|_{\Sigma} = 0 = \partial_{\nu} \Phi_{z,d}|_{\Sigma}. \quad (38)$$

Assume that $z \notin \text{out}_\Sigma D$. Then, there exists a relatively open $U \subseteq \bar{\Omega}$ that is connected to Σ and contains z . Hence, by unique continuation, it follows that $v|_U = \Phi_{z,d}|_U$, and we obtain the same contradiction as in the proof of Lemma 4. \square

Now, we can formulate and prove the Factorization Method for general piecewise analytic conductivities.

Theorem 8. *Let $\sigma \in L_+^\infty(\Omega)$, and let $\sigma_0 \in L_+^\infty(\Omega)$ be a piecewise analytic function. Let either*

$$\sigma(x) \geq \sigma_0(x) \quad \forall x \in \Omega \quad \text{or} \quad \sigma(x) \leq \sigma_0(x) \quad \forall x \in \Omega. \quad (39)$$

Then, for all $z \in \Omega$ that have a neighborhood in which σ_0 is analytic, as well as all unit vectors $d \in \mathbb{R}^n$, $\|d\| = 1$,

$$z \in \text{inn supp}(\sigma - \sigma_0) \quad \text{implies} \quad \Phi_{z,d}|_\Sigma \in \mathcal{R}\left(|\Lambda(\sigma) - \Lambda(\sigma_0)|^{1/2}\right), \quad (40)$$

and

$$\Phi_{z,d}|_\Sigma \in \mathcal{R}\left(|\Lambda(\sigma) - \Lambda(\sigma_0)|^{1/2}\right) \quad \text{implies} \quad z \in \text{out}_\Sigma \text{supp}(\sigma - \sigma_0). \quad (41)$$

Proof. Let $z \in \Omega$ have a neighborhood in which σ_0 is analytic, and let $d \in \mathbb{R}^n$ be a unit vector with $\|d\| = 1$. We only prove the assertions for $\sigma \geq \sigma_0$. The other case is completely analogous.

First, let $z \in \text{inn supp}(\sigma - \sigma_0)$. Then there exists a small ball $B_\epsilon(z)$ and $\delta > 0$ so that $\sigma - \sigma_0 \geq \delta$ on $B_\epsilon(z)$. Using the monotony Lemma 1, it follows that, for all $g \in L_\diamond^2(\partial\Omega)$,

$$\begin{aligned} & \int_\Sigma g(\Lambda(\sigma_0) - \Lambda(\sigma)) g ds \\ & \geq \int_\Omega \frac{\sigma_0}{\sigma} (\sigma - \sigma_0) |\nabla u_0|^2 dx \\ & \geq \delta \|\sigma_0\|_{L^\infty(\Omega)} \left\| \frac{1}{\sigma} \right\|_{L^\infty(\Omega)} \int_{B_\epsilon(z)} |\nabla u_0|^2 dx \\ & \geq \delta \|\sigma_0\|_{L^\infty(\Omega)} \left\| \frac{1}{\sigma} \right\|_{L^\infty(\Omega)} \|L_{B_\epsilon(z)}^* g\|^2. \end{aligned} \quad (42)$$

Using the functional analytic Lemma 3, we obtain that

$$\mathcal{R}(L_{B_\epsilon(z)}) \subseteq \mathcal{R}\left(|\Lambda(\sigma) - \Lambda(\sigma_0)|^{1/2}\right), \quad (43)$$

and Lemma 7 yields that

$$\Phi_{z,d}|_\Sigma \in \mathcal{R}(L_{B_\epsilon(z)}) \subseteq \mathcal{R}\left(|\Lambda(\sigma) - \Lambda(\sigma_0)|^{1/2}\right). \quad (44)$$

On the other hand, with $D := \text{supp}(\sigma - \sigma_0)$, the monotony Lemma 1 shows that for all $g \in L_\diamond^2(\partial\Omega)$,

$$\begin{aligned} & \int_\Sigma g(\Lambda(\sigma_0) - \Lambda(\sigma_1)) g ds \leq \int_\Omega (\sigma_1 - \sigma_0) |\nabla u_0|^2 dx \\ & \leq \|\sigma_1 - \sigma_0\|_{L^\infty(\Omega)} \int_D |\nabla u_0|^2 dx \\ & \leq \|\sigma_1 - \sigma_0\|_{L^\infty(\Omega)} \|L_D^* g\|^2, \end{aligned} \quad (45)$$

so that we obtain from the functional analytic Lemma 3

$$\mathcal{R}\left(|\Lambda(\sigma) - \Lambda(\sigma_0)|^{1/2}\right) \subseteq \mathcal{R}(L_D). \quad (46)$$

Hence, Lemma 7 yields that

$$\Phi_{z,d}|_\Sigma \in \mathcal{R}\left(|\Lambda(\sigma) - \Lambda(\sigma_0)|^{1/2}\right) \subseteq \mathcal{R}(L_D) \quad \text{implies} \quad (47)$$

$$z \in \text{out}_\Sigma(\text{supp}(\sigma - \sigma_0)) = \text{out}_\Sigma \text{supp}(\sigma - \sigma_0). \quad \square$$

Remark 9. Theorem 8 shows that the Factorization Method is able to detect the support of a conductivity difference up to the difference between the outer and the inner support, that is, roughly speaking, up to holes in the support that have no connections to the boundary. It leaves open whether points in such holes will fulfill the range criterion of the Factorization Method or not.

A result of Hyvönen and the author [30, Lemma 2.5] shows that for every smooth domain D with $\bar{D} \subset \Omega$ and every unit vector $d \in \mathbb{R}^n$, $\|d\| = 1$,

$$\Phi_{z,d}|_\Sigma \in \mathcal{R}\left(|\Lambda(\sigma) - \Lambda(\sigma_0)|^{1/2}\right) \quad \forall z \in \partial D \quad (48)$$

implies

$$\Phi_{z,d}|_\Sigma \in \mathcal{R}\left(|\Lambda(\sigma) - \Lambda(\sigma_0)|^{1/2}\right) \quad \forall z \in D. \quad (49)$$

In that sense, we can expect that holes in the support will be filled up and that the set detected by the Factorization Method is essentially the outer support of the conductivity difference.

3.3. The Factorization Method for the Indefinite Case. It is a long standing open theoretical problem whether the range criterion of the Factorization Method holds true without the *definiteness assumption* that $\sigma \geq \sigma_0$ on Ω or $\sigma \leq \sigma_0$ on Ω . However, Grinberg, Kirsch, and Schmitt [18, 31] showed how to *exclude* a region $E \subseteq \Omega$ from Ω , in such a way that the Factorization Method only requires the definiteness assumption on $\Omega \setminus E$. In this subsection, we show how their idea can be incorporated into our formulation of the method.

To point out the main idea, we first formulate the result for a simple special case. Let us stress that, for $\sigma = 1 + \chi_{D^+} - (1/2)\chi_{D^-}$, it is not known whether

$$z \in D^+ \cup D^- \quad \text{iff} \quad \Phi_{z,d}|_\Sigma \in \mathcal{R}\left(|\Lambda(\sigma) - \Lambda(1)|^{1/2}\right). \quad (50)$$

However, we can still use the Factorization Method if we have some a priori knowledge that separates D^+ and D^- . More precisely, if we know a subset E that contains D^- without intersecting D^+ , then we can use the Factorization Method to find $D^+ \cup E$ (and thus D^+).

Theorem 10. Let $\sigma_0 = 1$ and $\sigma = 1 + \chi_{D^+} - (1/2)\chi_{D^-}$, where $D^+, D^- \subseteq \Omega$ are open. Let $E \subseteq \Omega$ be an open set.

(a) If $D^+ \subseteq E$ and $\overline{D^- \cup E} \subseteq \Omega$ has a connected complement, then for all $z \in \Omega$, $z \notin \partial(D^- \cup E)$, and all dipole directions $d \in \mathbb{R}^n$, $\|d\| = 1$,

$$z \in D^- \cup E \quad \text{iff} \quad \Phi_{z,d}|_\Sigma \in \mathcal{R} \left(|\Lambda(\sigma) - \Lambda(1) + L_E L_E^*|^{1/2} \right). \quad (51)$$

(b) If $D^- \subseteq E$ and $\overline{D^+ \cup E} \subseteq \Omega$ has a connected complement, then for all $z \in \Omega$, $z \notin \partial(D^+ \cup E)$, and all dipole directions $d \in \mathbb{R}^n$, $\|d\| = 1$,

$$z \in D^+ \cup E \quad \text{iff} \quad \Phi_{z,d}|_\Sigma \in \mathcal{R} \left(|\Lambda(\sigma) - \Lambda(1) - L_E L_E^*|^{1/2} \right). \quad (52)$$

Proof. The monotony Lemma 1 yields that for all $g \in L^2_\diamond(\partial\Omega)$,

$$\begin{aligned} & \frac{1}{2} \int_{D^-} |\nabla u_0|^2 dx - \int_{D^+} |\nabla u_0|^2 dx \\ & \leq \int_\Sigma g (\Lambda(\sigma) - \Lambda(1)) g ds \\ & \leq \int_{D^-} |\nabla u_0|^2 dx - \frac{1}{2} \int_{D^+} |\nabla u_0|^2 dx. \end{aligned} \quad (53)$$

Since (cf. Lemma 2)

$$\int_\Sigma g (L_E L_E^*) g ds = \|L_E^* g\|^2 = \int_E |\nabla u_0|^2 dx, \quad (54)$$

it follows for case (a) that

$$\begin{aligned} \frac{1}{2} \int_{D^- \cup E} |\nabla u_0|^2 dx & \leq \int_\Sigma g (\Lambda(\sigma) - \Lambda(1) + 2L_E L_E^*) g ds \\ & \leq \int_{D^- \cup E} |\nabla u_0|^2 dx. \end{aligned} \quad (55)$$

Using the functional analytic Lemma 3, this implies that

$$\mathcal{R}(L_{D^- \cup E}) = \mathcal{R} \left(|\Lambda(\sigma) - \Lambda(1) + 2L_E L_E^*|^{1/2} \right), \quad (56)$$

so that the assertion (a) follows from Lemma 4.

In case (b), we obtain that

$$\begin{aligned} \frac{3}{2} \int_{D^+ \cup E} |\nabla u_0|^2 dx & \geq \int_\Sigma g (\Lambda(1) - \Lambda(\sigma) + 2L_E L_E^*) g ds \\ & \geq \frac{1}{2} \int_{D^+ \cup E} |\nabla u_0|^2 dx, \end{aligned} \quad (57)$$

and the same arguments as above yield the assertion. \square

We can also extend these ideas to the general setting of Section 3.2.

Theorem 11. Let $\sigma \in L^*_+(\Omega)$ and let $\sigma_0 \in L^*_+(\Omega)$ be a piecewise analytic function. Let $E \subseteq \Omega$ be a measurable set.

Choose $\alpha, \beta \in \mathbb{R}$ such that

$$\alpha > \|\sigma - \sigma_0\|_{L^\infty(\Omega)}, \quad \beta > \left\| \frac{\sigma_0}{\sigma} (\sigma_0 - \sigma) \right\|_{L^\infty(\Omega)}. \quad (58)$$

(a) If $\sigma \leq \sigma_0$ on $\Omega \setminus E$, then for all $z \in \Omega$ that have a neighborhood in which σ_0 is analytic, as well as all unit vectors $d \in \mathbb{R}^n$, $\|d\| = 1$,

$$\begin{aligned} z \in \text{inn supp}(\sigma - \sigma_0) \cup E \text{ implies} \\ \Phi_{z,d}|_\Sigma \in \mathcal{R} \left(|\Lambda(\sigma) - \Lambda(\sigma_0) + \alpha L_E L_E^*|^{1/2} \right), \end{aligned} \quad (59)$$

and

$$\begin{aligned} \Phi_{z,d}|_\Sigma \in \mathcal{R} \left(|\Lambda(\sigma) - \Lambda(\sigma_0) + \alpha L_E L_E^*|^{1/2} \right) \text{ implies} \\ z \in \text{out}_\Sigma(\text{supp}(\sigma - \sigma_0) \cup E). \end{aligned} \quad (60)$$

(b) If $\sigma \geq \sigma_0$ on $\Omega \setminus E$, then for all $z \in \Omega$ that have a neighborhood in which σ_0 is analytic, as well as all unit vectors $d \in \mathbb{R}^n$, $\|d\| = 1$,

$$\begin{aligned} z \in \text{inn supp}(\sigma - \sigma_0) \cup E, \text{ implies} \\ \Phi_{z,d}|_\Sigma \in \mathcal{R} \left(|\Lambda(\sigma) - \Lambda(\sigma_0) - \beta L_E L_E^*|^{1/2} \right) \end{aligned} \quad (61)$$

and

$$\begin{aligned} \Phi_{z,d}|_\Sigma \in \mathcal{R} \left(|\Lambda(\sigma) - \Lambda(\sigma_0) - \beta L_E L_E^*|^{1/2} \right) \text{ implies} \\ z \in \text{out}_\Sigma(\text{supp}(\sigma - \sigma_0) \cup E). \end{aligned} \quad (62)$$

Proof. For every $z \in \text{inn supp}(\sigma - \sigma_0)$ with $z \notin E$, there exists a small ball $B_\epsilon(z)$ and $\delta > 0$ so that $\sigma_0 - \sigma \geq \delta$ on $B_\epsilon(z)$. Using the monotony Lemma 1, it follows that, for all $g \in L^2_\diamond(\partial\Omega)$,

$$\begin{aligned} & \int_\Sigma g (\Lambda(\sigma) - \Lambda(\sigma_0) + \alpha L_E L_E^*) g ds \\ & \geq \int_\Omega (\sigma_0 - \sigma) |\nabla u_0|^2 dx + \alpha \int_E |\nabla u_0|^2 dx \\ & \geq \delta \int_{B_\epsilon(z)} |\nabla u_0|^2 dx + (\alpha - \|\sigma - \sigma_0\|_{L^\infty(\Omega)}) \int_E |\nabla u_0|^2 dx. \end{aligned} \quad (63)$$

As in the previous proofs, we obtain from Lemmas 2 and 3 that

$$\mathcal{R} \left(|\Lambda(\sigma) - \Lambda(\sigma_0) + \alpha L_E L_E^*|^{1/2} \right) \supseteq \mathcal{R} \left(L_{B_c(z) \cup E} \right), \quad (64)$$

so that the first implication of (a) follows from Lemma 7.

The monotony Lemma 1 also implies that

$$\begin{aligned} & \int_{\Sigma} g \left(\Lambda(\sigma) - \Lambda(\sigma_0) + \alpha L_E L_E^* \right) g \, ds \\ & \leq \int_{\Omega} \frac{\sigma_0}{\sigma} (\sigma_0 - \sigma) |\nabla u_0|^2 \, dx + \alpha \int_E |\nabla u_0|^2 \, dx \\ & \leq \left\| \frac{\sigma_0}{\sigma} (\sigma_0 - \sigma) \right\|_{L^\infty(\Omega)} \int_{\text{supp}(\sigma - \sigma_0)} |\nabla u_0|^2 \, dx \\ & \quad + \alpha \int_E |\nabla u_0|^2 \, dx, \end{aligned} \quad (65)$$

so that the second implication of (a) follows from Lemmas 2, 3, and 7. Assertion (b) can be proven analogously. \square

Remark 9 also applies to this case.

4. Conclusions and Remarks

The Factorization Method can be used to detect regions in which a conductivity differs from a known reference conductivity. In this work, we summarized the progress on the method's theoretical foundation. We formulated the method for general piecewise analytic conductivities and gave comparatively simple and self-contained proofs. We also showed how the idea of excluding a part of the imaging region can be incorporated into this formulation.

The regularity assumptions can be weakened even further. Our proofs only require unique continuation arguments for the reference conductivity σ_0 and the existence of the dipole functions.

Two major open theoretical questions still exist in the context of the Factorization Method. The theoretical justification of the method requires a definiteness condition (on the whole domain or after excluding an a priori known part of the domain). It is unknown whether the method's range criterion holds without such a definiteness condition. The second open question concerns the numerical stability of the method's range criterion. So far, there are no rigorous convergence results for numerical implementations of this range criterion (see, however, Lechleiter [32] for a first step in this direction). As a promising approach to overcome both problems, we would like to point out the recent work on monotony-based methods [28].

Acknowledgments

This paper was funded by the German Research Foundation (DFG) and the University of Würzburg in the funding programme Open Access Publishing.

References

- [1] A. Kirsch, "Characterization of the shape of a scattering obstacle using the spectral data of the far field operator," *Inverse Problems*, vol. 14, no. 6, pp. 1489–1512, 1998.
- [2] M. Brühl, *Gebietserkennung in der elektrischen Impedanztomographie [Ph.D. thesis]*, Universität Karlsruhe, 1999.
- [3] M. Brühl and M. Hanke, "Numerical implementation of two noniterative methods for locating inclusions by impedance tomography," *Inverse Problems*, vol. 16, no. 4, pp. 1029–1042, 2000.
- [4] M. Brühl, "Explicit characterization of inclusions in electrical impedance tomography," *SIAM Journal on Mathematical Analysis*, vol. 32, no. 6, pp. 1327–1341, 2001.
- [5] M. Hanke and M. Brühl, "Recent progress in electrical impedance tomography," *Inverse Problems*, vol. 19, no. 6, pp. S65–S90, 2003.
- [6] A. Kirsch and N. Grinberg, *The Factorization Method for Inverse Problems*, vol. 36 of *Oxford Lecture Series in Mathematics and Its Applications*, Oxford University Press, Oxford, UK, 2007.
- [7] M. Hanke and A. Kirsch, "Sampling methods," in *Handbook of Mathematical Models in Imaging*, O. Scherzer, Ed., pp. 501–550, Springer, 2011.
- [8] A. Kirsch, "The factorization method for a class of inverse elliptic problems," *Mathematische Nachrichten*, vol. 278, pp. 258–277, 2005.
- [9] B. Gebauer, "The Factorization Method for real elliptic problems," *Zeitschrift für Analysis und ihre Anwendung*, vol. 25, no. 1, pp. 81–102, 2006.
- [10] A. I. Nachman, L. Päiväranta, and A. Teirilä, "On imaging obstacles inside inhomogeneous media," *Journal of Functional Analysis*, vol. 252, no. 2, pp. 490–516, 2007.
- [11] M. Hanke and B. Schappel, "The factorization method for electrical impedance tomography in the half-space," *SIAM Journal on Applied Mathematics*, vol. 68, no. 4, pp. 907–924, 2008.
- [12] N. Hyvönen, "Complete electrode model of electrical impedance tomography: approximation properties and characterization of inclusions," *SIAM Journal on Applied Mathematics*, vol. 64, pp. 902–931, 2004.
- [13] A. Lechleiter, N. Hyvönen, and H. Hakula, "The factorization method applied to the complete electrode model of impedance tomography," *SIAM Journal on Applied Mathematics*, vol. 68, no. 4, pp. 1097–1121, 2008.
- [14] N. Hyvönen, H. Hakula, and S. Pursiainen, "Numerical implementation of the factorization method within the complete electrode model of electrical impedance tomography," *Inverse Problems and Imaging*, vol. 1, pp. 299–317, 2007.
- [15] H. Hakula and N. Hyvönen, "On computation of test dipoles for factorization method," *BIT Numerical Mathematics*, vol. 49, no. 1, pp. 75–91, 2009.
- [16] B. Harrach and J. K. Seo, "Detecting inclusions in electrical impedance tomography without reference measurements," *SIAM Journal on Applied Mathematics*, vol. 69, no. 6, pp. 1662–1681, 2009.
- [17] B. Harrach, J. K. Seo, and E. J. Woo, "Factorization method and its physical justification in frequency-difference electrical impedance tomography," *IEEE Transactions on Medical Imaging*, vol. 29, no. 11, pp. 1918–1926, 2010.
- [18] S. Schmitt, "The factorization method for EIT in the case of mixed inclusions," *Inverse Problems*, vol. 25, no. 6, Article ID 065012, 2009.

- [19] S. Schmitt and A. Kirsch, "A factorization scheme for determining conductivity contrasts in impedance tomography," *Inverse Problems*, vol. 27, Article ID 095005, 2011.
- [20] B. Gebauer and N. Hyvönen, "Factorization method and irregular inclusions in electrical impedance tomography," *Inverse Problems*, vol. 23, no. 5, pp. 2159–2170, 2007.
- [21] B. Gebauer, "Localized potentials in electrical impedance tomography," *Inverse Problems and Imaging*, vol. 2, pp. 251–269, 2008.
- [22] H. Kang, J. K. Seo, and D. Sheen, "The inverse conductivity problem with one measurement: Stability and estimation of size," *SIAM Journal on Mathematical Analysis*, vol. 28, no. 6, pp. 1389–1405, 1997.
- [23] M. Ikehata, "Size estimation of inclusion," *Journal of Inverse and Ill-Posed Problems*, vol. 6, no. 2, pp. 127–140, 1998.
- [24] T. Ide, H. Isozaki, S. Nakata, S. Siltanen, and G. Uhlmann, "Probing for electrical inclusions with complex spherical waves," *Communications on Pure and Applied Mathematics*, vol. 60, no. 10, pp. 1415–1442, 2007.
- [25] B. Harrach and J. K. Seo, "Exact shape-reconstruction by one-step linearization in electrical impedance tomography," *The SIAM Journal on Mathematical Analysis*, vol. 42, no. 4, pp. 1505–1518, 2010.
- [26] N. Bourbaki, *Elements of Mathematics, Topological Vector Spaces*, chapters 1–5, Springer, Berlin, Germany, 2003.
- [27] F. Frühauf, B. Gebauer, and O. Scherzer, "Detecting interfaces in a parabolic-elliptic problem from surface measurements," *SIAM Journal on Numerical Analysis*, vol. 45, no. 2, pp. 810–836, 2007.
- [28] B. Harrach and M. Ullrich, "Monotony based shape reconstruction in electrical impedance tomography," submitted for publication.
- [29] S. Kusiak and J. Sylvester, "The scattering support," *Communications on Pure and Applied Mathematics*, vol. 56, no. 11, pp. 1525–1548, 2003.
- [30] B. Gebauer and N. Hyvönen, "Factorization method and inclusions of mixed type in an inverse elliptic boundary value problem," *Inverse Problems and Imaging*, vol. 2, pp. 355–372, 2008.
- [31] N. I. Grinberg and A. Kirsch, "The factorization method for obstacles with a-priori separated sound-soft and sound-hard parts," *Mathematics and Computers in Simulation*, vol. 66, no. 4-5, pp. 267–279, 2004.
- [32] A. Lechleiter, "A regularization technique for the factorization method," *Inverse Problems*, vol. 22, no. 5, pp. 1605–1625, 2006.

Research Article

A Local Region of Interest Imaging Method for Electrical Impedance Tomography with Internal Electrodes

Hyeuknam Kwon,¹ Alistair L. McEwan,^{2,3} Tong In Oh,³ Adnan Farooq,³
Eung Je Woo,³ and Jin Keun Seo¹

¹ Department of Computational Science and Engineering, Yonsei University, Seoul 120-749, Republic of Korea

² The School of Electrical and Information Engineering, The University of Sydney, Sydney NSW 2006, Australia

³ Impedance Imaging Research Center and Department of Biomedical Engineering, Kyung Hee University, Yongin 446-701, Republic of Korea

Correspondence should be addressed to Tong In Oh; tioh@khu.ac.kr

Received 13 November 2012; Revised 1 June 2013; Accepted 10 June 2013

Academic Editor: Bill Lionheart

Copyright © 2013 Hyeuknam Kwon et al. This is an open access article distributed under the Creative Commons Attribution License, which permits unrestricted use, distribution, and reproduction in any medium, provided the original work is properly cited.

Electrical Impedance Tomography (EIT) is a very attractive functional imaging method despite the low sensitivity and resolution. The use of internal electrodes with the conventional reconstruction algorithms was not enough to enhance image resolution and accuracy in the region of interest (ROI). We propose a local ROI imaging method with internal electrodes developed from careful analysis of the sensitivity matrix that is designed to reduce the sensitivity of the voxels outside the local region and optimize the sensitivity of the voxel inside the local region. We perform numerical simulations and physical measurements to demonstrate the localized EIT imaging method. In preliminary results with multiple objects we show the benefits of using an internal electrode and the improved resolution due to the local ROI image reconstruction method. The sensitivity is further increased by allowing the surface electrodes to be unevenly spaced with a higher density of surface electrodes near the ROI. Also, we analyse how much the image quality is improved using several performance parameters for comparison. While these have not yet been studied in depth, it convincingly shows an improvement in local sensitivity in images obtained with an internal electrode in comparison to a standard reconstruction method.

1. Introduction

Electrical Impedance Tomography (EIT) is an attractive electrical properties imaging technique for medical applications due to its speed, safety, relatively low cost, and ability to display unique tissue conductivity information. Conventionally, surface electrodes are used to apply currents and record voltages from the boundary of the object of interest such as the thorax, breast, or head. These measurements are used to reconstruct the internal tissue impedances or conductivities using various image reconstruction methods where sensitivity matrix-based approaches are commonly used. Unfortunately, these measurements are insensitive to local impedance changes away from the measuring positions, whereas they are very sensitive to the boundary geometry and impedance changes near the electrodes. To improve

the sensitivity and distinguishability in some local internal regions, the use of internal electrodes has been suggested by several researchers [1, 2]. These previous works were concentrated in cardiac applications of EIT as catheters are routinely introduced into various locations during cardiac monitoring, electrophysiology (EP mapping), or cardiac radiofrequency ablation (RFA).

EIT with internal electrodes could also be applied to monitoring RFA of liver tumors. RFA is widely used for the treatment of liver tumors such as hepatocellular carcinoma (HCC) and metastatic tumors since many patients are not eligible for surgical resection due to advanced disease, unfavorable location, or impaired clinical condition [3]. Numerous studies have reported that RFA is the most minimally invasive treatment for liver tumors and evaluated it as a successful therapeutic modality, providing reliable outcomes

even though its posttreatment recurrence rate is higher than that of cryoablation and resection [4]. Ultrasound and magnetic resonance imaging (MRI) commonly provide the guidance of RFA because they allow real-time visualization of probe placement and high contrast images for tumor and normal tissues [5–8]. Contrast-enhanced computed tomography (CT) and MRI are widely used methods to evaluate ablated lesions by comparing the differences of lesions before and after RF ablation. However, none of these are able to continuously monitor the temperature and changes in properties of cancerous tissue and normal tissue during RFA process.

EIT does have this potential due to its high speed, sensitivity to the conductivity change of tumor and normal tissue at various frequencies [9, 10], and its ability to monitor tissue temperature in real time [11, 12]. In both cardiac EIT and EIT for monitoring liver tumour RFA, there are opportunities to add an additional internal electrode close to the region of interest (ROI) to improve EIT sensitivity to internal tissues and particularly to the tissue within the ROI. In both applications, a local imaging reconstruction method with high sensitivity within the ROI is desired since there are significant effects from conductivity changes outside the ROI such as ventilation, perfusion, movement of the lungs, diaphragm, gastric activity, and blood flow in large vessels [13].

In this paper, we propose a local sensitivity matrix-based imaging method to increase the sensitivity in a local region of interest near the internal electrode and decrease the sensitivity outside the region of interest to progress the application of EIT to cardiac monitoring and liver RFA. To further increase sensitivity to the ROI, we propose a new arrangement of surface electrodes where the electrode spacing is not equal but more near the ROI. In order to evaluate the performance of the local ROI imaging method, we perform numerical simulations and phantom experiments.

2. Method

2.1. Conventional EIT Reconstruction Method. Let a bounded domain Ω represent the subject to be imaged. Surface electrodes \mathcal{E}_j for $j = 1, 2, \dots, E$ are attached to the boundary $\partial\Omega$, where E is the total number of electrodes. Let $\gamma_{t,\omega}(\mathbf{r}) = \sigma_{t,\omega}(\mathbf{r}) + i\omega\epsilon_{t,\omega}(\mathbf{r})$ denote the complex conductivity at time t , angular frequency of ω , and position \mathbf{r} . When we inject a sinusoidal current $I \sin(\omega\tilde{t})$ at an angular frequency of ω between a chosen pair of electrodes, a voltage distribution $v_{t,\omega}(\mathbf{r})\sin(\omega\tilde{t} + \theta_{t,\omega}(\mathbf{r}))$ is formed at the position \mathbf{r} . Here, t is used for expressing a slow-time change in the complex conductivity distribution, and \tilde{t} is used for the fast-time change to represent time-harmonic fields. The induced time-harmonic potential $u_{t,\omega}(\mathbf{r}) = v_{t,\omega}(\mathbf{r})e^{i\theta_{t,\omega}(\mathbf{r})}$ satisfies the following elliptic partial differential equation [14]:

$$\begin{aligned} \nabla \cdot (\gamma_{t,\omega}(\mathbf{r}) \nabla u_{t,\omega}(\mathbf{r})) &= 0, \quad \text{for } \mathbf{r} \in \Omega, \\ -\gamma_{t,\omega} \nabla u_{t,\omega} \cdot \mathbf{n} &= g, \quad \text{on } \partial\Omega, \end{aligned} \quad (1)$$

where \mathbf{n} is the outward unit normal vector on $\partial\Omega$ and g is the corresponding Neumann data on $\partial\Omega$ due to the injection current.

Static imaging in EIT is difficult due to its fundamental limitations in handling boundary geometry and uncertainty in electrode position. Time-difference EIT (tdEIT) and frequency-difference EIT (fdEIT) use time and frequency difference data, respectively, so that the data subtraction can effectively cancel out common errors related to boundary geometry [14–18]. The difference imaging in EIT is based on linear approximations of the following identities:

- (i) time-difference EIT $\nabla \cdot ((\partial/\partial t)\gamma_{t,\omega}(\mathbf{r}) \nabla u_{t,\omega}(\mathbf{r})) = -\nabla \cdot (\gamma_{t,\omega}(\mathbf{r}) \nabla (\partial/\partial t)u_{t,\omega}(\mathbf{r}))$,
- (ii) frequency-difference EIT $\nabla \cdot ((\partial/\partial \omega)\gamma_{t,\omega}(\mathbf{r}) \nabla u_{t,\omega}(\mathbf{r})) = -\nabla \cdot (\gamma_{t,\omega}(\mathbf{r}) \nabla (\partial/\partial \omega)u_{t,\omega}(\mathbf{r}))$.

Let the angular frequency ω be fixed. Let $u_{t,\omega}^j$ denote the time-harmonic potential due to j th injection current between the adjacent pair of electrodes \mathcal{E}_j and \mathcal{E}_{j+1} . The boundary voltage between \mathcal{E}_k and \mathcal{E}_{k+1} due to the j th injection current can be approximated as

$$\begin{aligned} V_{j,k}(t) &\approx \frac{I}{|\mathcal{E}|} \left(\int_{\mathcal{E}_k} u_{t,\omega}^j dS - \int_{\mathcal{E}_{k+1}} u_{t,\omega}^j dS \right) \\ &\approx \int_{\Omega} \gamma_{t,\omega} \nabla u_{t,\omega}^j \cdot \nabla u_{t,\omega}^k d\mathbf{r} \quad \text{for } j, k = 1, \dots, E, \end{aligned} \quad (2)$$

where $|\mathcal{E}|$ is the surface area of the electrode. The last identity in (2) comes from (1) and divergence theorem. We collect E^2 number of boundary voltage data for a sequence of time $t = t_1, t_2, t_3, \dots$:

$$\mathbf{V}(t) := \begin{pmatrix} \underbrace{V_{1,1}(t), V_{1,2}(t), \dots, V_{1,E}(t)}_{\text{1st current}}, \\ \underbrace{V_{2,1}(t), \dots, V_{2,E}(t)}_{\text{2nd current}}, \dots, \underbrace{V_{E,1}(t), \dots, V_{E,E}(t)}_{\text{Eth current}} \end{pmatrix}^T, \quad (3)$$

where $()^T$ is the transpose. Here, any index number must be understood as a modulus of E .

The time-difference data due to the time change of $\delta\gamma := \gamma_{t_2,\omega} - \gamma_{t_1,\omega}$ has the following relation:

$$V_{j,k}(t_2) - V_{j,k}(t_1) = - \int_{\Omega} \frac{(\gamma_{t_2,\omega} - \gamma_{t_1,\omega})}{\delta\gamma} \nabla u_{t_2,\omega}^j \cdot \nabla u_{t_1,\omega}^j d\mathbf{r}. \quad (4)$$

The linearized method is based on the following rough approximation:

$$\delta\mathbf{V} := V_{j,k}(t_2) - V_{j,k}(t_1) \approx \int_{\Omega} \delta\gamma \nabla u_*^j \cdot \nabla u_*^k d\mathbf{r}, \quad (5)$$

where u_*^j is the potential of (1) corresponding to a reference conductivity $\gamma = \gamma_*$.

Discretizing the domain of interest into pixels and assuming that $\delta\gamma$ is constant on each pixel q_n , the time-difference

EIT problem of (5) can be changed to solve the following linear system:

$$\mathbb{S}\delta\boldsymbol{\gamma} = \delta\mathbf{V}. \quad (6)$$

The n th column of the sensitivity matrix \mathbb{S} is

$$\begin{aligned} \mathbf{s}_n = & \left(\int_{q_n} \nabla u_*^1 \cdot \nabla u_*^1 d\mathbf{r}, \dots, \int_{q_n} \nabla u_*^j \cdot \nabla u_*^k d\mathbf{r}, \right. \\ & \left. \dots, \int_{q_n} \nabla u_*^E \cdot \nabla u_*^E d\mathbf{r} \right)^T. \end{aligned} \quad (7)$$

Hence, the EIT problem is to find a best linear combination of column vectors $\mathbf{s}_1, \dots, \mathbf{s}_N$ which produces $\delta\mathbf{V}$:

$$\delta\mathbf{V} \approx \delta\gamma_1 \mathbf{s}_1 + \dots + \delta\gamma_N \mathbf{s}_N. \quad (8)$$

The column vector \mathbf{s}_k of \mathbb{S} represents sensitivity of current-voltage data at the fixed pixel p_k , whereas row vectors of \mathbb{S} represent sensitivity distribution for a fixed current-voltage data. We refer to this approach (combined with a regularization) to reconstruct images as the conventional method throughout this paper.

2.2. Local-ROI Imaging Method for EIT. The local-ROI imaging method for EIT is to provide the image of the conductivity change in a local region of interest (ROI) instead of the image in the entire domain Ω . Let a domain D be the local region of interest to be imaged. Imagine that the measured data $\delta\mathbf{V}$ in (5) is divided into two parts

$$\delta\mathbf{V} = \delta\mathbf{V}_D + \delta\mathbf{V}_{\Omega \setminus D}, \quad (9)$$

where $\delta\mathbf{V}_D$ is the voltage change in response to the conductivity perturbation $\delta\gamma$ in the local ROI D and $\delta\mathbf{V}_{\Omega \setminus D}$ is the voltage change in response to $\delta\gamma$ in $\Omega \setminus D$. With proper arrangement, we may assume that the first R column vectors of \mathbb{S} are sensitivity vectors to pixels in ROI D and the other column vectors are sensitivity vectors to pixels in $\Omega \setminus D$. Then the sensitivity matrix \mathbb{S} can be decomposed into

$$\mathbb{S} = [\mathbb{S}_D \quad \mathbf{O}] + [\mathbf{O} \quad \mathbb{S}_{\Omega \setminus D}], \quad (10)$$

where \mathbf{O} represents a proper size of zero matrix,

$$\mathbb{S}_D = \begin{bmatrix} | & & | \\ \mathbf{s}_1 & \cdots & \mathbf{s}_R \\ | & & | \end{bmatrix}, \quad \mathbb{S}_{\Omega \setminus D} = \begin{bmatrix} | & & | \\ \mathbf{s}_{R+1} & \cdots & \mathbf{s}_N \\ | & & | \end{bmatrix}. \quad (11)$$

If we could extract the data $\delta\mathbf{V}_D$ by filtering out $\delta\mathbf{V}_{\Omega \setminus D}$, the global problem (6) can be changed into the local problem:

$$\mathbb{S}_D \delta\boldsymbol{\gamma}_D = \delta\mathbf{V}_D, \quad (12)$$

where $\delta\boldsymbol{\gamma}_D = [\delta\gamma_1, \delta\gamma_2, \dots, \delta\gamma_R]^T$. Figure 1(c) shows the reconstructed image of $\delta\boldsymbol{\gamma}_D$ using the localized linear system (12) via numerical simulation. Comparing this local image with the standard EIT image reconstruction shown in Figure 1(b), it would be desirable to filter out $\delta\mathbf{V}_{\Omega \setminus D}$ to enhance image resolution.

For the local imaging in the ROI D , we aim to develop a method of extracting \mathbf{V}_D from the full data \mathbf{V} . In order to eliminate the unrelated data $\mathbf{V}_{\Omega \setminus D}$ in the linear system (6), we need to find an optimal matrix Φ such that

$$\Phi = \arg \min_{\Phi} \|\Phi^T \delta\mathbf{V} - \Phi^T \delta\mathbf{V}_D\|. \quad (13)$$

Here, $\arg \min_{\Phi} \eta(\Phi)$ gives a matrix Φ at which $\eta(\Phi)$ is minimized. If Φ satisfies $\|\Phi^T \delta\mathbf{V} - \Phi^T \delta\mathbf{V}_D\| \approx 0$, then it eliminates the unrelated data $\mathbf{V}_{\Omega \setminus D}$ and we get the localized linear system corresponding to (12):

$$\Phi^T \mathbb{S} \delta\boldsymbol{\gamma} \approx \Phi^T \delta\mathbf{V}_D \quad (\text{since } \Phi^T \delta\mathbf{V} \approx \Phi^T \delta\mathbf{V}_D). \quad (14)$$

Note that the quantity $\lambda_D := \min_{\Phi} \|\Phi^T \delta\mathbf{V} - \Phi^T \delta\mathbf{V}_D\|$ depends on the electrode configuration and mesh structure that determines the structure of column vectors of \mathbb{S} as shown in Figure 2. The λ_D may not be small when the sensitivity matrix \mathbb{S} is highly ill-conditioned. If the column vectors $\mathbf{s}_1, \dots, \mathbf{s}_R$ are orthogonal to $\mathbf{s}_{R+1}, \dots, \mathbf{s}_N$, then $\lambda_D = 0$ by choosing Φ whose rows consist of the column vectors $\mathbf{s}_1, \dots, \mathbf{s}_R$. But, this is not possible with the standard EIT electrode configuration. We try to find an optimal Φ which minimizes λ_D . Indeed, cross-correlation $\mu(j)$ of column vector in \mathbb{S} is big if \mathbf{s}_j is correlated with column vectors in ROI; cross-correlation is defined by

$$\mu(j) = \text{avg}_{p_i \in \Omega \setminus D} \frac{|\mathbf{s}_i^T \mathbf{s}_j|}{\|\mathbf{s}_i\|_2 \|\mathbf{s}_j\|_2}, \quad \text{for } p_j \in D. \quad (15)$$

Figure 3 shows that cross-correlation values decrease by placing internal electrode.

For finding proper Φ , we propose the following minimization

$$\phi_k = \arg \min_{\phi} \left(\sum_{p_j \notin D} |\mathbf{s}_j \cdot \phi|^2 + \alpha \|\phi - \mathbf{s}_k\|_2^2 \right), \quad p_k \in D, \quad (16)$$

where α is a suitable parameter. We should note that each ϕ_k is designed to be close and to be parallel to \mathbf{s}_k while orthogonal to \mathbf{s}_j for each $p_j \notin D$. The first term in (16), $\sum_{p_j \notin D} |\mathbf{s}_j \cdot \phi|^2$, is small when ϕ is orthogonal to $\{\mathbf{s}_j\}_{p_j \notin D}$. The second term in (16), $\|\phi - \mathbf{s}_k\|_2^2$, is small if ϕ is parallel to \mathbf{s}_k . We define a matrix Φ whose columns are consisted of $\{\phi_k\}_{p_k \in D}$:

$$\Phi = (\phi_1, \phi_2, \dots, \phi_R), \quad \text{where } \bigcup_{n=1}^R p_n = D. \quad (17)$$

We multiply Φ^T to the linearized system (6):

$$\Phi^T \mathbb{S} \delta\boldsymbol{\gamma} = \Phi^T \delta\mathbf{V}. \quad (18)$$

Now, we have the linear system (18) with the modified sensitivity matrix $\Phi^T \mathbb{S}$ with the modified data $\Phi^T \delta\mathbf{V}$. Here, $\Phi^T \delta\mathbf{V}$ is regarded as a rough approximation of $\Phi^T \delta\mathbf{V}_D$.

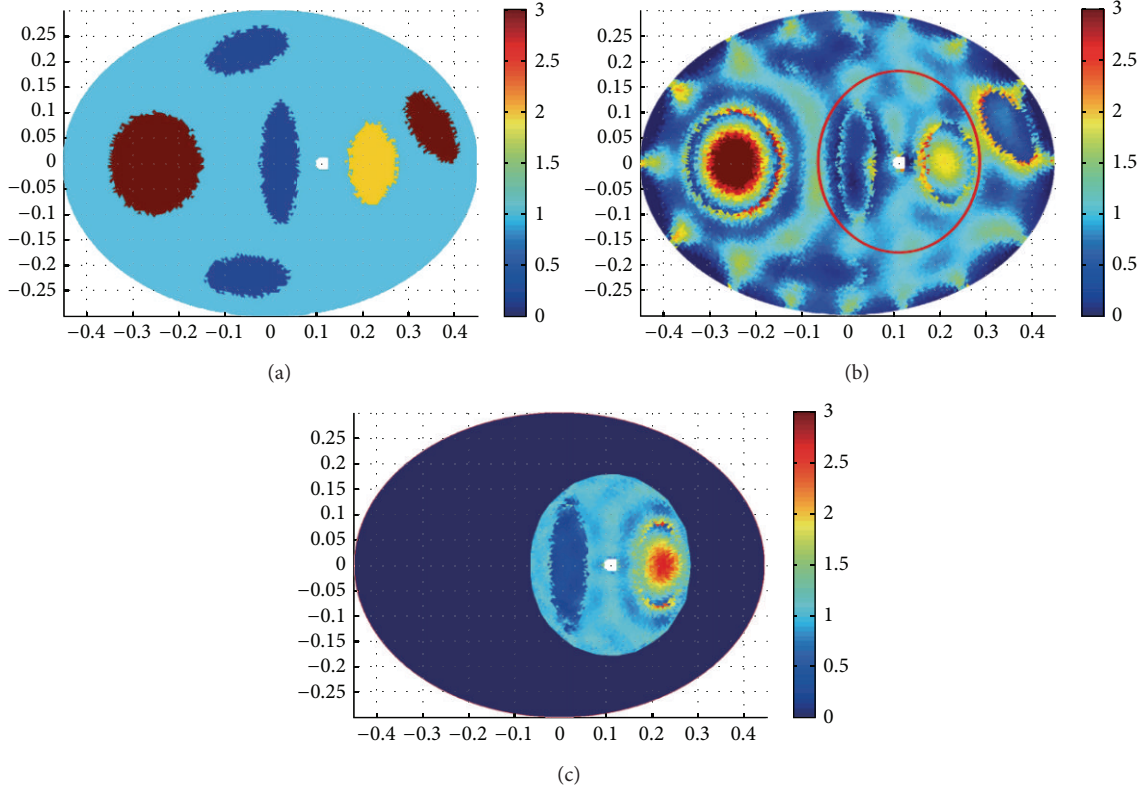


FIGURE 1: Reconstructed images using δV and δV_D via numerical simulations: (a) True image $\delta\gamma$, (b) reconstructed image using δV , and (c) reconstructed image using δV_D .

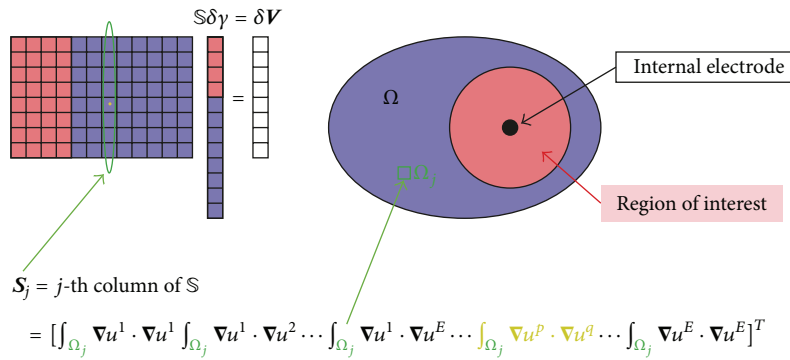


FIGURE 2: Column vectors of the sensitivity matrix are related with pixels in Ω .

3. Numerical Simulations

In order to analyse the boundary electrode position and the benefit of using an internal electrode with the proposed local-ROI imaging method, we prepared three different kinds of electrode configuration and applied the conventional and local-ROI imaging methods explained in the previous sections. Figure 4 shows the cylindrical phantoms with three different electrode configurations. Data obtained from all three electrode configurations were processed by the conventional TSVD reconstruction method. The local-ROI imaging

method uses an internal electrode so it was only applied to data obtained with the two internal electrode configurations (Figures 4(b) and 4(c), (Models 1 and 2)). We carry out a total of five numerical simulations, the standard method on Model 0, 1, 2 and the local-ROI method on models 1, 2.

To compare sensitivity and robustness to noise in the suggested five cases, we simulated an object of 2 S/m conductivity with 0.1428 diameter at (0.8, 0) in the ROI of 1 S/m saline tank. The radius of the ROI is defined by 5/6 of distance between internal electrode and closest boundary electrode. We used two performance indexes to assess the improvement when

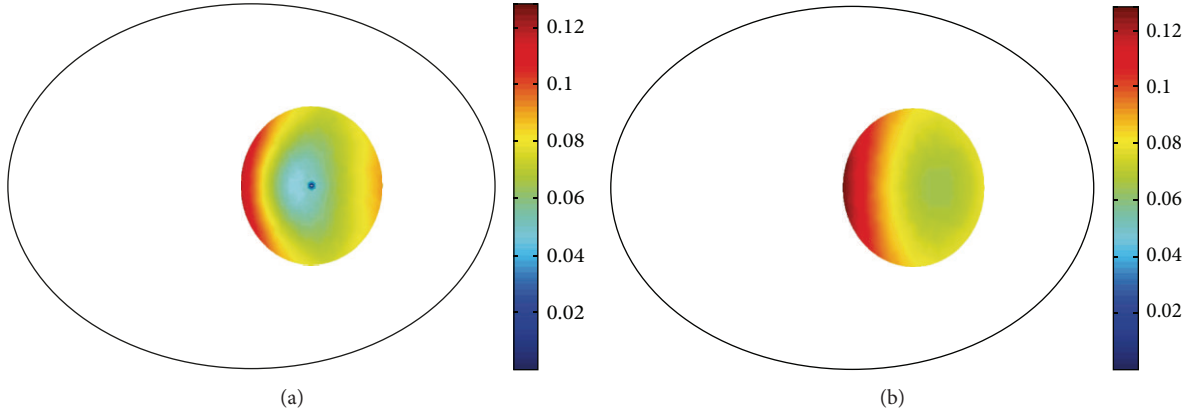


FIGURE 3: The cross-correlation distribution on D : (a) μ with internal electrode and (b) μ without internal electrode.

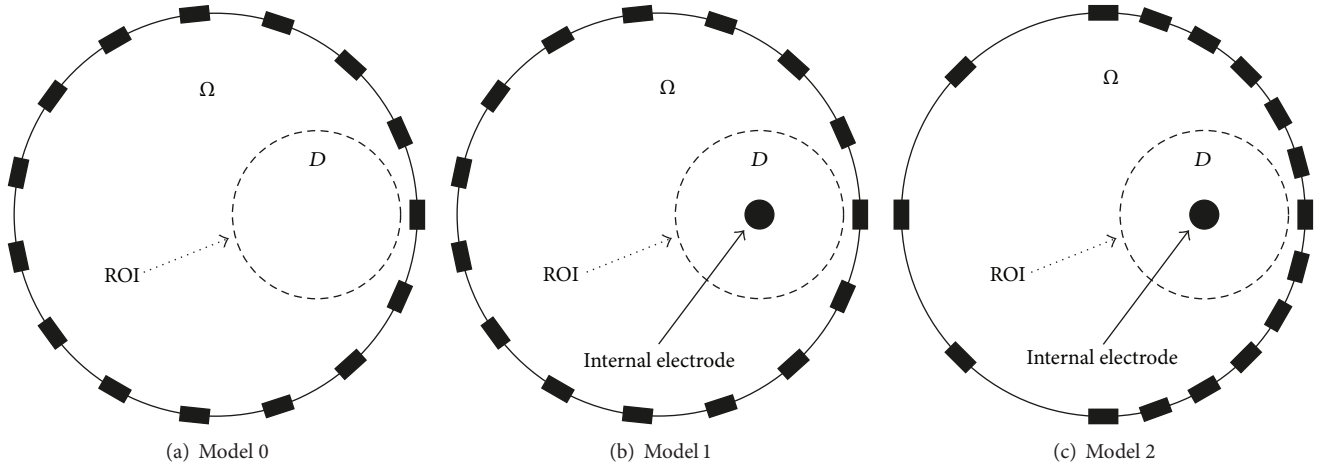


FIGURE 4: (a) Standard EIT phantom without using internal electrode, (b) equidistant surface electrodes with an internal electrode, and (c) unequally spaced surface electrodes with denser spacing near by the ROI with an internal electrode.

using an internal electrode and the proposed linear system (18). First, we computed the singular value threshold to produce the same conductivity contrast of image as shown in Figure 5(a). We repeatedly reconstruct images, updating the singular value threshold, until the same conductivity contrast is produced between the anomaly and background in the reconstructed image. Then we compared the singular value thresholds as a lower number of threshold is an indication of better noise robustness. When we used an internal electrode, the truncated singular value threshold was lower than that without using the internal electrode. Also, the performance of local-ROI imaging method was improved when it was used with unequally spaced surface electrodes with denser spacing near by the ROI. Second, we are concerned about the effect of high contrast anomalies outside the ROI. To investigate this, we examined the sensitivity values of \mathbb{S} and $\Phi^T \mathbb{S}$ for each simulation case. The normalized sensitivity values of \mathbb{S} and $\Phi^T \mathbb{S}$ from within the ROI and out of ROI are shown separately in Figure 5(b). There was an improved relative sensitivity to the ROI region with the proposed method $\Phi^T \mathbb{S}$. To show sensitivity values, we calculated the ratio of the

matrix norm $\|\mathbb{A}_{in}\|/\|\mathbb{A}\|$ and $\|\mathbb{A}_{out}\|/\|\mathbb{A}\|$ for inside ROI and outside ROI respectively, where

$$\begin{aligned} \mathbb{A} &\in \{\mathbb{S} \text{ of Model 0, 1, 2}, \Phi^T \mathbb{S} \text{ of Model 1, 2}\}, \\ \mathbb{A}_{in} &\text{ is a submatrix of } \mathbb{A} \text{ corresponding to ROI,} \\ \mathbb{A}_{out} &\text{ is a submatrix of } \mathbb{A} \text{ corresponding} \\ &\text{to outside ROI,} \\ \|\mathbb{A}\| &:= \sup_{\|\mathbf{x}\|=1} \|\mathbb{A}\mathbf{x}\|. \end{aligned}$$

Note that a matrix norm $\|\mathbb{A}\|$ shows how much \mathbb{A} deforms \mathbf{x} . So, $\|\mathbb{A}_{in}\|/\|\mathbb{A}\|$ and $\|\mathbb{A}_{out}\|/\|\mathbb{A}\|$ show maximum influence of submatrices \mathbb{A}_{in} and \mathbb{A}_{out} for multiplication of \mathbb{A} .

In order to compare the performance of the imaging methods in the reconstructed images, we placed multiple objects which had the same conductivity of 0.029 S/m with 0.01 diameter at (0.02, 0.015), (0.02, -0.015), (0.05, -0.015), and (0.05, -0.015) within the ROI of the 0.0418 S/m saline tank as shown in Figure 6(a). The conventional reconstructed image without an internal electrode was produced by the TSVD algorithm in Model 0 with diagonal current injection

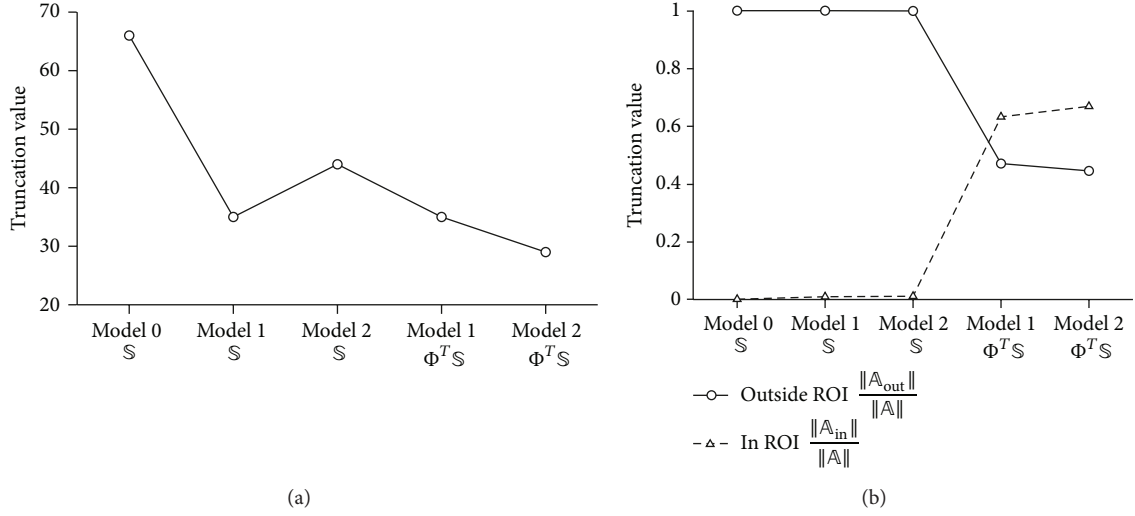


FIGURE 5: Comparison of the conventional and local-ROI imaging method by (a) singular values required to the same conductivity contrast in images and (b) ratio of norms for elements associated within the ROI and outside the ROI for each case.

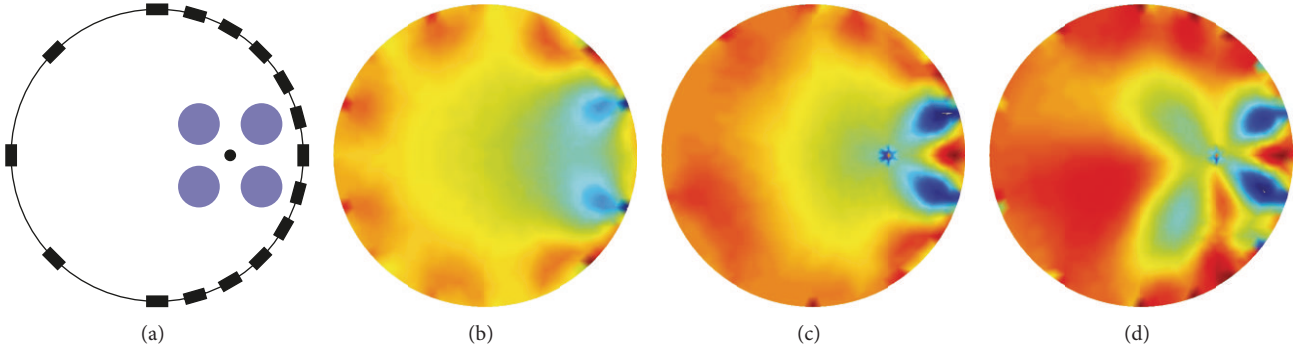


FIGURE 6: Reconstruction results using simulation data. (a) Simulation configuration for imaging test, (b) conventional TSVD reconstructed image using diagonal injection, (c) TSVD reconstructed image using (6) with an internal electrode, and (d) TSVD reconstructed image using local-ROI imaging method (12) with an internal electrode.

(Figure 6(b)). For comparison of the imaging methods using an internal electrode, we positioned an internal electrode at $(0.035, 0)$ in Model 2. Figures 6(b) and 6(c) show images using the conventional TSVD reconstruction algorithm and the local-ROI imaging method. The proposed method with an internal electrode has better sensitivity and detectability in the ROI.

4. Experimental Results

To evaluate the performance of the imaging methods in a physical model, we prepared a cylindrical saline tank with the same geometry, ROI, and electrode positions as Figures 4(a) and 4(c) since the denser clustering of boundary electrodes near the ROI (Figure 4(c)) produced better results than the conventional equally spaced electrodes (Figure 4(b)) in the simulation study. The diameter and height of saline tank were 14 cm and 6 cm, respectively. The boundary and internal electrodes were located 3 cm from the bottom in the z direction. The x and y positions of the internal electrode

were $(3.5, 0)$ cm relative to the origin $(0, 0)$ at the center of cylindrical tank. The diameter of internal electrode was 0.25 cm and it was covered with insulated rubber except for the end piece of exposed metal. The conductivity of saline was 0.042 S/m. All data was measured by the KHU Mark2.5 EIT system operated at 10 kHz [19].

We evaluated the imaging methods using two different situations. First, we located a piece of radish inside of ROI (case 0, 1, 2, 3 $(5.6, 0)$) and a piece of potato outside of ROI (case 1 $(-5.6, 0)$, case 2 $(-3.5, -4)$, case 3 $(0, -5.6)$) to assess how the sensitivity of each method is influenced by a high conductivity object in the surrounding area of ROI. The diameter and height of both objects were the same at 1.2 cm and 7 cm as shown in Figure 7. The conductivity of radish (0.038 S/m at 10 kHz) was 9.5% lower than saline and the potato (0.029 S/m at 10 kHz) was a higher contrast than the radish with 31% lower conductivity than saline. All data was obtained in the new configuration with an internal electrode and unequal surface electrode spacing as Model 2 in Figure 4(c). All measured data was processed by the conventional TSVD method and the local-ROI imaging method

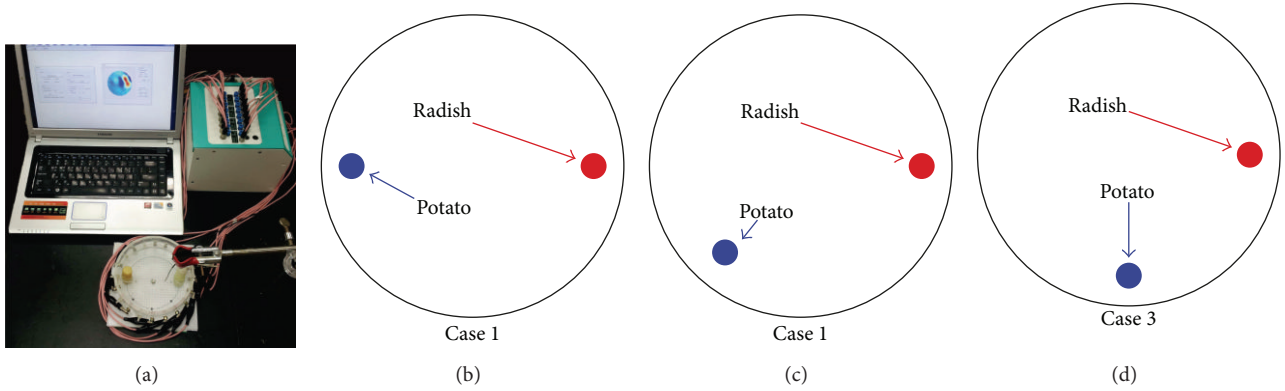


FIGURE 7: (a) Phantom experimental setup, (b) radish and potato position of case 1, (c) radish and potato position of case 2, and (d) radish and potato position of case 3.

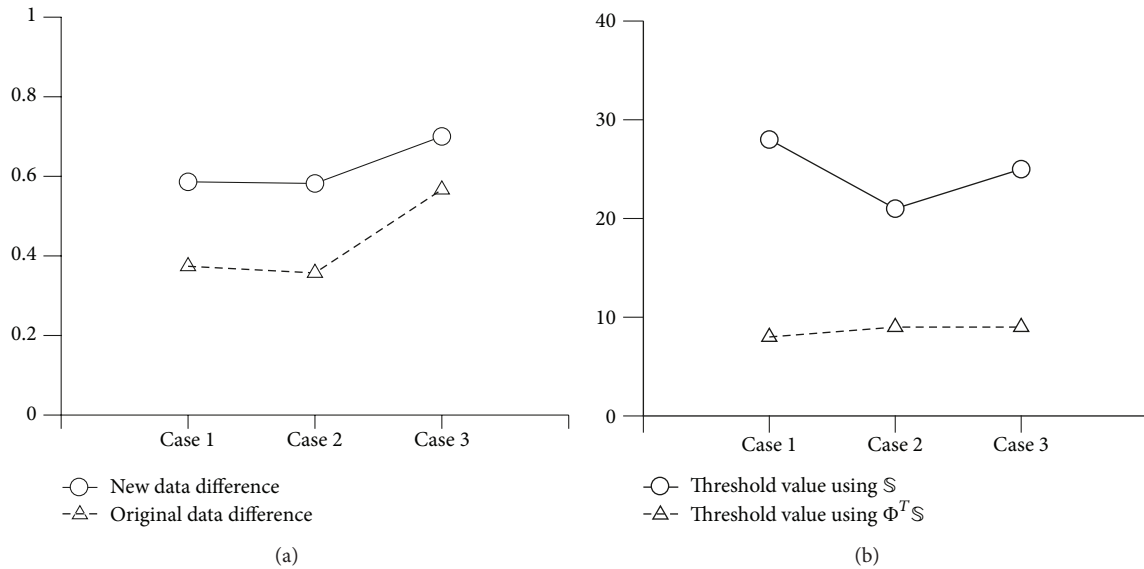


FIGURE 8: Norm values of difference in experimental data caused by an anomaly outside the ROI in the three different positions given in Figure 7.

for comparison. We present the norm values of the difference of $\delta\mathbf{V}$ and $\Phi^T \delta\mathbf{V}$ compared to those values of reference case 0 because it is difficult to analyze images directly from the artifacts due to the large anomaly outside the ROI. Here, we processed reference value by conventional method in case 0 which included only one anomaly (radish) in the ROI. Figure 8(a) shows the effect of the high conductivity contrasted object located outside of ROI. There is less effect with the new local-ROI imaging method when the object outside the ROI is in the opposite hemicycle to the ROI. As the object approaches the ROI (case 1 to case 3) both methods perform similarly.

Figure 8(b) shows the singular value threshold required to produce the same conductivity contrast for each case. The local-ROI imaging method had similar threshold values for all cases with less than 1.73% variation. However the conventional TSVD method showed larger singular values and large dependence on the high contrast anomaly position.

Secondly, we evaluated the methods from the reconstructed images in the same configuration as the numerical simulation. We put four carrot objects with 0.04 S/m conductivity at 10 kHz in the 0.06 S/m saline tank. The position of each object was (1.5, 2), (5.5, 2), (5.5, -2), and (1.5, -2) cm, respectively. All objects had the same diameter of 2 cm.

We obtained an image in configuration Model 0 during diagonal current injection and TSVD reconstruction. For algorithm comparison, we measured data in Model 2 and applied both methods separately. Figures 9(a)–9(c) show the reconstructed images. The proposed local-ROI imaging method with an internal electrode can distinguish inner objects better than conventional methods.

5. Conclusions and Discussions

The new local-ROI imaging method has been shown to improve the sensitivity in the ROI region and robustness to

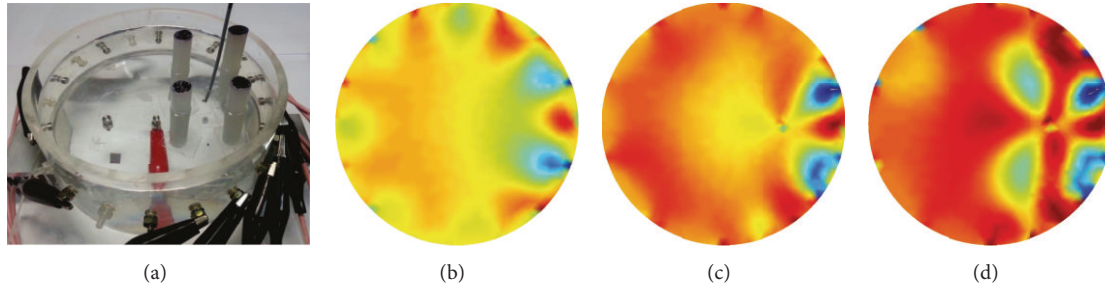


FIGURE 9: Reconstruction results using experimental data. (a) Experiment configuration for imaging test, (b) conventional TSVD reconstructed image using diagonal injection, (c) TSVD reconstructed image using (6) with an internal electrode, and (d) TSVD reconstructed image using local-ROI imaging method (12) with an internal electrode.

noise by comparison of sensitivity matrix values. It provided the approximated linear system with optimized sensitivity matrix to emphasize the detection in ROI. The ROI region is close to an internal electrode and surface electrodes were unequally spaced being more dense close to the ROI. The new method and setup is also less affected by the high conductivity contrasted object outside of ROI. These objects are mimicking a large vessel and several regions of hepatic and metastatic cancers treated by RFA, other gastric organs, or the lungs in cardiac monitoring.

Some performance indexes proposed in this paper described that the sensitivity and detectability were obviously improved in simulation and experiment results. However, the reconstructed images did not show improvements as dramatic as we initially expected. One of the major reasons was the ill-posedness of imaging problem. When we designed the optimal Φ^T matrix that satisfied condition (16), it could not eliminate the effect of unrelated data $\mathbf{V}_{\Omega \setminus D}$ completely. Also, the quality of the experimental reconstructed image was highly dependent on the position of an internal electrode and boundary electrodes because we placed the electrodes with denser spacing near by the ROI. Encouragingly with the pilot results of the local-ROI imaging method using an internal electrode, it shows the feasibility and suggests a new approach to improve the resolution of internal local region.

An additional improvement which was introduced in this paper was the nonequidistant spacing of electrodes, with the electrodes more densely spaced near the ROI in Model 2 (Figure 4(c)). This showed improved results in simulation and so was used in the experimental setup; however, this may be more sensitive to electrode positions, the location of the ROI, or noise. Interestingly in Figure 5(a) we found that this setup of non-equidistant electrodes (Model 2) showed less sensitivity with the conventional EIT method. This may reflect the preference for symmetry with EIT performed in a circular object. The single ROI we investigated was off centre and once we use our local-ROI focusing algorithm there is an improvement found in the non-equidistant electrode setup (model 2).

The application of EIT to RF ablation monitoring has high potential; however, we need to study more how to separate the conductivity variations which arise simultaneously from temperature changes and tissue property changes. While the temperature coefficient of conductivity in electrolytes of 2% per degree is well known for electrolytes, tissues also exhibit

a conductivity dependence on temperature-induced fluid volume shifts which is of the same order of magnitude [20].

Lower frequency measurements could be used to discriminate ablated and nonablated tumor and normal tissues. Liver tumour tissue has a higher conductivity than normal liver tissue over 10 Hz to 1 MHz shown by four terminal impedance measurements in excised tissue. Following an ablation, both tissue types showed significantly increased conductivity over the same frequency range indicating that electrical impedance may be used to differentiate tumor tissue diagnostically, for ablation planning and postablation assessment [10].

The suggested method may be applied in 3D domain without any additional changes to the algorithm. Here we used a 2D domain analysis because applying the suggested method requires a lot of computations on the column vectors of sensitivity matrix corresponding to pixels in ROI [21]. We need to optimize the local-ROI imaging algorithm by focusing on the ROI and investigate ways to increase the coverage area without moving the electrode position. We may combine the frequency-difference EIT [22, 23] with the local-ROI imaging method to apply frequency-difference data.

Acknowledgment

This work was supported by the National Research Foundation of Korea (NRF) grant funded by the Korea government (MSIP) (2010-0018275) and Basic Science Research Program through the National Research Foundation of Korea (NRF) funded by the Ministry of Education, Science and Technology (2011-0022779).

References

- [1] B. M. Eyiiboglu and T. C. Pilkington, "Intracavity electrical impedance tomography," in *Proceedings of the 12th Annual International Conference of the IEEE on Engineering in Medicine and Biology Society*, p. 130, 1990.
- [2] J. N. Tehrani, C. Jin, and A. L. McEwan, "Modelling of an oesophageal electrode for cardiac function tomography," *Computational and Mathematical Methods in Medicine*, vol. 2012, Article ID 585786, 10 pages, 2012.
- [3] A. R. Gillams, "The use of radiofrequency in cancer," *British Journal of Cancer*, vol. 92, no. 10, pp. 1825–1829, 2005.

- [4] E. K. Abdalla, J.-N. Vauthey, L. M. Ellis et al., "Recurrence and outcomes following hepatic resection, radiofrequency ablation, and combined resection/ablation for colorectal liver metastases," *Annals of Surgery*, vol. 239, no. 6, pp. 818–827, 2004.
- [5] N. J. McDannold and F. A. Jolesz, "Magnetic resonance image-guided thermal ablations," *Topics in Magnetic Resonance Imaging*, vol. 11, no. 3, pp. 191–202, 2000.
- [6] S. Terraz, A. Cernicanu, M. Lepetit-Coiffé et al., "Radiofrequency ablation of small liver malignancies under magnetic resonance guidance: progress in targeting and preliminary observations with temperature monitoring," *European Radiology*, vol. 20, no. 4, pp. 886–897, 2010.
- [7] S. N. Goldberg, G. S. Gazelle, and P. R. Mueller, "Thermal ablation therapy for focal malignancy: a unified approach to underlying principles, techniques, and diagnostic imaging guidance," *American Journal of Roentgenology*, vol. 174, no. 2, pp. 323–331, 2000.
- [8] S. N. Goldberg, C. J. Grassi, J. F. Cardella et al., "Image-guided tumor ablation: standardization of terminology and reporting criteria," *Radiology*, vol. 235, no. 3, pp. 728–739, 2005.
- [9] S. Laufer, A. Ivorra, V. E. Reuter, B. Rubinsky, and S. B. Solomon, "Electrical impedance characterization of normal and cancerous human hepatic tissue," *Physiological Measurement*, vol. 31, no. 7, pp. 995–1009, 2010.
- [10] D. Haemmerich, D. J. Schutt, A. W. Wright, J. G. Webster, and D. M. Mahvi, "Electrical conductivity measurement of excised human metastatic liver tumours before and after thermal ablation," *Physiological Measurement*, vol. 30, no. 5, pp. 459–466, 2009.
- [11] F. Ferraioli, A. Formisano, and R. Martone, "Effective exploitation of prior information in electrical impedance tomography for thermal monitoring of hyperthermia treatments," *IEEE Transactions on Magnetics*, vol. 45, no. 3, pp. 1554–1557, 2009.
- [12] H. Griffiths and A. Ahmed, "Applied potential tomography for non-invasive temperature mapping in hyperthermia," *Clinical Physics and Physiological Measurement*, vol. 8, no. 4, supplement A, article 019, pp. 147–153, 1987.
- [13] D. S. K. Lu, S. S. Raman, P. Limanond et al., "Influence of large peritumoral vessels on outcome of radiofrequency ablation of liver tumors," *Journal of Vascular and Interventional Radiology*, vol. 14, no. 10, pp. 1267–1274, 2003.
- [14] D. Holder, *Electrical Impedance Tomography: Methods, History and Applications*, IOP, Bristol, UK, 2005.
- [15] P. Metherall, D. C. Barber, R. H. Smallwood, and B. H. Brown, "Three-dimensional electrical impedance tomography," *Nature*, vol. 380, no. 6574, pp. 509–512, 1996.
- [16] M. Cheney, D. Isaacson, and J. C. Newell, "Electrical impedance tomography," *SIAM Review*, vol. 41, no. 1, pp. 85–101, 1999.
- [17] J. K. Seo, J. Lee, S. W. Kim, H. Zribi, and E. J. Woo, "Frequency-difference electrical impedance tomography (fdEIT): algorithm development and feasibility study," *Physiological Measurement*, vol. 29, no. 8, pp. 929–944, 2008.
- [18] J. K. Seo and E. J. Woo, *Nonlinear Inverse Problems in Imaging*, Wiley Press, New York, NY, USA, 2012.
- [19] H. Wi, H. Sohal, T. I. Oh, A. L. McEwan, and E. J. Woo, "Multi-frequency electrical impedance tomography system with automatic self-calibration for long-term monitoring: KHU Mark2.5," *IEEE Transactions on Biomedical Circuits and Systems*. In press.
- [20] E. Gersing, "Monitoring temperature-induced changes in tissue during hyperthermia by impedance methods," *Annals of the New York Academy of Sciences*, vol. 873, pp. 13–20, 1999.
- [21] W. R. B. Lionheart, "Uniqueness, shape, and dimension in EIT," *Annals of the New York Academy of Sciences*, vol. 873, pp. 466–471, 1999.
- [22] S. C. Jun, J. Kuen, J. Lee, E. J. Woo, D. Holder, and J. K. Seo, "Frequency-difference EIT (fdEIT) using weighted difference and equivalent homogeneous admittivity: validation by simulation and tank experiment," *Physiological Measurement*, vol. 30, no. 10, pp. 1087–1099, 2009.
- [23] J. Kuen, E. J. Woo, and J. K. Seo, "Multi-frequency time-difference complex conductivity imaging of canine and human lungs using the KHU Mark1 EIT system," *Physiological Measurement*, vol. 30, no. 6, pp. S149–S164, 2009.

Research Article

Numerical Simulations of MREIT Conductivity Imaging for Brain Tumor Detection

Zi Jun Meng,¹ Saurav Z. K. Sajib,¹ Munish Chauhan,¹ Rosalind J. Sadleir,^{1,2}
Hyung Joong Kim,¹ Oh In Kwon,³ and Eung Je Woo¹

¹ Department of Biomedical Engineering, Impedance Imaging Research Center (IIRC), Kyung Hee University, Yongin, Republic of Korea

² Department of Biomedical Engineering, University of Florida, Gainesville, FL, USA

³ Department of Mathematics, Konkuk University, Seoul, Republic of Korea

Correspondence should be addressed to Hyung Joong Kim; bmekim@khu.ac.kr

Received 21 December 2012; Revised 21 February 2013; Accepted 5 April 2013

Academic Editor: Ulrich Katscher

Copyright © 2013 Zi Jun Meng et al. This is an open access article distributed under the Creative Commons Attribution License, which permits unrestricted use, distribution, and reproduction in any medium, provided the original work is properly cited.

Magnetic resonance electrical impedance tomography (MREIT) is a new modality capable of imaging the electrical properties of human body using MRI phase information in conjunction with external current injection. Recent *in vivo* animal and human MREIT studies have revealed unique conductivity contrasts related to different physiological and pathological conditions of tissues or organs. When performing *in vivo* brain imaging, small imaging currents must be injected so as not to stimulate peripheral nerves in the skin, while delivery of imaging currents to the brain is relatively small due to the skull's low conductivity. As a result, injected imaging currents may induce small phase signals and the overall low phase SNR in brain tissues. In this study, we present numerical simulation results of the use of head MREIT for brain tumor detection. We used a realistic three-dimensional head model to compute signal levels produced as a consequence of a predicted doubling of conductivity occurring within simulated tumorous brain tissues. We determined the feasibility of measuring these changes in a time acceptable to human subjects by adding realistic noise levels measured from a candidate 3 T system. We also reconstructed conductivity contrast images, showing that such conductivity differences can be both detected and imaged.

1. Introduction

Brain tumors are serious and life-threatening because of their invasive and infiltrative characteristics [1]. Medical imaging plays a central role in the diagnosis of brain tumors [2, 3]. MRI is the preferred imaging modality for brain tumor diagnosis, providing detailed information of lesion type, size and location [4]. Although gadolinium-enhanced T_1 -weighted images and T_2 -weighted images are the MRI modalities of choice for the initial assessment, their usefulness in identifying tumor types, distinguishing tumors from nontumoral lesions, and assessing treatment effects is limited [4, 5]. For this reason, these scans may be used in combination with other advanced MRI techniques [5]. However, there is still a demand for new MR-based methods that can both detect and characterize brain lesions.

Magnetic resonance electrical impedance tomography (MREIT) is a technique that uses MRI to measure the internal magnetic flux density induced by externally injected currents

[6–8]. Since the magnetic flux density perturbs the main field of an MRI scanner, one can obtain the z -component of the induced magnetic flux density (B_z) by rescaling MR phase images [9–11]. Applying a conductivity image reconstruction algorithm [12–14], we can reconstruct high-resolution high-contrast conductivity image of the object. MREIT has been steadily developed from simulations, reconstruction algorithms, and imaging experiments using both phantoms and animals [12–17]. It has now reached a stage of *in vivo* human imaging experiments, and Kim et al. [18] recently reported the first such trial. Use of MREIT has also been suggested for neural activity detection in small-scale isolated neural structures [19] or as a means of understanding the effects of neuromodulation techniques such as deep brain stimulation or transcranial DC stimulation [20]. We believe that MREIT conductivity imaging will be of great use in providing *in vivo* conductivity information for biological tissues in what is known to be a physiologically relevant frequency range.

The delivery of imaging currents to the brain is difficult due to the low conductivity of skull bones. As a result, injected currents may induce a small phase signal, high noise level and low signal-to-noise-ratio (SNR) in brain tissue. Since the phase signals measured in MREIT may be quite small, SNR can be improved by increasing the imaging current amplitude or imaging time [8]. As in many other applications, intrinsic noise levels may be reduced by increased averaging or using higher field strengths. Therefore, in principle it should be possible to obtain sufficient SNR to observe brain tumors using MREIT, as long as imaging currents are applied for as long as possible, and if MR phase noise is low enough to allow averaging over a practical amount of time.

In this study, we are focused on the feasibility of applying MREIT to image *in vivo* brain tumors within the intact head. We approach this goal by constructing a finite element electromagnetic model of a realistically shaped human head, and simulating the effect of MREIT protocols with different sizes and locations of tumor conductivity changes.

2. Methods

2.1. Three-Dimensional Head Model. We built a three-dimensional finite element model based on a reference MRI data set consisting of 42 sagittal plane slices (3 mm thickness) over a 270 mm \times 270 mm field of view (FOV) with an image matrix size of 512 \times 512. Voxel sizes in the data set were therefore 0.53 mm \times 0.53 mm \times 3 mm. We used COMSOL (COMSOL Inc., Burlington, MA, USA) to extract the external head shape from the MRI data set. First, external contours of six transverse head projections were computed, then “lofted” together to form a three-dimensional solid structure. The resulting model had a volume of 4.2 L and a diameter at the temple of 17.5 cm. Four large MREIT electrodes (thicknesses 3 mm, area 64.5 cm², and conductivity 0.17 S/m) were then added to the outer surface of the head (Figure 1(a)). Using the MRI data set as a guide, the head was further segmented into significant brain components: scalp, skull, gray matter (volume 0.4 L), white matter (volume 1.1 L), a subarachnoid layer (160 mL), and lateral ventricles (total volume 5.2 mL), as shown in Figures 1(b) and 1(c).

Conductivities used with the finite element model are shown in Table 1 [21–26]. Where possible, we chose recently measured values that were gathered in situations close to *in vivo* conditions. Values measured near 100 Hz were selected because MREIT currents are typically low frequency square waves (ca. 10–20 ms periods at 50% duty cycle). In our model, we assumed that white matter has isotropic conductivity of 0.058 S/m. Since the scalp consists of skin, muscle, a vascular layer, and fat, we considered an average conductivity value of 0.24 S/m to be reasonable. An isotropic conductivity of 0.0042 S/m was used for the skull [24]. There have been several studies on the electrical conductivity of the human cerebrospinal fluid [21]. We chose to use a value of 1.2 S/m in the subarachnoid space to most appropriately reflect its MREIT properties. This choice was made because of the small thickness of the component (approximately 2 mm, smaller than most voxels), and the mixture and proportions of tissues

(bone, dura, CSF, and vessels) we expected to contribute to the properties of this region [22–26].

We included spherical anomalies of various diameters inside the brain component of the model to simulate tumors. The conductivity of these anomalies was chosen to be twice that of the surrounding normal brain tissues. In one version of the model, we introduced 8 spherical simple structured tumor-like anomalies, with diameters of 5, 7.5, 10, or 15 mm. In a second version of the model, we included 8 spherical complex structured anomalies consisting of angiogenic and necrotic tumor regions. The size of each region was half of the anomaly.

2.2. Numerical Simulation of Brain MREIT. The model was meshed into a large number (ca. 500000) of cubic tetrahedral finite elements as shown in Figure 1(c). In one head model containing a tumor-like anomaly, 448708 elements were created with a total number of degrees of freedom around 4.1×10^6 (Figure 1(c)). The minimum element quality in the model was about 6.8×10^{-3} (Figure 1(e)). We solved for the Laplace equation in our model:

$$\nabla \cdot (\sigma(x, y, z) \nabla \phi) = 0 \quad (1)$$

on the head (Ω), subject to

$$\sigma \frac{\partial \phi}{\partial \mathbf{n}} = j, \quad \sum_{d\Omega} j = 0, \quad (2)$$

where $d\Omega$ is the head surface, ϕ is the voltage distribution, j is the surface current density, and \mathbf{n} is a vector normal to the surface. The quantity $\sigma(x, y, z)$ is the conductivity distribution within the head. A total current of approximately 6.4 mA (a current density of 0.1 mA/cm² underneath the electrode) was applied through each electrode in either left-right (LR) or anterior-posterior (AP) directions.

Voltage solutions were computed on the head domain, and then converted to magnetic flux density (B_z) values within voxels of the size of $1.40 \times 1.40 \times 4$ mm³ using the Biot-Savart law [7, 8] or a fast Fourier transform method [29]. Data were computed over a 180×180 mm² field of view (FOV) and 8 slices in total were simulated, each slice having a thickness of 4 mm. The in-slice image matrix size was 128×128 . Wires (length 2 cm, conductivity 20000 S/m) were connected to the center of each electrode, and at right angles to each electrode’s surface to make the measurement more realistic. Further details of the simulation methods used in this paper may be found in Minhas et al. [29].

Reconstructions from B_z data to conductivity distributions at the selected resolution were performed using the harmonic B_z algorithm. This technique was first developed by Seo et al. [7, 15] and has been widely used in MREIT experiment studies. In this paper, conductivity reconstructions were performed using the CoReHA MREIT reconstruction package [28].

2.3. Noise Analysis in Brain Tumor Detection. We first examined the effect of introducing simple structured anomalies with 200% conductivity contrast with respect to the brain

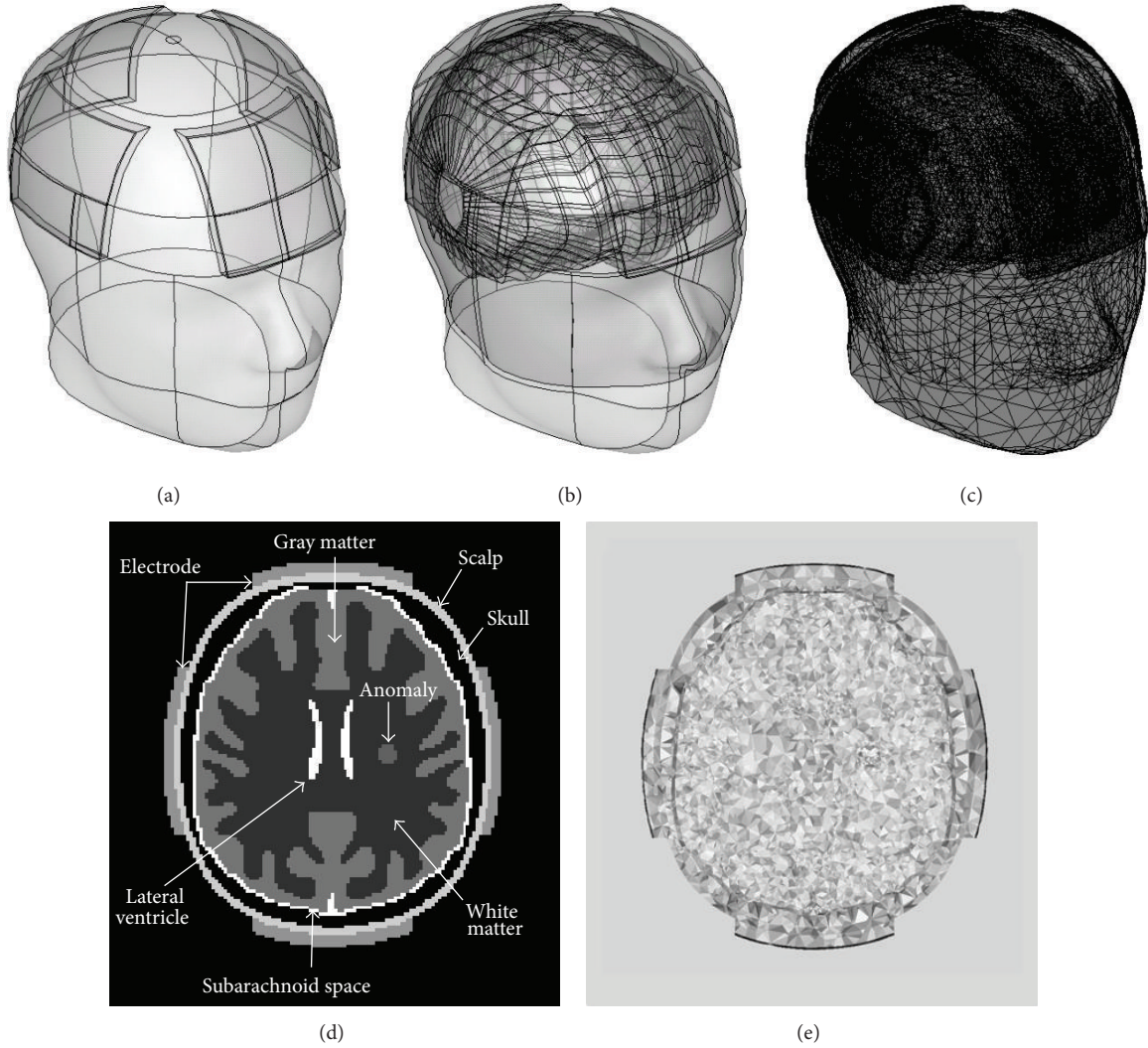


FIGURE 1: Overview of complete realistic head model. Shown here are (a) external geometry and electrode placement; (b) internal brain tissue; (c) completed mesh; (d) cross-sectional image of segmented structures, showing lateral ventricle, subarachnoid space, gray matter, white matter, skull, scalp, and 10 mm diameter tumor-like anomaly; and (e) cross-sectional image showing mesh quality at the same slice as shown in (d).

TABLE 1: Conductivities used in finite element models, with sources.

Component	Conductivity (S/m)	Comments/sources
Gray Matter	0.09	Gabriel et al. [22]
White Matter	0.06	Gabriel et al. [22]
CSF (ventricle)	1.80	Baumann et al. [21]
Subarachnoid space	1.20	Estimated from relative contributions of dura 0.5, CSF 1.8, skull 0.02, blood 0.67, and vessel 0.26 S/m per Gabriel et al. [22]
Skull	0.0042	Dannhauer et al. [24]
Scalp	0.24	Estimated from relative contributions of muscle 0.27, skin 0.00046, blood 0.67, vessel 0.26, and fat 0.02 S/m per Gabriel et al. [22]
Tumor-like anomaly in gray matter	0.20	2 times increase over gray matter value
Tumor-like anomaly in white matter	0.12	2 times increase over white matter value
Necrotic region	0.01	Oh et al. [27]
Hydrogel electrode	0.17	Jeon et al. [28]

background in which it appeared. We then examined signal and reconstructed images resulting from a complex structured anomaly model having necrotic and angiogenic tumor regions. The noise standard deviation was derived from experimental measurements of noise in a clinical 3T MRI system (Achieva TX, Philips Medical Systems, Best, The Netherlands) [30]. Noise was added to the simulated B_z voxel data based on

$$s = \frac{1}{\sqrt{2}\gamma T_c Y_M}, \quad (3)$$

where Y_M is the signal-to-noise ratio (SNR) in MR magnitude images, γ is the gyromagnetic ratio of hydrogen ($26.75 \times 10^7 \text{ radT}^{-1}\text{s}^{-1}$), and T_c is the injection current pulse duration. Since the T_1 , T_2 value of gray, white matter and cerebrospinal fluid (CSF) are different [31, 32], the standard deviations of noise levels from different tissues were calculated separately and summed. Noise levels in each tissue were approximately 0.16 nT, 0.03 nT, and 0.013 nT with one excitation, respectively. Consider MRI acquisition at a voxel sized at Δx , Δy , and Δz along the x , y , and z directions, respectively. Let N_x , N_y , and N_z be the number of k -space samples in each of these directions, with a total readout sampling duration of $T_s = N_x \times \Delta t$, where Δt is the time for one readout sample. Assuming that a spin-echo pulse sequence is used, the TR and TE dependence of the MR magnitude is given by

$$M = M_0 \left(1 - e^{-TR/T_1}\right) e^{-TE/T_2}, \quad (4)$$

where T_1 and T_2 are spin relaxation times, and M_0 is proton density. The magnitude image SNR, Y_M , is given by the following relation [33]:

$$Y_M = M \Delta x \Delta y \Delta z \sqrt{N_x N_y N_z \Delta t \text{NEX}}. \quad (5)$$

Substituting (5) into (3), we have

$$s = \frac{1}{\sqrt{2}\gamma T_c M \Delta x \Delta y \Delta z \sqrt{N_x N_y N_z \Delta t \text{NEX}}}. \quad (6)$$

We now compare two different MREIT experiments performed with the same total scan time, same injection current amplitude, and same number of protons. If we denote the B_z noise standard deviations in each case to be s_0 and s , respectively, then, substituting (4) into (6), we find that s_0 and s are related by

$$s = s_0 \times \left(\frac{T_c}{T_{c0}} \frac{\Delta x}{\Delta x_0} \frac{\Delta y}{\Delta y_0} \frac{\Delta z}{\Delta z_0} \frac{1 - e^{-TR/T_1}}{1 - e^{-TR_0/T_1}} \right) \times \left(\frac{e^{-TE/T_2}}{e^{-TE_0/T_2}} \sqrt{\frac{N N_x N_y N_z \Delta t}{N_0 N_{x0} N_{y0} N_{z0} \Delta t_0}} \right)^{-1}. \quad (7)$$

The standard deviation of B_z noise levels expected in the human head was calculated by adjusting this figure using typical TE (time to echo) and TR (repetition time) values, and adjusting for the voxel size and number of averages selected. In this study, we used a 1000 ms TR and a TE of 30 ms.

3. Results

3.1. Simulation Results. Figure 2 shows example data from the calculations with and without a single anomaly with 200% conductivity contrast for the case of 3 mA horizontal (LR) current and current application time T_c of 30 ms. The upper panels of the figure show plots of voltage (V), current density (A/m^2), and magnetic flux density B_z (T), respectively, without the anomaly present. The lower panels show the changes in voltage, current density, and B_z that resulted when the tumor anomaly was introduced. The average current density value within the tumor was 0.035 A/m^2 , much lower than the value of 1.2 A/m^2 that has been estimated as the threshold for neural excitation [34]. Changes in B_z due to the brain tumor were of the order of $\pm 10^{-10}$ T in this case. We found that the anomaly perturbed the distributions of V , J , and B_z and noted that the values of ΔB_z near the anomaly were greater than the noise level predicted in the measured B_z data. We found similar results for the second injection current I_2 .

Reconstructed conductivity images using B_z data gathered from the single anomaly model in Figure 2 are shown in Figure 3. Figure 3(a) shows the actual conductivity distribution, and Figures 3(b) and 3(c) are reconstructed conductivity images created without and with experimental noise, respectively. To better simulate *in vivo* brain images, we added Gaussian noise with standard deviation values of 0.080 nT, and 0.016 nT, 0.007 nT (gray matter, white matter, and CSF) to simulate noise-contaminated B_z data generated with a number of averages of $N = 4$. As a result, reconstructed images of gray matter appear much noisier than white matter compartments overall. These values were computed using (7). Regardless of experimental noise, the MREIT reconstruction method could qualitatively differentiate tumor-like anomalies with diameters larger than 10 mm when the current amplitude of 3 mA was used.

3.2. Brain Tumor Detection. To more comprehensively test the technique, we repeated the numerical simulations for the case of four different diameters of anomalies with 5, 7.5, 10, and 15 mm. Figures 4(a) and 4(b) show actual and reconstructed conductivity images of simple structure anomalies using noise-free B_z data. Because tumors can grow anywhere inside the brain, we placed anomalies inside both white and gray matter. Phase signals in anomalies near the boundaries of brain tissue had higher noise levels than those inside the brain. Figures 4(c) and 4(d) show images of complex structure anomalies we created to more realistically test our head model. Without noise, the MREIT reconstruction method could qualitatively differentiate tumor-like anomalies with diameters larger than the pixel size of 1.4 mm.

Figure 5 shows reconstructed conductivity images of the simulated head model with simple structure anomalies created from data collected using different numbers of averages N and current amplitudes. The images represent reconstruction results with the NEX (the number of average N) increasing from 1 to 8 (top to bottom) and the amplitude of injected currents increasing from 1 to 5 mA (left to right).

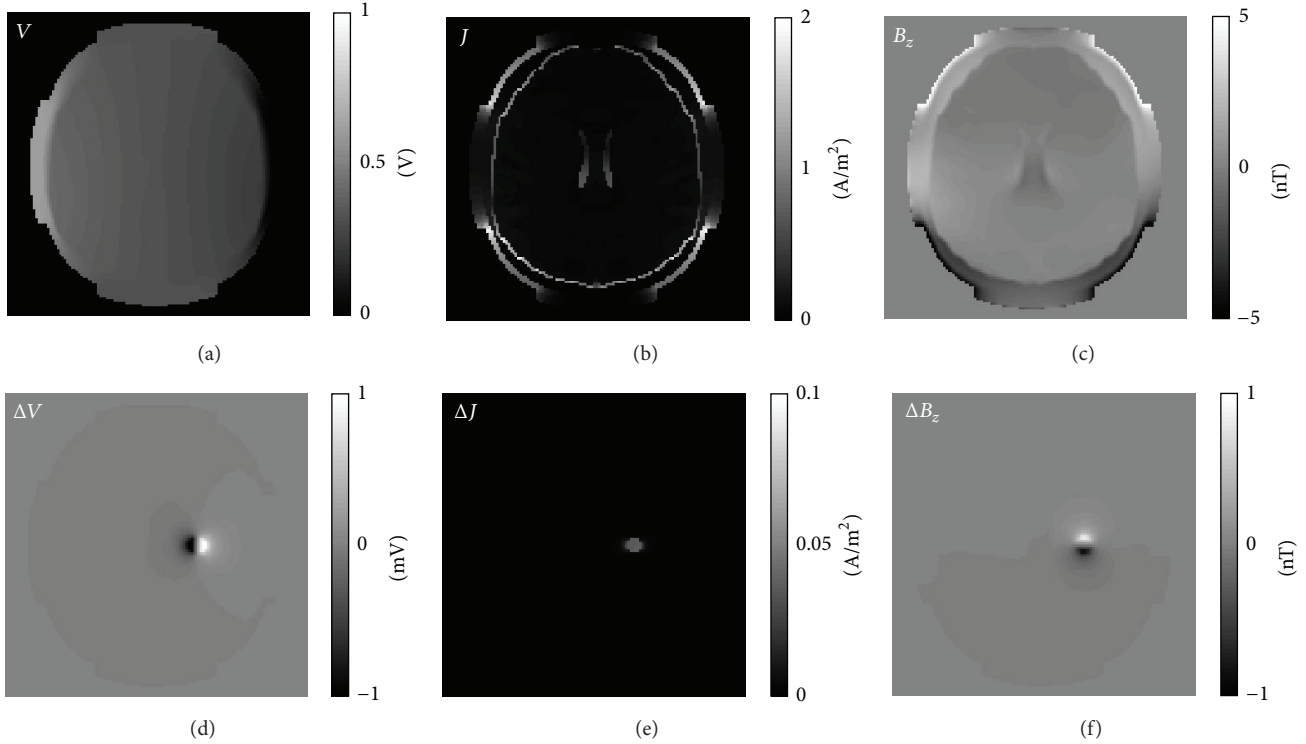


FIGURE 2: Axial slice of single anomaly model showing (a) voltage V , (b) current density magnitude J , and (c) magnetic flux density B_z values without anomaly present; and changes caused in the same slice with the anomaly having a 200% conductivity contrast from the brain background as (d) ΔV , (e) ΔJ , and (f) ΔB_z distributions. Results are shown for LR current flow only. The injected current had 3 mA amplitude and a total current pulse width of 30 ms.

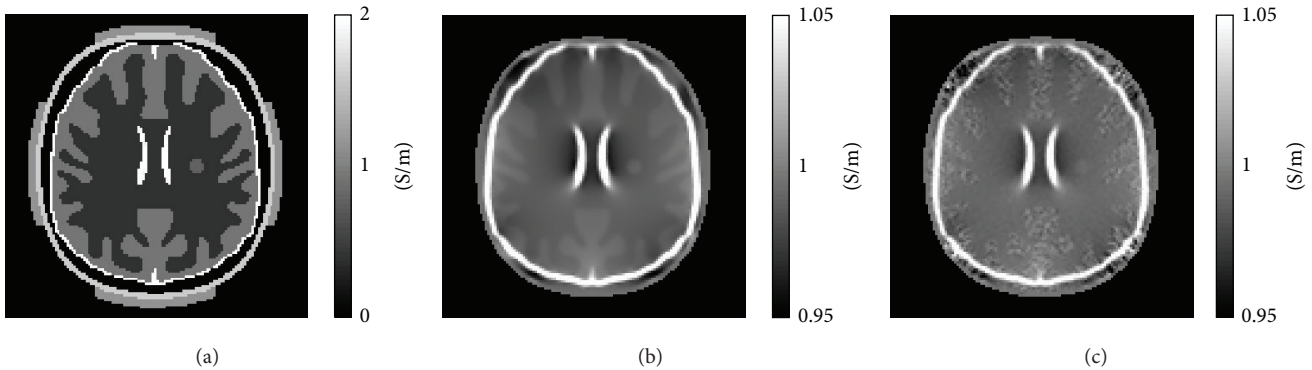


FIGURE 3: Conductivity images of brain model containing a single 10 mm diameter anomaly with 200% conductivity contrast. Image (a) shows the actual conductivity distribution. Images (b) and (c) show reconstructed conductivity images without and with noise, respectively. The injected current was 3 mA and the total current pulse width was 30 ms.

For any value of current amplitude, we can see that the image quality improves as we increase the number of averages N . Unfortunately, in the case of 1 mA imaging currents, even an anomaly having a 15 mm diameter could not be distinguished. For a fixed amount of noise in the B_z data (i.e., for a given value of N), we can improve image quality by increasing the current amplitude to produce B_z data with a larger dynamic range, that is, a higher SNR in the measured B_z data. For any value of N , and using either 3 or 5 mA injection currents, the 15 mm anomaly was clearly visible in reconstructions.

In the white matter, the 10 and 75 mm anomalies were distinguishable at any value of N , using either 3 or 5 mA injection currents. The 5 mm anomaly was distinguishable when $N = 4$ and 8 with 5 mA injection current. In gray matter, anomalies having a diameter smaller than 10 mm were not clearly visible, even with the lowest noise level ($N = 8$, 5 mA injection current). The 10 mm anomaly was only partially distinguishable when $N = 4$ or 8 with 5 mA current. Table 2 summarizes the standard deviations in conductivity values representing the improvement of the conductivity

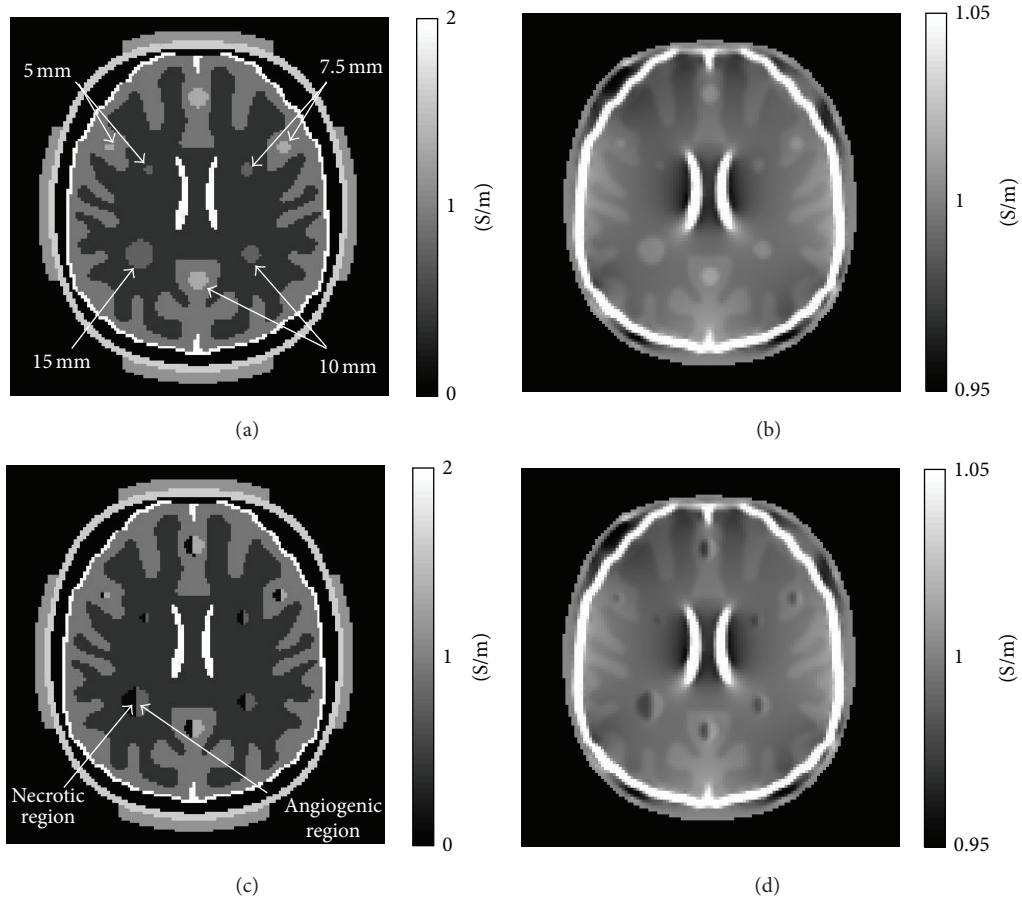


FIGURE 4: (a) Actual and (b) reconstructed conductivity images of 5, 7.5, 10 and 15 mm diameter anomalies having simple structures, using noise-free data. (c) and (d) are corresponding images of complex anomalies reconstructed using noise-free data.

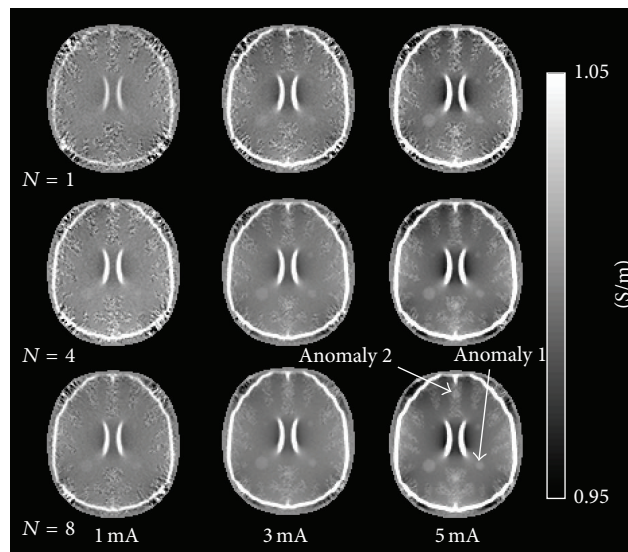


FIGURE 5: Reconstructed conductivity images of 5, 7.5, 10, and 15 mm diameter tumor-like anomalies having simple structures obtained using noisy data. Conductivity images were obtained at different numbers of averages N (top to bottom), and current amplitudes (left to right). Noise was added to the simulated B_z voxel data, based on experimental measurements of B_z noise in 3 T MR system.

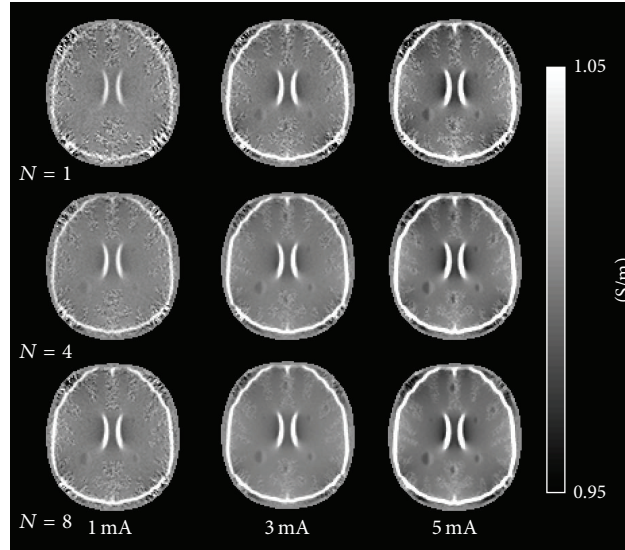


FIGURE 6: Reconstructed conductivity images of 5, 7.5, 10, and 15 mm diameter tumor-like anomalies having complex structures. The conductivity value of the angiogenic tumor region was two times higher than normal tissues and that of the necrotic region was 0.01 S/m. Conductivity images were obtained at different numbers of averages N (top to bottom) and current amplitudes (left to right). Noise was added to the simulated B_z voxel data, based on experimental measurements of B_z noise in 3 T MR system.

image in accordance with the different numbers of averages N and current amplitudes for simple structured anomalies.

Figure 6 shows the results of the same process applied to a complex structured anomaly model. As in the single anomaly cases, for 1 mA injection current, it was difficult to detect tumor-like anomalies when $N = 1, 4,$ and $8,$ except for a 15 mm anomaly in white matter. As current amplitude was increased, some of the anomalies were detectable as N was progressively increased. In white matter, a 5 mm complex anomaly was not clearly visible even at $N = 8$ and 5 mA injection current. Interestingly, in 10 and 15 mm diameter tumors, the conductivity differences between necrotic and angiogenic tumor regions were easily distinguished. When $N = 4$ or 8 with 5 mA injection current, 7.5 mm anomalies also showed this pattern. Unfortunately, in gray matter, the 10 mm anomalies were clearly visible only at $N = 4$ or 8 with 5 mA current. The 7.5 mm anomaly was detectable but did not display a conductivity contrast between the necrotic and angiogenic regions of the tumor.

3.3. Analysis of ΔB_z with Noise Level. For a tumor-like anomaly to be detected inside the brain, the change in the measured B_z , due to the presence of an anomaly, ΔB_z , must be larger than the noise level in measured B_z data. ΔB_z values are influenced by the injection current amplitude and anomaly size. We computed average values of ΔB_z inside anomaly regions, and compared them with noise levels s , which in turn are determined by imaging parameters and tissue properties of T_1 and T_2 as shown in (7). Figures 7(a) and 7(b) illustrate how the noise level s in measured B_z should change with pixel size $\Delta x = \Delta y$ as the number of averages N and the total current injection time T_c are varied in both white and gray matter. In both cases, the slice thickness Δz was 4 mm

and the diameter of the anomaly was 10 mm. These plots provide a useful guide for the selection of parameters such as $\Delta x, \Delta y, N,$ and T_c and the injection current amplitude required to produce B_z data that are capable of visualizing a certain anomaly in the presence of a particular estimated noise level. We may easily scale up and down the plots in Figure 7 for different situations.

4. Discussion

We have demonstrated that tumor-like anomalies with 200% conductivity contrast can straightforwardly be both detected and imaged by an existing 3 T system using total acquisition times below 30 minutes. Smaller anomalies (ca. 5 mm diameter) could not easily be discerned in images, even with 8 averages. However, it may be possible to detect these smaller anomalies when we alter imaging parameters further, such as by increasing the number of averages above 8, or increasing the image resolution, but this will of course increase overall averaging time. The 7.5, 10, and 15 mm diameter anomalies with 200% contrast were detectable in white matter, but the 10 mm gray matter anomaly was only visible at the lowest relative noise level. In the complex anomaly cases, the boundaries between the low-conductivity necrotic region and high-conductivity angiogenic regions were clearly contrasted in 10 and 15 mm diameter anomalies. These results may provide evidence that MREIT can be used not only to detect brain tumors, but may also provide useful tumor characterization information.

The model we have used here is detailed with respect to the principal conductivity contrasts within the head. Those critical to delivering the current to the head are scalp and skull conductivity, as well as CSF conductivity

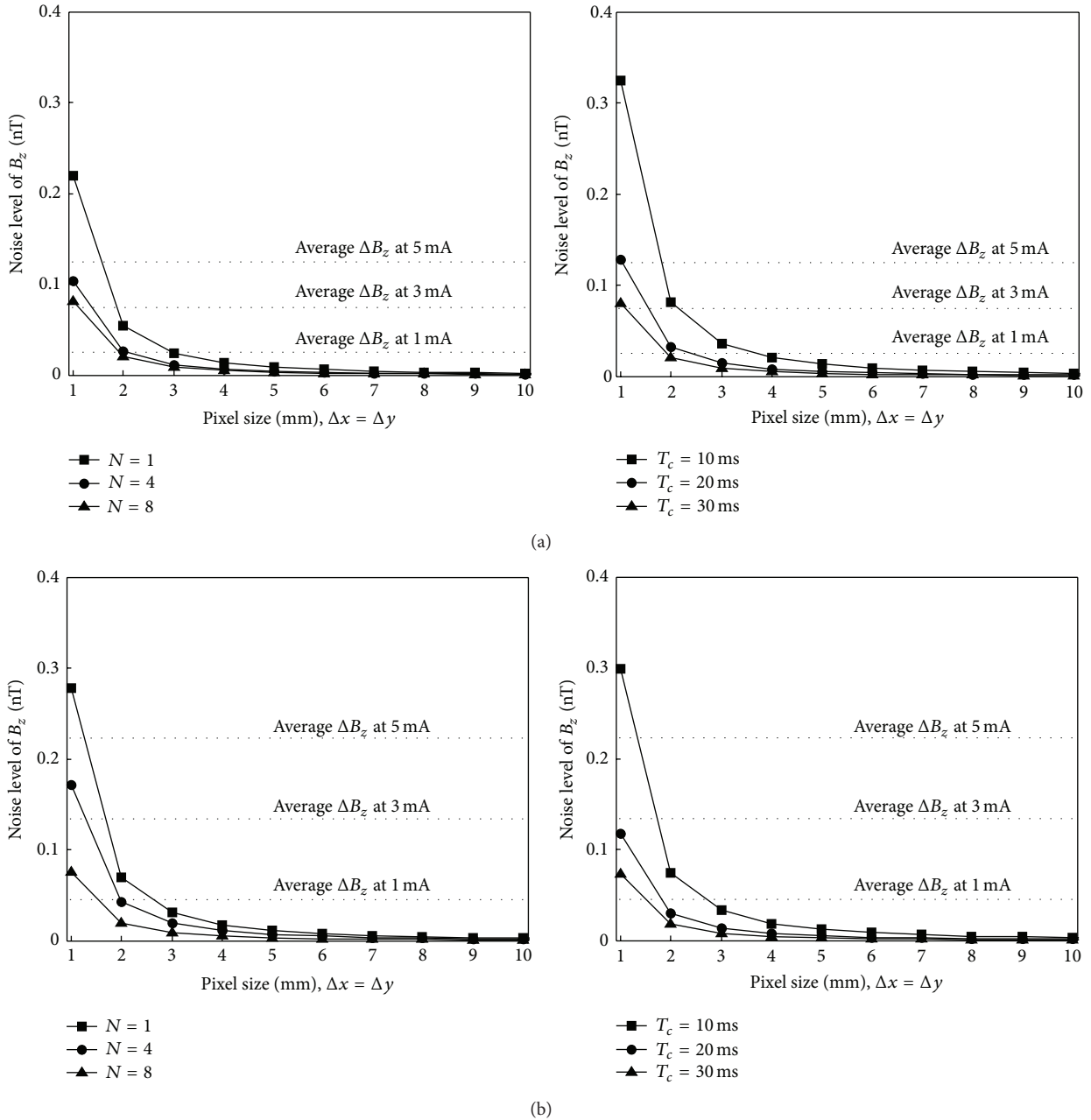


FIGURE 7: Nomogram showing predicted B_z noise levels compared to the estimated signal size at different pixel sizes using a fixed slice thickness of 4 mm and assuming a 10 mm anomaly diameter in both (a) white and (b) gray matter. Three different values of averaging NEX at T_c of 30 ms and three different values of total current injection time T_c at $N = 8$ were used. The values of average ΔB_z are compared for a simulated conductivity contrast of 200% and for an anomaly diameter of 10 mm.

TABLE 2: Measured standard deviation of reconstructed conductivity from Figure 5. ROI (region of interest) was located in the normal gray, white matter, and anomalies with the voxel size of $5 \times 5 \times 5 \text{ mm}^3$. Note CoReHA provides only conductivity contrast information. We therefore show standard deviation of conductivity values as a quantitative criterion representing an improvement in conductivity images.

Current	Measured standard deviation in conductivity (mS/m)								
	White (gray) matter			Anomaly 1			Anomaly 2		
	1 NEX	4 NEX	8 NEX	1 NEX	4 NEX	8 NEX	1 NEX	4 NEX	8 NEX
1 mA	1.4 (6.3)	0.9 (3.1)	0.6 (2.6)	1.3	0.6	0.4	5.4	2.7	2.4
3 mA	1.1 (5.9)	0.6 (2.4)	0.4 (2.1)	0.8	0.4	0.3	5.2	2.4	2.0
5 mA	0.9 (4.7)	0.4 (1.9)	0.3 (1.4)	0.6	0.4	0.2	3.2	2.3	1.9

[20]. There are several improvements that could be made to our model, including differentiation of both cortical and cancellous bone, and the use of anisotropic conductivity in white matter. These could cause some modification to the current density distribution and therefore to the predicted signal levels [35]. Another modification that we have included here is to differentiate between peripheral and ventricular CSF. MR data is intrinsically volumetric and therefore data in one voxel is averaged over all tissues within. The layer between the skull and cortex is very thin and made up of many different components, only one of which is CSF. Therefore, we estimated the value for conductivity in this area as a mix of CSF and other tissues not modeled, including the dura, skull, and blood vessels. The consideration of the model's construct validity extends to the inclusion of the expected conductivity change. While few estimates of the size of conductivity changes to be expected from brain tumors have been made, we selected the values that have been most widely used. Further modeling and experimentation will be guided by improvements in these basic measurements.

The B_z data in this study were collected using a conventional, simple spin echo MR sequence. More sensitive and faster pulse sequences are currently in development [8, 36] and may further improve phase data, signal-to-noise-ratio (SNR), and sensitivity. The use of multiple RF coils and newer, lower-noise systems should further enhance SNR.

The harmonic B_z algorithm implemented in CoReHA produces conductivity images with relative conductivity contrasts [28]. A variation of the harmonic B_z algorithm known as the local harmonic B_z algorithm (LBz) can be used to perform conductivity data within a specified region of interest [16, 17]. This approach has the benefit of avoiding reconstructions using data where SNR is particularly low. Additionally, denoising steps can greatly improve the quality of reconstructed images [37, 38]. While absolute conductivity images are advantageous in imaging tumors or other static physiological presentations, conductivity contrast images should be sufficient for most MREIT applications.

While we believe that this study shows that MREIT is realizable in human brain tumor detection, there are other considerations that must be taken into account when performing *in vivo* imaging. First, we are unsure of the extent to which physiological, and in particular hemodynamic-changes should affect signal-to-noise ratios. Only *in vivo* testing will allow us to determine the effect of these signals. We have shown that MREIT should be capable of imaging realistically sized brain tumor conductivity changes occurring within gray matter regions using conventional MR systems and over a practical period of time. Testing *in vivo* will allow us to determine the extent and size of physiological changes.

5. Conclusion

In this study, we have shown the feasibility of MREIT conductivity imaging for brain tumor detection. We simulated the effect of MREIT protocols with different sizes and locations of conductivity change, using a finite element electromagnetic

model of a human head. Conductivity values used in our models were taken from well-accepted and recent sources, with attention paid to compartment environments. As well as modeling the skull compartment conductivity accurately, it is also important in simulation studies to use realistic skull and head geometries and to appropriately segment the head model. To better apply this technique *in vivo*, advanced head MR imaging methods including pulse sequence (such as GRE, EPI, and SSFP), k -space sampling strategies, and multichannel high-sensitivity RF coils may be employed to minimize the noise level in measured magnetic flux density data and thus reduce the current and time needed to produce good conductivity resolution.

Acknowledgments

This work was supported by the Basic Science Research Program through the National Research Foundation of Korea (NRF) funded by the Ministry of Education, Science and Technology (no. 2012R1A1A2008477).

References

- [1] B. A. Moffat, T. L. Chenevert, T. S. Lawrence et al., "Functional diffusion map: a noninvasive MRI biomarker for early stratification of clinical brain tumor response," *Proceedings of the National Academy of Sciences of the United States of America*, vol. 102, no. 15, pp. 5524–5529, 2005.
- [2] C. Van de Wiele, C. Lahorte, W. Oyen et al., "Nuclear medicine imaging to predict response to radiotherapy: a review," *International Journal of Radiation Oncology Biology Physics*, vol. 55, no. 1, pp. 5–15, 2003.
- [3] W. D. Kaplan, T. Takvorian, and J. H. Morris, "Thallium-201 brain tumor imaging: a comparative study with pathologic correlation," *Journal of Nuclear Medicine*, vol. 28, no. 1, pp. 47–52, 1987.
- [4] R. F. Barajas Jr. and S. Cha, "Imaging diagnosis of brain metastasis," *Progress in Neurological Surgery*, vol. 25, pp. 55–73, 2012.
- [5] G. S. Young, "Advanced MRI of adult brain tumors," *Neurologic Clinics*, vol. 25, no. 4, pp. 947–973, 2007.
- [6] S. H. Oh, B. I. Lee, E. J. Woo et al., "Conductivity and current density image reconstruction using harmonic B_z algorithm in magnetic resonance electrical impedance tomography," *Physics in Medicine and Biology*, vol. 48, no. 19, pp. 3101–3116, 2003.
- [7] E. J. Woo and J. K. Seo, "Magnetic resonance electrical impedance tomography (MREIT) for high-resolution conductivity imaging," *Physiological Measurement*, vol. 29, no. 10, pp. R1–R26, 2008.
- [8] A. S. Minhas, W. C. Jeong, Y. T. Kim, Y. Q. Han, H. J. Kim, and E. J. Woo, "Experimental performance evaluation of multi-echo ICNE pulse sequence in magnetic resonance electrical impedance tomography," *Magnetic Resonance in Medicine*, vol. 66, pp. 957–965, 2011.
- [9] M. Joy, G. Scott, and M. Henkelman, "In vivo detection of applied electric currents by magnetic resonance imaging," *Magnetic Resonance Imaging*, vol. 7, no. 1, pp. 89–94, 1989.
- [10] G. C. Scott, M. L. G. Joy, R. L. Armstrong, and R. M. Henkelman, "Measurement of nonuniform current density by magnetic resonance," *IEEE Transactions on Medical Imaging*, vol. 10, no. 3, pp. 362–374, 1991.

- [11] G. C. Scott, M. L. G. Joy, R. L. Armstrong, and R. M. Henkelman, "Sensitivity of magnetic-resonance current-density imaging," *Journal of Magnetic Resonance*, vol. 97, no. 2, pp. 235–254, 1992.
- [12] C. Park, O. Kwon, E. J. Woo, and J. K. Seo, "Electrical conductivity imaging using gradient B_z decomposition algorithm in magnetic resonance electrical impedance tomography (MREIT)," *IEEE Transactions on Medical Imaging*, vol. 23, no. 3, pp. 388–394, 2004.
- [13] N. Gao, S. A. Zhu, and B. He, "A new magnetic resonance electrical impedance tomography (MREIT) algorithm: the RSM-MREIT algorithm with applications to estimation of human head conductivity," *Physics in Medicine and Biology*, vol. 51, no. 12, pp. 3067–3083, 2006.
- [14] O. Birgül, B. M. Eyüboğlu, and Y. Z. Ider, "Experimental results for 2D magnetic resonance electrical impedance tomography (MR-EIT) using magnetic flux density in one direction," *Physics in Medicine and Biology*, vol. 48, no. 21, pp. 3485–3504, 2003.
- [15] J. K. Seo, J. R. Yoon, E. J. Woo, and O. Kwon, "Reconstruction of conductivity and current density images using only one component of magnetic field measurements," *IEEE Transactions on Biomedical Engineering*, vol. 50, no. 9, pp. 1121–1124, 2003.
- [16] H. J. Kim, B. I. Lee, Y. Cho et al., "Conductivity imaging of canine brain using a 3 T MREIT system: postmortem experiments," *Physiological Measurement*, vol. 28, no. 11, pp. 1341–1353, 2007.
- [17] H. J. Kim, T. I. Oh, Y. T. Kim et al., "In vivo electrical conductivity imaging of a canine brain using a 3 T MREIT system," *Physiological Measurement*, vol. 29, no. 10, pp. 1145–1155, 2008.
- [18] H. J. Kim, Y. T. Kim, A. S. Minhas et al., "In vivo high-resolution conductivity imaging of the human leg using MREIT: the first human experiment," *IEEE Transactions on Medical Imaging*, vol. 28, no. 11, pp. 1681–1687, 2009.
- [19] R. J. Sadleir, S. C. Grant, and E. J. Woo, "Can high-field MREIT be used to directly detect neural activity? Theoretical considerations," *NeuroImage*, vol. 52, no. 1, pp. 205–216, 2010.
- [20] R. J. Sadleir, T. D. Vannorsdall, D. J. Schretlen, and B. Gordon, "Transcranial direct current stimulation (tDCS) in a realistic head model," *NeuroImage*, vol. 51, no. 4, pp. 1310–1318, 2010.
- [21] S. B. Baumann, D. R. Wozny, S. K. Kelly, and F. M. Meno, "The electrical conductivity of human cerebrospinal fluid at body temperature," *IEEE Transactions on Biomedical Engineering*, vol. 44, no. 3, pp. 220–223, 1997.
- [22] C. Gabriel, S. Gabriel, and E. Corthout, "The dielectric properties of biological tissues: I. Literature survey," *Physics in Medicine and Biology*, vol. 41, no. 11, pp. 2231–2249, 1996.
- [23] M. Akhtari, H. C. Bryant, A. N. Mamelak et al., "Conductivities of three-layer human skull," *Brain Topography*, vol. 13, no. 1, pp. 29–42, 2000.
- [24] M. Dannhauer, B. Lanfer, C. H. Wolters, and T. R. Knosche, "Modeling of the human skull in EEG source analysis," *Human Brain Mapping*, vol. 32, pp. 1383–1399, 2011.
- [25] T. F. Oostendorp, J. Delbeke, and D. F. Stegeman, "The conductivity of the human skull: results of in vivo and in vitro measurements," *IEEE Transactions on Biomedical Engineering*, vol. 47, no. 11, pp. 1487–1492, 2000.
- [26] J. Latikka, T. Kuurne, and H. Eskola, "Conductivity of living intracranial tissues," *Physics in Medicine and Biology*, vol. 46, no. 6, pp. 1611–1616, 2001.
- [27] T. I. Oh, W. C. Jeong, A. McEwan et al., "Feasibility of MREIT conductivity imaging to evaluate brain abscess lesion: in vivo canine model," *Journal of Magnetic Resonance Imaging*. In press.
- [28] K. Jeon, A. S. Minhas, Y. T. Kim et al., "MREIT conductivity imaging of the postmortem canine abdomen using CoReHA," *Physiological Measurement*, vol. 30, no. 9, pp. 957–966, 2009.
- [29] A. S. Minhas, H. H. Kim, Z. J. Meng, Y. T. Kim, H. J. Kim, and E. J. Woo, "Three-dimensional MREIT simulator of static bioelectromagnetism and MRI," *Biomedical Engineering Letters*, vol. 1, pp. 129–136, 2011.
- [30] R. Sadleir, S. Grant, U. Z. Sung et al., "Noise analysis in magnetic resonance electrical impedance tomography at 3 and 11 T field strengths," *Physiological Measurement*, vol. 26, no. 5, pp. 875–884, 2005.
- [31] G. J. Stanisiz, E. E. Odrobina, J. Pun et al., "T1, T2 relaxation and magnetization transfer in tissue at 3T," *Magnetic Resonance in Medicine*, vol. 54, no. 3, pp. 507–512, 2005.
- [32] P. Schmitt, M. A. Griswold, P. M. Jakob et al., "Inversion Recovery TrueFISP: quantification of T_1 , T_2 , and Spin Density," *Magnetic Resonance in Medicine*, vol. 51, no. 4, pp. 661–667, 2004.
- [33] E. M. Haacke, R. W. Brown, M. R. Thompson, and R. Venkatesan, *Magnetic Resonance Imaging: Physical Principles and Sequence Design*, Wiley-Liss, 1999.
- [34] J. P. Reilly, *Applied Bioelectricity, High-Voltage and High-Current Injuries*, Springer, New York, NY, USA, 1998.
- [35] R. J. Sadleir and A. Argibay, "Modeling skull electrical properties," *Annals of Biomedical Engineering*, vol. 35, no. 10, pp. 1699–1712, 2007.
- [36] H. S. Nam and O. I. Kwon, "Optimization of multiply acquired magnetic flux density B_z using ICNE-multiecho train in MREIT," *Physics in Medicine and Biology*, vol. 55, no. 9, pp. 2743–2759, 2010.
- [37] B. I. Lee, S. H. Lee, T. S. Kim, O. Kwon, E. J. Woo, and J. K. Seo, "Harmonic decomposition in PDE-based denoising technique for magnetic resonance electrical impedance tomography," *IEEE Transactions on Biomedical Engineering*, vol. 52, no. 11, pp. 1912–1920, 2005.
- [38] C. O. Lee, S. Ahn, and K. Jeon, *Denosing of B_z Data for Conductivity Reconstruction in Magnetic Resonance Electrical Impedance Tomography (MREIT)*, KAIST DMS BK21 Research Report Series, 2009.

Research Article

Effective Admittivity of Biological Tissues as a Coefficient of Elliptic PDE

Jin Keun Seo,¹ Tushar Kanti Bera,¹ Hyeuknam Kwon,¹ and Rosalind Sadleir²

¹ Department of Computational Science and Engineering, Advanced Science and Technology Center (ASTC), Yonsei University, 50 Yonsei-Ro, 134 Sinchon-dong, Seodaemun-gu, Seoul 120 749, Republic of Korea

² J. Crayton Pruitt Family Department of Biomedical Engineering, University of Florida, Biomedical Sciences Building JG-5, P.O. Box 116131, Gainesville, FL 32611, USA

Correspondence should be addressed to Tushar Kanti Bera; tkbera77@gmail.com

Received 26 October 2012; Accepted 15 January 2013

Academic Editor: Eung Je Woo

Copyright © 2013 Jin Keun Seo et al. This is an open access article distributed under the Creative Commons Attribution License, which permits unrestricted use, distribution, and reproduction in any medium, provided the original work is properly cited.

The electrical properties of biological tissues can be described by a complex tensor comprising a simple expression of the effective admittivity. The effective admittivities of biological tissues depend on scale, applied frequency, proportions of extra- and intracellular fluids, and membrane structures. The effective admittivity spectra of biological tissue can be used as a means of characterizing tissue structural information relating to the biological cell suspensions, and therefore measuring the frequency-dependent effective conductivity is important for understanding tissue's physiological conditions and structure. Although the concept of effective admittivity has been used widely, it seems that its precise definition has been overlooked. We consider how we can determine the effective admittivity for a cube-shaped object with several different biologically relevant compositions. These precise definitions of effective admittivity may suggest the ways of measuring it from boundary current and voltage data. As in the homogenization theory, the effective admittivity can be computed from pointwise admittivity by solving Maxwell equations. We compute the effective admittivity of simple models as a function of frequency to obtain Maxwell-Wagner interface effects and Debye relaxation starting from mathematical formulations. Finally, layer potentials are used to obtain the Maxwell-Wagner-Fricke expression for a dilute suspension of ellipses and membrane-covered spheres.

1. Introduction

The human body can be regarded as a complex electrical conductor comprising many tissues that have distinct electrical properties. Measurements of the electrical properties of biological tissues have shown that effective conductivity (σ^{ef}) and permittivity (ϵ^{ef}) values of biological tissues in the frequency range from a few Hz to MHz are influenced by physiological and pathological conditions [1–5]. The effective admittivity $\gamma^{\text{ef}} = \sigma^{\text{ef}} + i\omega\epsilon^{\text{ef}}$ of a biological tissue under the influence of a time-harmonic electric field at an angular frequency ω is determined by its ion concentrations in extra- and intracellular fluids, cellular structure and density, molecular compositions, membrane characteristics, and other factors. Cell membranes contribute to capacitance; the

intracellular fluid gives rise in an intracellular resistance; the extracellular fluid contributes to effective resistance. As a result, biological tissues show a variable response over the frequency range from a few Hz to MHz. For most biological tissues, $\gamma^{\text{ef}} \approx \sigma^{\text{ef}}$ at low frequencies below 10 kHz, whereas the $\omega\epsilon^{\text{ef}}$ term is not negligible beyond 10 kHz due to the abundant membranous structures in organisms.

The effective admittivity γ^{ef} can be regarded as a function of tissue composition and the applied angular frequency ω . Assume that a biological subject under consideration is a mixture of homogeneous tissue at macroscopic length scale and has a constant effective admittivity γ^{ef} in a particular cubic sample voxel. The γ^{ef} can be viewed as the effective tensor according to the well-known concept of homogenization when the admittivity $\gamma = \sigma + i\omega\epsilon$ is periodic [6]. The effective

admittivity γ^{ef} as a function of ω and the voxel V_{oxel} can be determined by Ohm's law:

$$\int_{V_{\text{oxel}}} \mathbf{J}(\mathbf{r}) d\mathbf{r} \approx \gamma^{\text{ef}}(\omega, V_{\text{oxel}}) \int_{V_{\text{oxel}}} \mathbf{E}(\mathbf{r}) d\mathbf{r} \quad (1)$$

for a time-harmonic electric field \mathbf{E} and the corresponding current density $\mathbf{J} = \gamma\mathbf{E}$ at angular frequency ω . Here, $\gamma^{\text{ef}}(\omega, V_{\text{oxel}})$ is a symmetric 3×3 matrix and $\mathbf{r} = (x, y, z)$ is the position within the voxel. If the quantity $(\int_{V_{\text{oxel}}} \mathbf{J}(\mathbf{r}) d\mathbf{r}) \times (\int_{V_{\text{oxel}}} \mathbf{E}(\mathbf{r}) d\mathbf{r}) \approx 0$ for any pair of electric field \mathbf{E} and current density \mathbf{J} , then γ^{ef} is scalar and the subject is isotropic. Otherwise, a subject is said to be anisotropic. Depending on the measurement scale used, anisotropy may or may not be detected. There have been numerous studies and models formulated for admittivity spectra $\{\gamma^{\text{ef}}(\omega, V_{\text{oxel}}) : 0 \leq \omega/2\pi \leq 100 \text{ MHz}\}$ of biological tissue as a means of characterizing tissue structural information relating to biological cell suspensions [7, 8]. In 1873, Maxwell [9] derived an expression of $\sigma^{\text{ef}}(\omega = 0)$ for the special case of a strongly dilute suspension of spherical particles and $\omega = 0$. Wagner extended the expression to a general γ^{ef} . Poisson [10] in 1826 and Faraday in 1827 dealt with the case of a suspension of infinitely conducting spheres in a background. In 1924, Fricke [7] provided an expression for γ^{ef} by considering the capacity due to a polarization at the interphases or the presence in the interphases of thin poorly conducting membranes. There have been also studies on an effective conductivity of cell suspensions, both analytically and numerically [11–17].

The concept of effective admittivity has been used widely, but it seems that its precise definition has been overlooked. How can we determine the effective admittivity of a given cubic region? In this paper we give precise definitions of effective admittivity to provide a way to measure it from boundary current and voltage data. As in the homogenization theory, the effective admittivity can be computed from pointwise admittivity by solving Maxwell equations. We compute the effective admittivity of simple models as a function of frequency to observe the Maxwell-Wagner interface effect and Debye relaxation using a mathematical point of view. Single layer and double layer potentials are used to produce the Maxwell-Wagner-Fricke expression for a dilute suspension of ellipses and a membrane-covered conductor, respectively. We also note that Maxwell equations make both microscopic and macroscopic senses.

2. Effective Admittivity Spectra of Biological Tissues

The concept of admittivity contains four key definitions: pointwise admittivity, effective admittivity, apparent admittivity, and equivalent admittivity.

- (i) Pointwise admittivity refers to electrical properties at microscopic scale.
- (ii) Effective admittivity is defined at macroscopic scale. Homogenization methods have been used to compute effective property of a periodic heterogeneous subject

from its pointwise structure [18]. It is used to describe the linear relationship between the ensemble mean current density and the ensemble mean electrical field. Effective admittivity depends only on the electrical properties of the sample.

- (iii) Apparent admittivity is defined as the admittivity of electrically homogeneous and isotropic medium that could yield the potential measured on the heterogeneous subject using the same applied current and arrangement of the electrodes.
- (iv) Two expressions that have the same effective admittivity are called equivalent admittivity. Pavlin and Miklavčič [19] use a simpler equivalent conductivity of a single cell for the purpose of computation of effective conductivity of a suspension of permeabilized cells.

Let Ω be a three-dimensional domain with a pointwise admittivity of $\gamma(\mathbf{r}, \omega) = \sigma(\mathbf{r}) + i\omega\epsilon(\mathbf{r})$, where the conductivity $\sigma(\mathbf{r})$ and the permittivity $\epsilon(\mathbf{r})$ values are assumed to depend only on position $\mathbf{r} = (x, y, z)$, and both are isotropic. Then, the domain Ω can be viewed as a union of many voxels V_{oxel} , and the effective properties mainly depend on the choice of voxels. With a given voxels, we can define the effective admittivity $\gamma^{\text{ef}}(\omega)$ that is a constant on each voxel $V_{\text{oxel}} \subset \Omega$. The effective admittivity is a tensor-valued function of the voxel V_{oxel} and the angular frequency ω such that

$$\gamma^{\text{ef}}(V_{\text{oxel}}, \omega) = \begin{pmatrix} \gamma_{xx}^{\text{ef}}(V_{\text{oxel}}, \omega) & \gamma_{xy}^{\text{ef}}(V_{\text{oxel}}, \omega) & \gamma_{xz}^{\text{ef}}(V_{\text{oxel}}, \omega) \\ \gamma_{xy}^{\text{ef}}(V_{\text{oxel}}, \omega) & \gamma_{yy}^{\text{ef}}(V_{\text{oxel}}, \omega) & \gamma_{yz}^{\text{ef}}(V_{\text{oxel}}, \omega) \\ \gamma_{xz}^{\text{ef}}(V_{\text{oxel}}, \omega) & \gamma_{yz}^{\text{ef}}(V_{\text{oxel}}, \omega) & \gamma_{zz}^{\text{ef}}(V_{\text{oxel}}, \omega) \end{pmatrix}. \quad (2)$$

The $\gamma^{\text{ef}}(V_{\text{oxel}}, \omega)$ must be the best approximation of the average of the pointwise admittivity γ over the voxel V_{oxel} in the sense that

$$\int_{V_{\text{oxel}}} \gamma(\mathbf{r}, \omega) \nabla u(\mathbf{r}, \omega) d\mathbf{r} \approx \gamma^{\text{ef}}(\omega, V_{\text{oxel}}) \int_{V_{\text{oxel}}} \nabla u(\mathbf{r}, \omega) d\mathbf{r} \\ \forall u \in H^1(\Omega) \text{ satisfying } \nabla \cdot (\gamma(\mathbf{r}, \omega) \nabla u) = 0 \text{ in } \Omega. \quad (3)$$

The physically meaningful solution u must have a finite energy [20]:

$$\Phi(v) = \int_{\Omega} \sigma(\mathbf{r}) |\nabla v(\mathbf{r})|^2 d\mathbf{r} < \infty. \quad (4)$$

Hence, the solution of the equation $\nabla \cdot (\gamma(\mathbf{r}, \omega) \nabla u) = 0$ should be contained in the set $\{v \in L^2(\Omega) : \Phi(v) < \infty\}$ [20]. Here, $H^1(\Omega)$ is the standard Sobolev space equipped with norm $\|u\| = \sqrt{\int_{\Omega} |\nabla u|^2 + |u|^2 d\mathbf{r}}$.

However, there is no such tensor $\gamma^{\text{ef}}(V_{\text{oxel}}, \omega)$ satisfying (3) exactly. Hence, we may take an appropriate $\gamma^{\text{ef}}(V_{\text{oxel}}, \omega)$ satisfying (3) approximately, and the choice of $\gamma^{\text{ef}}(V_{\text{oxel}}, \omega)$ may differ for a biological sample. To clearly define the effective admittivity, we need to select suitable potentials $u \in H^1(\Omega)$ satisfying $\nabla \cdot (\gamma(\mathbf{r}, \omega) \nabla u(\mathbf{r})) = 0$ in Ω .

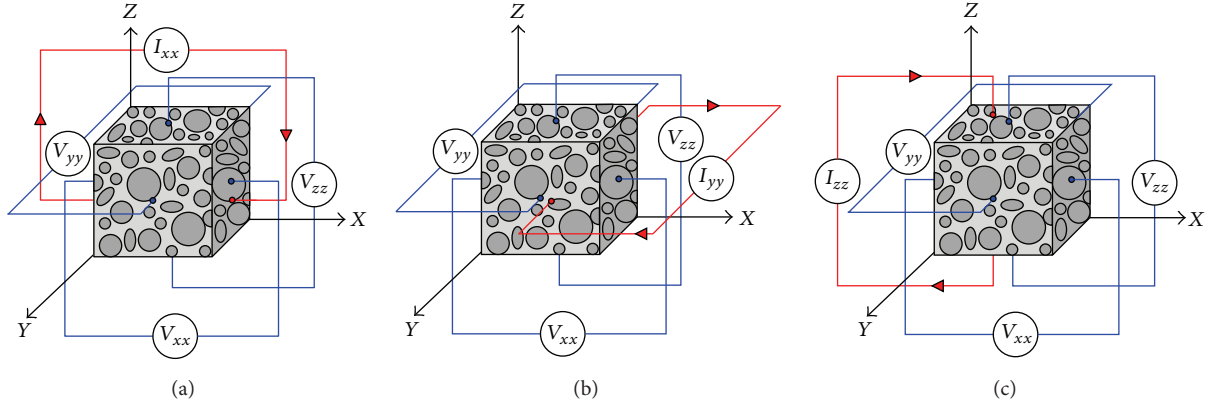


FIGURE 1: Admittivity measurement of a unit cube of anisotropic material: (a) current injection through \mathcal{E}_+^x and \mathcal{E}_-^x planes, (b) current injection through \mathcal{E}_+^y and \mathcal{E}_-^y planes, and (c) current injection through \mathcal{E}_+^z and \mathcal{E}_-^z planes.

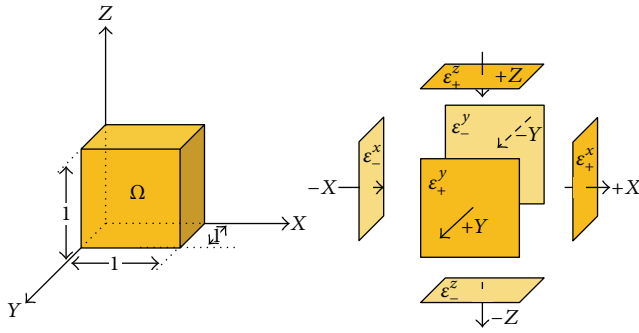


FIGURE 2: A tissue sample contained in the unit cube.

2.1. Definition of Effective Admittivity for a Cubic Sample.

Let us consider a rectangular-shaped tissue sample (Figure 1) occupied in the unit cube $\Omega = \{\mathbf{r} : 0 < x, y, z < 1 \text{ cm}\}$ with its three pairs of facing surfaces (Figure 2):

$$\begin{aligned} \mathcal{E}_+^x &= \{\mathbf{r} \in \partial\Omega : x = 1\}, & \mathcal{E}_-^x &= \{\mathbf{r} \in \partial\Omega : x = 0\}, \\ \mathcal{E}_+^y &= \{\mathbf{r} \in \partial\Omega : y = 1\}, & \mathcal{E}_-^y &= \{\mathbf{r} \in \partial\Omega : y = 0\}, \\ \mathcal{E}_+^z &= \{\mathbf{r} \in \partial\Omega : z = 1\}, & \mathcal{E}_-^z &= \{\mathbf{r} \in \partial\Omega : z = 0\}. \end{aligned} \quad (5)$$

Assume that the admittivity distribution of the sample at frequency $\omega/2\pi$ is given by $\gamma(\mathbf{r}, \omega) = \sigma(\mathbf{r}) + i\omega\epsilon(\mathbf{r})$, where the conductivity $\sigma(\mathbf{r})$ and the permittivity $\epsilon(\mathbf{r})$ values are scalar-valued functions depending only on position \mathbf{r} . Hence, $\gamma(\mathbf{r}, \omega)$ is isotropic on a microscopic scale. If we apply a current of $I(t) = I_0 \cos(\omega t)$ through the pair of electrodes attached on \mathcal{E}_+^a and \mathcal{E}_-^a , then the resulting time-harmonic potential $u^a(\mathbf{r}, \omega)$ satisfies the following equation from a suitable arrangement of Maxwell equations (at frequencies below about 100 kHz):

$$\begin{aligned} \nabla \cdot (\gamma(\mathbf{r}, \omega) \nabla u^a(\mathbf{r}, \omega)) &= 0 \quad \text{for } \mathbf{r} \in \Omega, \\ \mathbf{n} \cdot (\gamma \nabla u^a)|_{\mathcal{E}_+^a} &= I_0 = -\mathbf{n} \cdot (\gamma \nabla u^a)|_{\mathcal{E}_-^a} \quad (a \in \{x, y, z\}), \\ \mathbf{n} \cdot \nabla u^a|_{\partial\Omega \setminus (\mathcal{E}_+^a \cup \mathcal{E}_-^a)} &= 0, \end{aligned} \quad (6)$$

where \mathbf{n} is the unit outward normal vector on $\partial\Omega$. For each $a, b \in \{x, y, z\}$, we denote the voltage difference \mathcal{E}_+^b by

$$V^{ab}(\omega) = \int_{\mathcal{E}_+^b} u^a dS - \int_{\mathcal{E}_-^b} u^a dS. \quad (7)$$

Lemma 1 (reciprocity). *For $a, b \in \{x, y, z\}$, one has*

$$V^{ab}(\omega) = V^{ba}(\omega). \quad (8)$$

Proof. From the boundary conditions of u^b and divergence theorem, we have

$$V^{ba}(\omega) = \frac{1}{I_0} \int_{\mathcal{E}_+^b} \mathbf{n} \cdot (\gamma \nabla u^a) u^b dS = \frac{1}{I_0} \int_{\Omega} \gamma \nabla u^a \cdot \nabla u^b d\mathbf{r}. \quad (9)$$

Hence, the symmetry (8) follows from the reciprocity relation

$$\begin{aligned} V^{ab}(\omega) &= \frac{1}{I_0} \int_{\Omega} \gamma \nabla u^a \cdot \nabla u^b d\mathbf{r} = V^{ba}(\omega) \\ &\quad \forall a, b \in \{x, y, z\}. \end{aligned} \quad (10)$$

If $\nabla\gamma(\mathbf{r}, \omega) = 0$ (homogeneous), then $V^{xx}(\omega) = V^{yy}(\omega) = V^{zz}(\omega)$ and $V^{xy}(\omega) = V^{xz}(\omega) = V^{yz}(\omega) = 0$ and $\gamma^{\text{ef}}(\omega)$ must be $\gamma^{\text{ef}}(\omega) = \gamma(\omega) = I_0/V^{xx}$. If the effective admittivity $\gamma^{\text{ef}}(\omega)$ is a diagonal matrix satisfying

$$\begin{pmatrix} \gamma_{xx}^{\text{ef}} & 0 & 0 \\ 0 & \gamma_{yy}^{\text{ef}} & 0 \\ 0 & 0 & \gamma_{zz}^{\text{ef}} \end{pmatrix} \int_{\Omega} \nabla u^a(\mathbf{r}, \omega) d\mathbf{r} = \int_{\Omega} \gamma(\mathbf{r}, \omega) \nabla u^a(\mathbf{r}, \omega) d\mathbf{r} \quad \forall a \in \{x, y, z\}, \quad (11)$$

then it must be $\gamma_{xx}^{\text{ef}} = \frac{I_0}{V^{xx}}$, $\gamma_{yy}^{\text{ef}} = \frac{I_0}{V^{yy}}$, and $\gamma_{zz}^{\text{ef}} = \frac{I_0}{V^{zz}}$ due to the following theorem. \square

Theorem 2. If u^a is the solution of (6), then one has

$$\begin{aligned} \frac{I_0}{V^{xx}(\omega)} &= \frac{\int_{\Omega} \gamma(\mathbf{r}, \omega) \nabla u^x(\mathbf{r}, \omega) \cdot \nabla x d\mathbf{r}}{\int_{\Omega} \nabla u^x(\mathbf{r}, \omega) \cdot \nabla x d\mathbf{r}}, \\ \frac{I_0}{V^{yy}(\omega)} &= \frac{\int_{\Omega} \gamma \nabla u^y \cdot \nabla y d\mathbf{r}}{\int_{\Omega} \nabla u^y \cdot \nabla y d\mathbf{r}}, \\ \frac{I_0}{V^{zz}(\omega)} &= \frac{\int_{\Omega} \gamma \nabla u^z \cdot \nabla z d\mathbf{r}}{\int_{\Omega} \nabla u^z \cdot \nabla z d\mathbf{r}}. \end{aligned} \quad (12)$$

Proof. We will only prove $\gamma_{xx}^{\text{ef}}(\omega)$. From the definition of u^x , $x|_{\mathcal{G}_x^+} = 1$, and the divergence theorem, we have

$$\begin{aligned} I_0 &= \int_{\mathcal{G}_x^+} \gamma \nabla u^x \cdot \mathbf{n} dS = \int_{\mathcal{G}_x^+} (\gamma \nabla u^x \cdot \mathbf{n}) x dS \\ &= \int_{\Omega} \gamma(\mathbf{r}, \omega) \nabla u^x(\mathbf{r}, \omega) \cdot \nabla x d\mathbf{r}. \end{aligned} \quad (13)$$

Since $\nabla^2 x = 0$ and $\mathbf{n} \cdot \nabla x|_{\mathcal{G}_x^+} = 1$,

$$\begin{aligned} V^{xx}(\omega) &= \int_{\mathcal{G}_x^+} u^x dS - \int_{\mathcal{G}_x^-} u^x dS \\ &= \int_{\partial\Omega} u^x (\mathbf{n} \cdot \nabla x) dS = \int_{\Omega} \nabla u^x(\mathbf{r}, \omega) \cdot \nabla x d\mathbf{r}. \end{aligned} \quad (14)$$

This completes the proof of (12). \square

Now, we are ready to define the effective admittivity tensor $\gamma^{\text{ef}}(\omega)$.

Definition 3. For a given unit cubic Ω and each $a, b \in \{x, y, z\}$, let V^{ab} be the potential difference given in (7). Then the effective admittivity tensor $\gamma^{\text{ef}}(\omega)$ is defined by

$$\begin{aligned} [\gamma^{\text{ef}}(\omega)]^{-1} &= \begin{pmatrix} \gamma_{xx}^{\text{ef}}(\omega) & \gamma_{xy}^{\text{ef}}(\omega) & \gamma_{xz}^{\text{ef}}(\omega) \\ \gamma_{xy}^{\text{ef}}(\omega) & \gamma_{yy}^{\text{ef}}(\omega) & \gamma_{yz}^{\text{ef}}(\omega) \\ \gamma_{xz}^{\text{ef}}(\omega) & \gamma_{yz}^{\text{ef}}(\omega) & \gamma_{zz}^{\text{ef}}(\omega) \end{pmatrix}^{-1} \\ &:= \frac{1}{I_0} \begin{pmatrix} V^{xx}(\omega) & V^{xy}(\omega) & V^{xz}(\omega) \\ V^{xy}(\omega) & V^{yy}(\omega) & V^{yz}(\omega) \\ V^{xz}(\omega) & V^{yz}(\omega) & V^{zz}(\omega) \end{pmatrix}. \end{aligned} \quad (15)$$

The proposed definition may not have coordinate invariance due to its limitation of the tensor expression. For a proper invariance, we need to compute all the tensors (15) by rotating the coordinate system. We may define the effective admittivity tensor as the best fit of the minimization problem described in (3).

Next, we study how the distribution of $\gamma(\mathbf{r}, \omega) = \sigma(\mathbf{r}) + i\omega\epsilon(\mathbf{r})$ is related to the frequency-dependent behavior of $\{I^{ab}(\omega) : 0 \leq \omega/2\pi \leq 10^6, a, b \in \{x, y, z\}\}$.

2.2. One Dimensional Sample. We begin by considering a special sample (Figure 3) with γ depending only on the x -variable:

$$\gamma(x) = \begin{cases} \gamma^{\text{int}} = \sigma^{\text{int}} + i\omega\epsilon^{\text{int}} & \text{if } a < x < a + c \\ \gamma^{\text{ext}} = \sigma^{\text{ext}} + i\omega\epsilon^{\text{ext}} & \text{otherwise,} \end{cases} \quad (16)$$

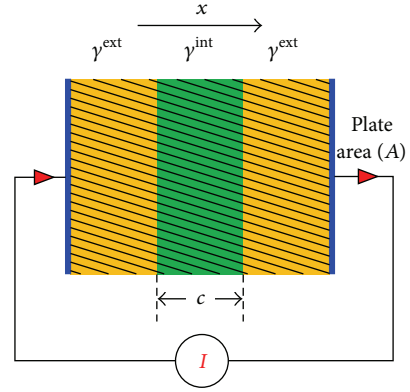


FIGURE 3: Double layer sandwich type capacitor: a one-dimensional structure.

where $\sigma^{\text{int}}, \epsilon^{\text{int}}, \sigma^{\text{ext}}$, and ϵ^{ext} are constants and $0 < a < a + c < 1$. For this sample, the potential $u(\mathbf{r}, \omega)$ in (6) depends only on x -variable, and

$$\begin{aligned} \frac{d}{dx} \left(\gamma(x, \omega) \frac{d}{dx} u(x, \omega) \right) &= 0 \quad \text{in } (0, 1), \\ \frac{d}{dx} u(1, \omega) &= I_0 = \frac{d}{dx} u(0, \omega). \end{aligned} \quad (17)$$

Since $\gamma(x, \omega)(d/dx)u(x, \omega)$ is a constant,

$$\begin{aligned} \gamma(x, \omega) \frac{d}{dx} u(x, \omega) &= \gamma(1, \omega) \frac{d}{dx} u(1, \omega) = I_0 \\ &\text{for } x \in (0, 1). \end{aligned} \quad (18)$$

Writing $V(\omega) := u(1, \omega) - u(0, \omega)$, we have

$$\begin{aligned} V(\omega) &= \int_0^1 \frac{d}{dx} u(x) dx = \int_0^1 \frac{1}{\gamma(x, \omega)} \underbrace{\frac{d}{dx} u(x)}_{I_0} dx \\ &= I_0 \int_0^1 \frac{1}{\gamma(x, \omega)} dx. \end{aligned} \quad (19)$$

Hence, it follows from the definition of (15) of γ^{ef} that

$$\gamma_{xx}^{\text{ef}}(\omega) = \frac{I_0}{V(\omega)} = \left(\int_0^1 \frac{1}{\gamma(x, \omega)} dx \right)^{-1}. \quad (20)$$

This means that $\gamma^{\text{ef}}(\omega)$ is the harmonic average of the admittivity that can be expressed as

$$\begin{aligned} \gamma_{xx}^{\text{ef}}(\omega) &= \left(\frac{1-c}{\gamma^{\text{ext}}(\omega)} + \frac{c}{\gamma^{\text{int}}(\omega)} \right)^{-1} \\ &= \frac{\gamma^{\text{ext}}(\omega) \gamma^{\text{int}}(\omega)}{(1-c) \gamma^{\text{int}}(\omega) + c \gamma^{\text{ext}}(\omega)}. \end{aligned} \quad (21)$$

From this, we have

$$\gamma_{xx}^{\text{ef}}(\omega) = \sigma_{xx}^{\text{ef}}(\omega) + i\omega\epsilon_{xx}^{\text{ef}}(\omega), \quad (22)$$

$$\sigma_{xx}^{\text{ef}}(\omega) = \sigma_{xx}^{\text{ef}}(0) + \left(\sigma_{xx}^{\text{ef}}(\infty) - \sigma_{xx}^{\text{ef}}(0)\right) \frac{\omega^2\tau^2}{1 + \omega^2\tau^2}, \quad (23)$$

$$\epsilon_{xx}^{\text{ef}}(\omega) = \epsilon_{xx}^{\text{ef}}(\infty) + \left(\epsilon_{xx}^{\text{ef}}(0) - \epsilon_{xx}^{\text{ef}}(\infty)\right) \frac{1}{1 + \omega^2\tau^2},$$

where

$$\tau = \frac{(1-c)\epsilon^{\text{int}} + c\epsilon^{\text{ext}}}{(1-c)\sigma^{\text{int}} + c\sigma^{\text{ext}}},$$

$$\sigma_{xx}^{\text{ef}}(0) = \frac{\sigma^{\text{ext}}\sigma^{\text{int}}}{(1-c)\sigma^{\text{int}} + c\sigma^{\text{ext}}},$$

$$\epsilon_{xx}^{\text{ef}}(\infty) = \frac{\epsilon^{\text{ext}}\epsilon^{\text{int}}}{(1-c)\epsilon^{\text{int}} + c\epsilon^{\text{ext}}}, \quad (24)$$

$$\sigma_{xx}^{\text{ef}}(\infty) = \frac{\sigma^{\text{int}}\epsilon^{\text{ext}} + \sigma^{\text{ext}}\epsilon^{\text{int}}}{(1-c)\epsilon^{\text{int}} + c\epsilon^{\text{ext}}} - \frac{\epsilon^{\text{ext}}\epsilon^{\text{int}}}{(1-c)\sigma^{\text{int}} + c\sigma^{\text{ext}}},$$

$$\epsilon_{xx}^{\text{ef}}(0) = \frac{\sigma^{\text{int}}\epsilon^{\text{ext}} + \sigma^{\text{ext}}\epsilon^{\text{int}}}{(1-c)\sigma^{\text{int}} + c\sigma^{\text{ext}}} - \frac{\sigma^{\text{ext}}\sigma^{\text{int}}}{(1-c)\epsilon^{\text{int}} + c\epsilon^{\text{ext}}}.$$

Writing $\Delta\sigma_{xx}^{\text{ef}} = \sigma_{xx}^{\text{ef}}(\infty) - \sigma_{xx}^{\text{ef}}(0)$ and $\Delta\epsilon_{xx}^{\text{ef}} = \epsilon_{xx}^{\text{ef}}(\infty) - \epsilon_{xx}^{\text{ef}}(0)$, we have

$$\Delta\epsilon_{xx}^{\text{ef}} = \tau\Delta\sigma_{xx}^{\text{ef}}. \quad (25)$$

Here, τ is referred to as a relaxation time, since its value controls polarization time [8, 21]. It is remarkable to observe that the relaxation time $\tau = ((1-c)\epsilon^{\text{int}} + c\epsilon^{\text{ext}})/((1-c)\sigma^{\text{int}} + c\sigma^{\text{ext}})$ may be obtained by solving the elliptic PDE (17).

Using (23), the average current density $\mathbf{J} = -\int_0^1 \gamma \nabla u$ generated inside the dielectric due to the average electric field $\mathbf{E} = -\int_0^1 \nabla u$ is given by

$$\mathbf{J} = \left(\sigma_{xx}^{\text{ef}}(\omega) + i\omega\epsilon_0\epsilon_{xx}^{\text{ef}}(\omega)\right)\mathbf{E}, \quad (26)$$

which can be expressed as

$$\mathbf{J} = \sigma_s \mathbf{E} + i\omega\epsilon_0 \left(\epsilon'_{xx}(\omega) - i\epsilon''_{xx}(\omega)\right)\mathbf{E}, \quad (27)$$

where $\sigma_s = \sigma_{xx}^{\text{ef}}(0)$ and

$$\begin{aligned} \epsilon'_{xx}(\omega) &= \epsilon_{xx}^{\text{ef}}(\infty) + \left(\epsilon_{xx}^{\text{ef}}(0) - \epsilon_{xx}^{\text{ef}}(\infty)\right) \frac{1}{1 + \omega^2\tau^2}, \\ \epsilon''_{xx}(\omega) &= \frac{1}{\omega\epsilon_0} \left(\left(\sigma_{xx}^{\text{ef}}(\infty) - \sigma_{xx}^{\text{ef}}(0)\right) \frac{\omega^2\tau^2}{1 + \omega^2\tau^2} \right). \end{aligned} \quad (28)$$

Here, $\epsilon'_{xx}(\omega)$ and $\epsilon''_{xx}(\omega)$ are referred to as the dielectric constant and loss factor of the dielectric material, respectively. The average current density can also be written as

$$\mathbf{J} = \underbrace{(\sigma_s + \omega\epsilon_0\epsilon''_{xx}(\omega))}_{\sigma^{\text{ef}}(\omega)}\mathbf{E} + i\omega\epsilon_0 \underbrace{\epsilon'_{xx}(\omega)}_{\epsilon^{\text{ef}}(\omega)}\mathbf{E}. \quad (29)$$

In biological materials σ_s is produced by the ionic conduction and $\omega\epsilon_0\epsilon''_{xx}(\omega)$ is produced by dielectric relaxation.

The dielectric response of biological tissues is always frequency dependent, and the electric charge movement inside the material in response to an externally applied electric field is controlled by the dielectric properties of the material. The free charge movement inside a material affected by an external field is controlled by its conductivity (σ). Biological tissues display extremely high dielectric constants at low frequencies, and as the excitation frequency is increased, the dielectric constants of the tissues fall off in more or less distinct steps [8]. Interfaces play a significant role in the frequency dependence of complex materials, particularly at audio and subaudio frequencies [8]. The frequency response of biological tissue admittivity is highly influenced by the dielectric polarization, dielectric relaxation, and dielectric dispersion.

Electric polarization (Figure 4) may be defined as the electric-field-induced disturbance (shift from average equilibrium positions) of the charge distribution in a region [8]. Dielectric dispersion in biological tissues can be assumed to depend upon the permittivity (Figure 5) of tissue material with applied electric field frequency [8]. In other words, a significant change in dielectric properties over a frequency range, by convention, is called a dielectric dispersion [21].

As there is always a lag between the changes in an applied electric field and changes in polarization, the permittivity of the biological tissues is a complex-valued function of the frequency of the applied electric field. The term dielectric relaxation [22] in a biological tissue connotes the delay or lag in its response to create the dielectric polarization following the application of electric field across the tissue sample. In other words, the dielectric relaxation of a tissue can be defined as the lag (momentary delay) in the dielectric constant which is usually caused by the delay in molecular polarization with respect to a change in applied electric field. According to the previous simple computations of (23) in the 1D model (17), the central frequency of the dispersion is $f_c = 1/2\pi\tau = (1/2\pi)((1-c)\sigma^{\text{int}} + c\sigma^{\text{ext}})/((1-c)\epsilon^{\text{int}} + c\epsilon^{\text{ext}})$.

Schwan [23, 24] studied the properties of biological tissue and cell suspensions over a large frequency range and observed that the dielectric properties of biological tissues are characterized by three major dispersions, α -dispersion [23, 24], β -dispersion [23, 24], and γ -dispersion [23, 24] occurring at low frequency, radio frequency, and microwave frequency, respectively. We consider each of these dispersions below.

- (i) α -dispersion ($10 \text{ Hz} \leq \omega/2\pi \leq 10 \text{ kHz}$): The α -dispersion is associated with tissue interfaces such as membranes [23]. Below about 10 kHz, the dielectric studies of biological or any other electrolyte systems become very complex and difficult to characterize. Foster and Schwan, 1989 [25], reported that α -dispersion is believed to be associated with a counterion layer (electrical double layer) polarization in tissues.
- (ii) β -dispersion ($10 \text{ kHz} \leq \omega/2\pi \leq 10 \text{ MHz}$): In biological tissues, the β -dispersion is caused by the

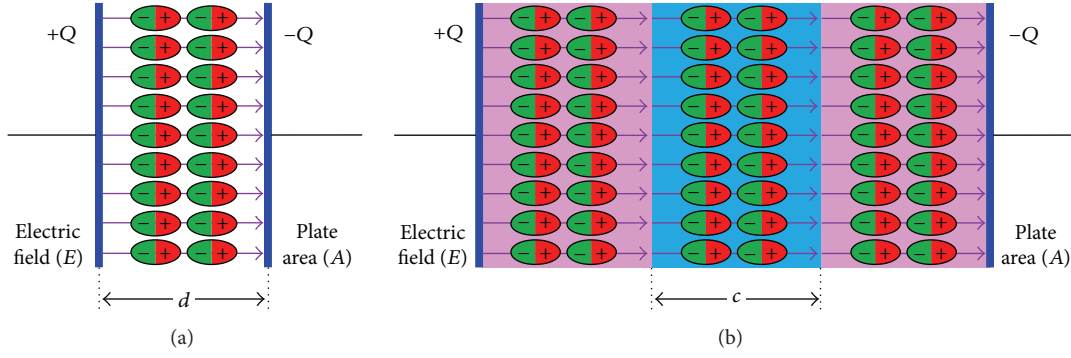


FIGURE 4: Dielectric polarization inside capacitors under an electric field E : (a) single dielectric capacitor and (b) double dielectric capacitor.

polarization of cellular membranes and polarization of protein and other organic macromolecules [23]. The β -dispersion arises, principally, from interfacial polarization (Maxwell-Wagner effect) [26] of cell membranes [21]. In the frequency range $10 \text{ kHz} \leq \omega/2\pi \leq 10 \text{ MHz}$, the dielectric behavior of the tissues is dominated by the heterogeneous composition and ionic activities inside the biological tissue. These effects are principally responsible for the β -dispersion. The radio frequency dispersion or β -dispersion has been recognized as a Maxwell-Wagner relaxation [26] caused by cell membranes [27]. A large magnitude, low frequency β -dispersion was observed by Schwan [28] in a muscle tissue. This effect is related, in part at least, to the tubular shape of muscle fibers [29]. The theoretical aspects of the low frequency dispersion of colloid particles in electrolyte solution have been studied by Schwarz in 1962 [30].

- (iii) γ -dispersion ($\omega/2\pi \geq 10 \text{ GHz}$). The γ -dispersion in biological tissues is caused by the reorientation of water molecules [18]. This dispersion has been well studied and has found many applications [31–33]. Rajewsky and Schwan [34] noted the γ -dispersion at microwave frequencies which is understood to be caused by abundant tissue water. Schwan conducted the extensive studies on the electrical properties of biological cell suspensions in 1993 [35] over a broad frequency range extending from less than 1 Hz to many GHz and summarized the mechanisms which contribute to the total frequency response. He studied the mechanisms responsible for electrical properties of tissues and cell suspensions, and he observed that the frequency changes of these properties obey causality, that is, the Kramers-Kronig relationships [35] which relate changes of dielectric constants to conductivity changes. A number of mechanisms which reflect the various compartments of the biological materials were identified such as membranes and their properties, biological macromolecules, and fluid compartments inside and outside membranes.

Membrane relaxation is anticipated from the Hodgkin-Huxley membrane model [36] and adds to the γ -effects [8],

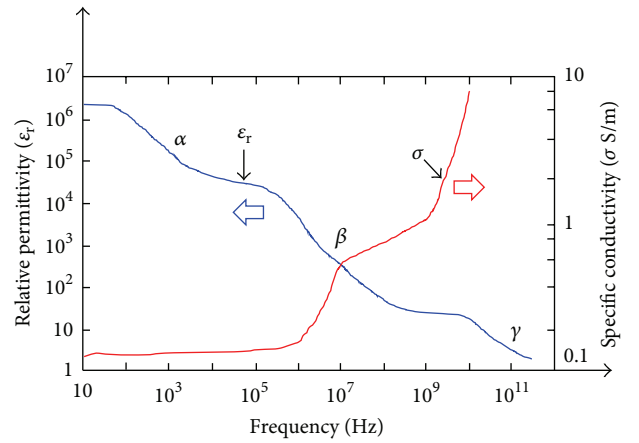


FIGURE 5: The variations of the complex permittivity of the biological tissues with frequency.

and hence a number of β -effects of small magnitude occur at the tail of the β -dispersion caused by proteins, protein-bound water (called δ -dispersion), and cell organelles such as mitochondria [37]. A second Maxwell-Wagner dispersion [26] which occurs at frequencies well above those of the main β -dispersion [8] is a characteristic of suspended particles surrounded by a shell and usually of small magnitude [14].

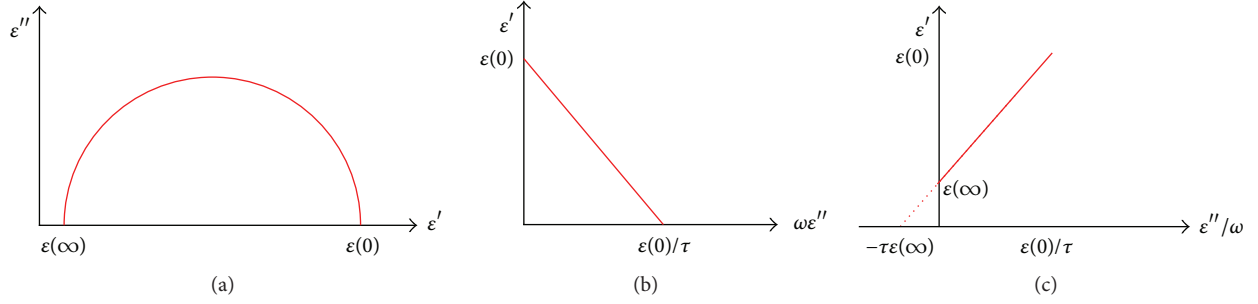
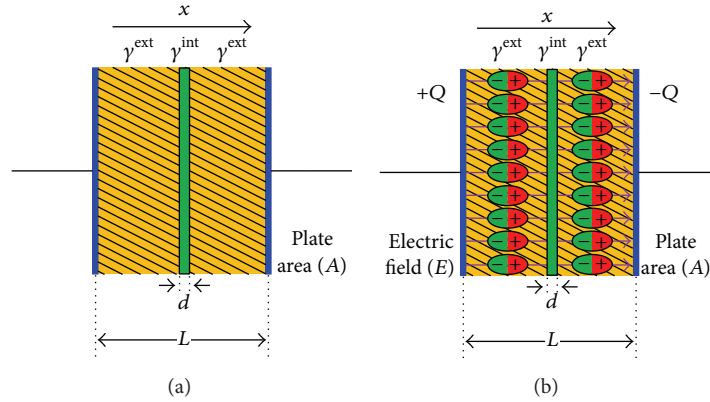
Figure 6(a) shows Cole-Cole plot explaining $(\epsilon' + (\epsilon_{xx}^{\text{ef}}(\infty) + \epsilon_{xx}^{\text{ef}}(0))/2)^2 + (\epsilon'')^2 = ((\epsilon_{xx}^{\text{ef}}(0) - \epsilon_{xx}^{\text{ef}}(\infty))/2)^2$. Figure 6(b) shows ϵ' versus $\omega\epsilon''$ line describing $\epsilon' = \epsilon_{xx}^{\text{ef}}(0) - \tau(\omega\epsilon'')$. Figure 6(c) shows ϵ' versus ϵ''/ω line.

Remark 4. In the case when c is sufficiently small (dilute suspension) so that $|1 - \gamma^{\text{ext}}/\gamma^{\text{int}}|c \ll 1$, (21) can be expressed as

$$\gamma_{xx}^{\text{ef}}(\omega) = \gamma^{\text{ext}}(\omega) \left(1 + \left(1 - \frac{\gamma^{\text{ext}}(\omega)}{\gamma^{\text{int}}(\omega)} \right) c + O(c^2) \right) \quad (30)$$

because $\gamma^{\text{ef}}(\omega) = \gamma^{\text{ext}}(\omega)/(1 - (1 - \gamma^{\text{ext}}(\omega)/\gamma^{\text{int}}(\omega))c)$. Neglecting $O(c^2)$ in (30), we get

$$\gamma^{\text{ef}}(\omega) \approx (\gamma^{\text{int}}(\omega) - (\gamma^{\text{ext}}(\omega) - \gamma^{\text{int}}(\omega))c) \frac{\gamma^{\text{ext}}(\omega)}{\gamma^{\text{int}}(\omega)}$$


 FIGURE 6: Dielectric dispersion curves: (a) Cole-Cole plot, (b) ϵ' versus $\omega\epsilon''$ line, and (c) ϵ' versus ϵ''/ω line.

 FIGURE 7: Dielectric phenomena inside a capacitor or a dilute suspension of a thin membrane, (a) capacitor with a thin membrane of thickness d , (b) dielectric polarization under an electric field E .

$$\begin{aligned}
 &= \left(\sigma^{\text{int}} + c \left(\sigma^{\text{int}} - \sigma^{\text{ext}} \right) + i\omega \left[\epsilon^{\text{int}} + c \left(\epsilon^{\text{int}} - \epsilon^{\text{ext}} \right) \right] \right) \\
 &\times \frac{\sigma^{\text{ext}} + i\omega\epsilon^{\text{ext}}}{\sigma^{\text{int}} + i\omega\epsilon^{\text{int}}}.
 \end{aligned} \tag{31}$$

In three dimensional heterogeneous medium, this type of dilute suspension model with neglecting $O(c^2)$ had been used in computation of the effective admittivity γ^{ef} .

Next, we will investigate the effective admittivity for dilute suspensions of membrane of materials. We will express potential of models comprising suspension of arbitrary-shaped membrane, using double layer potential technique.

2.3. Dilute Single Suspension of Ellipses in a Cube. Maxwell [9] and Wagner [38] analyzed expressions for the effective admittivity γ^{ef} of a strongly diluted suspension of spheres [7].

Let $\Omega = \{\mathbf{r} : -1 < x, y, z < 1\}$ be a cube, and let $D = \{\mathbf{r} \in \Omega : x^2/a_1^2 + y^2/a_2^2 + z^2/a_3^2 < 1\}$ be an ellipsoid with $0 < a_1 \leq a_2 \leq a_3 \ll 1$. As in the previous section, let the admittivity distribution γ (Figure 7) be given by

$$\gamma(\mathbf{r}) = \begin{cases} \gamma^{\text{int}} = \sigma^{\text{int}} + i\omega\epsilon^{\text{int}} & \text{for } \mathbf{r} \in D \\ \gamma^{\text{ext}} = \sigma^{\text{ext}} + i\omega\epsilon^{\text{ext}} & \text{for } \mathbf{r} \in \Omega \setminus D. \end{cases} \tag{32}$$

If $u \in H^1(\Omega)$ is a potential satisfying $\nabla \cdot (\gamma(\mathbf{r}, \omega)\nabla u(\mathbf{r}, \omega)) = 0$ in Ω , then it can be expressed as a sum of harmonic function $H(\mathbf{r}, \omega)$ in Ω and a single layer potential:

$$u(\mathbf{r}, \omega) = H(\mathbf{r}, \omega) + \int_{\partial D} \frac{1}{4\pi|\mathbf{r} - \mathbf{r}'|} \phi(\mathbf{r}', \omega) ds_{\mathbf{r}'} \tag{33}$$

for $\mathbf{r} \in \Omega$,

where ϕ is determined by

$$\left(\frac{\gamma^{\text{ext}} + \gamma^{\text{int}}}{2(\gamma^{\text{ext}} - \gamma^{\text{int}})} I - \mathcal{K}_D^* \right) \phi(\mathbf{r}, \omega) = \mathbf{n}(\mathbf{r}) \cdot \nabla H(\mathbf{r}, \omega) \tag{34}$$

for $\mathbf{r} \in \partial D$,

$$\mathcal{K}_D^* \phi(\mathbf{r}, \omega) = \int_{\partial D} \frac{\langle \mathbf{r} - \mathbf{r}', \mathbf{n}(\mathbf{r}) \rangle}{4\pi|\mathbf{r} - \mathbf{r}'|^3} \phi(\mathbf{r}', \omega) ds_{\mathbf{r}'}$$

for $\mathbf{r} \in \partial D$.

Assuming that the volume fraction $c = |D|/|\Omega|$ is small, Fricke obtained the following approximation:

$$\gamma_{xx}^{\text{ef}} \approx \gamma^{\text{ext}} I + c \left(\gamma^{\text{int}} - \gamma^{\text{ext}} \right) \begin{pmatrix} \beta_1 & 0 & 0 \\ 0 & \beta_2 & 0 \\ 0 & 0 & \beta_3 \end{pmatrix}, \tag{35}$$

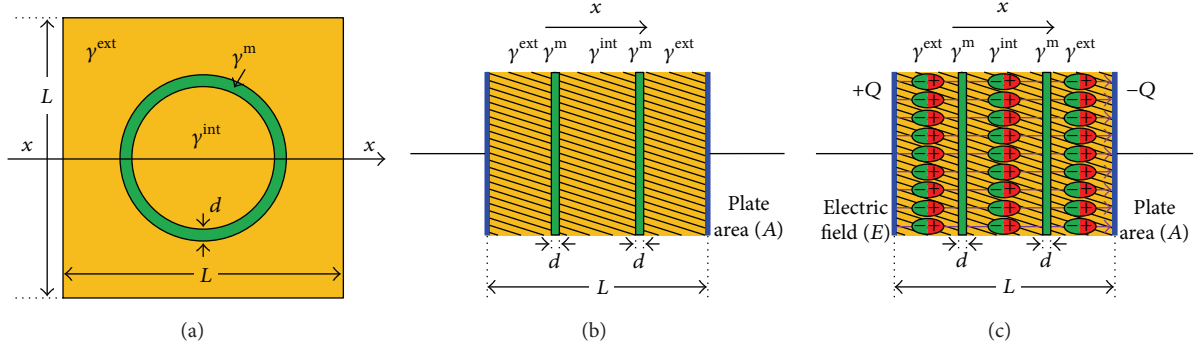


FIGURE 8: Dielectric phenomena inside a dilute single suspension of a thin membrane from Fricke's model (a) Fricke's model of a dilute single suspension of a thin membrane of thickness d , (b) 1D representation of the a dilute single suspension of a thin membrane from Fricke's model of a dilute single suspension of a thin membrane of thickness d , (c) dielectric polarization under an electric field E within a dilute single suspension of a thin membrane of thickness d in 1D.

where

$$\begin{aligned}\beta_j &= \frac{1 + \xi_j}{\xi_j + \gamma^{\text{int}}/\gamma^{\text{ext}}}, \\ \xi_j &= \frac{2 - a_1 a_2 a_3 L_j}{a_1 a_2 a_3 L_j}, \\ L_j &= \int_0^\infty \frac{d\lambda}{(a_j^2 + \lambda) \sqrt{(a_1^2 + \lambda)(a_2^2 + \lambda)(a_3^2 + \lambda)}} \\ &\quad (j = 1, 2, 3).\end{aligned}\quad (36)$$

When $\alpha_x = \alpha_y = \alpha_z$ (D is sphere) and the volume fraction $c = |D|/|\Omega|$ is small, Maxwell-Wagner [26] formula for $\gamma^{\text{ef}}(\omega)$ is given by

$$\begin{aligned}\gamma^{\text{ef}}(\omega) &= (\sigma^{\text{ext}} + i\omega\epsilon^{\text{ext}}) \\ &\times \left(1 + 3c \frac{(\sigma^{\text{int}} - \sigma^{\text{ext}}) + i\omega(\epsilon^{\text{int}} - \epsilon^{\text{ext}})}{(\sigma^{\text{int}} + 2\sigma^{\text{ext}}) + i\omega(\epsilon^{\text{int}} + 2\epsilon^{\text{ext}})} \right) \\ &+ O(c^2).\end{aligned}\quad (37)$$

With the aid of $\tau = (\epsilon^{\text{int}} + 2\epsilon^{\text{ext}})/(\sigma^{\text{int}} + 2\sigma^{\text{ext}})$, we can derive the Debye dispersion function for $\gamma^{\text{ef}}(\omega)$ as follows:

$$\begin{aligned}\gamma^{\text{ef}}(\omega) &= \underbrace{\sigma^{\text{ef}}(\infty)}_{\sigma^{\text{ef}}(\omega)} + \frac{(\sigma^{\text{ef}}(0) - \sigma^{\text{ef}}(\infty))\omega^2\tau^2}{1 + \omega^2\tau^2} \\ &+ i\omega \underbrace{\left[\epsilon^{\text{ef}}(\infty) + \frac{\epsilon^{\text{ef}}(0) - \epsilon^{\text{ef}}(\infty)}{1 + \omega^2\tau^2} \right]}_{\epsilon^{\text{ef}}(\omega)}.\end{aligned}\quad (38)$$

Next, we will investigate the effective admittivity for dilute suspensions of membranes.

2.4. Dilute Single Suspension of Membrane. Finally, consider the case of a dilute single suspension of membranes (Figure 8)

to investigate the role of the thin insulating membrane influencing the frequency-dependent behavior of the effective admittivity. In the model comprising a suspended membrane, there exists a thin membrane \mathcal{M}_d of a thickness d , as shown in Figure 6, within our target voxel. Assume that the admittivity distribution γ changes abruptly across the membrane

$$\begin{aligned}\gamma(\mathbf{r}, \omega) := \sigma(\mathbf{r}) + i\omega\epsilon(\mathbf{r}) &= \begin{cases} \sigma^{\text{int}} + i\omega\epsilon^{\text{int}} & \text{in } \mathcal{M}_d \\ \sigma^{\text{ext}} + i\omega\epsilon^{\text{ext}} & \text{in } \Omega \setminus \overline{\mathcal{M}_d}, \end{cases} \\ d \approx 0, \quad \frac{\sigma^{\text{int}}}{\sigma^{\text{ext}}} &\approx 0.\end{aligned}\quad (39)$$

In the case of a dilute suspension of a single membrane, any potential u satisfying $\nabla \cdot (\gamma \nabla u) = 0$ can be expressed as

$$u(\mathbf{r}) \approx H(\mathbf{r}) + d \left(\frac{\sigma^{\text{ext}} + i\omega\epsilon^{\text{ext}}}{\sigma^{\text{int}} + i\omega\epsilon^{\text{int}}} \right) \mathcal{D}_{\mathcal{M}}\phi(\mathbf{r}), \quad (40)$$

where \mathcal{M} is the surface of the membrane and

$$\mathcal{D}_{\mathcal{M}}\phi(\mathbf{r}) = \int_{\mathcal{M}} \frac{\langle \mathbf{r} - \mathbf{r}', \mathbf{n}(\mathbf{r}') \rangle}{4\pi|\mathbf{r} - \mathbf{r}'|^3} \phi(\mathbf{r}') ds. \quad (41)$$

The density ϕ is determined by membrane structure and the refraction index:

$$\phi = \frac{\partial u^{\text{ext}}}{\partial \mathbf{n}} \quad \text{on } \mathcal{M}. \quad (42)$$

Here, we recall $\mathcal{D}_{\mathcal{M}}\phi|_{\mathcal{M}^\pm} = ((\pm 1/2)I + \mathcal{K})\phi$ on the surface \mathcal{M} .

In 1955, Fricke [39] studied the equivalent admittivity for the case of a spherical membrane suspension using its pointwise admittivity distribution (Figure 7):

$$\gamma(\mathbf{r}, \omega) = \begin{cases} \gamma^{\text{int}} & \text{if } |\mathbf{r}| < R - d \\ \gamma^m & \text{on } \mathcal{M}_d = \{\mathbf{r} : R - d < |\mathbf{r}| < R\} \\ \gamma^{\text{ext}} & \text{if } |\mathbf{r}| > R. \end{cases} \quad (43)$$

Fricke's expression for the equivalent admittivity for the internal domain including the membrane and γ is

$$\gamma(\mathbf{r}, \omega) \approx \begin{cases} \gamma_{\diamond}^{\text{int}} = \sigma_{\diamond}^{\text{int}} + i\omega\epsilon_{\diamond}^{\text{int}} \\ \quad = \frac{\gamma^{\text{int}} - (2d/R)(\gamma^{\text{int}} - \gamma^m)}{(1 + d/R)((\gamma^{\text{int}} - \gamma^m)/\gamma^m)} & \text{if } |\mathbf{r}| < R \\ \gamma^{\text{ext}} & \text{if } |\mathbf{r}| > R. \end{cases} \quad (44)$$

Then the effective admittivity γ^{ef} can be computed by substituting this equivalent admittivity in Maxwell-Wagner-Fricke formula [40]. Under the assumption that three quantities $\sigma^m/\sigma^{\text{ext}}$, $\sigma^m/\sigma^{\text{int}}$, and d/R are very small, Pauly and Schwan [14] obtained

$$\begin{aligned} \sigma^{\text{ef}}(\omega) &= \underbrace{\sigma^{\text{ext}} \left(1 - \frac{3c}{2}\right)}_{\sigma^{\text{ef}}(0)} + \underbrace{\frac{9c\epsilon^m R}{4\epsilon_0 d \tau}}_{\Delta\sigma^{\text{ef}}} \frac{\omega\tau^2}{1 + \omega^2\tau^2}, \\ \epsilon^{\text{ef}}(\omega) &= \epsilon^{\text{ef}}(\infty) + \frac{9c\epsilon^m R}{4\epsilon_0 d} \frac{1}{1 + \omega^2\tau^2}, \end{aligned} \quad (45)$$

where

$$\tau = \frac{\epsilon^m R}{d} \left(\frac{1}{2\sigma^{\text{ext}}} + \frac{1}{\sigma_{\diamond}^{\text{int}}} \right). \quad (46)$$

Biological tissues are comprised of cells and an extracellular matrix of macromolecules and extracellular fluid. Cells have different shapes and sizes in the order of μm . The cell has a membrane whose thickness is in the order of several nm. Enclosed within the cell membrane is the cytoplasm containing the nucleus, organelles, and intracellular fluid. Although they are very thin and resistive, cell membranes play an important role in determining admittivity values of tissues. They usually account for large susceptibility values, even though there is little quantitative analysis on how membrane properties affect them.

Membrane suspensions in homogeneous media can be viewed as an equivalent biological tissue admittivity. Analysis of the simple membrane structures should enable us to interpret admittivity images from phantom experiments and numerical simulations.

3. Discussion and Conclusions

Tomographic imaging of the admittivity distributions inside biological subjects such as the human body has been an active research goal in electrical impedance tomography (EIT). Can EIT technique distinguish between cucumber and carrot or lung and liver? Measuring the frequency-dependent behavior of effective admittivity increases distinguishability and has a potential of expanding clinical applications. The effective conductivity of biological tissue is associated with the forward problem of an elliptic PDE, the Laplace equation, with a complex material parameters and thin insulating membranes, and there is little understanding about this kind of forward

problem. Since traditional electrical impedance tomography can only provide change in effective admittivity on a coarse scale due to its low spatial resolution, we will have a better understanding of EIT images if we can link microscopic cell structures to macroscopic (or effective) tissue admittivity images obtained from multifrequency EIT systems.

We defined the effective admittivity of a cubic voxel from its pointwise admittivity and the Maxwell equations. Because of the reciprocity property, the effective admittivity must be symmetric. Direct computation of effective admittivity using simple models produced the Maxwell-Wagner interface effect and Debye relaxation. The complex permittivity, dielectric constant, and loss factors were derived and modeled as the functions of frequencies, and the dielectric polarization, dispersions, and the relaxation time were studied in a mathematical framework. The single and double layer potentials were used to present a mathematical expression for the Maxwell-Wagner-Fricke expression for the subject containing various geometries of cells or membranes while previous work of Maxwell and Wagner only handles ellipses in a cube.

Conflict of Interests

All the authors declare that they have no conflict of interests.

Acknowledgment

The National Research Foundation of Korea (NRF) Grant funded by the Korea Government (MEST) No. 2011-0028868 (2012R1A2A1A03670512).

References

- [1] L. A. Geddes and L. E. Baker, "The specific resistance of biological material—a compendium of data for the biomedical engineer and physiologist," *Medical and Biological Engineering*, vol. 5, no. 3, pp. 271–293, 1967.
- [2] S. Gabriel, R. W. Lau, and C. Gabriel, "The dielectric properties of biological tissues: II. Measurements in the frequency range 10 Hz to 20 GHz," *Physics in Medicine and Biology*, vol. 41, no. 11, pp. 2251–2269, 1996.
- [3] C. Gabriel, S. Gabriel, and E. Corthout, "The dielectric properties of biological tissues: I. Literature survey," *Physics in Medicine and Biology*, vol. 41, no. 11, pp. 2231–2249, 1996.
- [4] S. Gabriel, R. W. Lau, and C. Gabriel, "The dielectric properties of biological tissues: III. Parametric models for the dielectric spectrum of tissues," *Physics in Medicine and Biology*, vol. 41, no. 11, pp. 2271–2293, 1996.
- [5] S. Grimnes and G. Martinsen, *Bioimpedance and Bioelectricity Basics*, Academic Press, San Diego, Calif, USA, 2008.
- [6] A. Bensoussan, J. L. Lions, and G. Papanicolaou, *Asymptotic Analysis for Periodic Structures*, Elsevier, 1978.
- [7] H. Fricke, "A mathematical treatment of the electrical conductivity of colloids and cell suspensions," *Journal of General Physiology*, vol. 4, pp. 375–383, 1924.
- [8] O. G. Martinsen, S. Grimnes, and H. P. Schwan, "Interface phenomena and dielectric properties of biological tissue," *Encyclopedia of Surface and Colloid Science*, vol. 20, pp. 2643–2653, 2002.

- [9] J. C. Maxwell, *Electricity and Magnetism*, 1st edition, 1873.
- [10] S. D. Poisson, *Mémoires De L'Académie Royale Des Sciences De L'Institut De France*, vol. 5, p. 488, 1826.
- [11] S. S. Dukhin, "Dielectric properties of disperse systems," in *Surface and Colloid Science*, E. Matijevic, Ed., vol. 3, pp. 83–165, Wiley-Interscience, New York, NY, USA, 1971.
- [12] M. Pavlin, T. Slivnik, and D. Miklavčič, "Effective conductivity of cell suspensions," *IEEE Transactions on Biomedical Engineering*, vol. 49, no. 1, pp. 77–80, 2002.
- [13] M. Pavlin, N. Pavšelj, and D. Miklavčič, "Dependence of induced transmembrane potential on cell density, arrangement, and cell position inside a cell system," *IEEE Transactions on Biomedical Engineering*, vol. 49, no. 6, pp. 605–612, 2002.
- [14] H. Pauly and H. P. Schwan, "Über die impedanz einer suspension von kugelförmigen teilchen mit einer schale," *Zeitschrift für Naturforschung B*, vol. 14, pp. 125–131, 1959.
- [15] H. Ammari, H. Kang, and K. Touibi, "Boundary layer techniques for deriving the effective properties of composite materials," *Asymptotic Analysis*, vol. 41, no. 2, pp. 119–140, 2005.
- [16] H. Ammari and H. Kang, *Polarization and Moment Tensors: With Applications to Inverse Problems and Effective Medium Theory*, vol. 162, Springer, 2007.
- [17] H. Ammari, P. Garapon, H. Kang, and H. Lee, "Effective viscosity properties of dilute suspensions of arbitrarily shaped particles," *The Journal of Physical Chemistry*, vol. 80, pp. 189–211, 2012.
- [18] W. Graeme, *Milton the Theory of Composites*, Cambridge University Press.
- [19] M. Pavlin and D. Miklavčič, "Effective conductivity of a suspension of permeabilized cells: A theoretical analysis," *Biophysical Journal*, vol. 85, no. 2, pp. 719–729, 2003.
- [20] J. K. Seo and E. J. Woo, *Nonlinear Inverse Problems in Imaging*, John Wiley & Sons, 2012.
- [21] W. Kuang and S. O. Nelson, "Low-frequency dielectric properties of biological tissues: a review with some new insights," *Transactions of the American Society of Agricultural Engineers*, vol. 41, no. 1, pp. 173–184, 1998.
- [22] W. E. Vaughan, "Dielectric relaxation," *Annual Review of Physical Chemistry*, vol. 30, pp. 103–124, 1979.
- [23] H. P. Schwan, "Electrical properties of tissue and cell suspensions," in *Advances in Biological and Medical Physics*, J. H. Lawrence and C. A. Tobias, Eds., vol. V, pp. 147–209, Academic Press, New York, NY, USA, 1957.
- [24] H. P. Schwan, "Electrical properties of tissues and cell suspensions: mechanisms and models," in *Proceedings of the 16th Annual International Conference of the IEEE*, vol. 1, pp. A70–A71, 1994.
- [25] K. R. Foster and H. P. Schwan, "Dielectric properties of tissues and biological materials: a critical review," *Critical Reviews in Biomedical Engineering*, vol. 17, no. 1, pp. 25–104, 1989.
- [26] T. Hao, *Electrorheological Fluids: The Non-Aqueous Suspensions*, Elsevier, 2005.
- [27] K. S. Cole, *Membranes, Ions and Impulses*, University of California Press, Berkeley, Calif, USA.
- [28] H. P. Schwan, "Electrical properties of muscle tissue at low frequencies," *Zeitschrift für Naturforschung B*, vol. 9, p. 245, 1954.
- [29] G. Falkand and P. Fatt, "Linear electrical properties of striated muscle fibers observed with intracellular electrodes," *Proceedings of the Royal Society of London B*, vol. 160, pp. 69–123, 1964.
- [30] G. Schwarz, "A theory of the low-frequency dielectric dispersion of colloidal particles in electrolyte solution," *Journal of Physical Chemistry*, vol. 66, no. 12, pp. 2636–2642, 1962.
- [31] J. Thuery, *Microwaves: Industrial, Scientific and Medical Applications*, Artech House, Boston, Mass, USA, 1991.
- [32] S. O. Nelson, "Dielectric properties of agricultural products measurements and applications," *IEEE Transactions on Electrical Insulation*, vol. 26, no. 5, pp. 845–869, 1991.
- [33] A. C. Metaxas and R. J. Meredith, *Industrial Microwave Heating*, Peter Peregrinus, London, UK, 1983.
- [34] B. Rajewsky and H. P. Schwan, "The dielectric constant and conductivity of blood at ultrahigh frequencies," *Naturwissenschaften*, vol. 35, p. 315, 1948.
- [35] H. P. Schwan, "Mechanisms responsible for electrical properties of tissues and cell suspensions," *Medical Progress through Technology*, vol. 19, no. 4, pp. 163–165, 1993.
- [36] H. M. Fishman, D. J. M. Poussart, L. E. Moore, and E. Siebenga, "K⁺ conduction description from the low frequency impedance and admittance of squid axon," *Journal of Membrane Biology*, vol. 32, no. 3-4, pp. 255–290, 1977.
- [37] R. D. Stoy, K. R. Foster, and H. P. Schwan, "Dielectric properties of mammalian tissues from 0.1 to 100 MHz; a summary of recent data," *Physics in Medicine and Biology*, vol. 27, no. 4, pp. 501–513, 1982.
- [38] K. W. Wagner, "Erklärung der dielectrischen nachwirkungsworgänge auf grund maxwellscher vorstellungen," *Archiv für Elektrotechnik*, vol. 2, pp. 371–387, 1914.
- [39] H. Fricke, "The complex conductivity of a suspension of stratified particles of spherical or cylindrical form," *Journal of Physical Chemistry*, vol. 59, no. 2, pp. 168–170, 1955.
- [40] D. Gakkai, "Japan society for medical electronics and biological engineering," in *Proceedings of 5th International Conference on Electrical Bio-Impedance*, p. 261, Business Center for Academic Societies Japan, 1888.

Research Article

Model Independent MRE Data Analysis

Kogo Yoshikawa¹ and Gen Nakamura^{1,2}

¹ Hokkaido University, Sapporo 060-0810, Japan

² Inha University, Incheon 402-751, Republic of Korea

Correspondence should be addressed to Kogo Yoshikawa; y4kw@math.sci.hokudai.ac.jp

Received 27 November 2012; Accepted 16 January 2013

Academic Editor: Jin Keun Seo

Copyright © 2013 K. Yoshikawa and G. Nakamura. This is an open access article distributed under the Creative Commons Attribution License, which permits unrestricted use, distribution, and reproduction in any medium, provided the original work is properly cited.

For the diagnosing modality called MRE (magnetic resonance elastography), the displacement vector of a wave propagating in a human tissue can be measured. The average of the local wavelength from this measured data could be an index for the diagnosing, because the local wave length becomes larger when the tissue is stiffer. By assuming that the local form of the wave is given approximately as multiple complex plane waves, we identify the real part of the complex linear phase of the strongest plane wave of this multiple complex plane waves, by first applying the FBI transform (Fourier-Bros-Iagolnitzer transform) with an appropriate size of Gaussian window and then taking the maximum of the modulus of the transform with respect to the Fourier variable. The real part of the linear phase is nothing but the real inner product of the wave vector and the position vector. Similarly the imaginary part of the linear phase describes the attenuation of the wave and it is given as a real inner product of a real vector and the position vector. This vector can also be recovered by our method. We also apply these methods to design some denoising and filtering for noisy MRE data.

1. Introduction

A new measurement modality called MRE (magnetic resonance elastography) consists of an MRI (magnetic resonance imaging), mechanical vibration system, and an additional MRI pulse sequence called MSG (motion sensitizing gradient) synchronized with the time harmonic vibration generated by the vibration system. Given a time harmonic external vibration generated by the vibration system to a human body which yields a wave in the human body, MRE gives a snapshot of the displacement vectors of the wave over each slice of the human body. We call this snapshot MRE data. The slice can be the cross section of the body by any one of the x_1 - x_2 plane, x_2 - x_3 plane, and x_3 - x_1 plane, where (x_1, x_2, x_3) is the Euclidean coordinates. If we can recover the stiffness of the tissue in a human body from the MRE data, MRE can provide a realization of doctors' palpation inside human bodies which has been dreamed about by all the doctors for many years (cf. [1, 2]). We call any procedure to recover the stiffness or extract any information about the stiffness MRE data analysis.

There are two kinds of MRE data analysis. The one is the model-independent MRE data analysis which only assumes

that any local wave forms of the wave are given approximately as multiple complex plane waves and recover the real part of the complex linear phase of the strongest wave in this multiple complex plane waves which can be represented by the so-called wave vector. We call this wave vector divided by the angular frequency of vibration the *local wave vector* of the multiple complex plane waves. The other is the model-dependent MRE data analysis which considers some partial differential equation to describe the wave and stiffness as its solutions and coefficient, respectively, and recover the coefficient from the MRE data via this equation. We will call such a partial differential equation the PDE model. In this paper we will give a model-independent MRE data analysis based on the FBI transformation (Fourier-Bros-Iagolnitzer transform). For the model-dependent MRE data analysis see, for instance, [2–6] and the references therein.

It is well known that the wave length becomes larger if the tissue becomes stiffer. In terms of the wave vector this means that the wave vector becomes shorter if the tissue become stiffer. Hence, by looking at the wave vectors in the tissues, we can qualitatively know a change of their stiffness. Since the modeling error is always a big problem in the MRE data

analysis, the model-independent analysis has some advantage if it is not so important to recover the stiffness quantitatively but qualitatively.

In the rest of this section we will explain more precisely about our model-independent MRE data analysis. Since the wave length of the longitudinal wave in human tissue is too long to be observed, we can only observe shear waves when the tissues is isotropic tissues and quasi-shear waves if the tissues is anisotropic. Suppose that a shear wave or quasi-shear wave is mainly propagating toward the x_2 direction and we are looking this wave over a slice parallel to the x_1 - x_2 plane which is the cross section of a human body. Then, let $\varphi = \varphi(x_1, x_2)$ be the one of the component of displacement vector of this wave perpendicular to x_2 direction, say x_3 component. We also take such a wave whose phase of the vibration is 90 degrees advanced and denotes its component similar as before by $\psi = \psi(x_1, x_2)$. For our data analysis, it is more convenient to consider

$$u = u(x) = \varphi(x) - i\psi(x) \quad (1)$$

than considering φ and ψ separately.

A naive way of looking at u near a point p in the cross section is that it is locally given by a finite linear combination of the complex plane wave $ae^{\omega(\alpha+i\beta)\cdot(x-p)}$ with an amplitude $a \in \mathbb{C}$, vectors $\alpha, \beta \in \mathbb{R}^2$ which do not depend on $x = (x_1, x_2)$, and the angular frequency $\omega/(2\pi)$ of the vibration system. Note that α and β describe the attenuation and propagation direction of the wave u , respectively. We call this form of u the *local single-wave form* if the linear combination consists of just one term and *local multiple-wave form* if otherwise.

Let u be described approximately as the local multiple-wave form near a point p in a region of interest (ROI) of a human tissue. Then, by our method called LWV method (local wave vector method) and LAV method (local attenuation vector method) which are based on the FBI transformation, we can recover β and α in the strongest local single-wave form of the local multiple-wave form. We will call these β and α in this strongest local single-wave form the *local wave vector* and *local attenuation vector*, respectively. Here the FBI transformation is a weighted Fourier transformation with the Gaussian window centered around p . Once we have recovered β at several points in the ROI, we can filter the wave fields with many waves interfering with each other in the ROI to a single major wave. If the ROI is located near the boundary of tissue, for instance the boundary between a tissue and organ, there is an interference of incoming waves and reflected waves from the boundary. In such a place of ROI the wave length and amplitude of wave could become smaller than the other parts of the ROI and hence the profiles of the distribution of the local wave vectors there will become quite complicated. But by our filtering method based on the LWV method, we can extrapolate the major wave up to the boundary in this ROI. As a consequence, we can get very clear filtered wave image having just a major wave in this ROI. We call this denoising method the LWV *denoising* of wave.

To transform the recovered local wave vector β and local attenuation vector α (Figure 16) to the stiffness of

tissue, we need to have a PDE model. Suppose that our tissue can be considered as nearly incompressible isotropic viscoelastic medium, then the above u can be considered approximately as the x_3 component of $\text{rot } v$, where v denotes the displacement vector of the wave and $\text{rot } v$ denotes the rotation of v . Then, each local single-wave form u' of the local multiple-wave form u should satisfy

$$(\rho\omega^2 + (G' + iG'')\Delta)u'(x) = 0 \quad (2)$$

approximately in a small neighborhood of p with the density $\rho \approx 10^3 \text{ kg/m}^3$, the storage modulus G' , and loss modulus G'' . We remark here that G', G'' can change from one region to another region where the local multiple-wave form of u changes. Further, we remark that u' always satisfies (2) approximately, if the tissue is modeled as whichever type of nearly incompressible isotropic viscoelastic media [3, 7]. Suppose that we have identified β and α in the strongest local single-wave form u' of u . Then, by substituting this local single-wave form into (2), we have

$$\rho + (G' + iG'')(\alpha + i\beta) \cdot (\alpha + i\beta) = 0 \quad (3)$$

which immediately implies that G', G'' are given by

$$\begin{pmatrix} G' \\ G'' \end{pmatrix} = \frac{\rho}{(|\alpha|^2 - |\beta|^2)^2 + 4(\alpha \cdot \beta)^2} \begin{pmatrix} |\beta|^2 - |\alpha|^2 \\ 2\alpha \cdot \beta \end{pmatrix}. \quad (4)$$

Hence (4) gives the link between α, β and G', G'' .

The rest of the paper is organized as follows. In Sections 2 and 3 we give the theories of the LWV method and LAV method, respectively. Then, in the succeeding section we will provide some numerical results for these two methods. Especially, in order to see the effectiveness of these method, we tested our methods by recovering G', G'' of a phantom made of PAAm gel by the MRE group in our university (Professor J. Gong, Laboratory of Soft and Wet Matter, Hokkaido University) and for a phantom made of agarose gel by Mayo Clinic so that we can compare our results with the other results obtained by different MRE data analysis. In the final section, we will apply our methods to the denoising and sharpening of the MRE data. Before closing this introduction, we would like to acknowledge Mayo Clinic providing us the data and emphasize that Mayo Clinic is the front runner of the MRE study.

2. LWV Method

In this section we will give the details of the LWV method mentioned in the introduction. Let $W(u; p, \sigma)(\xi)$ be the two dimensional FBI transform (cf. [8]) of a locally integrable function u in \mathbb{R}^2 with the Gaussian window of size σ localized around $p \in \mathbb{R}^2$ as follows:

$$W(u; p, \sigma)(\xi) = \int_{\mathbb{R}^2} e^{-ix \cdot \xi} u(x) e^{-|x-p|^2/2\sigma^2} dx \quad (\xi \in \mathbb{R}^2) \quad (5)$$

provided that this integral converges which is the case for the local multiple-wave form u . This transformation is also called

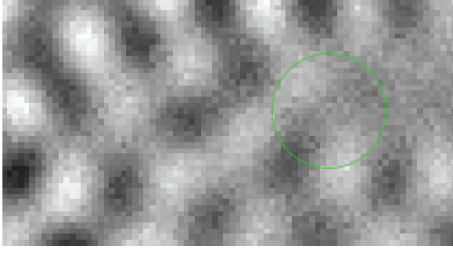
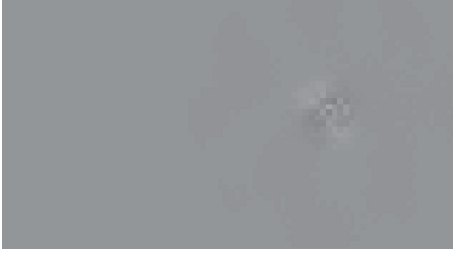

 FIGURE 1: Example of function $\text{Re } u(x)$ of (8).


FIGURE 2: Localization of Figure 1 by Gaussian.

the two dimensional continuous wavelet transform (cf. [9]). If we take $u(x)$ as a local single-wave form $u(x) = ae^{\omega(\alpha+i\beta)\cdot(x-p)}$, then $W(u; p, \sigma)(\xi)$ is expressed as

$$W(u; p, \sigma)(\xi) = 2\pi\alpha\sigma^2 \exp\left[i\omega^2\sigma^2\alpha \cdot \beta + \frac{\omega^2\sigma^2|\alpha|^2}{2}\right] \times \exp\left[-i(p + \omega\sigma^2\alpha) \cdot \xi - \frac{\sigma^2|\xi - \omega\beta|^2}{2}\right]. \quad (6)$$

Here we note that $\omega\beta$ is a unique Gaussian peak of $W(u; p, \sigma)$. The details of this derivation is given in the Appendix. The maximum $\arg \max_{\xi} |W(u; p, \sigma)(\xi)|$ of the modulus $|W(u; p, \sigma)(\xi)|$ for $\xi \in \mathbb{R}^2$ is clearly achieved at $\xi(p) = \xi = \omega\beta$. Hence, we have

$$\beta = \arg \max_{\xi} \frac{|W(u; p, \sigma)(\xi)|}{\omega}. \quad (7)$$

Here we note that σ^2 sitting in the denominator of the exponential of the Gaussian window will sit in the numerator of $W(u; p, \sigma)(\xi)$. This is nothing but the Heisenberg uncertainty principle about the window sizes in the *real space* x and *Fourier space* ξ . We have an option to tune a parameter σ that influences the localization in the real space and Fourier space.

If $u(x)$ is given as the multiple-wave form

$$u(x) = \sum_n c_n e^{\omega(\alpha_n+i\beta_n)\cdot(x-p)}, \quad c_n \in \mathbb{C}, \quad (8)$$

around p , $\arg \max_{\xi} |W(u; p, \sigma)(\xi)|$ can expect to give the local wave vector β_n of the strongest single-wave form $c_n e^{\omega(\alpha_n+i\beta_n)\cdot(x-p)}$ in its modulus. This can be understood by accepting a very reasonable interpretation which says that the

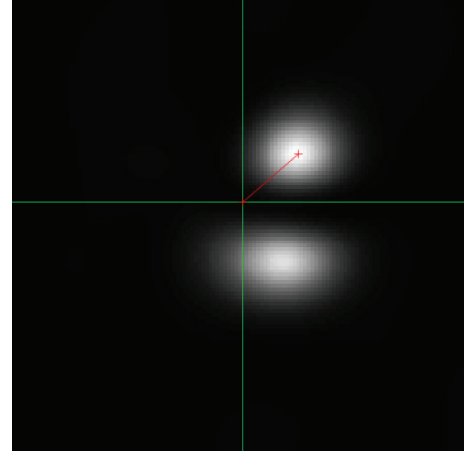
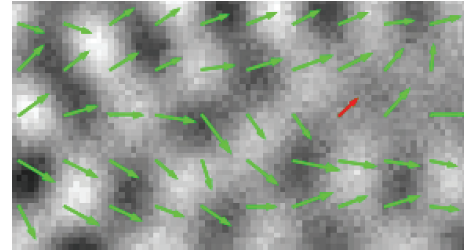

 FIGURE 3: Example of $|W(u; p, \sigma)(\xi)|$ in (7).


FIGURE 4: The vectors represent the wave vectors of the strongest waves. The red vector corresponds to that of Figure 3.

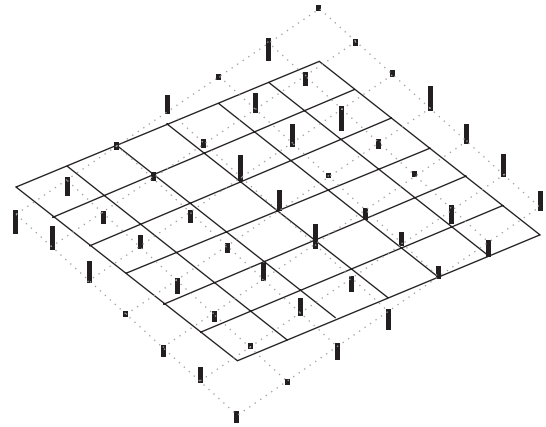


FIGURE 5: Least square method for 2-dimensional plane.

Gaussian peaks of the FBI-transformed u are well separated in most cases. We call this method to obtain the local wave vector β_n obtained above the local wave vector the LWV method.

We will show in several figures how the LWV method is performed. Figures 1 and 2 show the localization by a Gaussian window. Since the key to the LWV method is the assumption that the local approximate expression of the wave u is given by (8), we need to localize u to find the local wave vector of u .

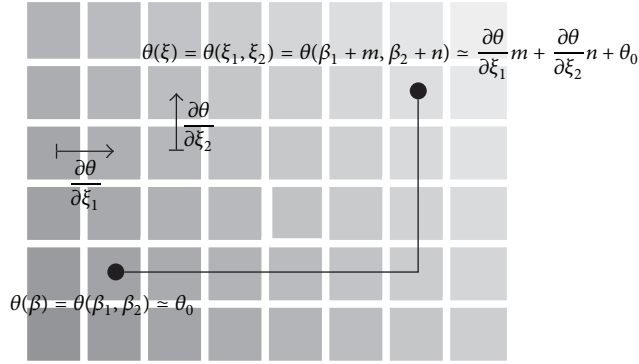
FIGURE 6: θ with respect to ξ .

Figure 3 is what can be seen in the Fourier space ξ . More precisely this is the FBI-transformed image of Figure 2.

In this figure, we find two Gaussian peaks in Figure 3 which means that there are basically two different directions to which the waves are propagating in Figure 2. This reasonably fits to Figure 1. It seems that in the Fourier space, the position of the peak of Gaussian is not strongly interfered by those of other peaks of Gaussian. Hence, the separation of interfered waves in the Fourier space should be quite good.

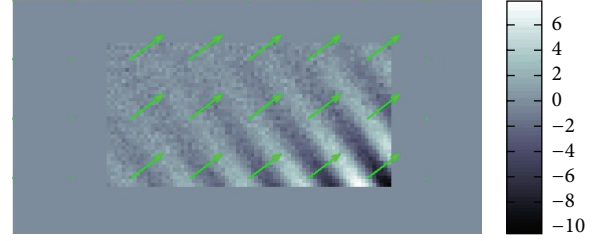
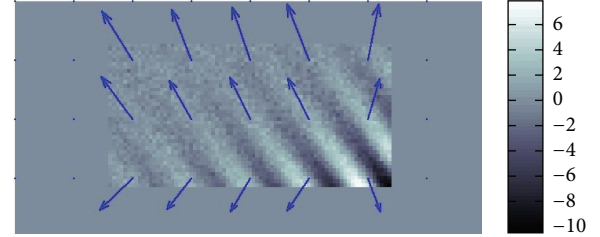
We repeated this process around enough sampled points and plotted the local wave vectors at the sampled points to obtain Figure 4 in which the sampled local wave vectors are superimposed over the figure of the real part of u .

Let us finish this section by giving several comments on the method. First of all, concerning the choice of the Gaussian window size σ , we usually take σ in the range from half wave length to one wave length for having reasonable recovery of β by our experiences. Taking $\arg \max$ may misfit β when there exists a strong noise with a specific frequency. But, for MRE data, it usually has only Gaussian-type white noise that does not have a specific frequency. Finally, we would like to emphasize here an advantage of the LWV method. That is, even in the case that several waves coming from different directions merge at a point $p \in \mathbb{R}^2$, the effect of each wave is quite localized in the Fourier space, so that if there are several different waves merging at p , we can separate these major propagating directions by the LWV method.

3. LAV Method

We will show in this section how to recover the local attenuation vector of the strongest wave in the local multiple-wave form (8). To begin with we first assume that $u(x)$ is given as a local single-wave form around a point $p \in \mathbb{R}^2$. Then the vector α at p in the local single-wave form with the wave vector β can be recovered by

$$\alpha = -\frac{1}{\omega\sigma^2} (\nabla_{\xi}\theta(p; \xi) - p), \quad (9)$$

FIGURE 7: Recovered β .FIGURE 8: Recovered α .

where $\theta(p; \xi)$ is defined by

$$\theta(p; \xi) := \arctan \left(\frac{\operatorname{Im} W(u; p, \sigma)(\xi)}{\operatorname{Re} W(u; p, \sigma)(\xi)} \right). \quad (10)$$

In fact, substituting (6) into the right hand side of (9), introducing θ_0 as an initial phase that does not depend of ξ , the right hand side of (10) becomes

$$\begin{aligned} \text{(RHS)} &= \arctan \left(\frac{\sin(-\omega\sigma^2\alpha \cdot \xi + \theta_0)}{\cos(-\omega\sigma^2\alpha \cdot \xi + \theta_0)} \right) \\ &= \arctan \left(\tan(-\omega\sigma^2\alpha \cdot \xi + \theta_0) \right) \\ &= -\omega\sigma^2\alpha \cdot \xi + \theta_0. \end{aligned} \quad (11)$$

Then, we will obtain (9) by taking the gradient of $\theta(p; \xi)$ with respect to ξ at $\xi = \omega\beta$ (Figure 6). In order to compute the gradient numerically we used the following least square method. Let $\xi = (\xi_1, \xi_2)$, $\beta = (\beta_1, \beta_2)$ and denote $m = \xi_1 - \beta_1$, $n = \xi_2 - \beta_2$. Then, the least square minimization to compute the gradient $(\nabla_{\xi}\theta)(p; \beta)$ is

$$\arg \min_{\alpha_1, \alpha_2} \sum_{m, n} w(m, n) (\theta(p; \xi) - \theta(p; \beta) - \alpha_1 m - \alpha_2 n)^2, \quad (12)$$

where $w(m, n) = e^{-(m^2+n^2)/2s^2}$ with some constant $s > 0$.

Figure 5 illustrates the 3-dimensional view of this minimization.

Even for u having the local multiple-wave form, we apply the same formula (9) to compute the attenuation vector α associated with the local wave vector β by expecting that we have already picked up the strongest local single-wave form with the local wave vector β in the local multiple wave form and the contribution coming from the other local single-wave forms is small. This is the precise description of the LAV method.

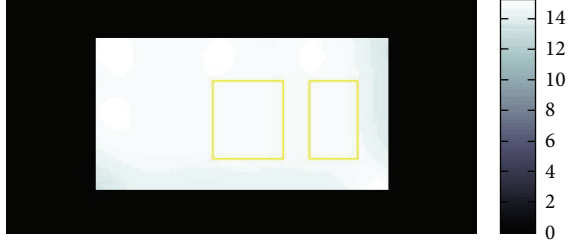

 FIGURE 9: Distribution of G' for simulated noisy data.

 TABLE 1: Estimation of G' .

Estimation of G'	Center	Right part
Average	14.89 kP	14.82 kP
Standard deviation	0.07 kP	0.11 kP

In the rest of this section, we give a reminder for programming the LAV method. That is to handle the discontinuities of (10) at $\theta = \pm\pi/2$. Instead of using the formula

$$\theta(p; \xi) - \theta(p; \xi_0) = \arctan\left(\frac{\text{Im } W(u; p, \sigma)(\xi)}{\text{Re } W(u; p, \sigma)(\xi)}\right) - \arctan\left(\frac{\text{Im } W(u; p, \sigma)(\xi_0)}{\text{Re } W(u; p, \sigma)(\xi_0)}\right), \quad (13)$$

we used as its reasonable approximation the following formula:

$$\theta(p; \xi) - \theta(p; \xi_0) = \text{Im}\left(\frac{W(u; p, \sigma)(\xi)}{W(u; p, \sigma)(\xi_0)}\right). \quad (14)$$

4. Numerical Testing of LWV and LAV Methods

In this section which consists of three subsections we will show some results on the numerical testing of our LWV and LAV methods. As we have mentioned before in Section 1, the methods are model-independent methods, but we will also show the numerical recoveries of G' , G'' in order to see the quantitative performance of our methods. The first subsection is for the numerical testing of our methods for simulated data and the succeeding two subsections are that for the real data obtained for phantoms by Mayo Clinic and MRE study group in our university, respectively. We call these real data the *phantom data* for simplicity. We did not test our methods for any clinical data, but the phantoms have some values close to the tissues of human livers.

4.1. Simulated Data. For simulated data in an unbounded domain without any boundary and noise, the results of the numerical testing of our methods are perfectly fine. Hence, we will directly go to the numerical testing for simulated data in a bounded domain with boundary and a noise. We added a considerably large Gaussian-type noise to a simulated

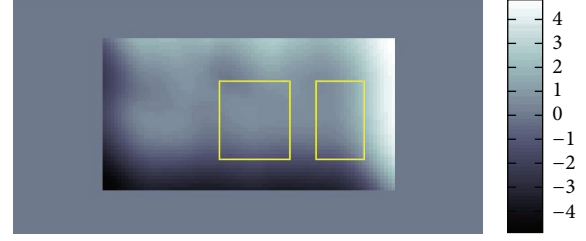

 FIGURE 10: Distribution of G'' for simulated noisy data.

 TABLE 2: Estimation of G'' .

Estimation of G''	Center	Right part
Average	0.17 kP	0.70 kP
Standard deviation	0.59 kP	0.79 kP

datum in order to see whether our methods work for the data with poor S/N ratio less than 0.1 which could be the case for real data. For the simulated datum, we made the length of α ten times longer than that of β which is the case for the phantoms data. Hence, the attenuation of wave is small. In other word, the amplitude of wave gradually decreases as the wave propagates. The superimposed arrows in Figures 7 and 8 show the recoveries of β and α . Hence, the variance of α in Figures 7 and 8 is smaller than it looks in Figure 8.

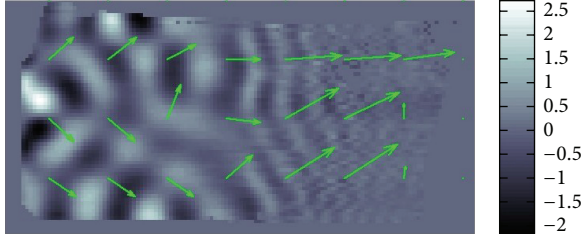
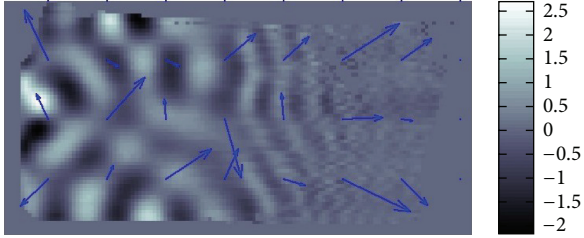
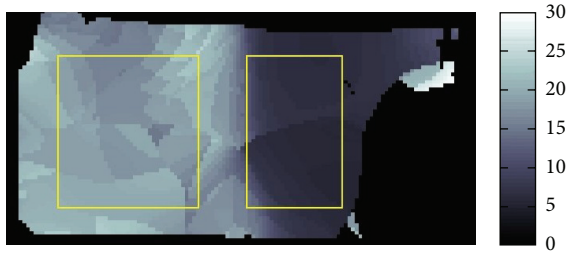
If there were no noise, then the recovered α and β should have been just constant vectors with the right upper direction and left upper direction for β and α , respectively. The recovery of β is quite good almost everywhere while that of α is less tolerant to noise and position.

Next we computed G' by using the formula (4). Figure 9 shows the distribution of the value G' , and Table 1 shows the average and standard deviation of the distributed values of G' . We note that the true value of G' was 14.4 kP. Hence, we can conclude from these that the recovery of β is quite good. We also observed by doing more numerical testing for simulated data that the estimate of G' is always stable even under poor S/N ratio like this simulated data. Further we give two remarks. Firstly, for example, around the part of upper left corner of Figure 7, the signal is much less than background noise and hence we are nearly unable to see the pattern of waves there. Secondly, if α is much smaller than β , the simple approximate formula (cf. [10])

$$G' = \frac{\rho}{|\beta|^2} \quad (15)$$

of G' works well.

We also computed G'' by using the formula (4). Figure 10 and Table 2 show the distribution of the value G'' and the average value, standard deviation of the distributed values of G'' . These results show that the recovery of G'' is not good in center, because expected value of G'' is 0.69 kP. This insufficient recovery of α can be explained as follows. As we have seen before that the recovered β is almost a constant vector, but the recovered α fluctuates near the lower boundary

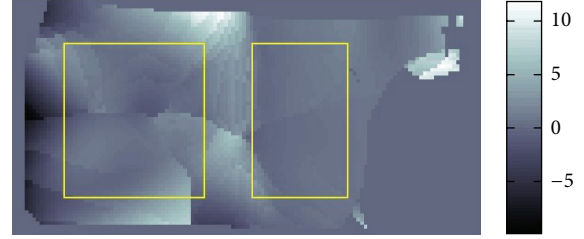
FIGURE 11: Fitting of β .FIGURE 12: Fitting of α .FIGURE 13: Distribution of G' for two-layer phantom.TABLE 3: Estimation of G' .

Estimation of G'	Center	Right part
Average	18.56 kPa	7.00 kPa
Standard deviation	1.47 kPa	1.83 kPa

almost completely changing its direction. Then, recalling the formula (4), the recovered G'' is influenced by this fluctuation of α which can have negative sign. As far as we know, any MRE data analysis has a difficulty recovering α in an efficient way and we do have the same difficulty.

4.2. Phantom Data from Micro-MRE System. Now, we will show the testing of our method to a phantom datum obtained from MRE study group in Hokkaido University. The MRE system in Hokkaido University consists of micro MRI with a 0.3 tesla permanent magnetic, function generator and vibrating system. We call this MRE system the *micro-MRE system*.

The resolution of the micro MRI is 1.2 mm square per pixel. The data obtained by this micro-MRE system for a phantom is given as the backgrounds of Figures 11 and 12 which are the same data for $\text{Re } u$. The phantom is a two-layered PAAm gel and it has the cross section given as the

FIGURE 14: Distribution of G'' for two-layer phantom.TABLE 4: Estimation of G'' .

Estimation of G''	Center	Right part
Average	0.68 kPa	0.60 kPa
Standard deviation	1.05 kPa	0.51 kPa

rectangular region given in Figures 11 and 12 about 6 cm times 12 cm which is the plane containing the vibrating source. In this cross section, the location of the vibrating source is at the middle of the left edge and interface of the two layers appears in the middle. The left part of the cross section is stiffer than the right part. Also, the wave is generated from this source by the vibration system with the 250 Hz angular frequency and it travels to the right direction. The wave field looks much complicated than what we have seen before for the simulated simple sinusoidal wave and we can observe reflection and refraction of waves at the boundaries and interface, respectively.

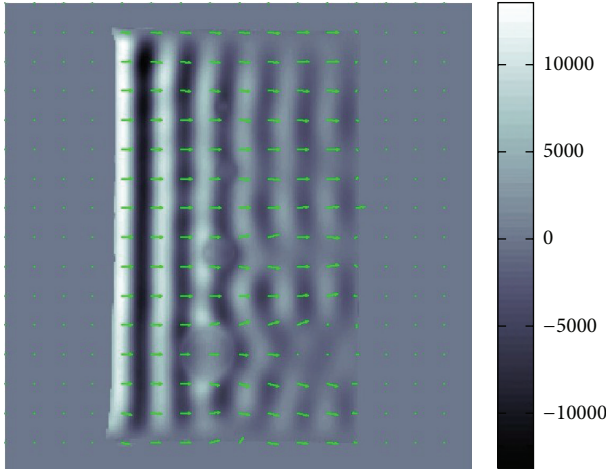
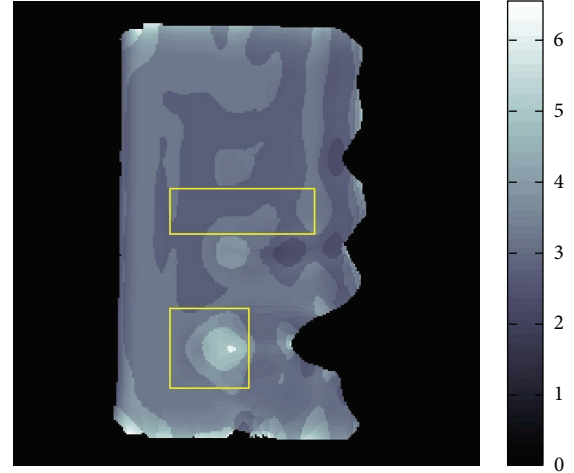
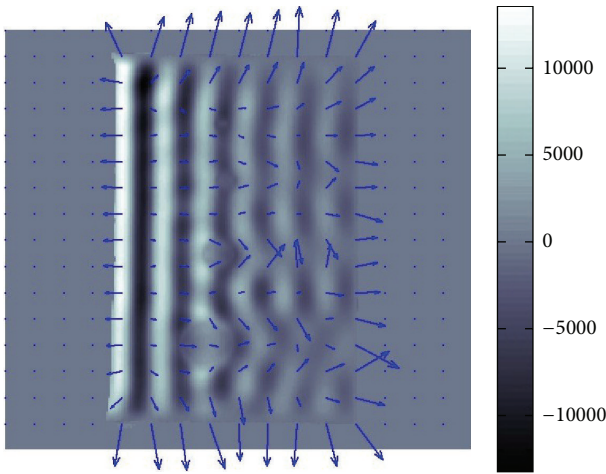
We applied our method to recover β and α . The recovered β and α are shown in Figures 11 and 12. The result for β given in Figure 11 matches quite well the profile of the wave field. From Figure 12, we can see that the direction of α is not the same as direction of β . By plotting the modulus of $u(x)$, that is, $|u(x)|$, we can observe that major waves, reflected waves, and transmitted waves are mixed together to yield standing waves which have small amplitude at some place and big amplitude antinode at other places creating some nodes. We can observe that α inclines to the nearest node.

By the formula (4), we can transform the recovered β , α into G' , G'' . The recovered G' is given in Figure 13 and Table 3.

The G' values of the two-layered phantom were also measured by a conventional rheometer giving the values 31.1 kPa and 10.7 kPa for the stiffer and softer parts of this phantom. The frequency of twisting the phantom was 10 Hz for this measurement. Since it is known that G' depends on the frequency (cf. [11]), we cannot directly compare our result with these G' values. The gray scale values in Figure 13 clearly show the location of the interface. Hence, we can say that our method can show the contrast of the stiffness. This is quite important in clinical application of MRE.

Figure 14 and Table 4 show the recovered G'' .

Although we could recover G'' to have a positive average value, comparing it with its standard deviation, the average value is smaller than its standard deviation. Looking more closer into the distribution of the recovered G'' (Figure 17), the average value in the center part is a small positive value, but there are some negative value in that part. Further the


 FIGURE 15: Fitting of β .

 FIGURE 17: Distribution of G' for Mayo Clinic data.

 FIGURE 16: Fitting of α .

average value in the right part is uniformly positive which means that this value is reliable. As far as we know, our result is quite good compared with the other recovered values of G'' by the direct method (cf. [12]) and modified integral method (cf. [3]). Nevertheless, we have to say that estimating the value of G'' is not easy because it is a small value compared with the value of G' .

4.3. Data of Mayo Clinic. We used the data by courtesy of Mayo Clinic. From the attached information, the view is 20 cm square composed of 256 pixels each size. On the left side of the gel phantom, external vibration is continuously applied with 100 Hz sinusoidal displacement. The sample has four cylindrical inclusions and their diameters are 5, 10, 16, and 25 mm. The inclusions are stiffer than container. The original data have eight snapshots in 360 degrees phase shift. We altered the data into one complex-valued datum $u(x)$ by using a weighted average for input of our method.

The original data is less noisy compared to our previous data. It is very near to the plain parallel wave except at the

 TABLE 5: Estimation of G' .

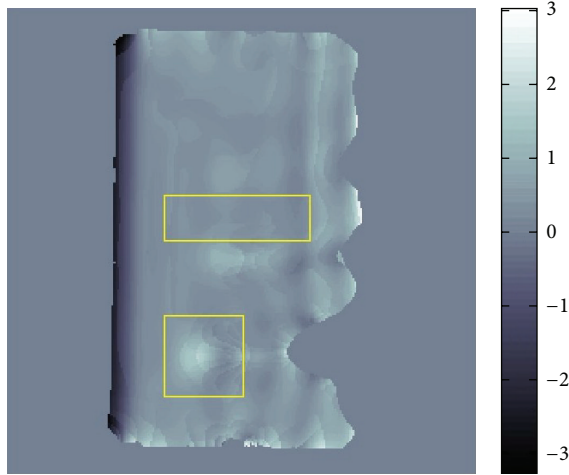
Estimation of G'	Bottom square	Center
Average	3.71 kPa	2.92 kPa
Standard deviation	0.62 kPa	0.24 kPa

parts of inclusions. The vectors β in Figure 15 are nearly constant throughout the image. They are perturbed slightly near at the inclusions and their backsides.

The vectors α change their directions more sensibly than those of vectors β . The lengths of the vectors α are represented ten times longer than those of the vectors β . Therefore, an average, the values of α are smaller than those of β .

Table 5 shows that G' in the bottom square is bigger than center. This gives the information that the inclusions are stiffer than the container. The value of standard deviation in bottom square is bigger than the another, because it nearly encloses the inclusion. On the result for the bottom square (Tables 3 and 6), we average G' at a biggest inclusion and its neighborhood. If we take the area to be smaller, the estimated value of G' goes higher. We compared our result with the result obtained by the modified integral method. The result by that method is believed to be stable and numerically reliable. It also supports our result of the average value because that output also has around 3.0 kPa in the region without inclusion part.

The recovered result of G' is not fully given. To be more specific, some part in the right hand side of the recovered result is intentionally cut off so that the result looks better. We have to explain why we did so. If β is zero or close to zero, we do not have any problem showing β as a vector. However in this case G' will become so large, because G' is proportional to $|\beta|^{-2}$ by (15). This happens in the shadowed parts of the inclusions. In fact it is very difficult to see the nodal points of wave in these parts which could be coming from unsuccessful unwrapping of the MRE data, that is to specify the nodal value of wave in the MRE data. If there are not any nodal points in these parts, then the wave length there becomes infinitely long and hence the modulus of β will be very close to zero.

FIGURE 18: Distribution of G'' for Mayo Clinic data.TABLE 6: Estimation of G'' .

Estimation of G''	Bottom square	Center
Average	0.58 kP	0.34 kP
Standard deviation	0.36 kP	0.08 kP

This means that we could not trust the MRE data in these parts and this is why we cut off such parts.

For the recovered values of G'' , the ratio of G'' to G' fits the ratio which is commonly believed; that is, G'' is about one-tenth order of G' .

5. Denoising and Sharpening

In this section, we will show that by a simple modification, the LWV method can be applied as a denoising for the MRE data. The principle behind this is as follows. For the local multiple-wave form u with n local single-wave forms, we have already observed that $W(u; p, \sigma)(\xi)$ in most cases would have n well-separated Gaussian peaks. This can be used to filter the MRE data which denoises and sharpens the data.

5.1. LWV Denoising of MRE Data. Figure 19 is the whole view of Figure 4 which will be denoised.

The profile of waves is not so clear due to the noise. Our purpose here is to filter the data to reduce the noise and interferences of waves in the data shown by Figure 19.

Figure 20 shows the distribution of the modulus of $W(u; p, \sigma)(\xi)$. From this we can know to which major directions the waves are propagating. Each Gaussian peak represents the major propagation direction for a certain group of waves. If these amplitudes of waves are large, then the peak becomes large also.

There are two ways to do the filtering. The one is to choose only the highest peak in the Fourier domain and remove the others. In detail, for each center point p of pixel, we replace $W(u; p, \sigma)(\xi)$ by

$$W(u; p, \sigma)(\xi) \delta(\xi - \xi(p)), \quad (16)$$

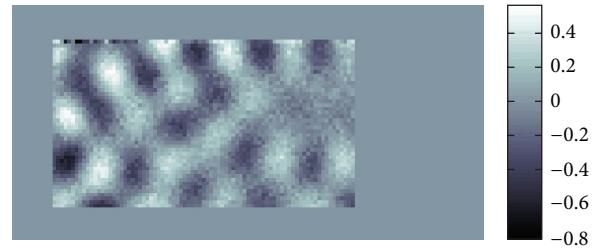


FIGURE 19: Real part in spatial domain.

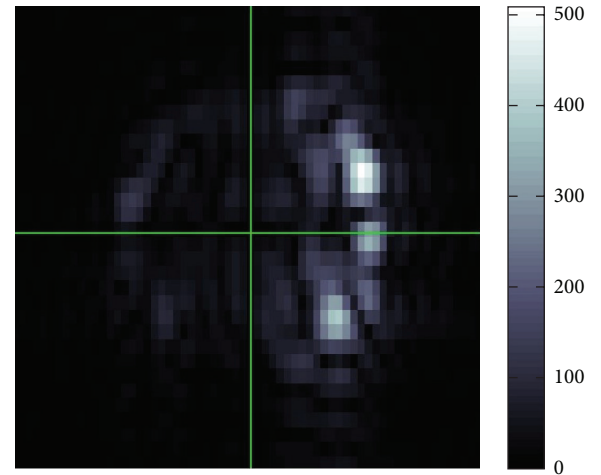


FIGURE 20: Modulus in Fourier domain.

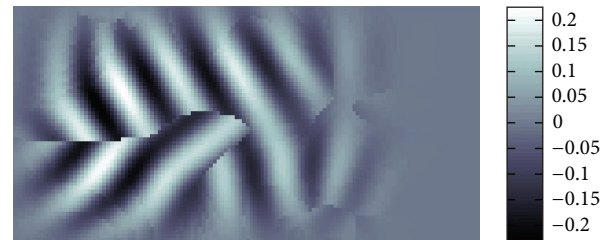


FIGURE 21: Real part in spatial domain.

where $\delta(\xi - \xi(p))$ is the delta function with a singularity at $\xi(p) = \arg \max_{\xi} |W(u; p, \sigma)(\xi)|$; that is, $\xi(p)$ gives the position of the peak of $|W(u; p, \sigma)(\xi)|$, and then takes the inverse Fourier transform of (16) which is multiplied by the characteristic function of the aforementioned pixel. This process is done for each pixel and we obtain filtered waves by superposition. As a result we have Figure 21. We can tune denoising effect by replacing $\delta(\xi - \xi(p))$ by a Gaussian window centered at $\xi(p)$.

Figure 22 gives the modulus of the Fourier transformation of Figure 21 and we can see that there are two peaks. Also, as can be seen in Figure 21, there will be a discontinuity where two waves correspond to these peaks. Comparing Figures 20 and 22, we know that Figure 22 has much more clear and sharp images of waves.

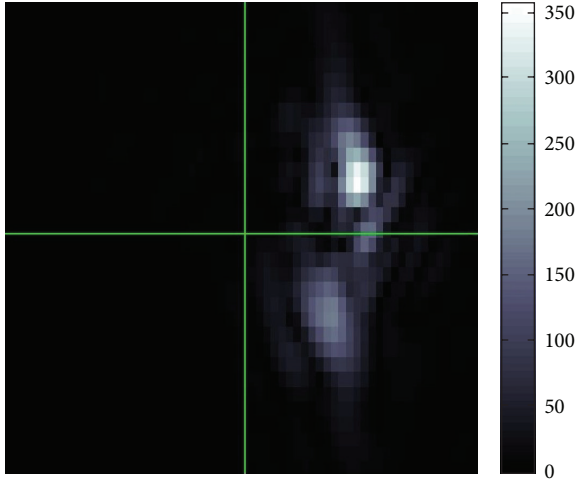


FIGURE 22: Modulus in Fourier domain.

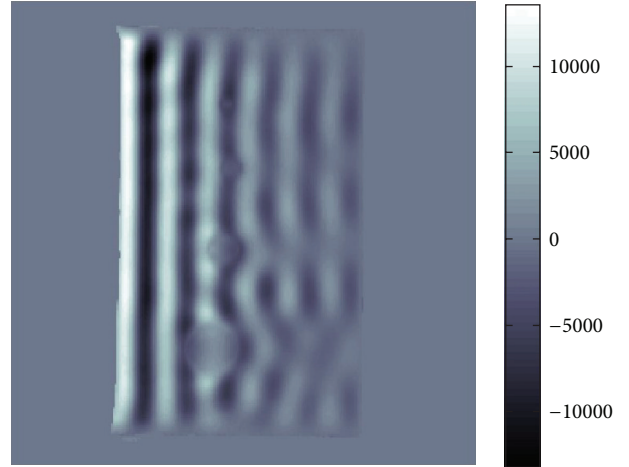


FIGURE 25: Data to be processed.

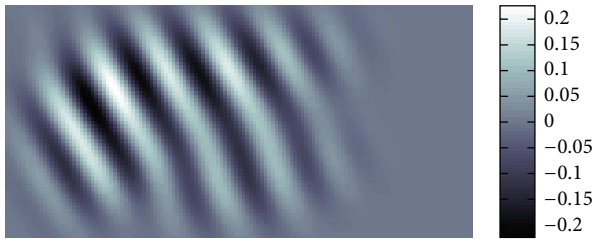


FIGURE 23: Real part in spatial domain.

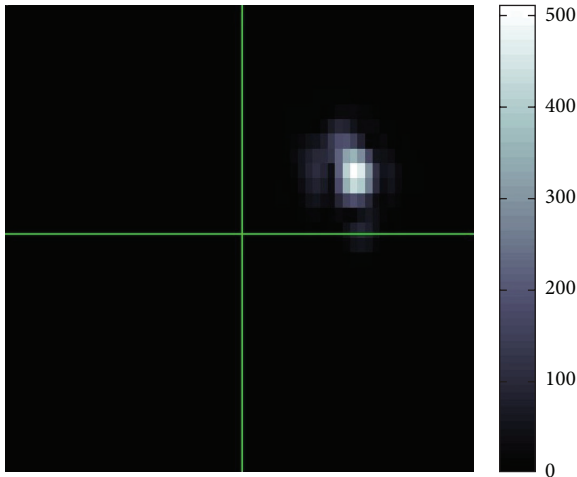


FIGURE 24: Modulus in Fourier domain.

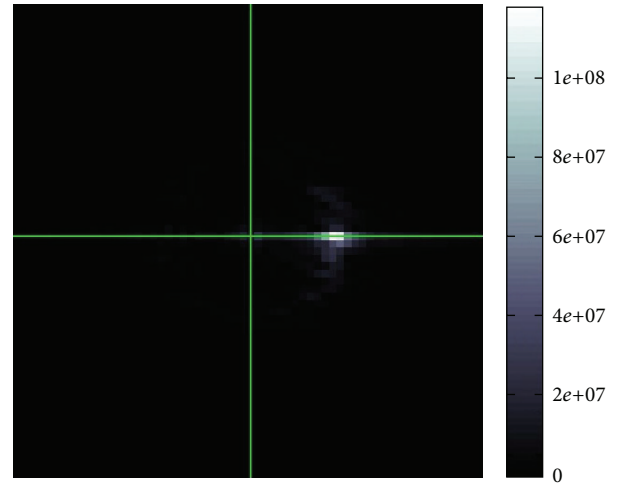


FIGURE 26: Modulus in Fourier domain.

Next, we will show another way of filtering. This is to filter the wave u around the globally strongest wave in the Fourier domain. That is let ξ_∞ be the peak of the modulus of the Fourier transform of u . Then this filtering is to filter u in the previous way just around ξ_∞ for each pixel. Then, we have Figures 23 and 24 for the filtered wave.

There is only a single wave which is close to a simple sinusoidal wave (Figure 23) and single peak in the Fourier domain (Figure 24).

5.2. *Testing with Mayo Clinic Data.* The LWV denoising always makes any data smooth taking off segmentations as well as noise in the data. Hence, if the input data is nearly free from noise, then the denoising process is unnecessary. For example, we applied the LWV denoising to the Mayo Clinic data (Figures 18 and 25).

Then, we obtained Figures 26, 27, and 28.

We can see that the denoising made the boundary of inclusions smoother and masked the inclusions.

6. Conclusions

We developed a model-independent data analysis for MRE data based on the FBI transformation to recover the local wave vector and local attenuation vector of the strongest local single wave assuming that waves in MRE data are locally given as a local multiwave form. This can be also applied to other wave images. We also linked the recovered local wave vector and local attenuation vector to the storage modulus and loss modulus by using a nearly incompressible isotropic

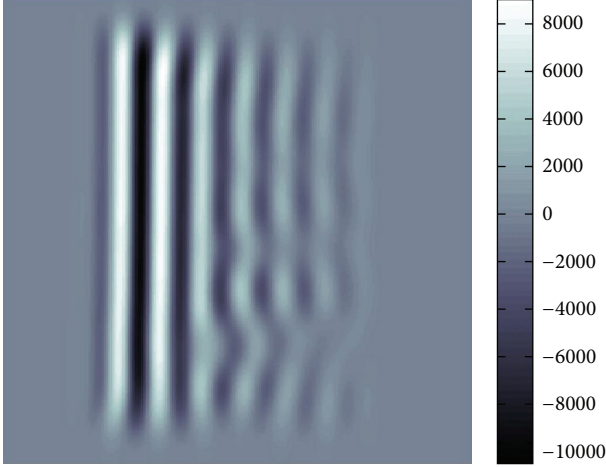


FIGURE 27: Filtering by the locally strongest wave.

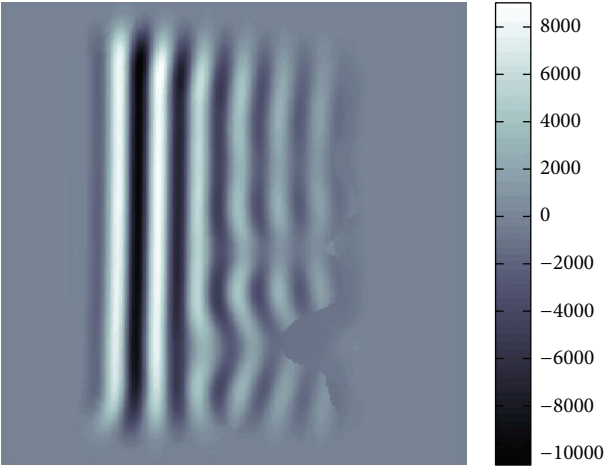


FIGURE 28: Filtering by the globally strongest wave.

viscoelastic equation which describes the displacement vector of time harmonic waves propagating in an MRE phantom. The recoveries of β and G' were quite good and stable. Further, we showed that a modified version of LWV method which enables to recover the local wave vector can be used to denoise the MRE data.

Our MRE data analysis was conducted using a numerical computational software on Linux-based ordinary desktop computer. The fast Fourier transformation is not so time consuming for maximum 256×256 pixels MRE data. The overall calculation finished in order of minutes.

Appendix

Fourier Transformation (FBI Transformation) of Waves

Let $u(x)$ be of a single-wave form around a point p given by

$$u(x) = e^{\omega(\alpha+i\beta) \cdot (x-p)}, \quad (\text{A.1})$$

with $\alpha, \beta \in \mathbb{R}^2$. Then we compute its FBI transform as follows. By taking $x - p$ as a new variable for the integration, we have

$$\begin{aligned} W(u; p, \sigma)(\xi) &= \int_{\mathbb{R}^2} e^{\omega(\alpha+i\beta) \cdot (x-p)} e^{-|x-p|^2/2\sigma^2} e^{-ix \cdot \xi} dx \\ &= e^{-ip \cdot \xi} \int_{\mathbb{R}^2} e^{\omega(\alpha+i\beta) \cdot x} e^{-|x|^2/2\sigma^2} e^{-ix \cdot \xi} dx. \end{aligned} \quad (\text{A.2})$$

Further, by $\omega\alpha \cdot x - (|x|^2/2\sigma^2) = (\omega^2\sigma^2|\alpha|^2/2) - (|x - \omega\sigma^2\alpha|^2/2\sigma^2)$ and taking $x - \omega\sigma^2\alpha$ as a new variable in the integration, we have

$$\begin{aligned} &\int_{\mathbb{R}^2} e^{\omega(\alpha+i\beta) \cdot x} e^{-|x|^2/2\sigma^2} e^{-ix \cdot \xi} dx \\ &= e^{\omega^2\sigma^2|\alpha|^2/2} e^{i\omega^2\sigma^2\alpha \cdot \beta} e^{-i\omega\sigma^2\alpha \cdot \xi} \int_{\mathbb{R}^2} e^{i\omega\beta \cdot x} e^{-|x|^2/2\sigma^2} e^{-ix \cdot \xi} dx. \end{aligned} \quad (\text{A.3})$$

Note that the integration in (A.3) is the Fourier transform of the Gaussian with respect to $\xi - \beta$. Hence,

$$\int_{\mathbb{R}^2} e^{i\omega\beta \cdot x} e^{-|x|^2/2\sigma^2} e^{-ix \cdot \xi} dx = 2\pi\sigma^2 e^{-\sigma^2|\xi - \omega\beta|^2/2}. \quad (\text{A.4})$$

After all, we have obtained

$$\begin{aligned} W(u; p, \sigma)(\xi) &= 2\pi\sigma^2 \exp \left[i\omega^2\sigma^2\alpha \cdot \beta + \frac{\omega^2\sigma^2|\alpha|^2}{2} \right] \\ &\quad \times \exp \left[-i(p + \omega\sigma^2\alpha) \cdot \xi - \frac{\sigma^2|\xi - \omega\beta|^2}{2} \right]. \end{aligned} \quad (\text{A.5})$$

Conflict of Interests

The authors have declared no conflict of interests.

Acknowledgments

The authors express their sincere thanks to Mayo Clinic for providing the MRE data for this paper. Also, the authors express their sincere thanks to Dr. Yu Jiang who provided the MRE data from the micro-MRE system for this paper and Professor Hideki Takuwa for some useful discussions on the FBI transformation.

References

- [1] R. Muthupillai, D. J. Lomas, P. J. Rossman, J. F. Greenleaf, A. Manduca, and R. L. Ehman, "Magnetic resonance elastography by direct visualization of propagating acoustic strain waves," *Science*, vol. 269, no. 5232, pp. 1854–1857, 1995.
- [2] H. Ammari, P. Garapon, H. Kang, and H. Lee, "A method of biological tissues elasticity reconstruction using magnetic resonance elastography measurements," *Quarterly of Applied Mathematics*, vol. 66, no. 1, pp. 139–175, 2008.
- [3] Y. Jiang and G. Nakamura, "Viscoelastic properties of soft tissues in a living body measured by MR elastography," *Journal of Physics: Conference Series*, vol. 290, no. 1, Article ID 012006, 2011.

- [4] N. Higashimori, "Identification of viscoelastic properties by magnetic resonance elastography," *Journal of Physics: Conference Series*, vol. 73, no. 1, Article ID 012009, 2007.
- [5] Y. Jiang, H. Fujiwara, and G. Nakamura, "Approximate steady state models for magnetic resonance elastography," *SIAM Journal on Applied Mathematics*, vol. 71, no. 6, pp. 1965–1989, 2011.
- [6] G. Nakamura, Y. Jiang, S. Nagayasu, and J. Cheng, "Inversion analysis for magnetic resonance elastography," *Applicable Analysis*, vol. 87, no. 2, pp. 165–179, 2008.
- [7] Y. Jiang, *Mathematical data analysis for magnetic resonance elastography [Ph.D. thesis]*, Department of Mathematics, Graduate School of Science, Hokkaido University, Japan, 2009.
- [8] D. Jean-Marc, *F.B.I. Transformation Second Microlocalization and Semilinear Caustics*, Springer.
- [9] P. S. Addison, *The Illustrated Wavelet Transform Handbook : Introductory Theory and Applications in Science, Engineering, Medicine and Finance*, Institute of Physics, Bristol, UK, 2002.
- [10] M. Suga, T. Matsuda, K. Minato et al., "Measurement of in vivo local shear modulus using MR elastography multiple-phase patchwork offsets," *IEEE Transactions on Biomedical Engineering*, vol. 50, no. 7, pp. 908–915, 2003.
- [11] R. M. Christensen, *Theory of Viscoelasticity*, Academic Press, 1982.
- [12] T. Oliphant, *Direct methods for dynamic elastography reconstruction: optimal inversion of the interior Helmholtz problem [Ph.D. thesis]*, Biomedical Sciences, Biomedical Imaging, Mayo Graduate School, 2001.

Research Article

Current Density Imaging Using Directly Measured Harmonic B_z Data in MREIT

Chunjae Park and Oh In Kwon

Department of Mathematics, Konkuk University, Seoul 143-701, Republic of Korea

Correspondence should be addressed to Oh In Kwon; oikwon@konkuk.ac.kr

Received 12 December 2012; Accepted 16 February 2013

Academic Editor: Ulrich Katscher

Copyright © 2013 C. Park and O. I. Kwon. This is an open access article distributed under the Creative Commons Attribution License, which permits unrestricted use, distribution, and reproduction in any medium, provided the original work is properly cited.

Magnetic resonance electrical impedance tomography (MREIT) measures magnetic flux density signals through the use of a magnetic resonance imaging (MRI) in order to visualize the internal conductivity and/or current density. Understanding the reconstruction procedure for the internal current density, we directly measure the second derivative of B_z data from the measured k -space data, from which we can avoid a tedious phase unwrapping to obtain the phase signal of B_z . We determine optimal weighting factors to combine the derivatives of magnetic flux density data, $\nabla^2 B_z$, measured using the multi-echo train. The proposed method reconstructs the internal current density using the relationships between the induced internal current and the measured $\nabla^2 B_z$ data. Results from a phantom experiment demonstrate that the proposed method reduces the scanning time and provides the internal current density, while suppressing the background field inhomogeneity. To implement the real experiment, we use a phantom with a saline solution including a balloon, which excludes other artifacts by any concentration gradient in the phantom.

1. Introduction

Magnetic resonance electrical impedance tomography (MREIT) visualizes a cross-sectional conductivity and/or current density inside the human body. The MREIT technique injects currents through attached electrodes in order to probe the imaging subject and then measures the induced magnetic flux density, inside the subject using an MRI scanner. The MRI scanner only measures the z -component of the induced magnetic flux density $\mathbf{B} = (B_x, B_y, B_z)$; therefore the MREIT techniques have focused on the reconstruction of the internal conductivity and/or current density by using the measurable B_z data instead of subject rotation [1–18].

The MREIT techniques used to reconstruct the conductivity and/or the current density have been widely developed and have reached the stage of imaging experiments for live animals and the human body [18, 19]. Due to the poor SNR of measured B_z data in current MREIT experiments, it is critical to reduce the scan time in MREIT, while maintaining the spatial-resolution and sufficient contrast, for practical *in vivo* implementations of MREIT.

In order to increase the quality of measured B_z data, a measurement technique called the injected current nonlinear encoding (ICNE) method was developed, which extends the duration of the injection current until the end of the read-out gradient in order to maximize the signal intensity of the magnetic flux density [20]. Motivated by the ICNE pulse sequence method, an ICNE-multiecho technique was developed and optimized by finding an optimal weighting factor for the multiple measured B_z data [21].

The MREIT technique typically uses an interleaved acquisition, which scans each phase encoding consecutively by injecting two currents possessing positive and negative polarities with the same scan duration and amplitude to double the B_z signal and cancel out the background field inhomogeneity. In order to reduce the scan time, for the measurement of B_z , [22] reconstructed the phase signal B_z by filling a partial k -space region using the interleaved measurement property.

Functional MRI (fMRI) has been applied to a wide range of neuroscience researches by visualizing neural activities inside the brain in a fast and direct way [23–25]. A fast MREIT imaging technique has been proposed as a promising imaging

technique for the continuous monitoring of internal electrical property inside the subject [26]. In this paper, we propose a method to monitor spatial and temporal internal current density changes in the subject by using a fast gradient multi-echo pulse sequence to maximize the measured B_z signal in a short scanning time. Moreover, we derive a direct method to measure $\nabla^2 B_z$ instead of B_z data from the measured k -space data. The proposed method can also avoid a tedious unwrapping procedure, which may introduce phase artifact in the recovered phase signal.

For the recovery of the internal current density, we investigate the reconstruction procedure for the internal current density from the measured $\nabla^2 B_z$ data. In the paper [27], a projected current \mathbf{J}^P was provided by the decomposition $\mathbf{J} = \mathbf{J}^P + \mathbf{J}^N$, where \mathbf{J} is the internal current density influenced by the injected current and \mathbf{J}^P is a determined component of \mathbf{J} from the measured B_z data. The projected current \mathbf{J}^P is identical to the true current \mathbf{J} when the z -component J_z of $\mathbf{J} = (J_x, J_y, J_z)$ is the same as J_z^0 where J_z^0 is the z -component of the background current \mathbf{J}^0 .

The projected current \mathbf{J}^P can be determined in a concrete form which consists of the background current \mathbf{J}^0 and the solution of a two-dimensional harmonic equation with the Dirichlet condition that matches the external injection current on the surface of the subject. To recover the internal current density \mathbf{J}^P with the generated B_z caused by the injected current, we only use the second derivatives of B_z and $\nabla^2 B_z$, which are required to solve the two-dimensional harmonic equation for \mathbf{J}^P .

To reduce the noise artifact, we apply the ICNE-multi-echo train based on the fast gradient echo and solve an optimal weighting factor of $\nabla^2 B_z^\ell$, $\ell = 1, \dots, N_E$, where N_E denotes the number of echoes at each RF pulse.

In order to verify how the proposed method works, we designed a phantom with a saline solution and fixed a balloon inside the phantom, inflating the balloon by injecting the same saline solution. The phantom was designed to provide a homogeneous magnitude image, but the recovered current density distinguishes inside the balloon. For the experiment, the total scan time was 12.36 seconds to obtain the complete k -space data using the interleaved acquisition in order to implement the proposed method with a 128×128 spacial matrix size. The phantom experiment demonstrates that the proposed method reduces the scanning time and recovers internal current density, while suppressing the measured noise artifact.

2. Methods

We inject the current I through the attached electrodes on a three-dimensional cylindrical conducting object Ω with its conductivity distribution σ . The injection currents I produce the voltage distribution u satisfying the following elliptic partial differential equation:

$$\begin{aligned} \nabla \cdot (\sigma \nabla u) &= 0 \quad \text{in } \Omega, \\ -\sigma \nabla u \cdot \mathbf{v} &= g \quad \text{on } \partial\Omega, \quad \int_{\partial\Omega} u ds = 0, \end{aligned} \quad (1)$$

where \mathbf{v} is the outward unit normal vector and g is the normal component of the current density on $\partial\Omega$. Clearly, $\int_{\partial\Omega} g ds = 0$ due to $\nabla \cdot (\sigma \nabla u) = 0$ in Ω . The current density $\mathbf{J} = -\sigma \nabla u$ and the magnetic flux density $\mathbf{B} = (B_x, B_y, B_z)$ in Ω satisfy the Ampère law $\mathbf{J} = \nabla \times \mathbf{B}/\mu_0$ and Biot-Savart law, where $\mu_0 = 4\pi 10^{-7}$ Tm/A is the magnetic permeability of the free space. We let $B_z(x, y) = B_z(x, y, z_0)$ where z_0 is the center of a selected imaging slice.

2.1. Measurement of B_z Using Interleaved ICNE Acquisition. For the interleaved ICNE acquisition method, we inject the positive and negative currents, I^+ and I^- , through the attached electrodes by scanning each phase encoding consecutively. For a standard spin echo pulse sequence without current injection, the k -space MR signal can be expressed as

$$S(n, m) = \int_{\mathbb{R}^2} \rho(x, y) e^{i\delta(x, y)} e^{-i2\pi(\Delta k_x n x + \Delta k_y m y)} dx dy, \quad (2)$$

where $\rho(x, y)$ is the real transverse magnetization, δ denotes the phase artifact of background field inhomogeneity, and Δk_x and Δk_y are the reciprocals of fields of view for the x direction and y direction, respectively. During the data acquisition, we set

$$\Delta k_x = \frac{\gamma}{2\pi} G_x \Delta t, \quad \Delta k_y = \frac{\gamma}{2\pi} \Delta G_y T_{pe}, \quad (3)$$

and sample the data in (2) finitely for

$$n = -\frac{N_x}{2}, \dots, \frac{N_x}{2} - 1, \quad m = -\frac{N_y}{2}, \dots, \frac{N_y}{2} - 1. \quad (4)$$

The names of the above parameters are

$\gamma = 26.75 \times 10^7$ rad/T · s: the gyromagnetic ratio of the proton,

G_x : the magnetic reading gradient strength,

Δt : the sampling interval,

ΔG_y : the phase encoding step,

T_{pe} : the phase encoding time interval,

N_x : the number of sampling points,

N_y : the number of phase encoding lines.

For the conventional MREIT case, we inject the current for the duration of T_c^0 from the end of the 90° RF pulse to the beginning of the reading gradient. In this case, the induced magnetic flux density B_z due to the injection current provides the additional dephasing of spins and consequently the extra phase is accumulated during T_c^0 . The corresponding k -space data for the injection currents I^\pm can be represented as

$$\begin{aligned} S^{I^\pm}(n, m) &= \int_{\mathbb{R}^2} \rho(x, y) e^{i\delta(x, y)} e^{\pm i\gamma T_c^0 B_z(x, y)} \\ &\quad \times e^{-i2\pi(\Delta k_x n x + \Delta k_y m y)} dx dy. \end{aligned} \quad (5)$$

Using the notations

$$\rho^\pm(x, y) = \rho(x, y) e^{i\delta(x, y)} e^{\pm i\gamma T_c^0 B_z(x, y)}, \quad (6)$$

we can compute the magnetic flux density B_z as

$$B_z(x, y) = \frac{1}{2\gamma T_c^0} \tan^{-1} \left(\frac{\alpha(x, y)}{\beta(x, y)} \right), \quad (7)$$

where α and β are the imaginary and real parts of ρ^+/ρ^- , respectively.

In the conventional MREIT case, the noise standard deviation of the measured B_z , sd_{B_z} , is given as a known quantity, which is inversely proportional to the current injection time T_c and the SNR of the MR magnitude image Y as follows [28, 29]:

$$sd_{B_z}(\mathbf{r}) = \frac{1}{2\gamma T_c Y(\mathbf{r})}. \quad (8)$$

Since the ICNE MR pulse sequence injects the current until the end of a read gradient, the total current injection time of the ICNE case is $T_c^T := T_c^0 + T_s$ and the k -space data is represented as

$$S^{C^\pm}(n, m) = \int_{\mathbb{R}^2} \rho(x, y) e^{i\delta(x, y)} e^{\pm i\gamma(T_c^0 + T_s/2)B_z(x, y)} \times e^{-i2\pi(\Delta k_x n x + \Delta k_y m y)} dx dy, \quad (9)$$

where $T_s = \Delta t N_x$ is the data acquisition time. In the usual spin echo, the ICNE current injection method demonstrates better SNR in the measured magnetic flux density data than the conventional current injection method. The optimal data acquisition time T_s^* has been calculated for the usual spin echo as

$$T_s^* = \frac{2\sqrt{3}}{3} T_E - \sqrt{3} \tau_{rf}, \quad (10)$$

which optimally reduces the noise in the B_z data, where τ_{rf} is the time of RF pulse [30].

In the ICNE MR pulse sequence case, the noise standard deviation of the measured B_z , $sd_{B_z}^{ICNE}$, is given as follows [30]:

$$sd_{B_z}^{ICNE}(\mathbf{r}) = \frac{1}{2\gamma(T_c^0 + T_s^*/2)Y(\mathbf{r})}. \quad (11)$$

The prolonged data acquisition time, however, may suffer from undesirable side artifacts such as blurring, chemical shift, and motion artifacts along the phase encoding direction. To reduce the undesirable side artifacts, we divide the prolonged data acquisition time into several short ones in the ICNE-multi-echo MR pulse sequence.

2.2. Measurement of $\tilde{\nabla}^2 B_z$ Using ICNE-Multiecho Train. Using the ICNE-multi-echo MR pulse sequence, the measured k -space data can be represented as

$$S^{\ell\pm}(n, m) = \int_{\mathbb{R}^2} \rho^\ell(x, y) e^{i\delta^\ell(x, y)} e^{\pm i\gamma T_c^\ell B_z(x, y)} \times e^{-i2\pi(\Delta k_x n x + \Delta k_y m y)} dx dy, \quad \ell = 1, \dots, N_E, \quad (12)$$

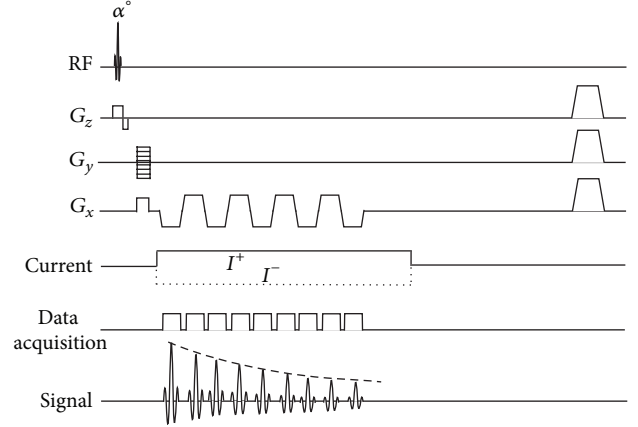


FIGURE 1: Diagram of the ICNE-multi-echo MR pulse sequence based on a gradient echo.

where N_E is the echo number, T_c^ℓ is the ℓ th time width of the injected current, and ρ^ℓ and δ^ℓ denote the ℓ th transverse magnetization and phase artifact, respectively.

Figure 1 presents a schematic diagram for the ICNE-multi-echo MR pulse sequence based on a gradient echo pulse sequence. By taking the inverse fast Fourier transform, the ICNE-multi-echo sequence generates multiple complex images with different magnitude amplitudes depending on T_2^* decay and different widths of current injection time:

$$\psi^{\ell\pm}(x, y) := \rho^\ell(x, y) e^{i\delta^\ell(x, y)} e^{\pm i\gamma T_c^\ell B_z(x, y)}, \quad \ell = 1, \dots, N_E. \quad (13)$$

Using the relation (13), we derive a formula for $\tilde{\nabla}^2 B_z^\ell$ as

$$\tilde{\nabla}^2 B_z^\ell(x, y) = \frac{1}{i\gamma T_c^\ell} \tilde{\nabla} \cdot \left(\frac{|\psi^{\ell+}(x, y)|}{|\psi^{\ell+}(x, y)|} \tilde{\nabla} \frac{\psi^{\ell+}(x, y)}{|\psi^{\ell+}(x, y)|} - \frac{|\psi^{\ell-}(x, y)|}{|\psi^{\ell-}(x, y)|} \tilde{\nabla} \frac{\psi^{\ell-}(x, y)}{|\psi^{\ell-}(x, y)|} \right), \quad (14)$$

where $\tilde{\nabla} B_z^\ell = (\partial B_z^\ell / \partial x, \partial B_z^\ell / \partial y)$ denotes the two-dimensional gradient of B_z^ℓ . The induced $\tilde{\nabla}^2 B_z^\ell$ in (14) removes the low-frequency phase artifact δ^ℓ by subtracting $\tilde{\nabla}^2 \delta^\ell$ in (14).

The calculated vector $(|\psi^{\ell\pm}|/|\psi^{\ell\pm}|)\tilde{\nabla}(|\psi^{\ell\pm}|/|\psi^{\ell\pm}|)$ corresponding to $i\gamma T_c^\ell \tilde{\nabla}(\delta^\ell \pm B_z^\ell)$ includes unavoidable measured noise. When we consider the decomposed form of $(|\psi^\ell|/|\psi^\ell|)\tilde{\nabla}(|\psi^\ell|/|\psi^\ell|) = \tilde{\nabla} f + \tilde{\nabla} \times \Psi$, where the curl term $\tilde{\nabla} \times \Psi$ is a part of unavoidable measured noise, the divergence procedure for $\tilde{\nabla}^2 B_z^\ell$ in (14) cancels $\tilde{\nabla} \times \Psi$, and therefore the measured $\tilde{\nabla}^2 B_z^\ell$ includes a denoising procedure by suppressing a part of the measured noise.

2.3. Optimal Combination of Measured $\tilde{\nabla}^2 B_z^\ell$, $\ell=1, \dots, N_E$. The measured $\tilde{\nabla}^2 B_z^\ell$, $\ell = 1, \dots, N_E$ includes different amounts of unavoidable noise since the intensity of transverse

magnetization and the width of injected current are different at each echo.

The noise standard deviation of $\tilde{\nabla}^2 B_z^\ell$ in (14) is given as

$$sd_{\tilde{\nabla}^2 B_z^\ell}(x, y) = \frac{C}{\gamma T_c^\ell Y^\ell(x, y)}, \quad (15)$$

where the constant C only relates to the numerical differentiations for $\tilde{\nabla}^2 B_z^\ell$, and Y^ℓ denotes the SNR of the ℓ th MR magnitude image.

Since the noise levels of the measured $\tilde{\nabla}^2 B_z^\ell$, $\ell = 1, \dots, N_E$ in (14) are given as known quantities, we can utilize the known information $sd_{\tilde{\nabla}^2 B_z^\ell}$ to determine an optimized $\tilde{\nabla}^2 B_z$ which combines the multiple $\tilde{\nabla}^2 B_z^\ell$:

$$\tilde{\nabla}^2 B_z(x, y) = \sum_{\ell=1}^{N_E} \omega^\ell(x, y) \tilde{\nabla}^2 B_z^\ell(x, y). \quad (16)$$

The problem of determining the weighting factors ω^ℓ for $\tilde{\nabla}^2 B_z^\ell$ can be formulated as

$$\begin{aligned} & \min_{\omega^\ell(x, y), \ell=1, \dots, N_E} \sum_{\ell=1}^{N_E} (\omega^\ell(x, y))^2 \text{Var}_{\tilde{\nabla}^2 B_z^\ell}(x, y) \\ & \text{subject to } \sum_{\ell=1}^{N_E} \omega^\ell(x, y) = 1, \quad \omega^\ell(x, y) > 0, \end{aligned} \quad (17)$$

where $\text{Var}_{\tilde{\nabla}^2 B_z^\ell}$ denotes the noise variance of $\tilde{\nabla}^2 B_z^\ell$, $\ell = 1, \dots, N_E$ in (14).

Following similar arguments in [21], the weighting factors ω^ℓ can be determined as

$$\omega^\ell(x, y) = \frac{(T_c^\ell)^2 |\psi^{\ell\pm}(x, y)|^2}{\sum_{m=1}^{N_E} (T_c^m)^2 |\psi^{m\pm}(x, y)|^2}, \quad \ell = 1, \dots, N_E, \quad (18)$$

where $\psi^{\ell\pm}$ in (13) is the inverse fast Fourier transform of the measured k -space data $S^{\ell\pm}$.

2.4. Recovery of Internal Current Density Using the Optimized $\tilde{\nabla}^2 B_z$. The internal current density $\mathbf{J} = -\sigma \nabla u$ and the magnetic flux density $\mathbf{B} = (B_x, B_y, B_z)$ in Ω satisfy the Ampère law $\mathbf{J} = \nabla \times \mathbf{B} / \mu_0$ where μ_0 is the magnetic permeability of the free space. The magnetic resonance current density imaging (MRCDI) technique, which allows the rotation of the object in the MRI scanner, directly visualizes the internal current density by measuring the full components of \mathbf{B} [31].

The MREIT techniques focus on visualizing the internal current density using only B_z component of \mathbf{B} without rotating the subject. A cylindrical imaging domain Ω can be represented as

$$\Omega = \bigcup_{t \in (-H, H)} \Omega_t, \quad \text{where } \Omega_t = \Omega \cap \{(x, y, z) \in \mathbb{R}^3 \mid z = t\}, \quad (19)$$

where Ω_0 denotes the middle slice of the imaging subject Ω .

In the paper [27], the only recoverable current from the measured B_z data can be represented as $\mathbf{J}^P = \mathbf{J}^0 + \mathbf{J}^*$, where $\mathbf{J}^0 = \nabla \alpha$ and $\mathbf{J}^* = (\partial \beta / \partial y, -\partial \beta / \partial x, 0)$. Here, α is a homogeneous voltage potential satisfying

$$\begin{aligned} \nabla^2 \alpha &= 0 \quad \text{in } \Omega, \\ \nabla \alpha \cdot \mathbf{v} &= \mathbf{J} \cdot \mathbf{v} \quad \text{on } \partial \Omega, \quad \int_{\partial \Omega} \alpha ds = 0, \end{aligned} \quad (20)$$

and $\beta_t(x, y) := \beta(x, y, t)$ satisfies the following two-dimensional Laplace equation for each slice $\Omega_t \subset \Omega$:

$$\begin{aligned} \tilde{\nabla}^2 \beta_t &= \frac{1}{\mu_0} \nabla^2 B_z \quad \text{in } \Omega_t, \\ \beta_t &= 0 \quad \text{on } \partial \Omega_t, \end{aligned} \quad (21)$$

where $\nabla = (\partial / \partial x, \partial / \partial y, \partial / \partial z)$ and $\tilde{\nabla} = (\partial / \partial x, \partial / \partial y)$. From the optimized $\tilde{\nabla}^2 B_z$ in (16) on each imaging slice Ω_t , we can estimate $\nabla^2 B_z$ in (21).

Equations (20) and (21) show that we can reconstruct the projected current \mathbf{J}^P from the optimized $\tilde{\nabla}^2 B_z$ immediately, instead of B_z , by solving two-dimensional Laplace equations in the region of interest (ROI). The projected current \mathbf{J}^P provides an optimal approximation of the true current \mathbf{J} and, moreover, the gap $\mathbf{J} - \mathbf{J}^P$ depends only on the longitudinal component $J_z - J_z^0$ of $\mathbf{J} - \mathbf{J}^0$.

2.5. Experimental Setup. In order to demonstrate the proposed method, we performed a phantom with a saline solution including a balloon for the visualization of internal current density. The internal of the balloon was filled with the same saline solution and the volume of the balloon was controlled by injecting the saline solution, which excluded other artifacts by any concentration gradient in the phantom. Figure 2(a) illustrates the used balloon for the phantom experiment, and Figures 2(b) and 2(c) show a phantom design to describe how to setup the balloon phantom.

After positioning the phantom inside a 3.0T MRI scanner (Achieva, Philips), we collected k -space data with 8-channel RF coil using the gradient multi-echo ICNE pulse sequence, which extends throughout the duration of the injection current until the end of a readout gradient [20]. The maximum amplitude of the injection current was 5 mA and the total imaging time was 12.36 seconds to measure the interleaved k -space $S^{\ell\pm}$ data, $\ell = 1, \dots, N_E$. The slice thickness was 5 mm, the number of axial slices was one, the repetition time $T_R = 60$ ms, the echo spacing $\Delta T_E = 6$ ms, the flip angle was 40 degree, and the multi-echo time $T_{E_\ell} = 6 + (\ell - 1) \times 6$ ms for $N_E = 9$. The FOV was $160 \times 160 \text{ mm}^2$ with a matrix size of 128×128 . The current injection time T_{c_ℓ} for each echo was almost the same as the multi-echo time $T_{E_\ell} = 6 + (\ell - 1) \times 6$, $\ell = 1, \dots, 9$ because the current was continuously injected until the end of the readout gradient.

3. Results

Figure 3(a) shows the acquired magnitude images $|\rho^\ell|$, $\ell = 1, \dots, 9$, where ρ^ℓ was the ℓ th measured T_2^* weighted complex

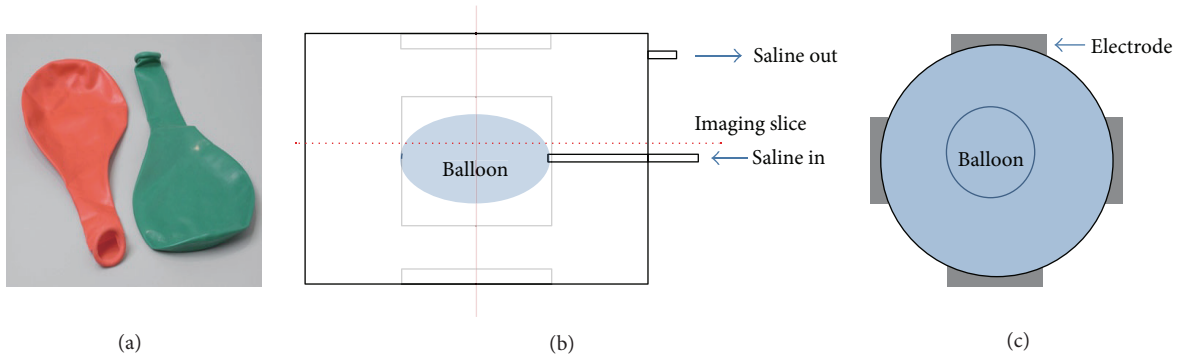


FIGURE 2: (a) Balloon used for the experiment, (b) and (c) balloon phantom design and the electrodes position, respectively.

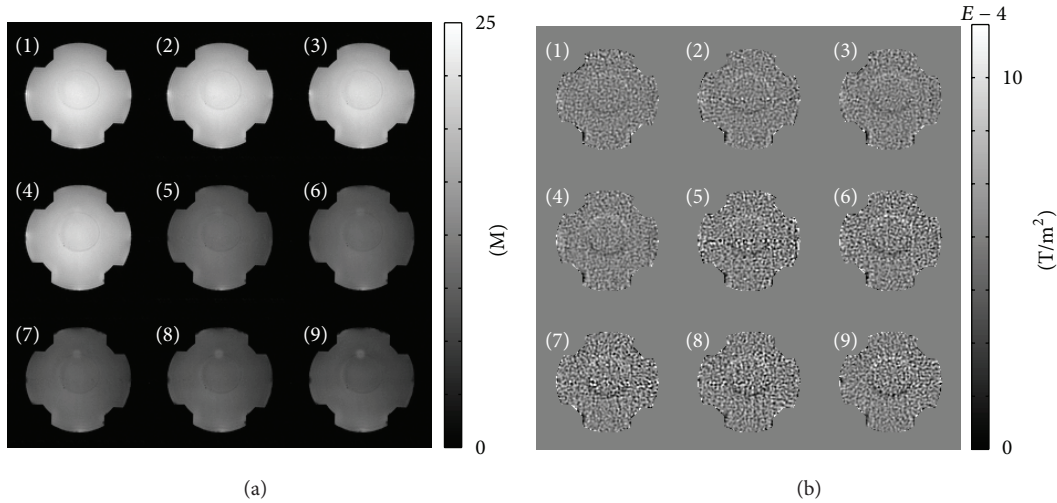


FIGURE 3: (a) Acquired magnitude images $|\rho^\ell|$, $\ell = 1, \dots, 9$, where ρ^ℓ was the ℓ th measured T_2^* weighted complex image, (b) measured $\bar{\nabla}^2 B_z^\ell$ images using (14) corresponding to the ℓ th k -space data $S^{\ell\pm}$, $\ell = 1, \dots, 9$.

image. Figure 3(b) shows the measured $\bar{\nabla}^2 B_z^\ell$ images using (14) corresponding to the ℓ th k -space data $S^{\ell\pm}$, $\ell = 1, \dots, 9$. Inside and outside of the balloon, the MR magnitude images are almost the same because of the same saline solution, but the measured $\bar{\nabla}^2 B_z^\ell$ images show distinguishable signals reflecting the conductivity changes inside and outside of the balloon.

Since both sides, inside and outside of the balloon, are homogeneous, the $\bar{\nabla}^2 B_z^\ell \approx -\mu_0 \nabla u \times \nabla \sigma$ should be near zero except the boundary of the balloon without noise effect because the conductivity value is constant in each region. To evaluate the noise level of B_z^ℓ , we calculated the discrete L^2 -norm:

$$\begin{aligned} \text{Err}_2 &:= \left\| \bar{\nabla}^2 B_z^\ell \right\|_{L^2(\Omega \setminus \partial D)} \\ &= \sqrt{\sum_{(x_i, y_j) \in \Omega \setminus \partial D} \bar{\nabla}^2 B_z^\ell(x_i, y_j)^2 |\Omega_{ij}|}, \end{aligned} \quad (22)$$

where Ω is the imaging ROI region, ∂D denotes the boundary of balloon, and $|\Omega_{ij}|$ is the pixel size.

Table 1 shows the L^2 -norm, Err_2 , in which the values depends on the T_2^* decay rate and the width of injected current.

The estimated noise levels were reduced up to the 4th echo, but increased in the following echoes because the intensity of magnitude images follows the exponential T_2^* decay, and the width of the injected current linearly increases.

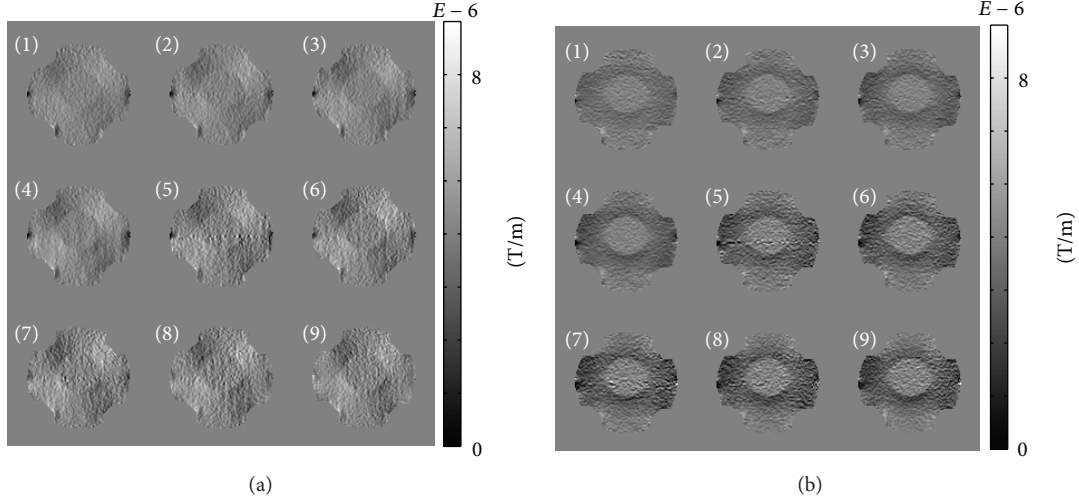
Figures 4(a) and 4(b) show the measured $\partial B_z^\ell / \partial x$ and $\partial B_z^\ell / \partial y$ images, respectively, where

$$\begin{aligned} \bar{\nabla} B_z^\ell(x, y) &= \frac{|\psi^{\ell+}(x, y)|}{\psi^{\ell+}(x, y)} \bar{\nabla} \psi^{\ell+}(x, y) \\ &\quad - \frac{|\psi^{\ell-}(x, y)|}{\psi^{\ell-}(x, y)} \bar{\nabla} \psi^{\ell-}(x, y), \quad \ell = 1, \dots, 9. \end{aligned} \quad (23)$$

Since the currents were transversally injected, the measured $\partial B_z^\ell / \partial y$ reflected dominant internal current flows.

TABLE 1: Noise level estimation of the measured $\tilde{\nabla}^2 B_z^\ell$, $\ell = 1, \dots, 9$, by calculating (22).

	1st	2nd	3rd	4th	5th	6th	7th	8th	9th
Err ₂	129.1	142.1	115.0	110.4	203.1	161.7	195.6	183.5	166.6

FIGURE 4: (a) Measured $\partial B_z^\ell / \partial x$ images, (b) measured $\partial B_z^\ell / \partial y$ images, $\ell = 1, \dots, 9$.TABLE 2: Noise level estimation of the recovered $\tilde{\nabla}^2 B_z^{\text{avg}}$ and $\tilde{\nabla}^2 B_z^{\text{opt}}$, by calculating (22).

	$\tilde{\nabla}^2 B_z^{\text{avg}} = (1/N_E) \sum_{\ell=1}^{N_E} \tilde{\nabla}^2 B_z^\ell$	$\tilde{\nabla}^2 B_z^{\text{opt}} = \sum_{\ell=1}^{N_E} \omega^\ell \tilde{\nabla}^2 B_z^\ell$
Err ₂	145.1	41.5

Figures 5(a) and 5(b) display the reconstructed $\tilde{\nabla}^2 B_z^{\text{avg}} = (1/N_E) \sum_{\ell=1}^{N_E} \tilde{\nabla}^2 B_z^\ell$ and $\tilde{\nabla}^2 B_z^{\text{opt}} = \sum_{\ell=1}^{N_E} \omega^\ell \tilde{\nabla}^2 B_z^\ell$ images, respectively, where ω^ℓ is the weighting factor by solving (17).

Figure 6 shows the recovered current density images, J_x^ℓ and J_y^ℓ , corresponding to the ℓ th echo. To obtain the current density images, we solved (20) for the background homogeneous current and the two-dimensional harmonic equation (21) to reflect the measured $\tilde{\nabla}^2 B_z^\ell$ data.

We recovered the current density \mathbf{J}^{opt} by solving (20) and (21) using the optimized $\tilde{\nabla}^2 B_z^{\text{opt}} = \sum_{\ell=1}^{N_E} \omega^\ell \tilde{\nabla}^2 B_z^\ell$, where ω^ℓ is the weighting factor by solving (17). The recovered J_x^{opt} and J_y^{opt} are displayed in Figure 7.

Table 2 shows the estimated noise level of the recovered $\tilde{\nabla}^2 B_z^{\text{avg}}$ and $\tilde{\nabla}^2 B_z^{\text{opt}}$, by calculating (22). The estimated noise levels validate the proposed method because the inside and outside of the balloon in the phantom should be homogeneous.

4. Discussion

Since the MREIT technique conventionally used the interleaved phase encoding acquisition scheme to measure the magnetic flux density by alternating two currents with positive and negative polarities, we could obtain the coil

sensitivity information without additional scans by product of $\psi^{c_j^+}$ and $\psi^{c_j^-}$:

$$\begin{aligned} \Psi^{c_j}(x, y) &:= \psi^{c_j^+}(x, y) \psi^{c_j^-}(x, y) \\ &= (\rho^{c_j}(x, y))^2 e^{2i\delta_{c_j}(x, y)}, \quad j = 1, \dots, N_C, \end{aligned} \quad (24)$$

where δ_{c_j} is the j th coil sensitivity and N_C is the number of coils. For a fast MRI, using the *a priori* spatial information from the multiple receiver coils, the sensitivity encoding (SENSE) technique enables one to reduce the number of Fourier encoding steps while preserving the spatial resolution [32]. For a temporal variation of the internal conductivity, if we estimate the reference coil sensitivity using (24), which is independent of the injected current, the SENSE technique can be applicable to the proposed method to visualize the internal current density combining the multi-echo train.

In this paper, we directly measure $\tilde{\nabla}^2 B_z$, which is sufficient to reconstruct the internal current density using the injected current information. The proposed method to measure $\tilde{\nabla}^2 B_z$ in (14) can avoid a tedious unwrapping procedure. The proposed method may exhibit potential to be applied for conventional phase imaging techniques.

The optimal combination of multiple echoes by determining optimal weighting factor in (17) effectively reduces the noise level of measured $\tilde{\nabla}^2 B_z$. Since the decay rate of magnitude and the width of injected current can be determined pixel by pixel, we can determine a pixel-wise noise level of the optimized $\tilde{\nabla}^2 B_z$ data. Since most algorithms for the MREIT technique visualize the internal conductivity and/or current density in an entire imaging region due to the relationships between the external injection current and the

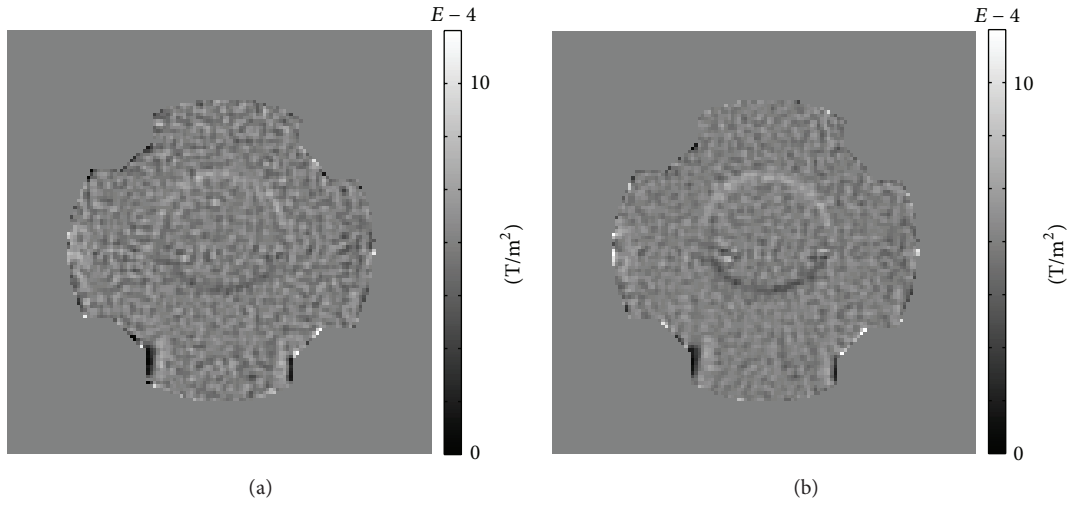


FIGURE 5: (a) Reconstructed $\tilde{\nabla}^2 B_z^{\text{avg}} = (1/N_E) \sum_{\ell=1}^{N_E} \tilde{\nabla}^2 B_z^\ell$ images, (b) reconstructed $\tilde{\nabla}^2 B_z^{\text{opt}} = \sum_{\ell=1}^{N_E} \omega^\ell \tilde{\nabla}^2 B_z^\ell$ images, where ω^ℓ is the weighting factor by solving (17).

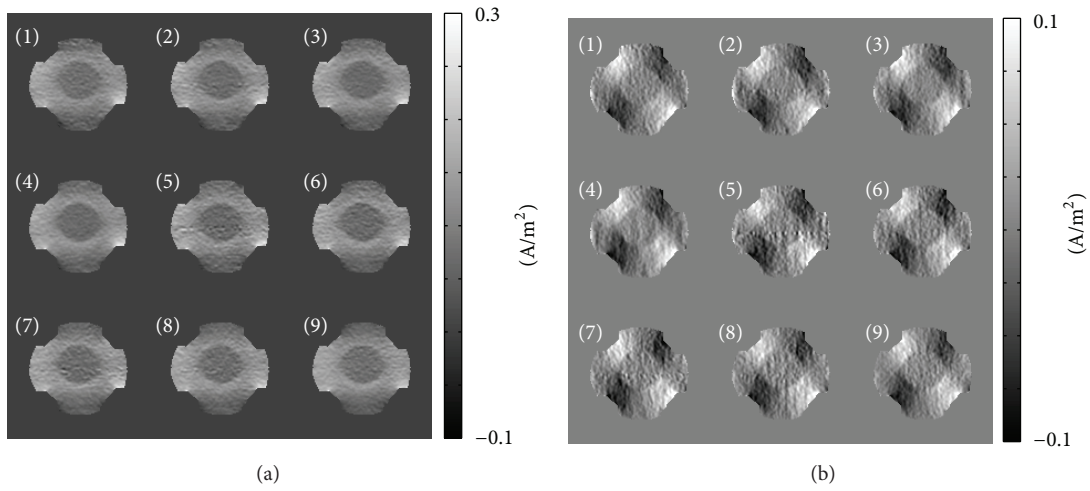


FIGURE 6: Recovered current density by solving (20) and (21). (a) Recovered J_x^ℓ images, (b) recovered J_y^ℓ images, $\ell = 1, \dots, 9$.

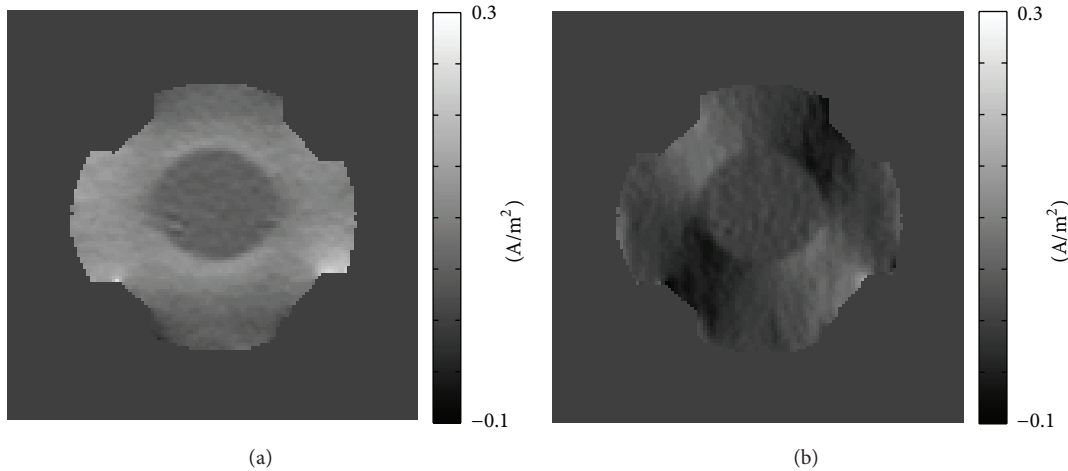


FIGURE 7: Recovered current density by solving (20) and (21). (a) Reconstructed J_x^{opt} images, (b) J_y^{opt} images by using B_z^{opt} .

internal measured magnetic flux density data, the estimated noise level of B_z can be used to determine the denoising level of the measured data in defective regions.

To optimize the multiple echoes, we consider only the uniformly distributed random noise effect, but unavoidable spike or different nonuniform noise may deteriorate a combined measured data. Thus it is important to develop a method to discard the non-uniform noises in the optimizing process in order to enhance the quality of B_z .

Our future studies will focus on reducing the imaging time with a feasible noise level to produce conductivity images for the application of functional MREIT imaging to animal brains in order to visualize the rapidly changing conductivity associated with neural activation.

5. Conclusion

We have visualized the internal current density using a fast ICNE-multi-echo MR pulse sequence based on a gradient echo by two measurements in the interleaved acquisition. The interleaved acquisition method in MREIT is a conventional method to suppress the background field inhomogeneity phase artifact and to increase the SNR of B_z by doubling the accumulated phase signal. We used the multi-echo pulse sequence, which acquires multiple sampling points within each repetition time. The proposed method directly measures the Laplacian of B_z from the measured k -space data, which can avoid a tedious unwrapping procedure and include a denoising effect by removing a part of the measured noise. We determined an optimal combination of the magnetic flux densities from the multi-echo in order to reduce the noise level. Using the optimization of $\nabla^2 B_z$, the proposed method visualized the internal current density using the relationships between the induced internal current and the measured $\nabla^2 B_z$ data, while suppressing the background field inhomogeneity. A real phantom experiment with a saline solution including a balloon was carried out to verify that the proposed method can be feasibly applied in real experiments. The total scan time in the phantom experiment was less than 13 seconds to visualize the current density with a 128×128 spacial matrix size.

Acknowledgment

This paper was supported by Basic Science Research Program through the National Research Foundation of Korea (NRF) funded by the Ministry of Education, Science and Technology (2010-0022398, 2012R1A1A2009509).

References

- [1] Y. Z. Ider and O. Birgul, "Use of the magnetic field generated by the internal distribution of injected currents for Electrical Impedance Tomography (MR-EIT)," *Elektrik*, vol. 6, no. 3, pp. 215–225, 1998.
- [2] O. I. Kwon, E. J. Woo, J. R. Yoon, and J. K. Seo, "Magnetic resonance electrical impedance tomography (MREIT): simulation study of J-substitution algorithm," *IEEE Transactions on Biomedical Engineering*, vol. 49, no. 2, pp. 160–167, 2002.
- [3] Y. Z. Ider, S. Onart, and W. R. B. Lionheart, "Uniqueness and reconstruction in magnetic resonance-electrical impedance tomography (MR-EIT)," *Physiological Measurement*, vol. 24, no. 2, pp. 591–604, 2003.
- [4] O. Birgul, B. M. Eyuboglu, and Y. Z. Ider, "Current constrained voltage scaled reconstruction (CCVSR) algorithm for MR-EIT and its performance with different probing current patterns," *Physics in Medicine and Biology*, vol. 48, no. 5, pp. 653–671, 2003.
- [5] S. H. Oh, B. I. Lee, E. J. Woo et al., "Conductivity and current density image reconstruction using harmonic B_z algorithm in magnetic resonance electrical impedance tomography," *Physics in Medicine and Biology*, vol. 48, no. 19, pp. 3101–3116, 2003.
- [6] J. K. Seo, J. R. Yoon, E. J. Woo, and O. I. Kwon, "Reconstruction of conductivity and current density images using only one component of magnetic field measurements," *IEEE Transactions on Biomedical Engineering*, vol. 50, no. 9, pp. 1121–1124, 2003.
- [7] M. L. G. Joy, "MR current density and conductivity imaging: the state of the art Proc," in *Proceedings of the 26th Annual International Conference of the IEEE Engineering in Medicine and Biology Society (EMBS '04)*, pp. 5315–5319, San Francisco, Calif, USA, 2004.
- [8] L. T. Muftuler, M. Hamamura, O. Birgul, and O. Nalcioglu, "Resolution and contrast in magnetic resonance electrical impedance tomography (MREIT) and its application to cancer imaging," *Technology in Cancer Research and Treatment*, vol. 3, no. 6, pp. 599–609, 2004.
- [9] M. Ozdemir, B. M. Eyuboglu, and O. Ozbek, "Equipotential projection-based magnetic resonance electrical impedance tomography and experimental realization," *Physics in Medicine and Biology*, vol. 49, no. 20, pp. 4765–4783, 2004.
- [10] C. Park, O. Kwon, E. J. Woo, and J. K. Seo, "Electrical conductivity imaging using gradient B_z decomposition algorithm in Magnetic Resonance Electrical Impedance Tomography (MREIT)," *IEEE Transactions on Medical Imaging*, vol. 23, no. 3, pp. 388–394, 2004.
- [11] J. K. Seo, H. C. Pyo, C. J. Park, O. I. Kwon, and E. J. Woo, "Image reconstruction of anisotropic conductivity tensor distribution in MREIT: computer simulation study," *Physics in Medicine and Biology*, vol. 49, no. 18, pp. 4371–4382, 2004.
- [12] S. H. Oh, B. I. Lee, E. J. Woo et al., "Electrical conductivity images of biological tissue phantoms in MREIT," *Physiological Measurement*, vol. 26, no. 2, pp. S279–S288, 2005.
- [13] N. Gao, S. A. Zhu, and B. A. He, "A new magnetic resonance electrical impedance tomography (MREIT) algorithm: the RSM-MREIT algorithm with applications to estimation of human head conductivity," *Physics in Medicine and Biology*, vol. 51, no. 12, pp. 3067–3083, 2006.
- [14] O. Birgul, M. J. Hamamura, L. T. Muftuler, and O. Nalcioglu, "Contrast and spatial resolution in MREIT using low amplitude current," *Physics in Medicine and Biology*, vol. 51, no. 19, pp. 5035–5049, 2006.
- [15] M. J. Hamamura, L. Tugan Muftuler, O. Birgul, and O. Nalcioglu, "Measurement of ion diffusion using magnetic resonance electrical impedance tomography," *Physics in Medicine and Biology*, vol. 51, no. 11, pp. 2753–2762, 2006.
- [16] M. J. Hamamura and L. T. Muftuler, "Fast imaging for magnetic resonance electrical impedance tomography," *Magnetic Resonance Imaging*, vol. 26, no. 6, pp. 739–745, 2008.
- [17] E. J. Woo and J. K. Seo, "Magnetic resonance electrical impedance tomography (MREIT) for high-resolution conductivity imaging," *Physiological Measurement*, vol. 29, no. 10, pp. R1–R26, 2008.

- [18] H. J. Kim, Y. T. Kim, A. S. Minhas et al., "In vivo high-resolution conductivity imaging of the human leg using MREIT: the first human experiment," *IEEE Transactions on Medical Imaging*, vol. 28, no. 11, pp. 1681–1687, 2009.
- [19] H. J. Kim, T. I. Oh, Y. T. Kim et al., "In vivo electrical conductivity imaging of a canine brain using a 3 T MREIT system," *Physiological Measurement*, vol. 29, no. 10, pp. 1145–1155, 2008.
- [20] C. Park, B. I. Lee, O. I. Kwon, and E. J. Woo, "Measurement of induced magnetic flux density using injection current nonlinear encoding (ICNE) in MREIT," *Physiological Measurement*, vol. 28, no. 2, pp. 117–127, 2007.
- [21] H. S. Nam and O. I. Kwon, "Optimization of multiply acquired magnetic flux density B_z using ICNE-Multiecho train in MREIT," *Physics in Medicine and Biology*, vol. 55, no. 9, pp. 2743–2759, 2010.
- [22] H. M. Park, H. S. Nam, and O. I. Kwon, "Magnetic flux density reconstruction using interleaved partial Fourier acquisitions in MREIT," *Physics in Medicine and Biology*, vol. 56, no. 7, pp. 2059–2073, 2011.
- [23] P. A. Bandettini, E. C. Wong, R. S. Hinks, R. S. Tikofsky, and J. S. Hyde, "Time course EPI of human brain function during task activation," *Magnetic Resonance in Medicine*, vol. 25, no. 2, pp. 390–397, 1992.
- [24] R. B. Buxton, E. C. Wong, and L. R. Frank, "Dynamics of blood flow and oxygenation changes during brain activation: the balloon model," *Magnetic Resonance in Medicine*, vol. 39, no. 6, pp. 855–864, 1998.
- [25] N. K. Logothetis, "What we can do and what we cannot do with fMRI," *Nature*, vol. 453, no. 7197, pp. 869–878, 2008.
- [26] R. J. Sadleir, S. C. Grant, and E. J. Woo, "Can high-field MREIT be used to directly detect neural activity? Theoretical considerations," *NeuroImage*, vol. 52, no. 1, pp. 205–216, 2010.
- [27] C. Park, B. I. Lee, and O. I. Kwon, "Analysis of recoverable current from one component of magnetic flux density in MREIT and MRCDI," *Physics in Medicine and Biology*, vol. 52, no. 11, pp. 3001–3013, 2007.
- [28] G. C. Scott, M. L. G. Joy, R. L. Armstrong, and R. M. Henkelman, "Sensitivity of magnetic-resonance current-density imaging," *Journal of Magnetic Resonance*, vol. 97, no. 2, pp. 235–254, 1992.
- [29] R. J. Sadleir, S. C. Grant, and E. J. Woo, "Can high-field MREIT be used to directly detect neural activity? Theoretical considerations," *NeuroImage*, vol. 52, no. 1, pp. 205–216, 2005.
- [30] O. I. Kwon, B. I. Lee, H. S. Nam, and C. Park, "Noise analysis and MR pulse sequence optimization in MREIT using an injected current nonlinear encoding (ICNE) method," *Physiological Measurement*, vol. 28, no. 11, pp. 1391–1404, 2007.
- [31] G. C. Scott, M. L. G. Joy, R. L. Armstrong, and R. M. Henkelman, "Measurement of nonuniform current density by magnetic resonance," *IEEE Transactions on Medical Imaging*, vol. 10, no. 3, pp. 362–374, 1991.
- [32] L. T. Muftuler, G. Chen, M. J. Hamamura, and S. H. Ha, "MREIT with SENSE acceleration using a dedicated RF coil design," *Physiological Measurement*, vol. 30, no. 9, pp. 913–929, 2009.

Research Article

Robust Myocardial Motion Tracking for Echocardiography: Variational Framework Integrating Local-to-Global Deformation

Chi Young Ahn

Department of Computational Science and Engineering, Yonsei University, Seoul 120-749, Republic of Korea

Correspondence should be addressed to Chi Young Ahn; chiyoung@yonsei.ac.kr

Received 30 October 2012; Accepted 28 January 2013

Academic Editor: Jin Keun Seo

Copyright © 2013 Chi Young Ahn. This is an open access article distributed under the Creative Commons Attribution License, which permits unrestricted use, distribution, and reproduction in any medium, provided the original work is properly cited.

This paper proposes a robust real-time myocardial border tracking algorithm for echocardiography. Commonly, after an initial contour of LV border is traced at one or two frames from the entire cardiac cycle, LV contour tracking is performed over the remaining frames. Among a variety of tracking techniques, optical flow method is the most widely used for motion estimation of moving objects. However, when echocardiography data is heavily corrupted in some local regions, the errors bring the tracking point out of the endocardial border, resulting in distorted LV contours. This shape distortion often occurs in practice since the data acquisition is affected by ultrasound artifacts, dropouts, or shadowing phenomena of cardiac walls. The proposed method is designed to deal with this shape distortion problem by integrating local optical flow motion and global deformation into a variational framework. The proposed descent method controls the individual tracking points to follow the local motions of a specific speckle pattern, while their overall motions are confined to the global motion constraint being approximately an affine transform of the initial tracking points. Many real experiments show that the proposed method achieves better overall performance than conventional methods.

1. Introduction

In company with the development of real-time three-dimensional echocardiography (RT3DE), the demands for automated analysis methods of left ventricle (LV) assessment such as ejection fraction, motion analysis, and strain analysis are rapidly increasing. Nevertheless, most of the analysis methods are still based on the measurements in a few two-dimensional (2D) slices, because they are available in clinical practice [1, 2]. In general, the quantitative assessment for heart function is performed by manually tracing endocardial border in some 2D slices of different view at frames (such as end-systole (ES) or end-diastole (ED) frames) selected from the entire cardiac cycle and automatically tracking the traced LV contour over the remaining frames [3, 4]. The motion tracking of LV is carried out by observing the speckle pattern associated with deforming tissue. Speckle pattern is an inherent appearance in ultrasound imaging and its local brightness reflects the local echogeneity of the underlying scatterers. Since it is a difficult task to automatically track the motion of

endocardial border in ultrasound images due to ultrasound artifacts, dropouts or shadowing phenomena, low contrast, and so on, user intervention is somewhat required for stable and successful tracking of endocardial border.

In the last decades, there have been numerous studies for tracking of LV wall motion such as the tracking methods using deformable models [5–8], active shape models [9–11], and optical flow methods [2, 12–15]. Those methods have some limitations to practical application of endocardial border motion tracking. In deformable models, their methods are relatively time consuming due to iterative contour evolution with stopping criteria and often need preprocessing for speckle reduction before wall motion tracking. Active shape models are the statistical methods based on the dataset of trained images so that they require additional effort to train on many images. Both deformable models and active shape models provide the motion information of LV border and enable user to measure the volume inside LV, whereas they are somewhat inadequate for strain analysis related to the motion and deformation of heart, because they are not speckle

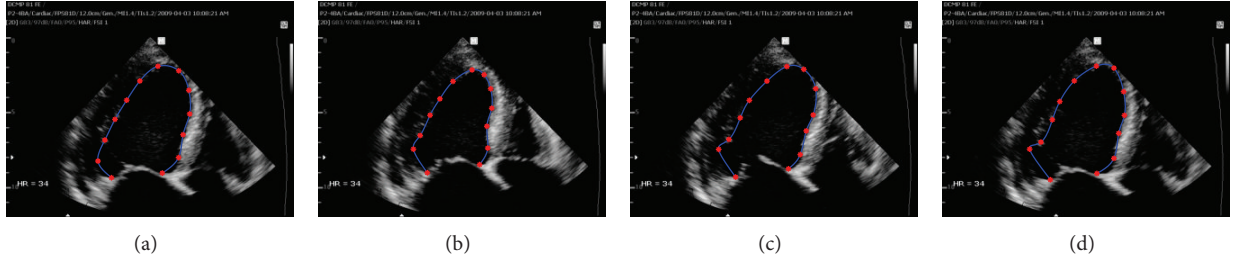


FIGURE 1: The estimation of endocardial border by the Lucas-Kanade optical flow method. Case 1: a tracking point getting out from the real LV shape distorts the whole shape near the border with weak edges; (a) initially traced endocardial border and its tracking points at an ED frame, (b) the tracked result at the ES frame, (c) at the frame between ES and ED, and (d) at the next ED frame.

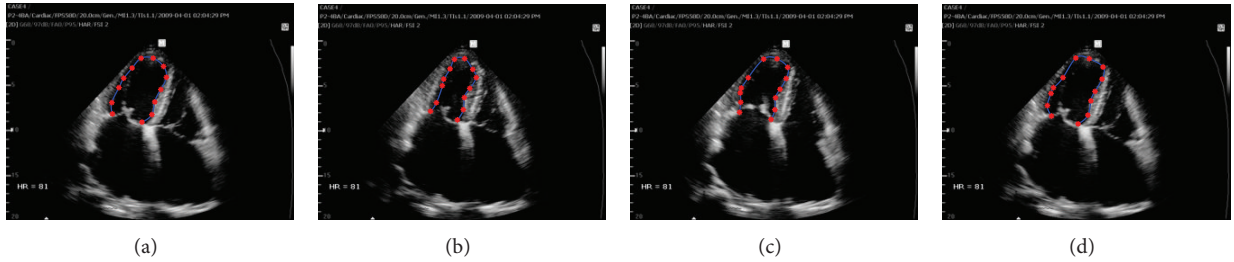


FIGURE 2: The estimation of endocardial border by the Lucas-Kanade optical flow method. Case 2: the tracked points are irregularly spaced by indistinguishable speckle patterns; (a) initially traced endocardial border and its tracking points at an ED frame, (b) the tracked result at the ES frame, (c) at the frame between ES and ED, and (d) at the next ED frame.

tracking-based methods providing motion information of local region on the myocardium but shape-based tracking methods.

On the other hand, optical flow methods, which use the assumption that the intensity of a moving object is constant over time, provide the local motion information of myocardium. They are capable of measuring the LV volume as well as the myocardial wall motion analysis or strain analysis to detect LV abnormalities. After an initial contour of endocardial border is traced, each point on the contour tracks the specific intensity and speckle pattern in sequential images. However, it is problematic to track the endocardial border in ultrasound images with unclear speckle pattern or weak signals. In practical environment, there often exist some incorrectly tracked points due to ultrasound artifacts, dropouts, or shadowing phenomena of cardiac wall [16]. When edge dropout or indistinguishable speckle pattern is present in a local neighborhood of a tracking point, the errors bring the tracking point out of the endocardial border, resulting in distorted LV contours throughout the entire cardiac cycle as shown in Figure 1 or irregular distances between the tracked points in Figure 2. These distorted results affect LV volume measurement or strain analysis.

In order to cope with these problems, we develop a new optical flow method equipped with a global motion constraint that is designed to prevent each tracking point from getting out of the endocardial border. In the proposed model, the Lucas-Kanade (LK) optical flow method [17] and a global motion constraint being approximately an affine transformation of the initial tracking points are incorporated into a variational framework. So the individual tracking points follow speckle patterns (corresponding to each tracking point)

and their overall motions are confined to the global motion constraint. The global motion constraint is based on the results [18, 19] that heart motion is regarded as the non-rigid motion by rotation, contraction/expansion, and shear. Typically, nonrigid motion consists of global deformation and local deformation. The global deformation is modeled by an affine transformation while the local deformation is described by a free-form deformation.

The proposed algorithm is capable of tracking LV border in real-time since its movement is directly computed from the difference between two sequential images via a simple matrix multiplication. For performance evaluation, we carry out various real experiments with Samsung Medison R&D Center (<http://www.samsungmedison.com/>). Numerous experiments show better performance of the proposed tracking methods compared to the conventional tracking methods.

2. Methods

2.1. Conventional Optical Flow Tracking Methods. Let $I(\mathbf{r}, t)$ represent the intensity of echocardiography at the location $\mathbf{r} = (x, y)$ and the time t . Optical flow tracking methods are based on the assumption that the intensity of a moving object is constant over time, so that the noisy time-varying images $I(\mathbf{r}, t)$ approximately satisfy

$$\mathbf{u}(\mathbf{r}, t) \cdot \nabla I(\mathbf{r}, t) + \frac{\partial}{\partial t} I(\mathbf{r}, t) \approx 0, \quad (1)$$

where $\mathbf{u}(\mathbf{r}, t)$ is the velocity vector to be estimated. Based on (1), numerous approaches for estimating the velocity vector $\mathbf{u}(\mathbf{r}, t)$ have been proposed and those were applied to LV border tracking in echocardiography [2, 13–15].

Horn and Schunk [20] proposed the optical flow technique incorporating the smoothness of the motion vector in the entire image as a global constraint. In their model, the velocity $\mathbf{u}(\mathbf{r}, t)$ at each time t is determined by minimizing the energy functional:

$$E_t(\mathbf{u}) := \int_{\Omega} \left(\mathbf{u}(\mathbf{r}) \cdot \nabla I(\mathbf{r}, t) + \frac{\partial}{\partial t} I(\mathbf{r}, t) \right)^2 + \lambda |\nabla \mathbf{u}(\mathbf{r})|^2 d\mathbf{r}, \quad (2)$$

where Ω is the image domain and λ a regularization parameter which controls the balance between the optical flow term and the smoothness on \mathbf{u} . The velocity $\mathbf{u}(\mathbf{r}, t)$ at each time t can be computed by solving the corresponding Euler-Lagrange equation that is a reaction-diffusion equation. In [21], it has been observed that this global method with the global smoothness constraint is significantly more sensitive to noise than the local method used by Lucas and Kanade [17].

Lucas and Kanade [17] used the assumption of locally constant motion to compute the velocity $\mathbf{u}(\mathbf{r}_0, t)$ at a target location $\mathbf{r}_0 = (x_0, y_0)$ and time t by forcing constant velocity in a local neighborhood of a point $\mathbf{r}_0 = (x_0, y_0)$, denoted by $\mathcal{N}(\mathbf{r}_0)$. Following Lucas and Kanade, Barron et al. [21] estimated the velocity $\mathbf{u}(\mathbf{r}_0, t)$ by minimizing the weighted least square criterion in the neighborhood $\mathcal{N}(\mathbf{r}_0)$:

$$\mathbf{u}(\mathbf{r}_0, t) := \arg \min_{\mathbf{u}} \int_{\mathcal{N}(\mathbf{r}_0)} \left[w(\mathbf{r} - \mathbf{r}_0) \left(\mathbf{u} \cdot \nabla I(\mathbf{r}, t) + \frac{\partial}{\partial t} I(\mathbf{r}, t) \right) \right]^2 d\mathbf{r}, \quad (3)$$

where w is a weight function that enables to give more relevance to central terms rather than the ones in the periphery. Here, ‘‘arg min’’ stands for the argument of the minimum, that is, the vector \mathbf{u} for which the right integral attains its minimum value. Since this method determines $\mathbf{u}(\mathbf{r}_0, t)$ at each location \mathbf{r}_0 by combining information from all pixels in the neighborhood of \mathbf{r}_0 , it is reasonably robust against image noise. We used (3) as the Lucas-Kanade method, because this weighted window LK method is essentially same as the LK method. When the weight function w is uniform, the form is the same as the Lucas and Kanade one, in fact.

As we mentioned in Section 1, there often exist some incorrectly tracked points due to weak signal on cardiac wall since echocardiography data is acquired through transmitting and receiving ultrasound signals between the ribs, causing considerable shadowing of cardiac wall [16]. Due to these incorrectly tracked points, LK method may produce significantly distorted LV shape.

Recently, Sühling et al. [13] improved the weighted window LK method (3) by introducing a linear model for the velocity along the time direction, and the displacement

$\mathbf{u}(\mathbf{r}_0, t)$ is obtained by evaluating \mathbf{u} such that $\mathbf{u}, \mathbf{b} \in \mathbb{R}^2$ and 2×2 matrix A minimize the following energy functional:

$$E_t(\mathbf{u}, A, \mathbf{b}) := \int_{-\infty}^{\infty} \int_{\mathbb{R}^2} \left[w(\mathbf{r} - \mathbf{r}_0, s) \left(\begin{array}{c} (\mathbf{u} + A(\mathbf{r} - \mathbf{r}_0) + \mathbf{s}\mathbf{b}) \cdot \nabla I(\mathbf{r}, t + s) \\ + \frac{\partial}{\partial t} I(\mathbf{r}, t + s) \end{array} \right) \right]^2 d\mathbf{r} ds, \quad (4)$$

where w is the symmetric window function, which gives more weight to constraints at the center of the local spatiotemporal region than to those at the periphery. Since this method uses multiple frames centering around the time t , it is more robust than the LK method (3) using the single frame at t . However, the same problem of LV shape distortion as in LK method still remains.

Compared with the approaches based on the LK method, Duan et al. [15] used the region-based tracking method (also known as the block matching or pattern matching method) with the cross-correlation coefficients as a similarity measure. For given two consecutive images I at time t and $t + \Delta t$, the velocity vector $\mathbf{u} = (u, v)$ for each pixel $\mathbf{r} = (x, y) \in \Omega$ is estimated by maximizing the cross-correlation coefficients:

$$\mathbf{u}(\mathbf{r}_0, t) := \arg \max_{\mathbf{u}} \left\{ \frac{\int_{\mathcal{N}(\mathbf{r}_0)} [I(\mathbf{r}, t) I(\mathbf{r} + \mathbf{u}, t + \Delta t)] d\mathbf{r}}{\sqrt{\int_{\mathcal{N}(\mathbf{r}_0)} [I(\mathbf{r}, t)]^2 d\mathbf{r}} \sqrt{\int_{\mathcal{N}(\mathbf{r}_0)} [I(\mathbf{r} + \mathbf{u}, t + \Delta t)]^2 d\mathbf{r}}} \right\}. \quad (5)$$

Instead of maximizing the cross-correlation coefficients, the velocity vector can be estimated by minimizing the sum-of-squared difference (SSD) [21] as follows:

$$\mathbf{u}(\mathbf{r}_0, t) := \arg \min_{\mathbf{u}} \int_{\mathcal{N}(\mathbf{r}_0)} w(\mathbf{r} - \mathbf{r}_0) [I(\mathbf{r}, t) - I(\mathbf{r} + \mathbf{u}, t + \Delta t)]^2 d\mathbf{r}. \quad (6)$$

The block matching method uses similarity measures that are less sensitive to noise, of fast motion, and of potential occlusions and discontinuities [15].

The above three local methods have drawback in dealing with the problem of the contour shape distortion in the presence of locally weak signal corrupted by rib shadowing and other factors. Hence, we need to develop a method alleviating shape distortion.

2.2. Proposed Method. The proposed method uses an affine transformation to describe a global motion that is synthesized by integrating local deformations. We denote the endocardial border traced at initially selected frame (e.g., end-systole or

end-diastole frame) by a parametric contour $\mathcal{C}^* = \{\mathbf{r}^*(s) = (x^*(s), y^*(s)) \mid 0 \leq s \leq 1\}$ that can be identified as its n tracking points $\mathbf{r}_1^* = \mathbf{r}^*(s_1), \dots, \mathbf{r}_n^* = \mathbf{r}^*(s_n)$. Here, $0 = s_1 < s_2 < \dots < s_n = 1$. Let $\mathcal{C}(t) = \{\mathbf{r}(s, t) = (x(s, t), y(s, t)) \mid 0 \leq s \leq 1\}$ be the contour deformed from $\mathcal{C}(0) = \mathcal{C}^*$ at time t . The motion of the contour $\mathcal{C}(t)$ will be determined by an appropriately chosen velocity $\mathbf{U}(t)$ indicating a time change of tracking points $(\mathbf{r}_1(t), \dots, \mathbf{r}_n(t))$:

$$\mathbf{U}(t) := \begin{bmatrix} \mathbf{u}_1(t) \\ \vdots \\ \mathbf{u}_n(t) \end{bmatrix} = \frac{d}{dt} \begin{bmatrix} \mathbf{r}_1(t) \\ \vdots \\ \mathbf{r}_n(t) \end{bmatrix} \quad \text{with} \quad \begin{bmatrix} \mathbf{r}_1(0) \\ \vdots \\ \mathbf{r}_n(0) \end{bmatrix} = \begin{bmatrix} \mathbf{r}_1^* \\ \vdots \\ \mathbf{r}_n^* \end{bmatrix}. \quad (7)$$

Here, we identify the contour $\mathcal{C}(t)$ with tracking points $(\mathbf{r}_1(t), \dots, \mathbf{r}_n(t))$.

In our method, $\mathbf{U}(t)$ for each time t is a minimizer of the following energy functional reflecting local-to-global deformation:

$$\begin{aligned} \mathcal{E}_t(\mathbf{U}) &:= \frac{1}{2} \sum_{i=1}^n \left[\int_{\mathcal{N}(\mathbf{r}_i(t))} w(\mathbf{r}' - \mathbf{r}_i(t)) \left\{ \mathbf{u}_i \cdot \nabla I(\mathbf{r}', t) + \frac{\partial}{\partial t} I(\mathbf{r}', t) \right\}^2 d\mathbf{r}' \right. \\ &\quad \left. + \lambda \left| \mathbf{r}_i(t) + \mathbf{u}_i - \begin{bmatrix} a_1(\mathbf{U}) & a_2(\mathbf{U}) \\ a_3(\mathbf{U}) & a_4(\mathbf{U}) \end{bmatrix} \mathbf{r}_i^* - \begin{bmatrix} a_5(\mathbf{U}) \\ a_6(\mathbf{U}) \end{bmatrix} \right|^2 \right], \end{aligned} \quad (8)$$

where λ is a nonnegative parameter, w is the weight function as used in the LK method, and the affine coefficients $a_1(\mathbf{U}), \dots, a_6(\mathbf{U})$ at time t are given by

$$\begin{bmatrix} a_1(\mathbf{U}) & a_3(\mathbf{U}) \\ a_2(\mathbf{U}) & a_4(\mathbf{U}) \\ a_5(\mathbf{U}) & a_6(\mathbf{U}) \end{bmatrix} = \left(\Phi(\mathcal{C}^*)^T \Phi(\mathcal{C}^*) \right)^{-1} \Phi(\mathcal{C}^*)^T \times \begin{bmatrix} (\mathbf{r}_1(t) + \mathbf{u}_1)^T \\ \vdots \\ (\mathbf{r}_n(t) + \mathbf{u}_n)^T \end{bmatrix}, \quad (9)$$

where

$$\Phi(\mathcal{C}^*) := \begin{bmatrix} \mathbf{r}_1^{*T} & 1 \\ \vdots & \vdots \\ \mathbf{r}_n^{*T} & 1 \end{bmatrix}. \quad (10)$$

The first term in (8) controls the individual tracking points to follow the local motions of a specific speckle pattern, while the second term controls their overall motions to be confined to the global motion constraint being approximately an affine transform of the initial tracking points.

The first term in (8) reflects the well-known LK optical flow (3) that probes local motions using blood-to-tissue intensity ratio.

The second term concerns a misfit between the estimated tracking points and their projection onto the space \mathcal{W} , the space of affine transforms of the initial tracking points, given by

$$\mathcal{W} = \left\{ \begin{bmatrix} \mathbf{r}_1^{*T} & 1 \\ \vdots & \vdots \\ \mathbf{r}_n^{*T} & 1 \end{bmatrix} \begin{bmatrix} a_1 & a_3 \\ a_2 & a_4 \\ a_5 & a_6 \end{bmatrix} : a_1, \dots, a_6 \in \mathbb{R} \right\} \subset \mathbb{R}^{n \times 2}. \quad (11)$$

To be precise, a careful computation yields

$$\begin{aligned} &\text{the projection of } \begin{bmatrix} (\mathbf{r}_1(t) + \mathbf{u}_1)^T \\ \vdots \\ (\mathbf{r}_n(t) + \mathbf{u}_n)^T \end{bmatrix} \text{ onto } \mathcal{W} \\ &= \Phi(\mathcal{C}^*) \left(\Phi(\mathcal{C}^*)^T \Phi(\mathcal{C}^*) \right)^{-1} \Phi(\mathcal{C}^*)^T \begin{bmatrix} (\mathbf{r}_1(t) + \mathbf{u}_1)^T \\ \vdots \\ (\mathbf{r}_n(t) + \mathbf{u}_n)^T \end{bmatrix} \\ &= \begin{bmatrix} \mathbf{r}_1^{*T} & 1 \\ \vdots & \vdots \\ \mathbf{r}_n^{*T} & 1 \end{bmatrix} \begin{bmatrix} a_1(\mathbf{U}) & a_3(\mathbf{U}) \\ a_2(\mathbf{U}) & a_4(\mathbf{U}) \\ a_5(\mathbf{U}) & a_6(\mathbf{U}) \end{bmatrix}. \end{aligned} \quad (12)$$

Hence, the second term in (8) with the above identity reflects a global motion involving contraction, expansion, translation, and rotation.

To compute the minimizer \mathbf{U} of the energy functional (8), we need to derive the Euler-Lagrange equation which can be obtained by taking partial derivative of \mathcal{E}_t with respect to each \mathbf{u}_j :

$$\begin{aligned} \mathbf{0} &= \frac{\partial \mathcal{E}_t}{\partial \mathbf{u}_j} \\ &= \int_{\mathcal{N}(\mathbf{r}_j(t))} w(\mathbf{r} - \mathbf{r}_j(t)) \nabla I(\mathbf{r}, t) \\ &\quad \times \left\{ \mathbf{u}_j \cdot \nabla I(\mathbf{r}, t) + \frac{\partial}{\partial t} I(\mathbf{r}, t) \right\} d\mathbf{r} \\ &\quad + \lambda \left\{ \mathbf{r}_j(t) + \mathbf{u}_j - \sum_{i=1}^n d(i, j) (\mathbf{r}_i(t) + \mathbf{u}_i) \right\}, \end{aligned} \quad (13)$$

for $j = 1, \dots, n$,

where $d(i, j)$ is the (i, j) -component of the $n \times n$ matrix

$$\mathcal{D}(\mathcal{C}^*) := \Phi(\mathcal{C}^*) \left(\Phi(\mathcal{C}^*)^T \Phi(\mathcal{C}^*) \right)^{-1} \Phi(\mathcal{C}^*)^T. \quad (14)$$

The derivation of the Euler-Lagrange equation is given in the appendix.

For numerical algorithm, we replace the integral over $\mathcal{N}(\mathbf{r}_j(t))$ in (13) by summation over pixels around $\mathbf{r}_j(t)$.

Assuming that the neighborhood $\mathcal{N}(\mathbf{r}_j(t))$ consists of m pixels $\mathbf{r}_{j1}, \dots, \mathbf{r}_{jm}$, (13) becomes

$$\mathbf{0} = A_j^T W_j A_j \mathbf{u}_j + A_j^T W_j \mathbf{b}_j + \lambda \times \left\{ \mathbf{r}_j(t) + \mathbf{u}_j - \sum_{i=1}^n d(i, j) (\mathbf{r}_i(t) + \mathbf{u}_i) \right\}, \quad (15)$$

where $A_j = [\nabla I(\mathbf{r}_{j1}, t), \dots, \nabla I(\mathbf{r}_{jm}, t)]^T$, $W_j = \text{diag}(w(\mathbf{r}_{j1} - \mathbf{r}_j(t)), \dots, w(\mathbf{r}_{jm} - \mathbf{r}_j(t)))$, and $\mathbf{b}_j = [(\partial/\partial t)I(\mathbf{r}_{j1}, t), \dots, (\partial/\partial t)I(\mathbf{r}_{jm}, t)]^T$.

For notational simplicity, let the time t be fixed and let

$$\mathbf{u}_j := \begin{bmatrix} u_j \\ v_j \end{bmatrix}, \quad \mathbf{r}_j(t) = \begin{bmatrix} x_j \\ y_j \end{bmatrix},$$

$$\begin{bmatrix} \alpha_j & \beta_j \\ \beta_j & \gamma_j \end{bmatrix} := A_j^T W_j A_j + \lambda I, \quad \begin{bmatrix} \xi_j \\ \eta_j \end{bmatrix} = A_j^T W_j \mathbf{b}_j + \lambda \mathbf{r}_j(t). \quad (16)$$

Then, the system (15) can also be represented by

$$0 = \alpha_j u_j + \beta_j v_j - \lambda \sum_{i=1}^n d(i, j) u_i + \xi_j - \lambda \sum_{i=1}^n d(i, j) x_i, \quad (17)$$

$$0 = \beta_j u_j + \gamma_j v_j - \lambda \sum_{i=1}^n d(i, j) v_i + \eta_j - \lambda \sum_{i=1}^n d(i, j) y_i.$$

This can be concisely written by

$$(\Lambda - \lambda \mathcal{P}(\mathcal{E}^*))U + BV = -\Xi + \lambda \mathcal{P}(\mathcal{E}^*)X, \quad (18)$$

$$BU + (\Gamma - \lambda \mathcal{P}(\mathcal{E}^*))V = -\Pi + \lambda \mathcal{P}(\mathcal{E}^*)Y,$$

where $\Lambda = \text{diag}(\alpha_1, \dots, \alpha_n)$, $B = \text{diag}(\beta_1, \dots, \beta_n)$, $\Gamma = \text{diag}(\gamma_1, \dots, \gamma_n)$, $U = [u_1, \dots, u_n]^T$, $V = [v_1, \dots, v_n]^T$, $\Xi = [\xi_1, \dots, \xi_n]^T$, $\Pi = [\eta_1, \dots, \eta_n]^T$, $X = [x_1, \dots, x_n]^T$, and $Y = [y_1, \dots, y_n]^T$. Using the block matrix form, we can rewrite it as the system of linear equations:

$$\begin{bmatrix} (\Lambda - \lambda \mathcal{P}(\mathcal{E}^*)) & B \\ B & (\Gamma - \lambda \mathcal{P}(\mathcal{E}^*)) \end{bmatrix} \begin{bmatrix} U \\ V \end{bmatrix} = \begin{bmatrix} -\Xi + \lambda \mathcal{P}(\mathcal{E}^*)X \\ -\Pi + \lambda \mathcal{P}(\mathcal{E}^*)Y \end{bmatrix}. \quad (19)$$

Therefore, we can directly compute the movement $\mathbf{U} = [U \ V]$ of size $n \times 2$ from the formula:

$$\begin{bmatrix} U \\ V \end{bmatrix} = \begin{bmatrix} (\Lambda - \lambda \mathcal{P}(\mathcal{E}^*)) & B \\ B & (\Gamma - \lambda \mathcal{P}(\mathcal{E}^*)) \end{bmatrix}^{-1} \begin{bmatrix} -\Xi + \lambda \mathcal{P}(\mathcal{E}^*)X \\ -\Pi + \lambda \mathcal{P}(\mathcal{E}^*)Y \end{bmatrix}, \quad (20)$$

because the column vectors of the block matrix $\begin{bmatrix} (\Lambda - \lambda \mathcal{P}(\mathcal{E}^*)) & B \\ B & (\Gamma - \lambda \mathcal{P}(\mathcal{E}^*)) \end{bmatrix}$ of size $2n \times 2n$ are linearly independent.

For the parameter $\lambda = 0$, the displacements \mathbf{u}_j ($j \in \{1, \dots, n\}$) by (15) are exactly the same as those by the LK optical flow. However, (20) has a distinction to be capable of controlling the global shape in that the bigger the parameter λ is, the stronger the shape constraint is imposed. The LK optical flow performs a role as the local deformation subject to the global shape constraint, which is represented by the relationship of all n tracking points. Therefore, each point efficiently tracks maintaining the global deformation of initial LV contour.

2.3. Heuristic Choice of Parameter λ . For heuristic choice of parameter λ , we use various datasets of manually delineated LV borders by clinical experts. With manually defined data \mathbf{r}_j , \mathcal{E}^* , and $\mathbf{U}(t)$ in a given image I , we define the parameter $\tilde{\lambda}$ as a function of quantity \mathbf{r}_j , \mathcal{E}^* , $\mathbf{U}(t)$, I , and time t :

$$\tilde{\lambda} := \sqrt{\frac{\sum_{j=1}^n \|A_j^T W_j A_j \mathbf{u}_j(t) + A_j^T W_j \mathbf{b}_j\|_2^2}{\sum_{j=1}^n \|\mathbf{r}_j(t) + \mathbf{u}_j(t) - \sum_{i=1}^n d(i, j) (\mathbf{r}_i(t) + \mathbf{u}_i(t))\|_2^2}}. \quad (21)$$

We should note that if $\mathbf{u}_j(t)$ satisfies (15) for all t and $j = 1, \dots, n$, then $\tilde{\lambda} = \lambda$, the constant independent of time t .

From numerous experiments, we observed that $\tilde{\lambda}$ tends to depend mainly on the contrast of the image I , and its dependency on time t is relatively small. We found a linear relationship between $\log(I_{\text{tissue}}/I_{\text{blood}})$ and $\tilde{\lambda}$, where $I_{\text{tissue}}/I_{\text{blood}}$ is an overall tissue/blood intensity ratio.

To investigate behavior of the parameter $\tilde{\lambda}$, we generate synthetic speckle images consisting of tissue and blood regions and test them by changing conditions including tissue/blood contrast as shown in Figure 3. We use an apical long-axis view template shown in Figure 4(a). When the synthetic images are generated, it is assumed that speckle is fully developed so that the statistics of echo envelope follow the Rayleigh distribution ([22, 23]) and, by log-compression, the distribution of the intensities is changed into the Fisher-Tippett distribution ([24, 25])

$$f_\sigma(I) = \frac{2}{\alpha_1} \exp \left\{ \frac{2}{\alpha_1} (I - \alpha_2) - \ln(2\sigma^2) - \exp \left(\frac{2}{\alpha_1} (I - \alpha_2) - \ln(2\sigma^2) \right) \right\}, \quad (22)$$

where σ is the distribution parameter represented in Rayleigh distribution and α_1, α_2 are the predetermined system parameters for log-compression of echo envelope. Finally, the synthetic images are smoothed by low-pass filter (in Figures 4(b), 4(c), and 4(d), resp.).

For modeling of heart motion, we simulate a heart with the nonrigid motion integrating global and local deformations. Figure 5(a) illustrates the deformation of LV in four simulated images. LV contours are represented by 13 tracking



FIGURE 3: Image frames by varying tissue/blood intensity ratio. We use echographic texture modeling and heart motion modeling to generate image frames with various contrasts.

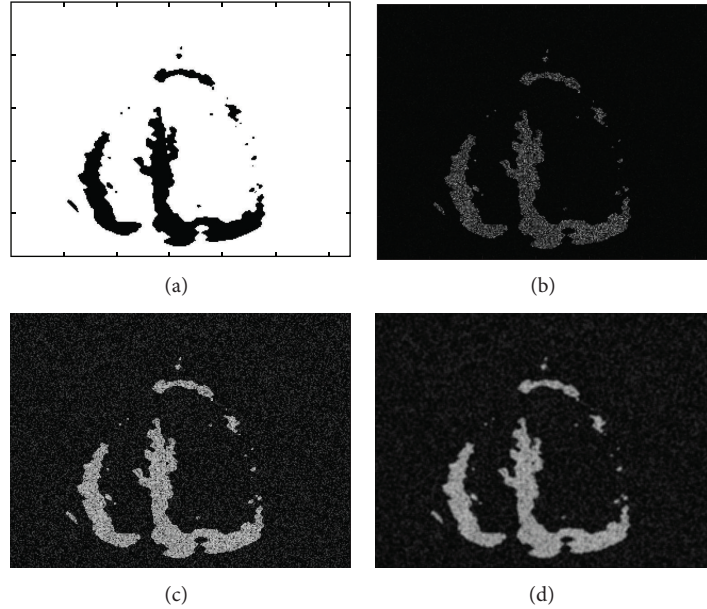


FIGURE 4: Synthetic images: (a) original LV template, (b) speckle image with Rayleigh distribution, (c) with Fisher-Tippett distribution, and (d) its smoothed image by a Gaussian filter.

points and a natural cubic spline connecting them, which are denoted by \mathbf{r}_i at each time. Their xy -coordinates and displacements \mathbf{u}_i from previous tracking points to next tracking points are listed in Table 1. For the sake of convenience in computation, it is assumed that the global deformation is modeled by an affine transformation of coefficients $a_1 = 0.92$, $a_2 = -0.03$, $a_3 = -0.01$, $a_4 = 0.89$, $a_5 = 20$, and $a_6 = 6$, which illustrate a contraction, and the local deformation is modeled by a free-form deformation of 0.1% variants with respect to the global deformation. In the first row of Figure 5(a), the blue solid lines and the red asterisks are showed as LV contour and tracking points by the defined heart motion, respectively. The green lines and asterisks mean LV contour at the previous frame. To generate the sequential images indicating the heart deformation, we also generate the tracking points of the epicardial contours so that the wall thickness between two contours is changed from 20 to 25 pixels in the sequential images. Using node points containing the endocardial and epicardial tracking points, the Delaunay triangulation meshes are generated and the sequential images are filled using linear spatial transformation from each mesh at previous image to the corresponding mesh at next image (second row).

We first test the dependency of $\tilde{\lambda}$ on the time t . For the given sequential synthetic images and tracking points at each time step, we compute $\tilde{\lambda}$ and plot the change of $\tilde{\lambda}$ with time t . The parameter $\tilde{\lambda}$ varies within the range of 250 to 350 as shown in Figure 5(b). Using $\lambda = 300$, the mean value of $\tilde{\lambda}$, we again compute (20) and get the displacements having the errors within 1 pixel compared to the reference displacements in Table 1(b). In this test, we use the 2-dimensional Gaussian function of variance $\sigma_x^2 = \sigma_y^2 = 5^2$ (pixel size) for the weight function w over the square neighborhood with side length 21 pixels. From this test, we observe that the dependency of $\tilde{\lambda}$ on the time t is negligibly small.

Next, we test the dependency of $\tilde{\lambda}$ on the tissue/blood intensity ratio. We generate the two consecutive images by varying the intensity of tissues as mentioned in Figure 3 and evaluate the change of $\tilde{\lambda}$ with respect to the tissue/blood intensity ratio. Figure 6 shows that the relationship between the image intensity contrast and $\log_{10}\tilde{\lambda}$ is approximately linear. This linear relationship enables us to provide a way of choosing the parameter λ depending on the tissue/blood intensity ratio effectively.

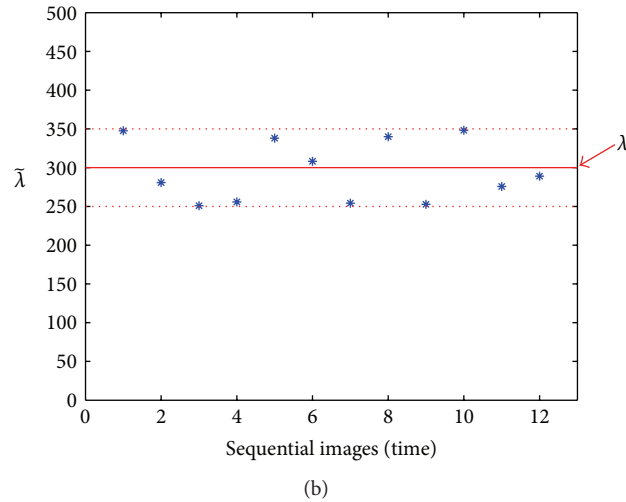
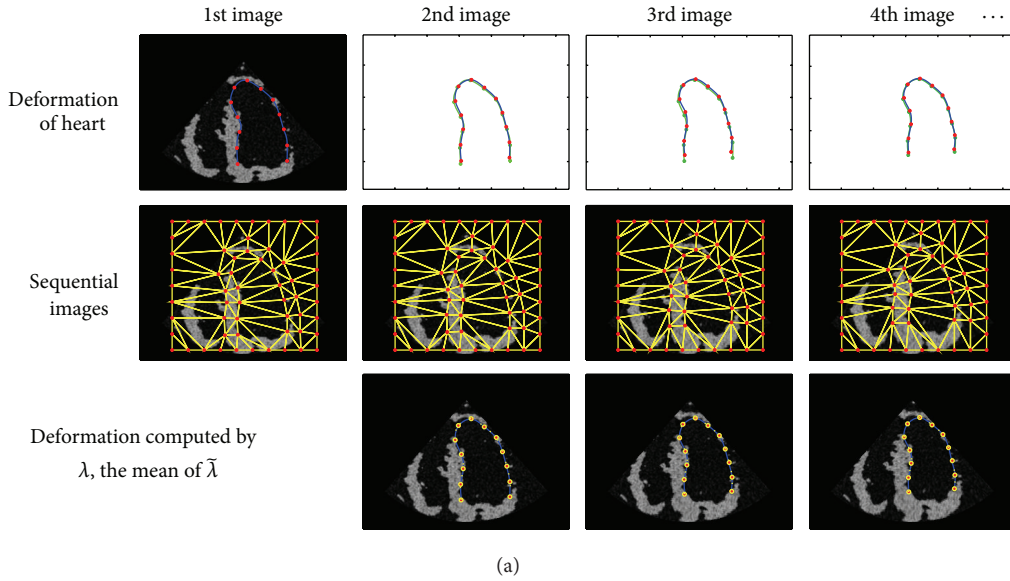


FIGURE 5: Result showing the independency of $\bar{\lambda}$ with time t : (a) sequential synthetic images for myocardial motion. The first row shows the synthetic initial image and the tracking points representing the sequential motion of heart, the second row the sequential images corresponding to the motion of the tracking points, and the last row the tracking points (yellow “o” marks) and LV contour (yellow dotted line) by the displacements computed using $\lambda = 300$ and the mean value of $\bar{\lambda}$ computed using the sequential images. (b) The change of $\bar{\lambda}$ according to t . The $\bar{\lambda}$ value varies within the range of [250, 350].

3. Experimental Results

We test the proposed algorithm in clinical setting using many real data. We compare the performance of the proposed algorithm with some widely used tracking algorithms including the block matching tracking methods using sum-of-squared difference (SSD) and cross-correlation coefficient, and the LK optical flow. For experiments, we use the 35 cases of 240×320 size 2D echocardiography data acquired using a Samsung Medison V10 ultrasound system (Seoul, Republic of Korea) and a phased array transducer P2-4BA (2–4 MHz). We use 19 tracking points to track the endocardial border and make the LV contour connecting the points using the natural cubic

spline. All the experiments were conducted using MATLAB 7.5 and laptop computer (Inter processor U7300 at 1.3 GHz and 1 GB RAM), and the computational time was about 40 milliseconds at each frame.

3.1. Assessment of LV Border Tracing. A quantitative evaluation on the performance of the proposed tracking algorithm is done on real 2D image sequences. For computation of $\mathbf{u} \cdot \nabla I + (\partial/\partial t)I$, we use the standard finite difference method. We use the Hausdorff distance ε_H [26, 27] to compare the automated LV contours produced by algorithms with manually traced contours by a clinical expert. Here, the

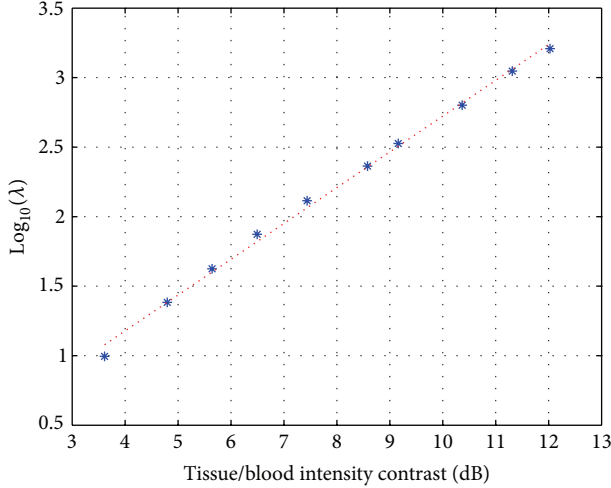


FIGURE 6: Graphs showing the relationship between $\bar{\lambda}$ and the tissue/blood intensity contrast. The stars are the points obtained from the simulation; the straight line fits these points.

Hausdorff distance between the contour \mathcal{C}_1 and \mathcal{C}_2 is given by

$$\varepsilon_H(\mathcal{C}_1, \mathcal{C}_2) = \max \left\{ \sup_{\mathbf{r}_1 \in \mathcal{C}_1} \left(\min_{\mathbf{r}_2 \in \mathcal{C}_2} \|\mathbf{r}_1 - \mathbf{r}_2\| \right), \sup_{\mathbf{r}_2 \in \mathcal{C}_2} \left(\min_{\mathbf{r}_1 \in \mathcal{C}_1} \|\mathbf{r}_1 - \mathbf{r}_2\| \right) \right\}. \quad (23)$$

For two representative cases among the 35 cases of 2D echocardiography data, the LV tracking results of the proposed method and the conventional methods are shown in Figures 7 and 8, respectively. For the sake of a name, we call them Cases I and II.

In Figure 7, the first row is manually traced LV contours by a clinical expert for images at ED, ES, and ED frames in the entire cycle. The next two rows are results by two block matching tracking methods using the different similarity measures of sum-of-squared difference (SSD) and cross-correlation. The fourth and fifth rows are obtained by the LK optical flow and the proposed method, respectively. The three conventional methods produce distorted LV contours due to a few incorrect tracking points alienated from the real LV border. On the other hand, the proposed method successfully follows local speckle patterns without distorting the whole LV shape.

For initial 10 sequential images, we compute $\bar{\lambda}$ by manually identifying each tracking point to the corresponding position on each image. From the computed parameters $\bar{\lambda}$, λ is set to 120 according to the λ -choice method described in Section 2.3.

In Figure 8, we test for real images having indistinguishable speckle patterns near endocardial border. Due to the presence of indistinguishable speckle patterns, the three conventional methods produce irregular distribution of tracking points as shown in second, third, and fourth rows in Figure 8. The proposed method keeps regular distribution of

TABLE 1: The tracking points and displacements used in sequential synthetic images.

(a) Tracking points				
i	\mathbf{r}_i at 1st I	\mathbf{r}_i at 2nd I	\mathbf{r}_i at 3rd I	\mathbf{r}_i at 4th I
1	(152, 201)	(153, 196)	(154, 187)	(154, 183)
2	(151, 176)	(152, 171)	(153, 165)	(154, 161)
3	(155, 151)	(156, 147)	(157, 142)	(158, 139)
4	(152, 128)	(153, 125)	(155, 120)	(156, 118)
5	(142, 105)	(144, 103)	(146, 100)	(147, 98)
6	(147, 82)	(149, 80)	(152, 78)	(153, 77)
7	(167, 71)	(169, 70)	(171, 69)	(172, 68)
8	(188, 84)	(189, 82)	(190, 80)	(191, 79)
9	(207, 101)	(207, 99)	(207, 96)	(207, 94)
10	(217, 124)	(217, 121)	(216, 116)	(216, 114)
11	(224, 147)	(223, 143)	(222, 138)	(221, 135)
12	(229, 172)	(228, 167)	(227, 160)	(226, 156)
13	(229, 196)	(228, 191)	(226, 182)	(225, 178)

(b) Displacements			
i	\mathbf{u}_i at 1st I	\mathbf{u}_i at 2nd I	\mathbf{u}_i at 3rd I
1	(1, -5)	(1, -9)	(0, -4)
2	(1, -5)	(1, -6)	(1, -4)
3	(1, -4)	(1, -5)	(1, -3)
4	(1, -3)	(2, -5)	(1, -2)
5	(2, -2)	(2, -3)	(1, -2)
6	(2, -2)	(3, -2)	(1, -1)
7	(2, -1)	(2, -1)	(1, -1)
8	(1, -2)	(1, -2)	(1, -1)
9	(0, -2)	(0, -3)	(0, -2)
10	(0, -3)	(-1, -5)	(0, -2)
11	(-1, -4)	(-1, -5)	(-1, -3)
12	(-1, -5)	(-1, -7)	(-1, -4)
13	(-1, -5)	(-2, -9)	(-1, -4)

tracking points and successfully track local speckle patterns. For Case II, λ is set to 100.

Figure 9 shows the comparison results of four different methods using Hausdorff distance between contours drawn manually and contours generated automatically for the entire cycle from an ED frame to the next ED frame. The proposed method provides the smallest errors in final tracking results of both Cases I and II.

3.2. Assessment of Individual Tracking Point Errors. For performance evaluation of the proposed algorithm, we propose an additional assessment regarding the repeatability of local point along the forward and backward entire cardiac cycle. Let $\{\mathbf{r}_1^{\text{initial}}, \dots, \mathbf{r}_n^{\text{initial}}\}$ be the set of initial tracking points on a manually delineated contour (see the images of the left column in Figure 7). Let t_R be a time interval of a one cycle image between ED frame and the next ED frame. Using one

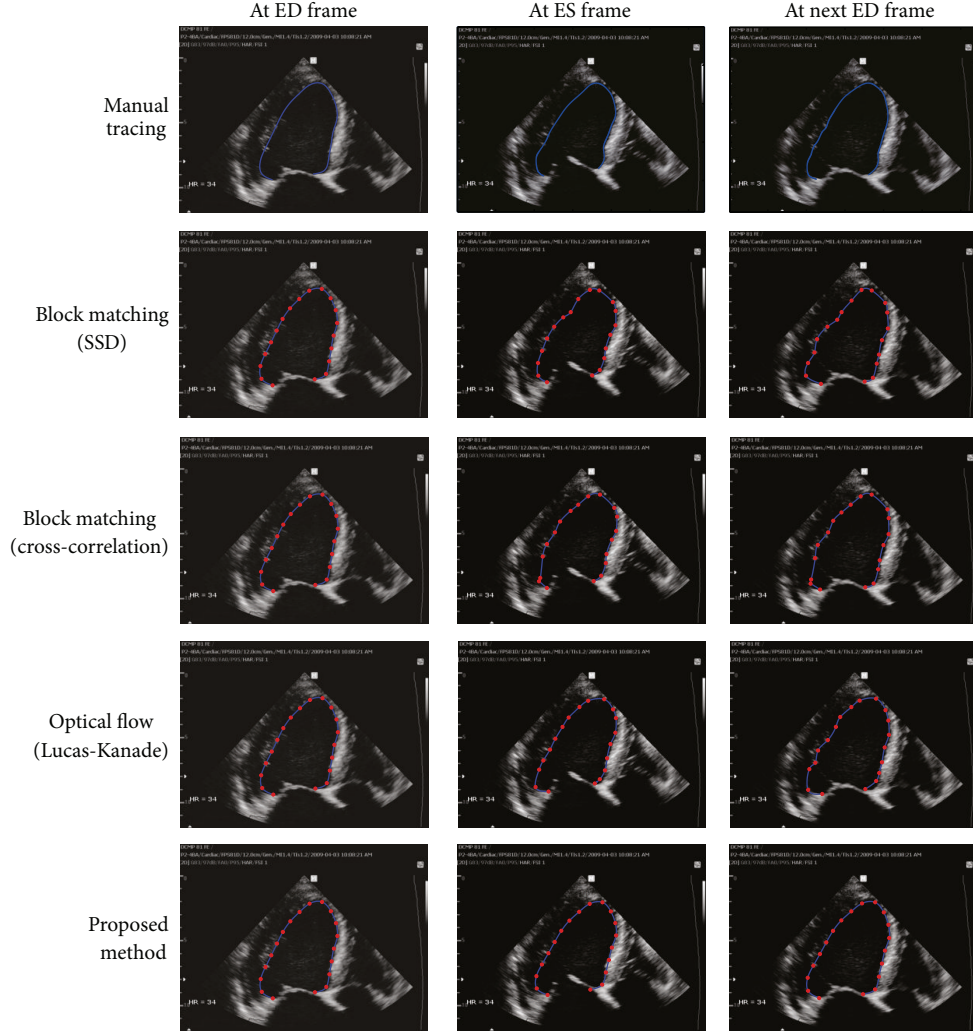


FIGURE 7: Case I: real images with weak signals in endocardial border. The second and third rows are the results by region-based tracking methods using sum-of-squared difference (SSD) and cross-correlation, respectively. The fourth row is the result by the LK optical flow and the final row is the result by the proposed method ($\lambda = 120$).

cycle image $I(\mathbf{r}, t)$, $0 \leq t \leq t_R$, we generate a forward-backward image defined by

$$\tilde{I}(\mathbf{r}, t) = \begin{cases} I(\mathbf{r}, t) & \text{if } 0 \leq t \leq t_R \\ I(\mathbf{r}, 2t_R - t) & \text{if } t_R \leq t \leq 2t_R. \end{cases} \quad (24)$$

Using this forward-backward image $\tilde{I}(\mathbf{r}, t)$, $0 \leq t \leq 2t_R$, we apply an automated tracking algorithm to get the returning tracking position $\mathbf{r}_j^{\text{returning}}$ at time $t = 2t_R$. The local tracking point assessment is obtained by estimating the distance between the initial position $\mathbf{r}_j^{\text{initial}}$ and the corresponding returning position $\mathbf{r}_j^{\text{returning}}$:

Forward-backward point tracking error (FBTE)

$$= \sqrt{\frac{1}{n} \sum_{i=1}^n |\mathbf{r}_i^{\text{initial}} - \mathbf{r}_i^{\text{returning}}|^2}. \quad (25)$$

TABLE 2: The comparison results of the proposed method with the conventional methods using FBTE, for Case I and Case II (in pixels).

Method	Case I	Case II
Block matching (SSD)	3.6992	4.6566
Block matching (cross-correlation)	2.3396	5.5866
Optical flow (LK)	2.6326	2.1521
Proposed method	0.4052	0.7930

For the previous two representative cases, Cases I and II, Table 2 shows the comparison results of the proposed method with the conventional methods using the FBTE.

Table 3 shows the mean and standard deviation of the forward-backward point tracking errors of the results obtained by the three conventional tracking methods and the proposed method. Tables 2 and 3 reveal that the proposed method provides improved performance compared with the conventional tracking methods.

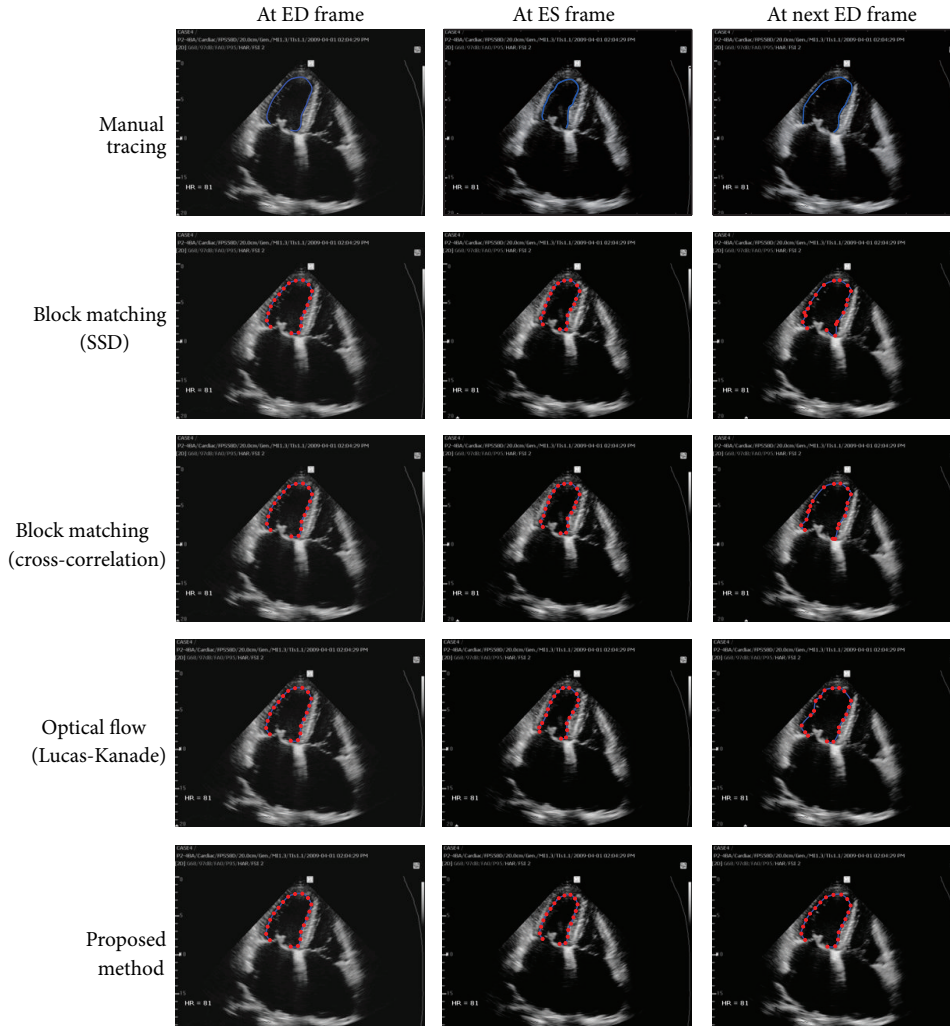


FIGURE 8: Case II: real images with indistinguishable speckle patterns in endocardial border. The second and third rows are the results by region-based tracking methods using sum-of-squared difference (SSD) and cross-correlation, respectively. The fourth row is the result by the LK optical flow and the fifth row by the proposed method ($\lambda = 100$).

TABLE 3: The comparison results of the tracking algorithms for the total experimental dataset of 35 cases. The errors are measured using the FBTE (in pixels).

Method	Mean of errors	Standard deviation of errors
Block matching (SSD)	4.1936	2.4456
Block matching (cross-correlation)	4.4173	2.5684
Optical flow (LK)	3.0685	1.2997
Proposed method	0.6344	0.2884

4. Discussion and Conclusion

The proposed method controls the individual tracking points following optical flow by confining their overall motions by penalizing the misfit between the estimated tracking points and their projection onto the affine transform space \mathcal{W} in (11) of the initial tracking points.

We have experimentally demonstrated that the proposed method is capable of performing robust real-time LV border tracking even in the presence of indistinguishable portions of the LV walls in echocardiography data. In practice, echocardiography data often contains edge dropout or indistinguishable speckle patterns in a local neighborhood of a tracking point which may bring the tracking point out of the endocardial border, resulting in distorted LV contours. The proposed method effectively deals with these problems by taking advantage of an LV shape space describing a global motion that is synthesized by integrating local deformations governed by the LK optical flow model. Various experiments show that the proposed method achieves better overall performance than the widely used conventional methods including the block matching tracking methods using sum-of-squared difference (SSD) and cross-correlation, and the LK optical flow.

The proposed method performs the LV border tracking by directly computing the displacements between two

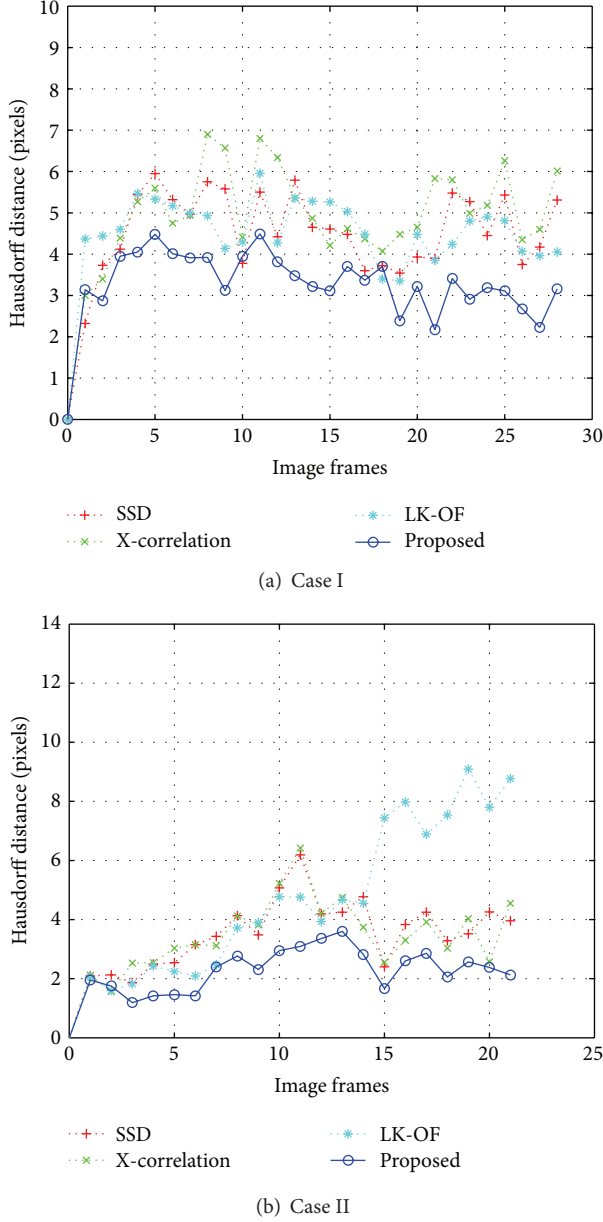


FIGURE 9: Comparison results of LV contours using the Hausdorff distance ε_H for the entire images of (a) Case I and (b) Case II, which are shown in Figures 7 and 8, respectively.

sequential images via a simple matrix multiplication. The computational time is affected by the size of the matrix, depending on the number of tracking points.

We also proposed a new performance evaluation method for LV tracking that is based on the forward-backward tracking error estimation as shown in Section 3.2. The conventional evaluation of global tracking performance using the delineated LV contours has some limitations in estimating errors of individual tracking points; in the case when tracking points erroneously move along LV border, the LV contour connecting the tracking points cannot reveal those individual tracking errors. The forward-backward point tracking error

estimation provides a better local tracking performance assessment in the whole cycle.

The proposed technique can be extended to three dimensions by using 3D affine transformation as a global deformation.

APPENDIX

Derivation of the Euler-Lagrange Equation (13)

In this appendix, we derive the Euler-Lagrange equation (13) from (8). From (9), we have

$$\begin{bmatrix} \frac{\partial a_1}{\partial u_j} \\ \frac{\partial a_2}{\partial u_j} \\ \frac{\partial a_5}{\partial u_j} \end{bmatrix} = \left(\Phi(\mathcal{E}^*)^T \Phi(\mathcal{E}^*) \right)^{-1} \begin{bmatrix} x_j^* \\ y_j^* \\ 1 \end{bmatrix},$$

$$\begin{bmatrix} \frac{\partial a_3}{\partial u_j} \\ \frac{\partial a_4}{\partial u_j} \\ \frac{\partial a_6}{\partial u_j} \end{bmatrix} = \begin{bmatrix} 0 \\ 0 \\ 0 \end{bmatrix}, \quad \begin{bmatrix} \frac{\partial a_1}{\partial v_j} \\ \frac{\partial a_2}{\partial v_j} \\ \frac{\partial a_5}{\partial v_j} \end{bmatrix} = \begin{bmatrix} 0 \\ 0 \\ 0 \end{bmatrix}, \quad (\text{A.1})$$

$$\begin{bmatrix} \frac{\partial a_3}{\partial v_j} \\ \frac{\partial a_4}{\partial v_j} \\ \frac{\partial a_6}{\partial v_j} \end{bmatrix} = \left(\Phi(\mathcal{E}^*)^T \Phi(\mathcal{E}^*) \right)^{-1} \begin{bmatrix} x_j^* \\ y_j^* \\ 1 \end{bmatrix},$$

for $j = 1, 2, \dots, n$. From the first and fourth identities of (A.1), we have

$$d(i, j) = \frac{\partial a_1}{\partial u_j} x_i^* + \frac{\partial a_2}{\partial u_j} y_i^* + \frac{\partial a_5}{\partial u_j}$$

$$= [x_i^* \ y_i^* \ 1] \begin{bmatrix} \frac{\partial a_1}{\partial u_j} \\ \frac{\partial a_2}{\partial u_j} \\ \frac{\partial a_5}{\partial u_j} \end{bmatrix}$$

$$= [x_i^* \ y_i^* \ 1] \left(\Phi(\mathcal{E}^*)^T \Phi(\mathcal{E}^*) \right)^{-1} \begin{bmatrix} x_j^* \\ y_j^* \\ 1 \end{bmatrix}$$

$$\begin{aligned}
&= [x_i^* \ y_i^* \ 1] \begin{bmatrix} \frac{\partial a_3}{\partial v_j} \\ \frac{\partial a_4}{\partial v_j} \\ \frac{\partial a_6}{\partial v_j} \end{bmatrix} \\
&= \frac{\partial a_3}{\partial v_j} x_i^* + \frac{\partial a_4}{\partial v_j} y_i^* + \frac{\partial a_6}{\partial v_j}.
\end{aligned} \tag{A.2}$$

Using (A.1) and (A.2), the partial derivatives $\partial \mathcal{E}_t / \partial u_j$ and $\partial \mathcal{E}_t / \partial v_j$ of \mathcal{E}_t with respect to $\mathbf{u}_j = (u_j, v_j)$ are computed by

$$\begin{aligned}
&\frac{\partial \mathcal{E}_t}{\partial u_j} \\
&= \int_{\mathcal{N}(\mathbf{r}_j(t))} w(\mathbf{r}' - \mathbf{r}_j(t)) \\
&\quad \times \left\{ \mathbf{u}_j \cdot \nabla I(\mathbf{r}', t) + \frac{\partial}{\partial t} I(\mathbf{r}', t) \right\} \frac{\partial}{\partial x} I(\mathbf{r}', t) d\mathbf{r}' \\
&\quad + \lambda \left[\begin{array}{c} \{x_j + u_j - (a_1 x_j^* + a_2 y_j^* + a_5)\} \\ - \sum_{i=1}^n \{x_i + u_i - (a_1 x_i^* + a_2 y_i^* + a_5)\} \left(\frac{\partial a_1}{\partial u_j} x_i^* + \frac{\partial a_2}{\partial u_j} y_i^* + \frac{\partial a_5}{\partial u_j} \right) \end{array} \right] \\
&= \int_{\mathcal{N}(\mathbf{r}_j(t))} w(\mathbf{r}' - \mathbf{r}_j(t)) \\
&\quad \times \left\{ \mathbf{u}_j \cdot \nabla I(\mathbf{r}', t) + \frac{\partial}{\partial t} I(\mathbf{r}', t) \right\} \frac{\partial}{\partial x} I(\mathbf{r}', t) d\mathbf{r}' \\
&\quad + \lambda \left[\begin{array}{c} \{x_j + u_j - (a_1 x_j^* + a_2 y_j^* + a_5)\} \\ - \sum_{i=1}^n d(i, j) \{x_i + u_i - (a_1 x_i^* + a_2 y_i^* + a_5)\} \end{array} \right],
\end{aligned} \tag{A.3}$$

$$\begin{aligned}
&\frac{\partial \mathcal{E}_t}{\partial v_j} \\
&= \int_{\mathcal{N}(\mathbf{r}_j(t))} w(\mathbf{r}' - \mathbf{r}_j(t)) \\
&\quad \times \left\{ \mathbf{u}_j \cdot \nabla I(\mathbf{r}', t) + \frac{\partial}{\partial t} I(\mathbf{r}', t) \right\} \frac{\partial}{\partial y} I(\mathbf{r}', t) d\mathbf{r}' \\
&\quad + \lambda \left[\begin{array}{c} \{y_j + v_j - (a_3 x_j^* + a_4 y_j^* + a_6)\} \\ - \sum_{i=1}^n \{y_i + v_i - (a_3 x_i^* + a_4 y_i^* + a_6)\} \left(\frac{\partial a_3}{\partial v_j} x_i^* + \frac{\partial a_4}{\partial v_j} y_i^* + \frac{\partial a_6}{\partial v_j} \right) \end{array} \right]
\end{aligned}$$

$$\begin{aligned}
&= \int_{\mathcal{N}(\mathbf{r}_j(t))} w(\mathbf{r}' - \mathbf{r}_j(t)) \\
&\quad \times \left\{ \mathbf{u}_j \cdot \nabla I(\mathbf{r}', t) + \frac{\partial}{\partial t} I(\mathbf{r}', t) \right\} \frac{\partial}{\partial y} I(\mathbf{r}', t) d\mathbf{r}' \\
&\quad + \lambda \left[\begin{array}{c} \{y_j + v_j - (a_3 x_j^* + a_4 y_j^* + a_6)\} \\ - \sum_{i=1}^n d(i, j) \{y_i + v_i - (a_3 x_i^* + a_4 y_i^* + a_6)\} \end{array} \right].
\end{aligned} \tag{A.4}$$

Simple arrangement of the above identities leads to the Euler-Lagrange equation:

$$\begin{aligned}
\mathbf{0} &= \frac{\partial \mathcal{E}_t}{\partial \mathbf{u}_j} \\
&= \int_{\mathcal{N}(\mathbf{r}_j(t))} w(\mathbf{r} - \mathbf{r}_j(t)) \nabla I(\mathbf{r}, t) \\
&\quad \times \left\{ \mathbf{u}_j \cdot \nabla I(\mathbf{r}, t) + \frac{\partial}{\partial t} I(\mathbf{r}, t) \right\} d\mathbf{r} \\
&\quad + \lambda \left\{ \mathbf{r}_j(t) + \mathbf{u}_j - \mathbf{g}_j(\mathbf{U}) \right. \\
&\quad \left. - \sum_{i=1}^n d(i, j) (\mathbf{r}_i(t) + \mathbf{u}_i - \mathbf{g}_i(\mathbf{U})) \right\},
\end{aligned} \tag{A.5}$$

where $\mathbf{g}_i(\mathbf{U}) = \begin{bmatrix} a_1(\mathbf{U}) & a_2(\mathbf{U}) \\ a_3(\mathbf{U}) & a_4(\mathbf{U}) \end{bmatrix} \mathbf{r}_i^* + \begin{bmatrix} a_5(\mathbf{U}) \\ a_6(\mathbf{U}) \end{bmatrix}$. The Euler-Lagrange equation (13) can be obtained by a careful rearrangement of (13) using the identity

$$\mathbf{g}_j(\mathbf{U}) = \sum_{i=1}^n d(i, j) \mathbf{g}_i(\mathbf{U}). \tag{A.6}$$

Hence, it remains to prove the above identity. It suffices to prove

$$\sum_{i=1}^n x_i^* d(i, j) = x_j^*, \quad \sum_{i=1}^n y_i^* d(i, j) = y_j^*, \quad \sum_{i=1}^n d(i, j) = 1, \tag{A.7}$$

for $j = 1, 2, \dots, n$. To compute $\sum_{i=1}^n x_i^* d(i, j)$ simply, denote

$$\begin{bmatrix} \phi_j \\ \varphi_j \\ \psi_j \end{bmatrix} := \begin{bmatrix} \sum_{k=1}^n x_k^{*2} & \sum_{k=1}^n x_k^* y_k^* & \sum_{k=1}^n x_k^* \\ \sum_{k=1}^n x_k^* y_k^* & \sum_{k=1}^n y_k^{*2} & \sum_{k=1}^n y_k^* \\ \sum_{k=1}^n x_k^* & \sum_{k=1}^n y_k^* & n \end{bmatrix}^{-1} \begin{bmatrix} x_j^* \\ y_j^* \\ 1 \end{bmatrix}. \tag{A.8}$$

Then $\sum_{i=1}^n x_i^* d(i, j)$ can be simplified by

$$\begin{aligned}
& \sum_{i=1}^n x_i^* d(i, j) \\
&= \sum_{i=1}^n x_i^* [x_i^* \ y_i^* \ 1] \\
&\quad \times \left(\begin{bmatrix} x_1^* & y_1^* & 1 \\ \vdots & \vdots & \vdots \\ x_n^* & y_n^* & 1 \end{bmatrix}^T \begin{bmatrix} x_1^* & y_1^* & 1 \\ \vdots & \vdots & \vdots \\ x_n^* & y_n^* & 1 \end{bmatrix} \right)^{-1} \begin{bmatrix} x_j^* \\ y_j^* \\ 1 \end{bmatrix} \\
&= \begin{bmatrix} \sum_{i=1}^n x_i^{*2} & \sum_{i=1}^n x_i^* y_i^* & \sum_{i=1}^n x_i^* \\ \sum_{k=1}^n x_k^{*2} & \sum_{k=1}^n x_k^* y_k^* & \sum_{k=1}^n x_k^* \\ \sum_{k=1}^n x_k^* y_k^* & \sum_{k=1}^n y_k^{*2} & \sum_{k=1}^n y_k^* \\ \sum_{k=1}^n x_k^* & \sum_{k=1}^n y_k^* & n \end{bmatrix}^{-1} \begin{bmatrix} x_j^* \\ y_j^* \\ 1 \end{bmatrix} \quad (\text{A.9}) \\
&= \begin{bmatrix} \sum_{i=1}^n x_i^{*2} & \sum_{i=1}^n x_i^* y_i^* & \sum_{i=1}^n x_i^* \\ \sum_{i=1}^n x_i^{*2} & \sum_{i=1}^n x_i^* y_i^* & \sum_{i=1}^n x_i^* \\ \sum_{i=1}^n x_i^{*2} & \sum_{i=1}^n x_i^* y_i^* & \sum_{i=1}^n x_i^* \end{bmatrix} \begin{bmatrix} \phi_j \\ \varphi_j \\ \psi_j \end{bmatrix} \\
&= \phi_j \sum_{i=1}^n x_i^{*2} + \varphi_j \sum_{i=1}^n x_i^* y_i^* + \psi_j \sum_{i=1}^n x_i^* \\
&= x_j^*.
\end{aligned}$$

This completes the first identity of (A.7). Similarly, we can get the remaining two identities of (A.7).

Acknowledgments

The author would like to thank Samsung Medison R&D Center for supporting many ultrasound data and valuable suggestions. This work was supported by the National Research Foundation of Korea (NRF) funded by the Ministry of Education, Science and Technology (no. 2012-8-1798 and no. 2011-8-1782).

References

- [1] V. Mor-Avi, L. Sugeng, L. Weinert et al., "Fast measurement of left ventricular mass with real-time three-dimensional echocardiography: comparison with magnetic resonance imaging," *Circulation*, vol. 110, no. 13, pp. 1814–1818, 2004.
- [2] F. Veronesi, C. Corsi, E. G. Caiani, A. Sarti, and C. Lamberti, "Tracking of left ventricular long axis from real-time three-dimensional echocardiography using optical flow techniques," *IEEE Transactions on Information Technology in Biomedicine*, vol. 10, no. 1, pp. 174–181, 2006.
- [3] J. Hansegård, S. Urheim, K. Lunde, S. Malm, and S. I. Rabben, "Semi-automated quantification of left ventricular volumes and

- ejection fraction by real-time three-dimensional echocardiography," *Cardiovascular Ultrasound*, vol. 7, no. 1, article 18, 2009.
- [4] K. Y. E. Leung and J. G. Bosch, "Automated border detection in three-dimensional echocardiography: principles and promises," *European Journal of Echocardiography*, vol. 11, no. 2, pp. 97–108, 2010.
- [5] E. D. Angelini, A. F. Laine, S. Takuma, J. W. Holmes, and S. Homma, "LV volume quantification via spatiotemporal analysis of real-time 3-D echocardiography," *IEEE Transactions on Medical Imaging*, vol. 20, no. 6, pp. 457–469, 2001.
- [6] M. M. Nillesen, R. G. P. Lopata, I. H. Gerrits et al., "Segmentation of the heart muscle in 3-D pediatric echocardiographic images," *Ultrasound in Medicine and Biology*, vol. 33, no. 9, pp. 1453–1462, 2007.
- [7] O. I. I. Soliman, B. J. Krenning, M. L. Geleijnse et al., "Quantification of left ventricular volumes and function in patients with cardiomyopathies by real-time three-dimensional echocardiography: a head-to-head comparison between two different semiautomated endocardial border detection algorithms," *Journal of the American Society of Echocardiography*, vol. 20, no. 9, pp. 1042–1049, 2007.
- [8] E. O. Chukwu, E. Barasch, D. G. Mihalatos et al., "Relative importance of errors in left ventricular quantitation by two-dimensional echocardiography: insights from three-dimensional echocardiography and cardiac magnetic resonance imaging," *Journal of the American Society of Echocardiography*, vol. 21, no. 9, pp. 990–997, 2008.
- [9] J. Hansegård, F. Orderud, and S. I. Rabben, "Real-time active shape models for segmentation of 3D cardiac ultrasound," in *Computer Analysis of Images and Patterns*, vol. 4673 of *Lecture Notes in Computer Science*, pp. 157–164, Springer, New York, NY, USA, 2007.
- [10] F. Orderud and S. I. Rabben, "Real-time 3D segmentation of the left ventricle using deformable subdivision surfaces," in *Proceedings of the IEEE Conference on Computer Vision and Pattern Recognition (CVPR'08)*, pp. 1–8, Anchorage, Alaska, USA, June 2008.
- [11] M. Ma, M. van Stralen, J. H. C. Reiber, J. G. Bosch, and B. P. F. Lelieveldt, "Model driven quantification of left ventricular function from sparse single-beat 3D echocardiography," *Medical Image Analysis*, vol. 14, no. 4, pp. 582–593, 2010.
- [12] P. Baraldi, A. Sarti, C. Lamberti, A. Prandini, and F. Sgallari, "Evaluation of differential optical flow techniques on synthesized echo images," *IEEE Transactions on Biomedical Engineering*, vol. 43, no. 3, pp. 259–272, 1996.
- [13] M. Sühling, M. Arigovindan, C. Jansen, P. Hunziker, and M. Unser, "Myocardial motion analysis from B-mode echocardiograms," *IEEE Transactions on Image Processing*, vol. 14, no. 4, pp. 525–536, 2005.
- [14] M. G. Linguraru, N. V. Vasilyev, G. R. Marx, W. Tworetzky, P. J. del Nido, and R. D. Howe, "Fast block flow tracking of atrial septal defects in 4D echocardiography," *Medical Image Analysis*, vol. 12, no. 4, pp. 397–412, 2008.
- [15] Q. Duan, E. D. Angelini, S. L. Herz et al., "Region-based endocardium tracking on real-time three-dimensional ultrasound," *Ultrasound in Medicine and Biology*, vol. 35, no. 2, pp. 256–265, 2009.
- [16] K. Y. E. Leung, M. G. Danilouchkine, M. van Stralen, N. de Jong, A. F. W. van der Steen, and J. G. Bosch, "Left ventricular border tracking using cardiac motion models and optical flow," *Ultrasound in Medicine and Biology*, vol. 37, no. 4, pp. 605–616, 2011.

- [17] B. Lucas and T. Kanade, "An iterative image restoration technique with an application to stereo vision," in *Proceedings of the 7th International Joint Conference on Artificial Intelligence (IJCAI'81)*, vol. 2, pp. 121–130, 1981.
- [18] A. A. Amini, R. W. Curwen, J. C. Gore, and Snakes a, "nd splines for tracking non-rigid heart motion," in *Computer Vision—ECCV'96*, vol. 1065 of *Lecture Notes in Computer Science*, pp. 249–261, Springer, New York, NY, USA, 1996.
- [19] M. Li, C. Kambhamettu, and M. Stone, "Nonrigid motion recovery for 3D surfaces," *Image and Vision Computing*, vol. 25, no. 3, pp. 250–261, 2007.
- [20] B. Horn and B. Schunk, "Determining optical flow," *Artificial Intelligence*, vol. 17, no. 2, pp. 185–203, 1981.
- [21] J. L. Barron, D. J. Fleet, and S. S. Beauchemin, "Performance of optical flow techniques," *International Journal of Computer Vision*, vol. 12, no. 1, pp. 43–77, 1994.
- [22] E. Brusseau, C. L. de Korte, F. Mastik, J. Schaar, and A. F. W. van der Steen, "Fully automatic luminal contour segmentation in intracoronary ultrasound imaging—a statistical approach," *IEEE Transactions on Medical Imaging*, vol. 23, no. 5, pp. 554–566, 2004.
- [23] A. Sarti, C. Corsi, E. Mazzini, and C. Lamberti, "Maximum likelihood segmentation of ultrasound images with rayleigh distribution," *IEEE Transactions on Ultrasonics, Ferroelectrics, and Frequency Control*, vol. 52, no. 6, pp. 947–960, 2005.
- [24] D. Kaplan and Q. Ma, "On the statistical characteristics of log-compressed Rayleigh signals: theoretical formulation and experimental results," *Journal of the Acoustical Society of America*, vol. 95, no. 3, pp. 1396–1400, 1994.
- [25] G. Slabaugh, G. Unal, M. Wels, T. Fang, and B. Rao, "Statistical region-based segmentation of ultrasound images," *Ultrasound in Medicine and Biology*, vol. 35, no. 5, pp. 781–795, 2009.
- [26] D. P. Huttenlocher, G. A. Klanderman, and W. J. Rucklidge, "Comparing images using the Hausdorff distance," *IEEE Transactions on Pattern Analysis and Machine Intelligence*, vol. 15, no. 9, pp. 850–863, 1993.
- [27] E. Belogay, C. Cabrelli, U. Molter, and R. Shonkwiler, "Calculating the Hausdorff distance between curves," *Information Processing Letters*, vol. 64, no. 1, pp. 17–22, 1997.

Research Article

Noninvasive Measurement of Conductivity Anisotropy at Larmor Frequency Using MRI

Joonsung Lee,¹ Yizhuang Song,² Narae Choi,¹ Sungmin Cho,¹
Jin Keun Seo,² and Dong-Hyun Kim¹

¹ Department of Electrical and Electronic Engineering, Yonsei University, Seoul 120-749, Republic of Korea

² Department of Computational Science & Engineering, Yonsei University, Seoul 120-749, Republic of Korea

Correspondence should be addressed to Dong-Hyun Kim; donghyunkim@yonsei.ac.kr

Received 15 October 2012; Revised 2 January 2013; Accepted 18 January 2013

Academic Editor: Ulrich Katscher

Copyright © 2013 Joonsung Lee et al. This is an open access article distributed under the Creative Commons Attribution License, which permits unrestricted use, distribution, and reproduction in any medium, provided the original work is properly cited.

Anisotropic electrical properties can be found in biological tissues such as muscles and nerves. Conductivity tensor is a simplified model to express the effective electrical anisotropic information and depends on the imaging resolution. The determination of the conductivity tensor should be based on Ohm's law. In other words, the measurement of partial information of current density and the electric fields should be made. Since the direct measurements of the electric field and the current density are difficult, we use MRI to measure their partial information such as B1 map; it measures circulating current density and circulating electric field. In this work, the ratio of the two circulating fields, termed circulating admittivity, is proposed as measures of the conductivity anisotropy at Larmor frequency. Given eigenvectors of the conductivity tensor, quantitative measurement of the eigenvalues can be achieved from circulating admittivity for special tissue models. Without eigenvectors, qualitative information of anisotropy still can be acquired from circulating admittivity. The limitation of the circulating admittivity is that at least two components of the magnetic fields should be measured to capture anisotropic information.

1. Introduction

Noninvasive measurement of electrical properties for biological tissues can be useful in EEG/MEG and electromagnetic source imaging [1] and in providing diagnostics information about the physiological and pathological states of the tissues [2–5]. For isotropic conductivity, many approaches have been developed to measure the conductivity at low frequencies and at Larmor frequencies [6]. At low frequencies below 1 kHz, Magnetic Resonance Electrical Impedance Tomography (MREIT) [7] can probe the conductivity distribution. At Larmor frequencies of about 100 MHz, Magnetic Resonance Electrical Property Tomography (MREPT) [8, 9] measures both electric conductivity and permittivity distributions using measurements of positively rotating magnetic fields generated by transmit RF coil, B1+ maps, from MRI.

Microscopically, the conductivity of the biological tissues could be isotropic. However, depending on the imaging resolution, the conductivity of an imaging voxel can be

anisotropic. Macroscopically, in other words, if several tissues with different electrical properties are combined in the imaging voxel, the conductivity of the imaging voxel differs when measured in different directions so that it becomes anisotropic. Especially in biological tissues, anisotropic electrical conductivity can be found in muscles and nerves [2–5]. The conductivity tensor is a simplified model with three eigenvectors and three eigenvalues which can include these anisotropic cases.

The eigenvectors of the conductivity tensor at low frequencies (<1 kHz) can be inferred from a prior knowledge of the object or the diffusion tensor imaging [1, 10]. However, at Larmor frequency of about 100 MHz, there have been a few studies on measuring three eigenvectors and eigenvalues of the conductivity tensor. Recently, Katscher et al. [11] proposed a way to estimate partial information of conductivity anisotropy especially in the special case where two minimum eigenvalues are almost equal to zero. In this work, based on Katscher's approach [11], we generalized and considered more

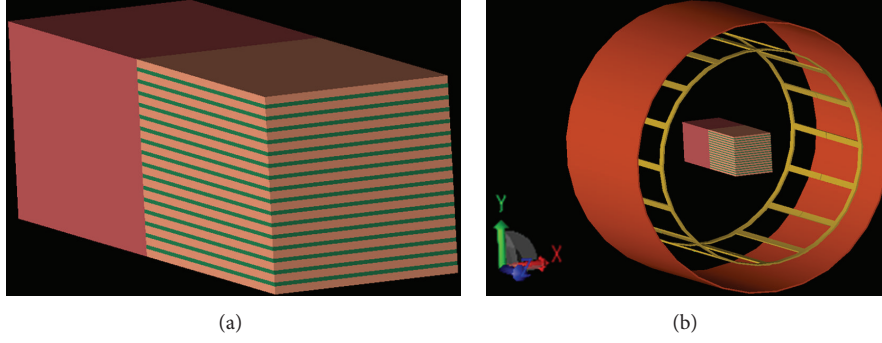


FIGURE 1: (a) Numerical phantom with anisotropic effective admittivity by stacking periodic binary medium, (b) placement of the imaging object inside the RF coil.

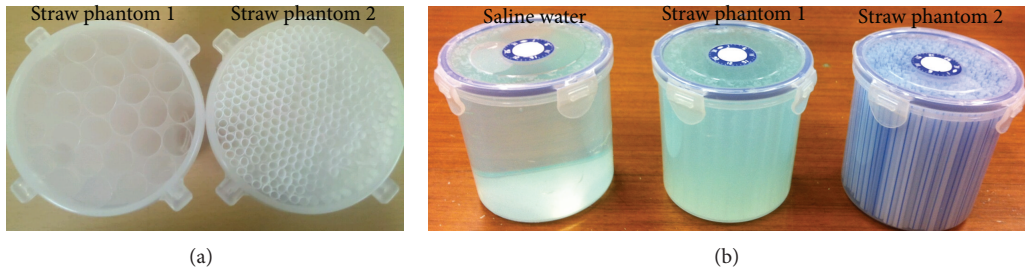


FIGURE 2: (a) Two straw phantoms before filling saline water, (b) three phantoms filled with saline water.

possible cases. Based on numerical phantom simulations and phantom experiments, the performance was evaluated and the limitations and future directions were proposed.

2. Materials and Methods

2.1. Admittivity Tensor Model. Admittivity tensor denoted by $\boldsymbol{\kappa}(\mathbf{r}) = \boldsymbol{\sigma}(\mathbf{r}) + i\omega\boldsymbol{\epsilon}(\mathbf{r})$ is a simplified model for the electrical anisotropic information at the angular frequency ω , where $\boldsymbol{\sigma}(\mathbf{r})$ and $\boldsymbol{\epsilon}(\mathbf{r})$ are conductivity and permittivity tensors, respectively.

The admittivity tensor can be represented with six parameters:

$$\boldsymbol{\kappa}(\mathbf{r}) = \begin{pmatrix} \kappa_{xx}(\mathbf{r}) & \kappa_{xy}(\mathbf{r}) & \kappa_{xz}(\mathbf{r}) \\ \kappa_{xy}(\mathbf{r}) & \kappa_{yy}(\mathbf{r}) & \kappa_{yz}(\mathbf{r}) \\ \kappa_{xz}(\mathbf{r}) & \kappa_{yz}(\mathbf{r}) & \kappa_{zz}(\mathbf{r}) \end{pmatrix}. \quad (1)$$

Expressing its eigenvectors $\mathbf{v}_1, \mathbf{v}_2, \mathbf{v}_3$ (unit vectors) and its corresponding eigenvalues $\kappa_1, \kappa_2, \kappa_3$, the admittivity tensor can be also expressed as

$$\boldsymbol{\kappa} = (\mathbf{v}_1 \ \mathbf{v}_2 \ \mathbf{v}_3) \begin{pmatrix} \kappa_1 & & \\ & \kappa_2 & \\ & & \kappa_3 \end{pmatrix} \begin{pmatrix} \mathbf{v}_1^T \\ \mathbf{v}_2^T \\ \mathbf{v}_3^T \end{pmatrix}. \quad (2)$$

We should note that three equations of Ohm's law $\mathbf{J} = \boldsymbol{\kappa}\mathbf{E}$ alone are insufficient to identify six unknown components

of $\boldsymbol{\kappa}$. However, the eigenvectors of the conductivity tensor $\boldsymbol{\kappa}$ could be estimated from prior knowledge of the object or can be determined by measuring the diffusion tensors [1] using MRI. Under the assumption that the eigenvectors of the admittivity tensor are known *a priori*, using the eigenvectors $\mathbf{v}_1, \mathbf{v}_2, \mathbf{v}_3$ of the matrix $\boldsymbol{\kappa}$, the conductivity tensor can be decomposed as

$$\begin{aligned} \sum_{j=1}^3 J_j(\mathbf{r}) \mathbf{v}_j = \mathbf{J}(\mathbf{r}) = \boldsymbol{\kappa}(\mathbf{r}) \mathbf{E}(\mathbf{r}) = \boldsymbol{\kappa}(\mathbf{r}) \left[\sum_{j=1}^3 E_j(\mathbf{r}) \mathbf{v}_j \right] \\ = \sum_{j=1}^3 \kappa_j E_j(\mathbf{r}) \mathbf{v}_j, \end{aligned} \quad (3)$$

where $J_j = \mathbf{J} \cdot \mathbf{v}_j$ and $E_j = \mathbf{E} \cdot \mathbf{v}_j$. In other words, $J_j(\mathbf{r}) = \kappa_j E_j(\mathbf{r})$.

2.2. Reconstruction of Admittivity Anisotropy Using Measured Magnetic Fields: Circulating Admittivity. Assume that the three eigenvectors are known. The effective admittivity, $\boldsymbol{\kappa} = \boldsymbol{\sigma} + i\omega\boldsymbol{\epsilon}$, in a voxel can be determined from Ohm's law as follows:

$$\kappa_j \int_{\text{Voxel}} \mathbf{E}(\mathbf{r}) \cdot \mathbf{v}_j \, d\mathbf{r} = \int_{\text{Voxel}} \mathbf{J}(\mathbf{r}) \cdot \mathbf{v}_j \, d\mathbf{r}. \quad (4)$$

However in MRI, \mathbf{E} and \mathbf{J} are hard to measure. Instead, partial knowledge of the magnetic fields \mathbf{H} can be acquired from B_1 mapping techniques [12–15]. Katscher et al. [11] extended the direct inversion method in MREPT [9] and proposed a way to estimate anisotropy of $\boldsymbol{\kappa}$ using the relationship

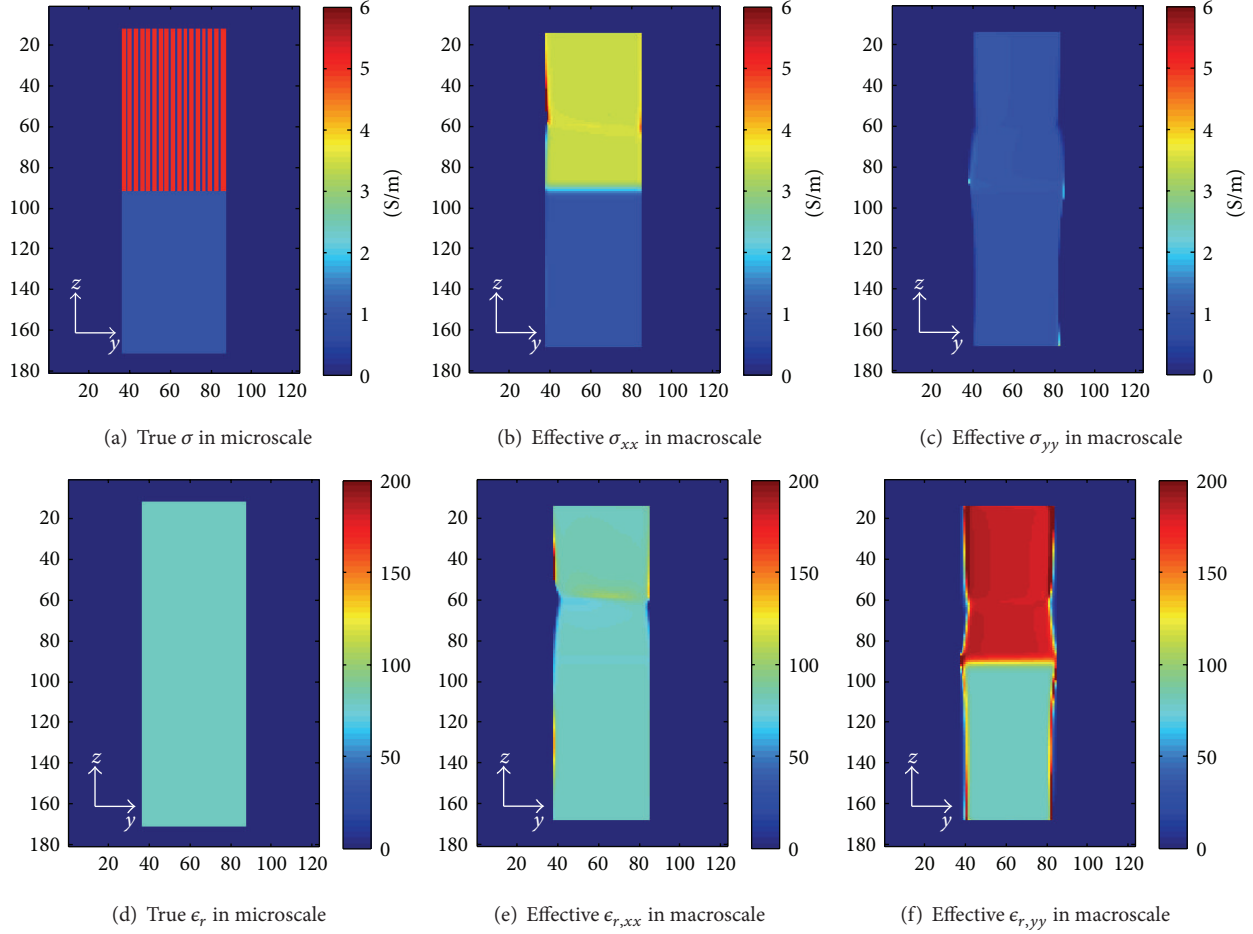


FIGURE 3: (a) and (d) depict the true conductivity and the relative permittivity values in the microscopic scale. (b)–(f) illustrate the true effective σ_{xx} , σ_{yy} , ϵ_{xx} , and ϵ_{yy} , respectively.

between circulating currents and circulating electric fields over a surface, which can be estimated from the measured magnetic fields.

From time-harmonic Maxwell Equations, the relationship among the current density, electric fields, and the magnetic fields can be expressed as

$$\mathbf{J}(\mathbf{r}) = \nabla \times \mathbf{H}(\mathbf{r}), \quad \oint_{\partial A(\mathbf{n})} \mathbf{E} \cdot d\mathbf{l} = -i\omega\mu \int_{A(\mathbf{n})} \mathbf{H} \cdot d\mathbf{s}, \quad (5)$$

where $A(\mathbf{n})$ is a surface whose normal vector is \mathbf{n} .

Based on the work by Katscher et al. [11], we define the circulating admittivity, $\bar{\kappa}$, as the ratio of the circulating currents and the circulating electric fields over the surface $A(\mathbf{n})$ with rotating the normal vector \mathbf{n} :

$$\begin{aligned} \bar{\kappa}(A(\mathbf{n})) &:= \frac{\oint_{\partial A(\mathbf{n})} \mathbf{J} \cdot d\mathbf{l}}{\oint_{\partial A(\mathbf{n})} \mathbf{E} \cdot d\mathbf{l}} = -\frac{1}{i\omega\mu} \frac{\oint_{\partial A(\mathbf{n})} \nabla \times \mathbf{H} \cdot d\mathbf{l}}{\int_{A(\mathbf{n})} \mathbf{H} \cdot d\mathbf{s}} \\ &= \frac{1}{i\omega\mu} \frac{\int_{A(\mathbf{n})} \nabla^2 \mathbf{H} \cdot d\mathbf{s}}{\int_{A(\mathbf{n})} \mathbf{H} \cdot d\mathbf{s}}, \end{aligned} \quad (6)$$

where \mathbf{s} is parallel to the normal vector \mathbf{n} . In (6), the relationship between the curl integral of $\nabla \times \mathbf{H}$ and the surface integral of $\nabla^2 \mathbf{H}$ hold for homogeneous region of admittivity and can generate artifacts at tissue boundaries [16].

In this work, we investigated the relationship between the circulating admittivity and the admittivity tensor for simple cases. First, if the admittivity tensor is isotropic, the circulating admittivity is also isotropic and equal to the isotropic admittivity. Second, if two eigenvalues of the admittivity tensor are the same, $\kappa_2 = \kappa_3$, the eigenvalue can be determined from the circulating admittivity over a surface with a normal vector, \mathbf{v}_1 , perpendicular to the eigenvectors corresponding to the two eigenvalues, κ_2, κ_3 . That is

$$\begin{aligned} \bar{\kappa}(A(\mathbf{v}_1)) &:= \frac{\oint_{\partial A(\mathbf{v}_1)} \mathbf{J} \cdot d\mathbf{l}}{\oint_{\partial A(\mathbf{v}_1)} \mathbf{E} \cdot d\mathbf{l}} = \frac{\oint_{\partial A(\mathbf{v}_1)} (\kappa_2 E_2 \mathbf{v}_2 + \kappa_3 E_3 \mathbf{v}_3) \cdot d\mathbf{l}}{\oint_{\partial A(\mathbf{v}_1)} (E_2 \mathbf{v}_2 + E_3 \mathbf{v}_3) \cdot d\mathbf{l}} \\ &= \kappa_2, \end{aligned} \quad (7)$$

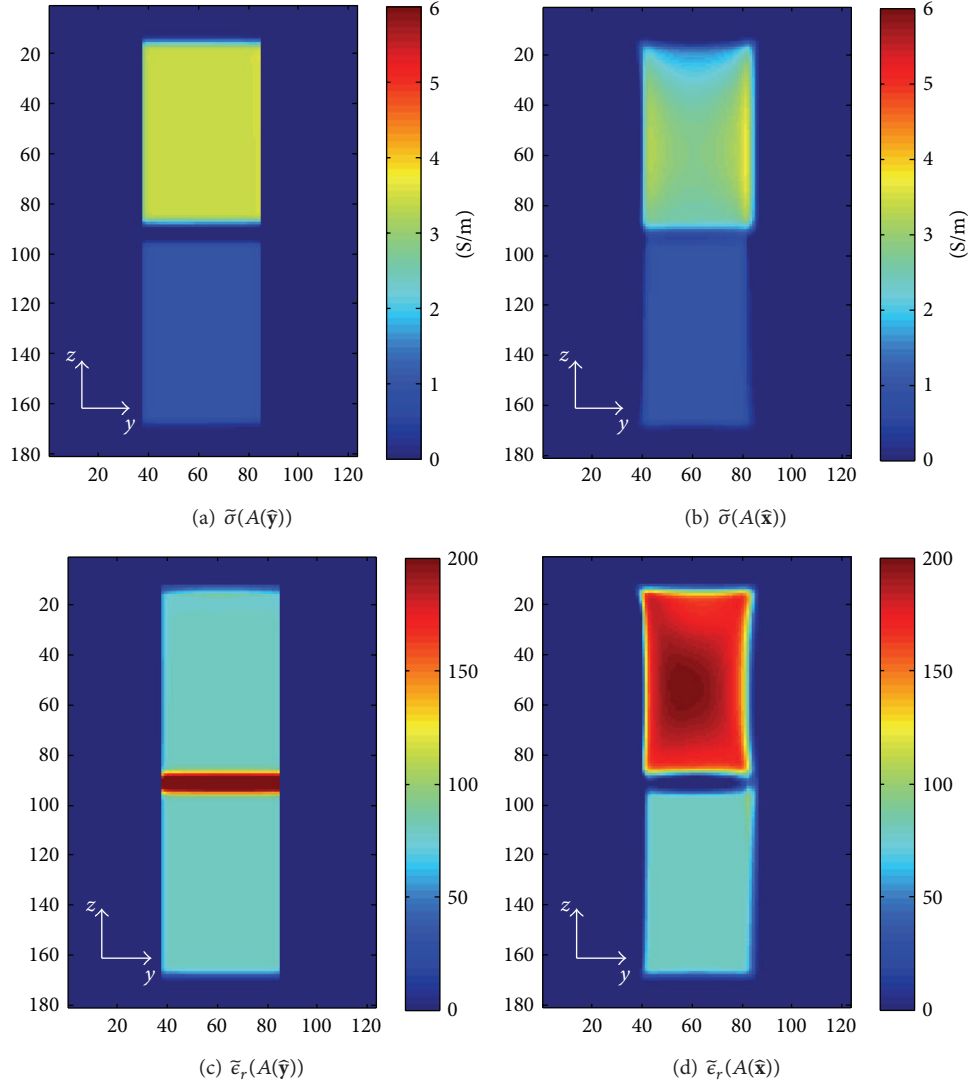


FIGURE 4: Circulating conductivity and relative permittivity derived from H^+ and H^- : (a) $\bar{\sigma}(A(\bar{\gamma}))$, (b) $\bar{\sigma}(A(\bar{\kappa}))$, (c) $\bar{\epsilon}_r(A(\bar{\gamma}))$, and (d) $\bar{\epsilon}_r(A(\bar{\kappa}))$.

since the normal vector \mathbf{v}_1 is perpendicular to the vector $d\mathbf{l}$ over a line $\partial A(\mathbf{v}_1)$ and the two eigenvalues are the same $\kappa_2 = \kappa_3$.

In addition, as it is considered in [9], if two smaller eigenvalues of the admittivity tensor, κ_2, κ_3 , are equal to zero, the largest eigenvalue, κ_1 , can be determined from the circulating admittivity directly:

$$\bar{\kappa}(A(\mathbf{n})) = \frac{\oint_{\partial A(\mathbf{n})} \kappa_{j1} E_1 \mathbf{v}_1 \cdot d\mathbf{l}}{\oint_{\partial A(\mathbf{n})} E_1 \mathbf{v}_1 \cdot d\mathbf{l}} = \kappa_1 \frac{\oint_{\partial A(\mathbf{n})} E_1 \mathbf{v}_1 \cdot d\mathbf{l}}{\oint_{\partial A(\mathbf{n})} E_1 \mathbf{v}_1 \cdot d\mathbf{l}} = \kappa_1. \quad (8)$$

As a combination of last two cases, if the largest eigenvalue is much bigger than the two smaller eigenvalues of the admittivity tensor and the two smaller eigenvalues are the same, by measuring the circulating admittivity for several directions of the normal vector, all three eigenvalues could be estimated.

2.3. Unknown Directions of Eigenvectors: Effective Admittivity Map (EAM) and Circulating Admittivity Map (CAM). In the previous section, we determined the admittivity tensor under the assumption that the eigenvectors of the admittivity tensor were known *a priori*. Even without the prior knowledge of the eigenvectors, we can still provide a qualitative measurement of anisotropy by computing the dependency on the normal vector, \mathbf{n} , in (6). For a qualitative measurement of the anisotropy, we define the effective admittivity map, $\bar{\kappa}(\mathbf{r}, \mathbf{n})$, and the circulating admittivity map, $\hat{\kappa}(\mathbf{r}, \mathbf{n})$, that describe the distributions of effective admittivity and circulating admittivity over the normal vector, respectively:

$$\begin{aligned} \bar{\kappa}(\mathbf{r}, \mathbf{n}) &:= \frac{\int \mathbf{J}(\mathbf{r}) \cdot \mathbf{n} \, d\mathbf{r}}{\int \mathbf{E}(\mathbf{r}) \cdot \mathbf{n} \, d\mathbf{r}}, \\ \hat{\kappa}(\mathbf{r}, \mathbf{n}) &:= \frac{1}{i\omega\mu} \frac{\int \nabla^2 \mathbf{H}(\mathbf{r}) \cdot \mathbf{n} \, d\mathbf{r}}{\int \mathbf{H}(\mathbf{r}) \cdot \mathbf{n} \, d\mathbf{r}}. \end{aligned} \quad (9)$$

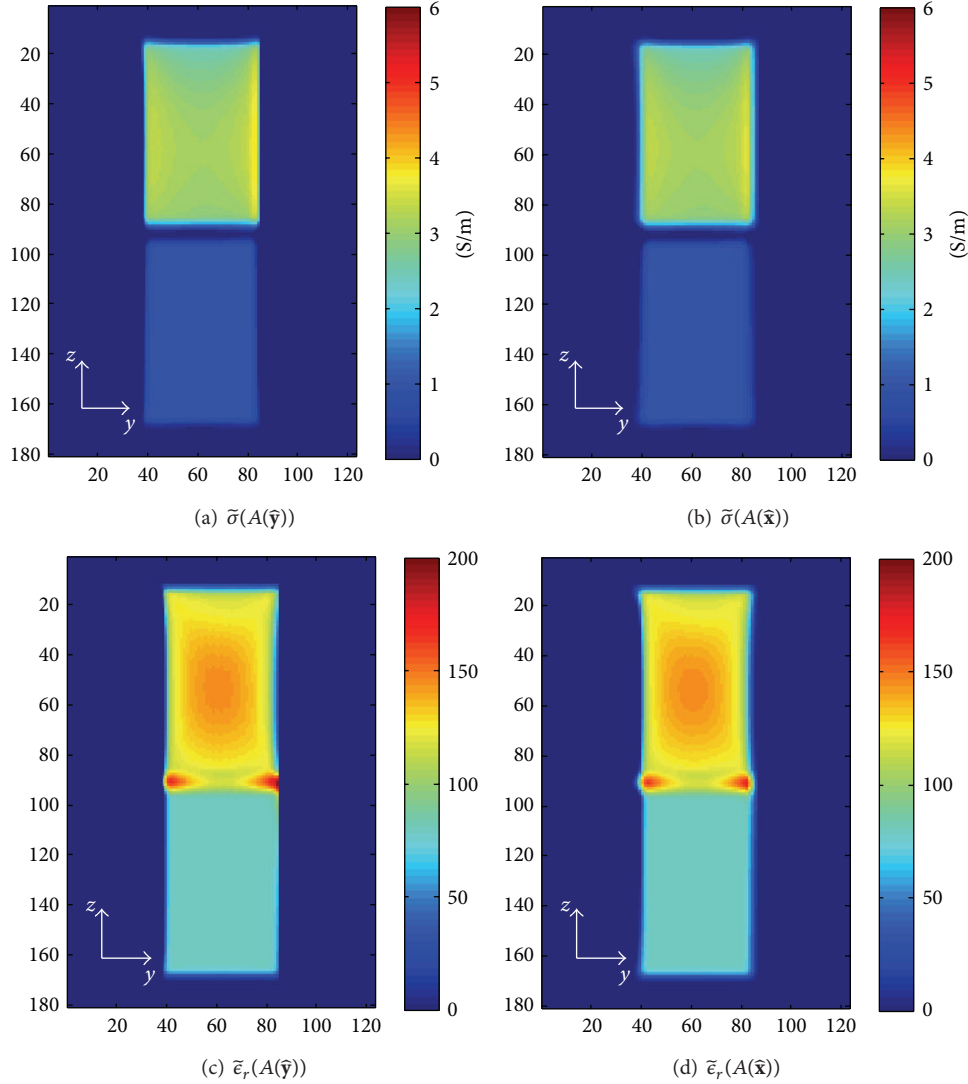


FIGURE 5: Circulating conductivity and relative permittivity derived from only H^+ : (a) $\bar{\sigma}(A(\bar{y}))$, (b) $\bar{\sigma}(A(\bar{x}))$, (c) $\bar{\epsilon}_r(A(\bar{y}))$, and (d) $\bar{\epsilon}_r(A(\bar{x}))$.

As shown in Figure 7, in a later section, the effective admittivity map (EAM) and the circulating admittivity map (CAM) can be drawn with the use of two angles, θ_{xy} and θ_{xz} which describe the direction of the normal vector. That is, the normal vector was initially located at the positive z -axis, was rotated along y -axis by θ_{xz} , and then was rotated along z -axis by θ_{xy} .

2.4. Numerical Simulation: Numerical Phantom Model with Anisotropic Effective Admittivity. For numerical evaluation, a numerical phantom with anisotropic effective admittivity can be generated using periodic binary medium. According to homogenization theory, anisotropy can be derived from pointwise admittivity, $\kappa(\mathbf{r})$, that is distributed periodically with respect to the y -variable:

$$\kappa(\mathbf{r}) := \begin{cases} \kappa_1 = \sigma_1 + i\omega\epsilon_1 & \text{if } 0 \leq Ny - [Ny] < c, \\ \kappa_2 = \sigma_2 + i\omega\epsilon_2 & \text{if } c \leq Ny - [Ny] < 1, \end{cases} \quad (10)$$

where $0 < c < 1$ is a constant depending on the binary medium, N is a large positive integer, and $[Ny]$ is the largest integer not greater than Ny .

In this numerical experiment the imaging subject is the box $\Omega := [-50, 50] \times [-50, 50] \times [-80, 80] \text{ mm}^3$. We divided the domain Ω into two subdomains $\Omega^0 := \{\mathbf{r} \in \Omega : z < 0\}$ and $\Omega^a := \{\mathbf{r} \in \Omega : z > 0\}$. In Ω^0 the admittivity is homogeneous with the value $\kappa = 1 + i\omega\epsilon$, where the permittivity $\epsilon = 80\epsilon_0$ with ϵ_0 the permittivity in the free space. In Ω^a 33 layers were stacked alternatively with the thickness of 2 mm, the admittivity value $\kappa_1 = 5 + i\omega\epsilon$ and the thickness of 1 mm, and the admittivity value $\kappa_2 = 0.3 + i\omega\epsilon$ in (10) with setting c to be $2/3$. Figure 1(a) shows the construction of the imaging object.

Driven by a birdcage coil at 3T ($\omega = 128 \text{ MHz}$) as shown in Figure 1(b), the electric fields, the magnetic fields, and the current densities in microscale were calculated using finite-difference time domain (FDTD) numerical simulations using REMCOM (REMCOM, State College, PA) with the

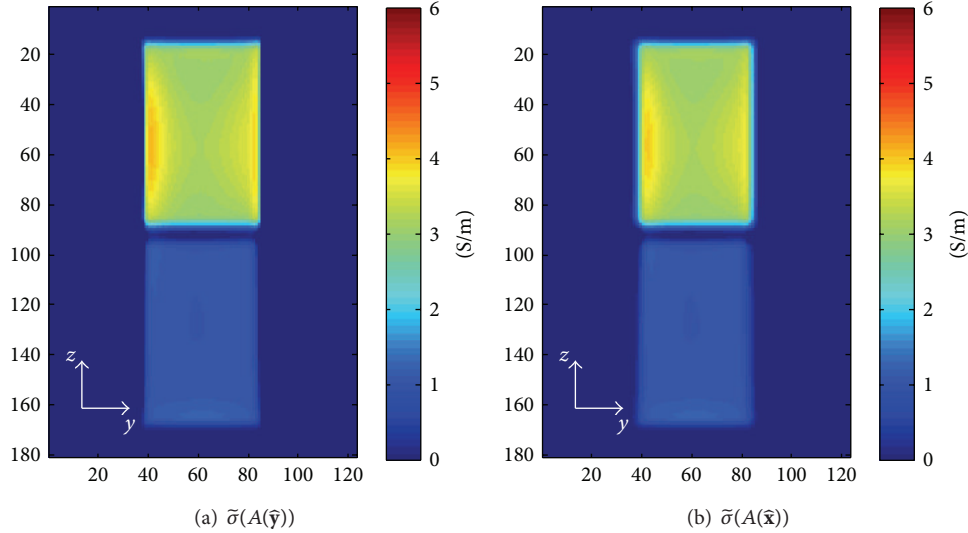


FIGURE 6: Circulating conductivity derived with only phase of H^+ , (a) $\bar{\sigma}(A(\hat{y}))$, (b) $\bar{\sigma}(A(\hat{x}))$.

resolution of $1 \text{ mm} \times 1 \text{ mm} \times 1 \text{ mm}$. Then, to determine the effective admittivity in macroscale, that is, the ratio of the ensemble mean current density to the ensemble mean electrical field, three-dimensional Gaussian filter with the size of $17 \times 17 \times 17 \text{ mm}^3$ and the standard deviation of 2.0 mm , which increases the effective voxel size from $(1 \text{ mm})^3$ to $(5 \text{ mm})^3$, was applied to the simulated fields.

2.5. MRI Experiments. Two phantoms with anisotropic admittivity were generated using straws as shown in Figure 2. As a comparison, one water phantom with isotropic admittivity was made without straws. Three phantoms were cylindrical with the height of 120 mm and the radius of 50 mm . The diameters of the straws are 12 mm for straw phantom 1 and 6 mm for straw phantom 2. All three phantoms were filled with the saline water of 0.35 M NaCl concentration as shown in Figure 2.

Using a single-channel transceive head coil, MR images were measured. The phantoms were located at the isocenter of the coil with the straw orientation of left-right. Only the phase of H^+ was measured and the circulating conductivity was determined by the phase-based approximation in MREPT [17]. Three-dimensional balanced steady-state free precession (bSSFP) was acquired with resolution of $3 \text{ mm} \times 3 \text{ mm} \times 3 \text{ mm}$, field of view (FOV) of $384 \text{ mm} \times 192 \text{ mm} \times 144 \text{ mm}$, and image size of $128 \times 64 \times 48$. The other imaging parameters were the flip angle of 30 degrees, TE of 1.8 ms , TR of 3.6 ms , and the scan time of 5 minutes with 27 averages. All measurements were performed on a 3T Siemens Tim Trio scanner. The phase of H^+ was estimated as the half of the measured phase of the image [17].

3. Results

3.1. The Effective Admittivity of the Numerical Phantom. Based on (4), by dividing the filtered current densities and

filtered electric fields, the effective anisotropic material can be acquired. Figures 3(a) and 3(d) illustrate the conductivity and the relative permittivity in microscale of 1 mm resolution in the slice at $\{x = 10 \text{ mm}\}$ that we set in this simulation, respectively. The effective conductivities in macroscale σ_{xx} , σ_{yy} are shown in Figures 3(b) and 3(c) and the effective relative permittivities are shown in Figures 3(e) and 3(f). For the subdomain of homogeneous tissue, Ω^0 , the conductivity and relative permittivity are constant and the same microscopically and macroscopically. The effective conductivity and relative permittivity are almost constant for the subdomain of the alternating layers of tissues, Ω^a except some distortions, we think, due to simulation errors. Since in this experiment κ_{zz} is the same as κ_{xx} , κ_{zz} was not shown here.

3.2. Observation of Anisotropy Using Circulating Admittivity (6). In MRI, only partial information of the magnetic fields can be measured. Using conventional single-transmit channel MR scanner, the circularly polarized component of the magnetic fields, $H^+ := (H_x + iH_y)/2$, can be measured but the other two components, $H^- := (H_x - iH_y)/2$, H_z , are hard to measure. Using a specialized scanner, parallel transmit system, the anticircularly polarized component could be measured [15]. Here, we considered two cases: (1) using H^+ and H^- , (2) using only H^+ . For the computation of the circulating admittivity using a partial information of the magnetic fields, the unmeasured magnetic fields were assumed to be zero.

Figure 4 illustrates the values of circulating conductivity and the relative permittivity, $\bar{\sigma}(A(\mathbf{n})) := \Re(\bar{\kappa}(A(\mathbf{n})))$ and $\bar{\epsilon}_r(A(\mathbf{n})) := \Im(\bar{\kappa}(A(\mathbf{n}))) / \omega\epsilon_0$, with H^+ and H^- at the slice, $x = 10 \text{ mm}$. The surface $A(\mathbf{n})$ for the integration (6) was chosen as a plane with the size of $5 \times 5 \times 1 \text{ pixels}^3$ and the normal vector, \mathbf{n} , of $\hat{\mathbf{x}}$, $\hat{\mathbf{y}}$. In this case, the two components of the magnetic fields, H^+ and H^- , were assumed to be

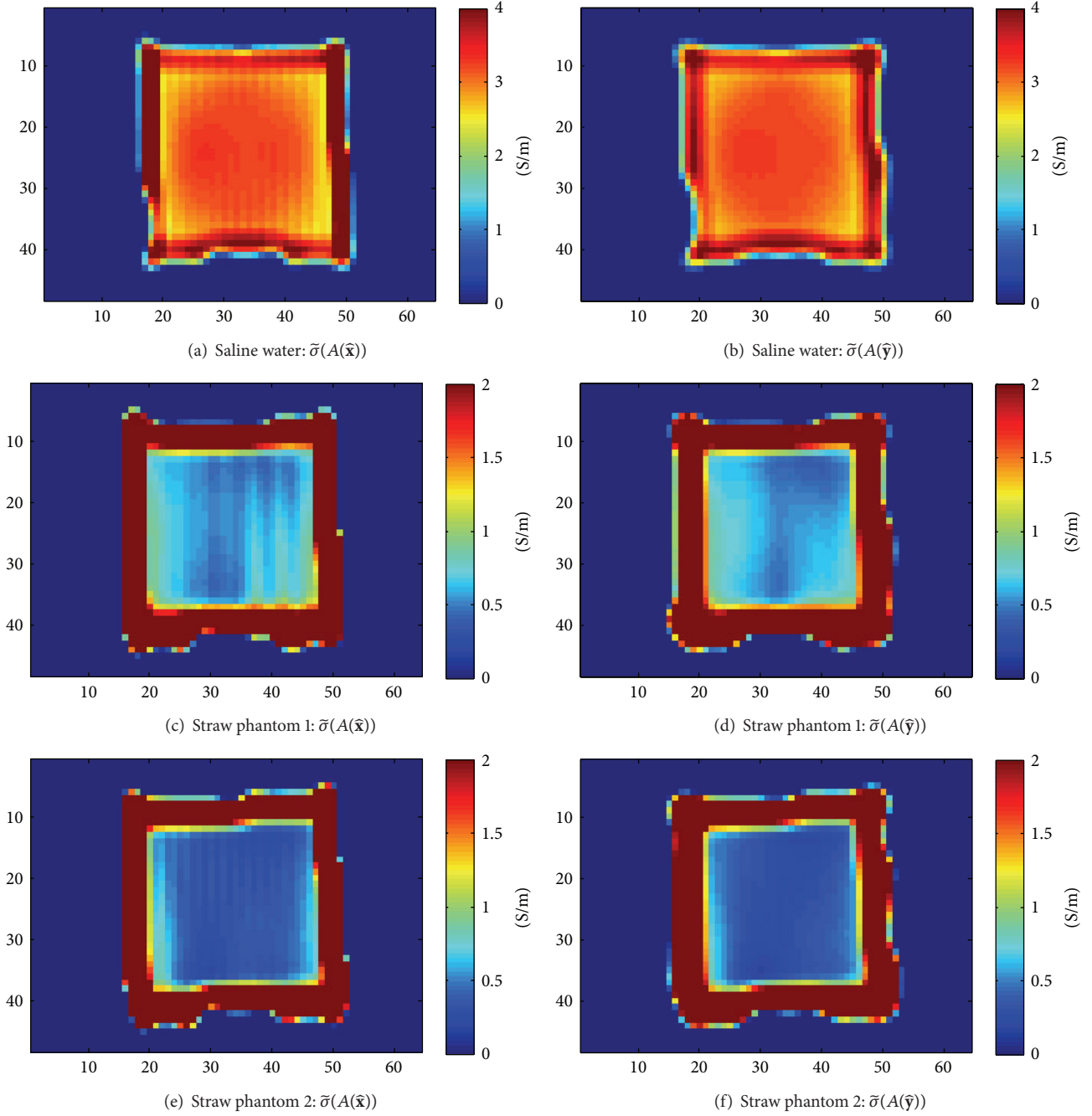


FIGURE 7: Experiment results: circulating conductivity of phantoms with measured H^+ , Coronal Slice, (a) $\bar{\sigma}(A(\hat{x}))$ of saline water, (b) $\bar{\sigma}(A(\hat{y}))$ of saline water, (c) $\bar{\sigma}(A(\hat{x}))$ of straw phantom 1, (d) $\bar{\sigma}(A(\hat{y}))$ of straw phantom 1, (e) $\bar{\sigma}(A(\hat{x}))$ of straw phantom 2, (f) $\bar{\sigma}(A(\hat{y}))$ of straw phantom 2.

known and used to reconstruct the circulating admittivity. As derived in (7), the circulating admittivity with the normal vector of \hat{y} , which is perpendicular on the two eigenvectors of the effective admittivity tensor with the same eigenvalues, is close to the effective admittivity in \hat{x} direction except at the tissue boundaries. For the normal vector of \hat{x} , the circulating admittivity is a weighted average of the effective admittivities, κ_{xx} , κ_{yy} , κ_{zz} . Thus, the circulating conductivity with the normal vector of \hat{x} is bigger than the effective conductivity

corresponding to the smallest eigenvalue of the effective admittivity tensor, σ_{yy} , shown in Figure 3(c).

However, as shown in Figures 5 and 6, if only one component, H^+ , is available, the dependency on the normal vector was lost in the circulating admittivity.

The circulating conductivities were determined from phantom experiments in which only the phase of H^+ is measurable. As shown in Figure 7, the dependency on the normal vector was also lost in the experimental results.

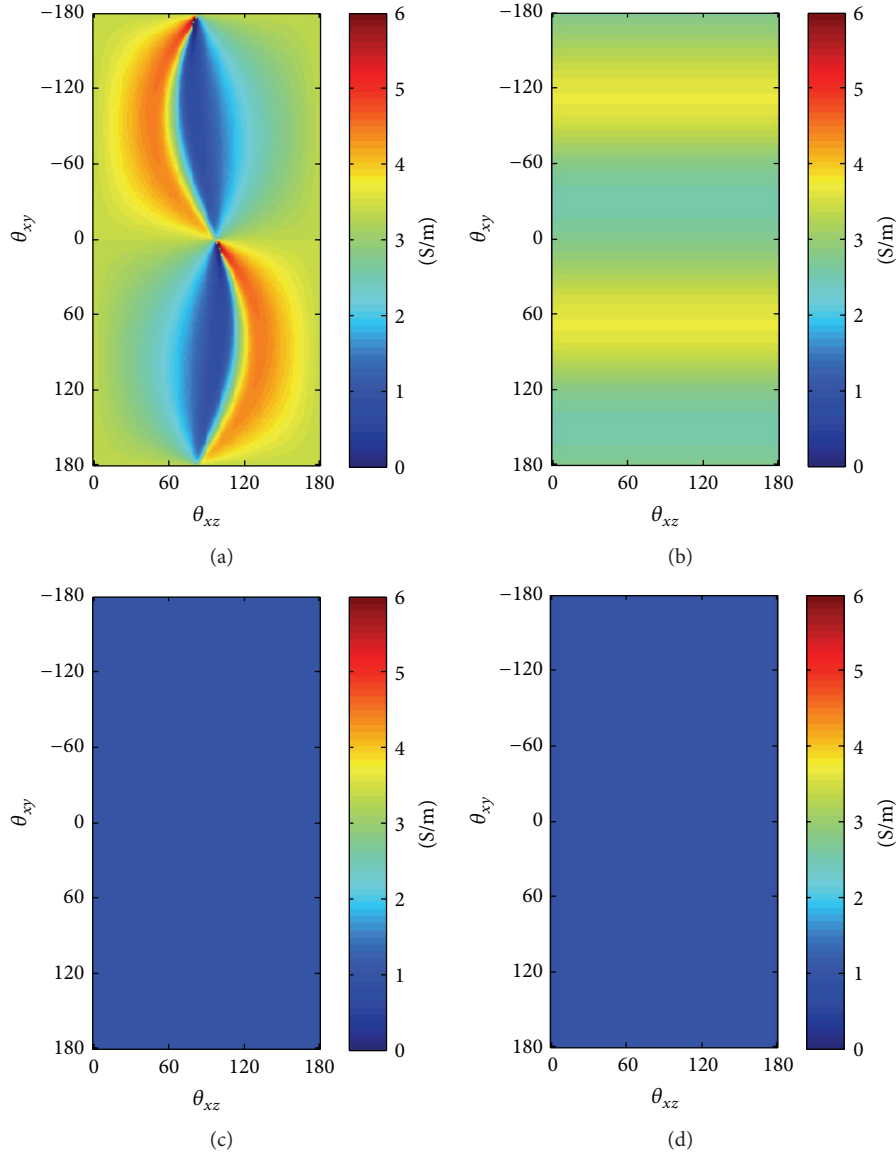


FIGURE 8: Effective conductivity maps and circulating conductivity maps of one anisotropic voxel and one isotropic voxel: (a) effective conductivity map of anisotropic voxel, $x = 10$ mm, $y = 0$ mm, $z = 40$ mm, (b) circulating conductivity map of anisotropic voxel, $x = 10$ mm, $y = 0$ mm, $z = 40$ mm, (c) effective conductivity map of isotropic voxel, $x = 10$ mm, $y = 0$ mm, $z = -40$ mm, (d) circulating conductivity map of isotropic voxel, $x = 10$ mm, $y = 0$ mm, $z = -40$ mm.

However, the decrease of the conductivity due to the plastic straws was observed.

3.3. Distribution of the Admittivity: Circulating Admittivity Map (CAM). Using simulated magnetic fields, H^+ and H^- , the circulating admittivity map (CAM) was computed for the numerical phantom. As a comparison, the effective conductivity map was also computed using simulated current density and electric fields. The θ_{xy} and θ_{xz} , which determined the direction of the normal vector \mathbf{n} , varied from $-180^\circ \sim 180^\circ$ and $0^\circ \sim 180^\circ$ by one degree. Figure 8 shows the effective conductivity maps, the real part of the EAM, and the circulating conductivity maps, the real part of the CAM, of

one anisotropic voxel located at $x = 10$ mm, $y = 0$ mm, and $z = 40$ mm and one isotropic voxel located at $x = 10$ mm, $y = 0$ mm, and $z = -40$ mm.

For the isotropic voxel, the values of the effective conductivity map and circulating conductivity map were equal to the conductivity of the tissue. For the anisotropic voxel, the circulating conductivity map is also uniform along the direction θ_{xz} since only H^+ and H^- were used. In both effective conductivity maps and circulating conductivity maps, the direction that maximizes or minimizes the conductivity value does not match with any eigenvector of the admittivity tensor. Thus, with CAM alone, the eigenvectors of the admittivity tensor may be hard to determine and thus a quantitative measurement of the eigenvalues may be hard.

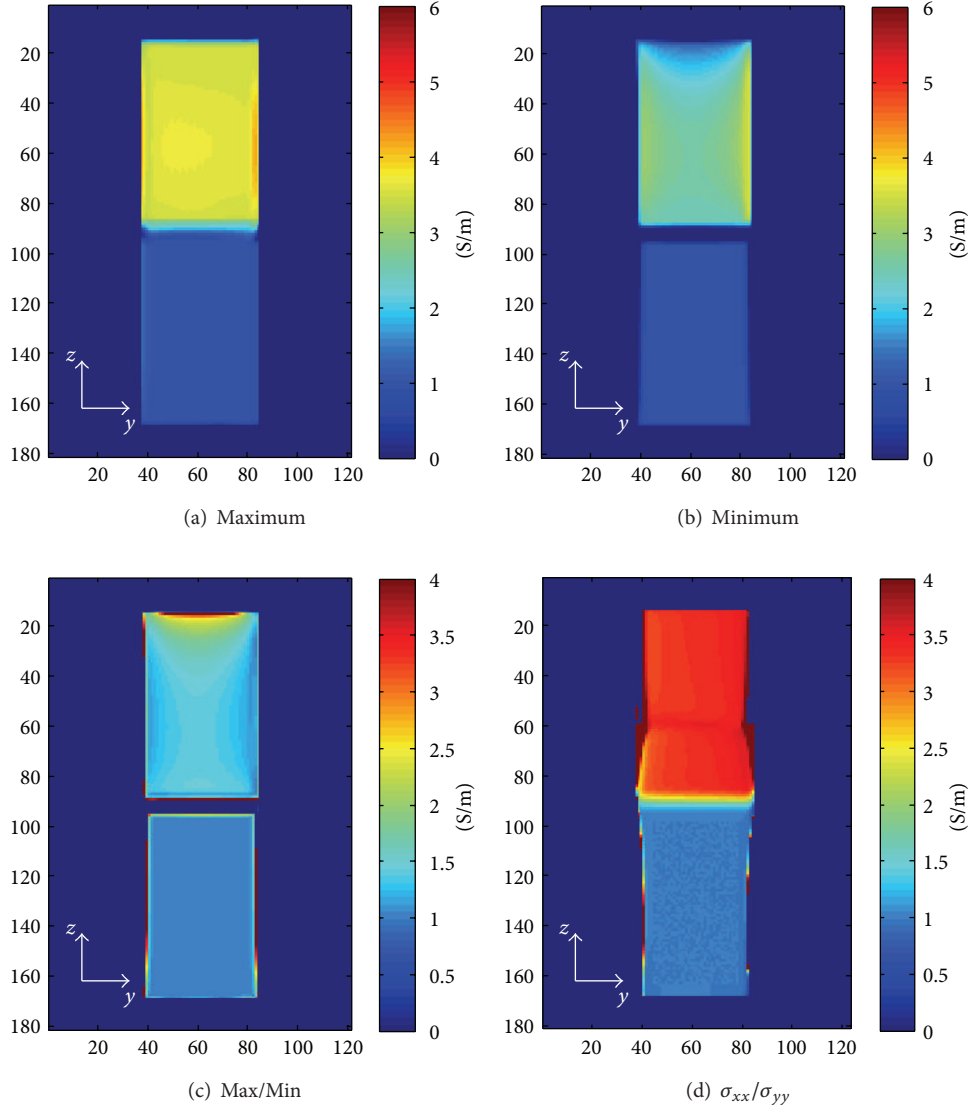


FIGURE 9: The distribution of the circulating conductivity: (a) the maximum values for the circulating conductivity maps, (b) the minimum values for the circulating conductivity maps, (c) the ratio of the maximum to the minimum, (d) the ratio of two eigenvalues in the conductivity tensor.

For a qualitative analysis, at each voxel, the maximum value, the minimum value, and the ratio of the maximum to the minimum of the circulating conductivity maps were computed with H^+ and H^- . As shown in Figure 9, in this case, the maximum values were almost constant over anisotropic tissues, but the minimum values were not constant. The ratio of the maximum to minimum, which could be used as a qualitative measurement of the anisotropy, was not constant over anisotropic tissues and was smaller than the ratio of the maximum eigenvalue, σ_{xx} , to the minimum eigenvalue, σ_{yy} , of the conductivity tensor; that is, using CAM, the contrast between isotropic and anisotropic tissues was reduced. However, CAM still can separate anisotropic tissues from isotropic tissues without knowing the eigenvectors of the admittivity tensor.

4. Discussion

Conductivity tensor is a simplified anisotropy model. Given three eigenvectors, the tensor can be estimated if the electric current densities and electric fields can be measured. In MRI, however, electric fields are hard to be measure without knowing or estimating the conductivity and permittivity of tissues. In this work, using MREPT formulae, the circulating admittivity is proposed as a measure to analyze the anisotropy of the tissues. Circulating admittivity was defined as the ratio of circulating current densities to the circulating electric fields, which can be determined from the magnetic fields. We did not fully investigate, but we derived the relationship between the admittivity tensor for special cases. Using numerical phantom simulations, we verified the relationship

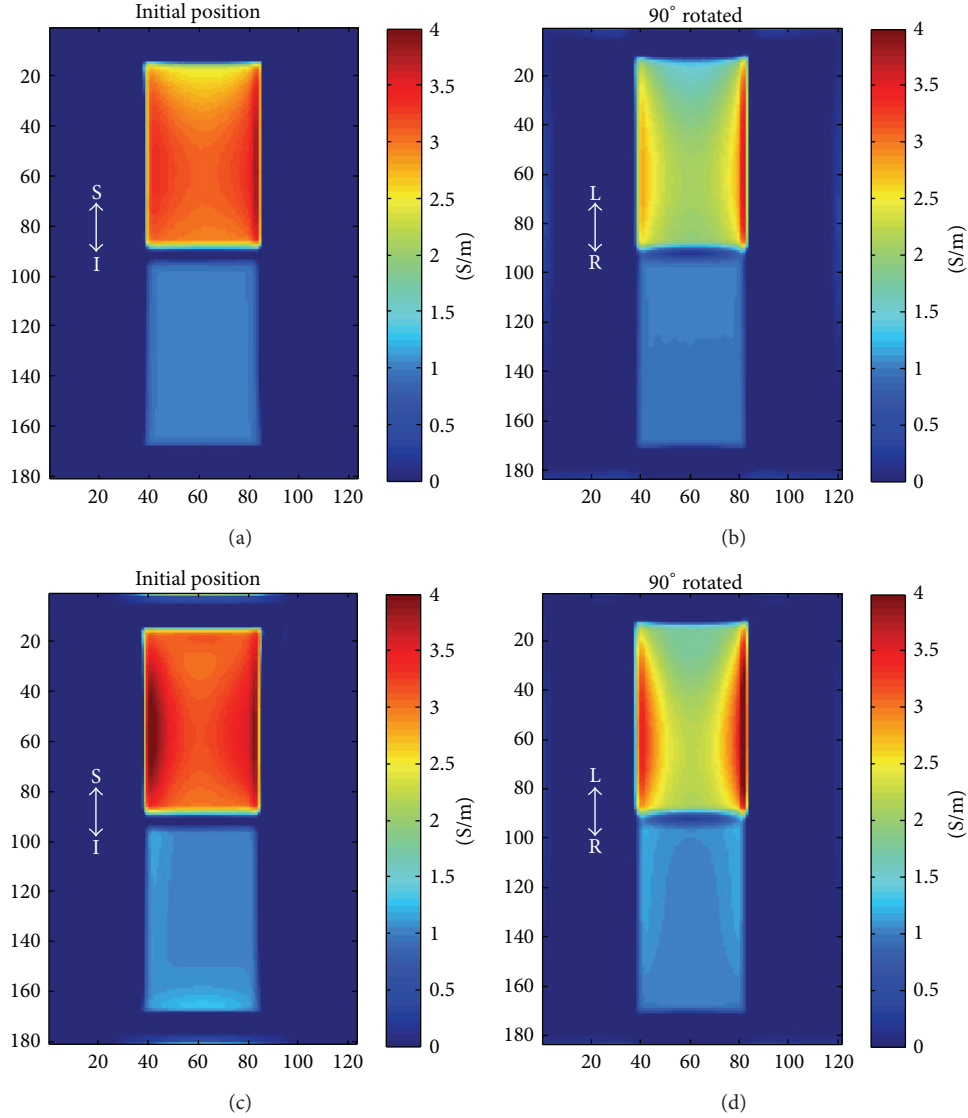


FIGURE 10: Simulation results: circulating conductivity of simulated phantoms with measured H^+ , coronal slice: (a) initial position using both magnitude and phase of H^+ , (b) 90° rotated using both magnitude and phase of H^+ , (c) initial position using only the phase of H^+ , and (d) 90° rotated using only the phase of H^+ .

for the first two cases: (1) isotropic tissues and (2) two eigenvalues of the admittivity tensor are the same. As a future work, more realistic cases would be considered.

In this work, to deal with unknown eigenvectors, the circulating admittivity map (CAM) was proposed as a qualitative measure. The ratio of the maximum to the minimum conductivity was reduced but still anisotropic tissues can be separated from isotropic tissues.

In the conventional single-transmit channel MR scanner, the circularly polarized magnetic field, H^+ , can be measured by B_1 mapping methods, but the other two components are hard to measure. If only one measurement of magnetic fields, H^+ is available, the anisotropic information is lost in the estimate of the circulating admittivity. Even if only one component of the magnetic fields, H^+ , can be measured, the anisotropic information can be acquired by measuring

several H^+ by rotating the object with respect to transmit coil. In Figures 10 and 11, the circulating conductivities only with H^+ for two positions of the object, that is, initial position and 90° rotated, are shown. For simulation data shown in Figure 10, the circulating conductivities were computed with both magnitude and phase of H^+ or with only phase of H^+ . For experimental data shown in Figure 11, only the phase of the H^+ was used. For isotropic tissues, circulating conductivity was not related to the position, but for anisotropic tissues, the circulating conductivity at the center of the phantom was changed. At the boundary of the phantom, very high or negative, especially at the top and the bottom of the phantom after rotating 90° , conductivity values were observed. We think that boundary artifacts [16] created at the air-water boundary were spread inside the phantom due to the spatial filtering used to reduce the noise in the conductivity estimates

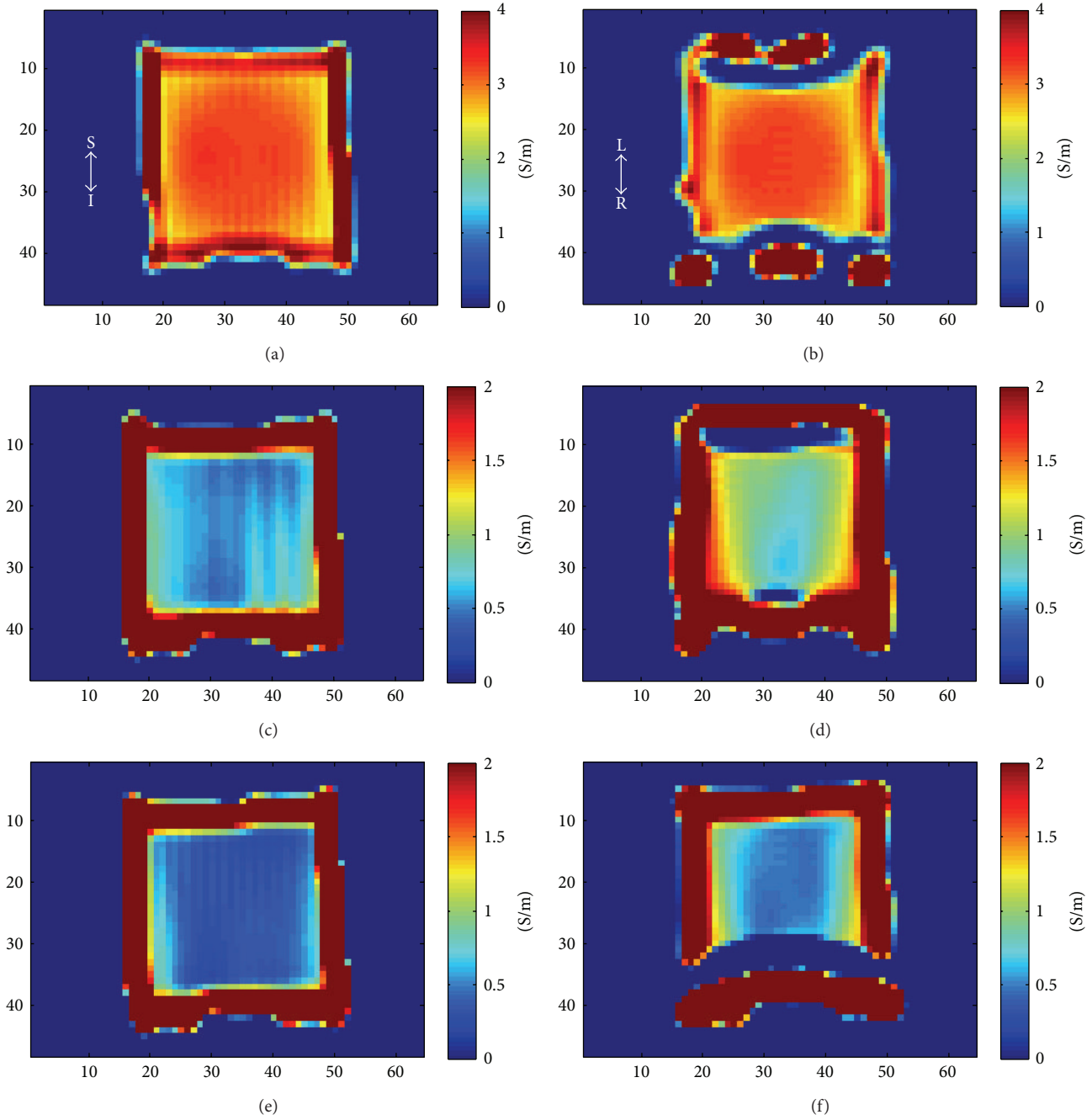


FIGURE 11: Experiment results: circulating conductivity of phantoms with measured H^+ , coronal slice, (a) saline water: initial position, (b) saline water: 90° rotated, (c) straw phantom 1: initial position, (d) straw phantom 1: 90° rotated, (e) straw phantom 2: initial position, (f) straw phantom 2: 90° rotated.

and thus our conductivity estimates at the boundary of the phantom were not reliable.

5. Conclusions

Noninvasive measurement of conductivity tensor at Larmor frequency could be achieved using MRI. Using measured B_1 maps from MRI, circulating current density and circulating electric fields can be estimated. In this work, the ratio of the

two, called circulating admittivity, was proposed as measure of the conductivity anisotropy at Larmor frequency. Given eigenvectors of the conductivity tensor, quantitative measurement of the eigenvalues can be achieved from circulating admittivity for special tissue models. Without eigenvectors, qualitative information of anisotropy still can be acquired from the distribution of the circulating admittivity. The limitation of the circulating admittivity is that the anisotropic information is lost if only one component of the magnetic

field is available. At least, an additional acquisition, either by rotating the object or some other scheme, needs to be performed for anisotropic information.

Acknowledgments

This work was supported by the National Research Foundation of Korea (NRF) Grant funded by Korea Government (MEST) (no. 2012-009903 to J. Lee, N. Choi, and D. H. Kim and no. 2011-8-1782 to Y. Song and J. K. Seo). The authors acknowledge Ulrich Katscher for beneficial discussions.

References

- [1] D. S. Tuch, V. J. Wedeen, A. M. Dale, J. S. George, and J. W. Belliveau, "Conductivity tensor mapping of the human brain using diffusion tensor MRI," *Proceedings of the National Academy of Sciences of the United States of America*, vol. 98, no. 20, pp. 11697–11701, 2001.
- [2] C. Gabriel, S. Gabriel, and E. Corthout, "The dielectric properties of biological tissues: I. Literature survey," *Physics in Medicine and Biology*, vol. 41, no. 11, pp. 2231–2249, 1996.
- [3] S. Gabriel, R. W. Lau, and C. Gabriel, "The dielectric properties of biological tissues: II. Measurements in the frequency range 10 Hz to 20 GHz," *Physics in Medicine and Biology*, vol. 41, no. 11, pp. 2251–2269, 1996.
- [4] L. A. Geddes and L. E. Baker, "The specific resistance of biological material—a compendium of data for the biomedical engineer and physiologist," *Medical and Biological Engineering*, vol. 5, no. 3, pp. 271–293, 1967.
- [5] S. Grimnes and O. G. Martinsen, *Bioimpedance and Bioelectricity Basics*, Academic Press, London, UK, 2000.
- [6] J. K. Seo, D. H. Kim, J. Lee, O. I. Kwon, S. Sajib, and E. J. Woo, "Electrical tissue property imaging using MRI at dc and Larmor frequency," *Inverse Problems*, vol. 28, Article ID 084002, 2012.
- [7] H. S. Khang, B. I. Lee, S. H. Oh et al., "J-substitution algorithm in magnetic resonance electrical impedance tomography (MREIT): phantom experiments for static resistivity images," *IEEE Transactions on Medical Imaging*, vol. 21, no. 6, pp. 695–702, 2002.
- [8] E. M. Haacke, L. S. Pappas, E. W. Nilges, and D. H. Wu, "Extraction of conductivity and permittivity using magnetic resonance imaging," *Physics in Medicine and Biology*, vol. 36, no. 6, pp. 723–733, 1991.
- [9] U. Katscher, T. Voigt, C. Findelee, P. Vernickel, K. Nehrke, and O. Dossel, "Determination of electrical conductivity and local SAR via B1 mapping," *IEEE Transactions on Medical Imaging*, vol. 28, pp. 1365–1374, 2009.
- [10] A. K. Sen and S. Torquato, "Effective conductivity of anisotropic two-phase composite media," *Physical Review B*, vol. 39, no. 7, pp. 4504–4515, 1989.
- [11] U. Katscher, T. Voigt, and C. Findelee, "Estimation of anisotropy of electric conductivity via B1 mapping," in *Proceedings of the 18th Annual Meeting of ISMRM*, p. 2866, Stockholm, Sweden, 2010.
- [12] S. Akoka, F. Franconi, F. Seguin, and A. Le Pape, "Radiofrequency map of an NMR coil by imaging," *Magnetic Resonance Imaging*, vol. 11, no. 3, pp. 437–441, 1993.
- [13] R. Stollberger and P. Wach, "Imaging of the active B1 field in vivo," *Magnetic Resonance in Medicine*, vol. 35, pp. 246–251, 1996.
- [14] V. L. Yarnykh, "Actual flip-angle imaging in the pulsed steady state: a method for rapid three-dimensional mapping of the transmitted radiofrequency field," *Magnetic Resonance in Medicine*, vol. 57, no. 1, pp. 192–200, 2007.
- [15] X. Zhang, P. F. V. de Moortele, S. Schmitter, and B. He, "Complex B1 mapping and electrical properties imaging of the human brain using a 16-channel transceiver coil at 7T," *Magnetic Resonance in Medicine*, 2012.
- [16] J. Seo, M. Kim, J. Lee et al., "Error analysis of non-constant admittivity for MR-based electric property imaging," *IEEE Transactions on Medical Imaging*, vol. 31, pp. 430–437, 2011.
- [17] T. Voigt, U. Katscher, and O. Doessel, "Quantitative conductivity and permittivity imaging of the human brain using electric properties tomography," *Magnetic Resonance in Medicine*, vol. 66, no. 2, pp. 456–466, 2011.

Review Article

Recent Progress and Future Challenges in MR Electric Properties Tomography

Ulrich Katscher,¹ Dong-Hyun Kim,² and Jin Keun Seo³

¹ Philips Technologie GmbH, Research Laboratories, Roentgenstraße 24-26, 22335 Hamburg, Germany

² Department of Electrical and Electronic Engineering, Yonsei University, Seoul 120-749, Republic of Korea

³ Department of Computational Science and Engineering, Yonsei University, Seoul 120-749, Republic of Korea

Correspondence should be addressed to Ulrich Katscher; ulrich.katscher@philips.com

Received 14 December 2012; Accepted 7 February 2013

Academic Editor: Eung Je Woo

Copyright © 2013 Ulrich Katscher et al. This is an open access article distributed under the Creative Commons Attribution License, which permits unrestricted use, distribution, and reproduction in any medium, provided the original work is properly cited.

MR Electric Properties Tomography (EPT) is a lately developed medical imaging modality capable of visualizing both conductivity and permittivity of the patient at the Larmor frequency using B_1 maps. The paper discusses the development of EPT reconstructions, EPT sequences, EPT experiments, and challenging issues of EPT.

1. Introduction

The knowledge of electrical tissue properties is expected to be beneficial for clinical diagnosis, therapy monitoring, and RF patient safety. Electrical tissue properties can be described by conductivity σ and permittivity ϵ , and they exhibit frequency-dependent behavior since tissues are heterogenous substances comprising insulating cell membranes and conducting electrolytes. Visualization of frequency-dependent conductivity and permittivity distribution in the range from almost dc to hundreds of MHz may expand our ability to provide diagnostic information about the physiological and pathological state of tissues and organs [1].

Due to its electromagnetic background, MRI would be a top candidate for delivering this desired knowledge of electrical tissue properties. The complex permittivity $\kappa := \epsilon - i(\sigma/\omega)$ at an angular frequency ω (assumed to be below microwave range) can be probed by the time-harmonic magnetic field $\mathbf{H} = (H_x, H_y, H_z)$ through the following arrangement of time Maxwell equations (so-called Helmholtz equation):

$$-\nabla^2 \mathbf{H} = \frac{\nabla \kappa}{\kappa} \times [\nabla \times \mathbf{H}] + \omega^2 \mu \kappa \mathbf{H}, \quad (1)$$

where μ is the magnetic permeability and κ is assumed to be isotropic. Here, the corresponding time-varying field is $\text{Re}\{\mathbf{H}e^{i\omega t}\}$.

At frequencies below 1 kHz, Joy et al. in 1989 [2] introduced MR current density imaging (MRCDI) which aims to provide noninvasive visualization of current density $\mathbf{J} = \nabla \times \mathbf{H}$ inside a body by externally injecting dc current using a pair of surface electrodes and measuring the induced magnetic field \mathbf{H} using MRI. In MRCDI, the induced current density \mathbf{J} produces a change of the main dc magnetic field, and H_z is a measurable quantity by MRI since it alters the MR phase image. Hence, from MRCDI, obtaining an image of $\mathbf{J} = \nabla \times \mathbf{H}$ requires mechanical rotation of the subject inside MRI to measure all three components of \mathbf{H} [3]. In 1994 [4], MR electrical impedance tomography (MREIT) was proposed to perform the conductivity imaging at dc using the MRCDI technique. In 2001 [5], an imaging technique of MREIT without mechanical rotation, called harmonic B_z algorithm, was developed to provide both conductivity image and current density image. After invention of the harmonic B_z algorithm, MREIT has advanced rapidly [6, 7]. However, it still remains a technical problem to reduce the injection current down to a level for routine clinical use while maintaining the spatial resolution of the resulting conductivity images.

At frequencies above 1MHz, the currents required to image electric properties have not necessarily to be injected by external surface electrodes as in MREIT. Alternatively, eddy currents can be induced by applying magnetic RF fields, avoiding the sensation of pain frequently connected with external current injection. Since magnetic RF fields are an inherent component of MRI, the desired currents can be created by standard MR systems and standard MR sequences. The resulting imaging technique, called Electric Properties Tomography (EPT) [8–11], is the subject of this paper. The basic idea of EPT is that the electric properties of the patient distort B_1 , the component of the magnetic RF field responsible for spin excitation. Measuring this distorted B_1 by B_1 mapping techniques (see, e.g., [12–17]) allows to reconstruct the electric properties causing the observed distortions. This basic idea of EPT is illustrated in Figure 1, depicting the change of the phase of the magnetic RF field due to a brain tumor with a diameter of 1 cm. This phase change increases with the applied frequency, that is, the main field B_0 of the MR system used. This phase change also increases with the conductivity of the tumor. The obtained phase changes of several degrees are in a measurable range. Phase changes further increase with increasing tumor size.

RF currents induced in the tissue cause not only a distortion of B_1 , which is utilized for EPT as discussed above, but also off-resonance effects. As in MRCDI, these off-resonance effects can be utilized to measure the current density along the direction of B_0 , called RF-CDI. RF-CDI is not part of this paper, and interested readers might be referred to the corresponding literature [18–20]. The following chapters review the development of EPT reconstructions, EPT sequences, and EPT experiments.

2. Development of EPT Reconstruction

Without calling the approach EPT, the first mentioning of EPT was in the early nineties by Haacke et al. [8]. It was suggested to calculate both conductivity σ and permittivity ϵ via the homogeneous Helmholtz equation

$$\kappa(\mathbf{r}) = \frac{-1}{\omega^2 \mu_0} \frac{\nabla^2 H^+(\mathbf{r})}{H^+(\mathbf{r})}, \quad (2)$$

where $\mathbf{r} := (x, y, z)$ and $H^+ := (H_x + iH_y)/2$, the positive circularly polarized component of the magnetic field corresponding to the RF transmit field. Here, the main magnetic field is $\mathbf{B}_0 = -B_0 \hat{\mathbf{z}}$, and the corresponding complex rotating vector is $\mathbf{a}_+ = \hat{\mathbf{x}} - i\hat{\mathbf{y}}$, where $\hat{\mathbf{x}} = (1, 0, 0)$, $\hat{\mathbf{y}} = (0, 1, 0)$, $\hat{\mathbf{z}} = (0, 0, 1)$, and $B_0 > 0$. From (2), σ and ϵ can be expressed as

$$\sigma = \frac{1}{\omega \mu_0} \operatorname{Im} \left\{ \frac{\nabla^2 H^+}{H^+} \right\}, \quad \epsilon = \frac{-1}{\omega^2 \mu_0} \operatorname{Re} \left\{ \frac{\nabla^2 H^+}{H^+} \right\}. \quad (3)$$

Equation (2) is derived from (1) with the following assumptions.

- (A1) A locally (“piecewise”) constant $\kappa(\mathbf{r})$, that is; $\nabla \kappa(\mathbf{r}) = 0$. This assumption has severe consequences, which has to be discussed extensively later on.

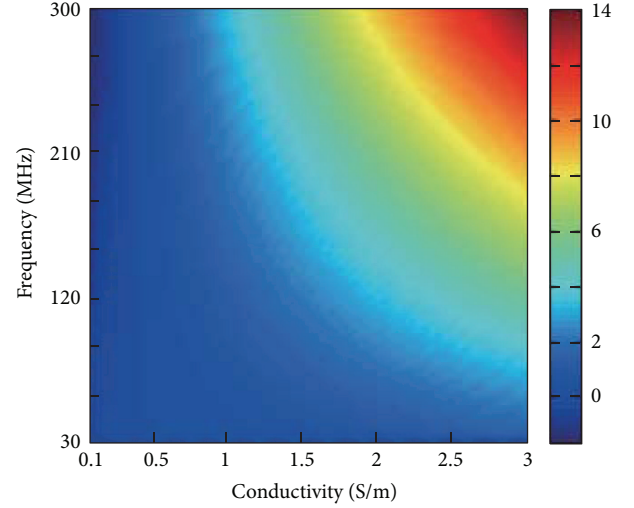


FIGURE 1: Change of magnetic RF field phase due to a brain tumor with a diameter of 1 cm. This phase change increases with the applied frequency (corresponding to the system’s main field B_0) as well as with the conductivity of the tumor. A mean conductivity of 0.4 S/m was assumed for the healthy parts of the brain, and thus, negative phase changes appear for assumed tumor conductivities below 0.4 S/m.

- (A2) A constant $\mu(\mathbf{r}) = \mu_0 = 4\pi \times 10^{-7}$, the magnetic permeability of the free space. This assumption is fairly fulfilled in the human body and does not require further discussion.
- (A3) Isotropic κ . At the Larmor frequency of 128 MHz at 3 T, anisotropy is small in most tissues but yields an interesting niche application of EPT.
- (A4) $|H^+|$ is assumed to be larger than zero to avoid singularities in (2). This is obviously the case in areas of nonzero MR signal.

An invaluable advantage is the cancelation of the scaling of H^+ in the numerator and denominator of the expression (2). Given this cancelation, (2) yields absolute values of κ , even for arbitrary scaling of H^+ . This feature ennobles EPT to the class of quantitative MR methods, opening the chance to directly compare κ between different patients and different lesions. However, in the named publication [8], EPT was not pursued further due to “*spurious phase effects unrelated to RF penetration which makes a simple extraction difficult.*” Although the mentioned spurious phase effects predominantly belonged to imperfections of the MR systems back in the early nineties, which greatly reduced since then, phase effects unrelated to RF penetration are still one of the major issues for EPT, particularly for in vivo measurements. Instead of the mentioned “*simple extraction*” of κ , Haacke et al. developed a heterogeneous layer model as a workaround for the observed spurious phase effects [8].

The first successful application of EPT (still not called EPT) described by Wen [9] is dated more than 10 years after Haacke’s initial article. In this conference abstract, the expressions (3) are used again. Two further observations

are mentioned by Wen, which later on turned out to be of central importance for EPT.

- (O1) Computations of (3) require both magnitude and phase of $H^+ = |H^+|e^{i\phi^+}$. Unfortunately, only the magnitude $|H^+|$ enters the MR signal in a nonlinear way; for each nominal flip angle α of the sequence, the following MR signal is measured:

$$S(\mathbf{r}) = V_1 M_0(\mathbf{r}) H^-(\mathbf{r}) \exp(i\phi^+(\mathbf{r})) \sin(V_2 \alpha |H^+(\mathbf{r})|), \quad (4)$$

where M_0 is the MR magnitude image containing relaxation and spin density effects, $H^- = (H_x - iH_y)/2$, and V_1, V_2 system-dependent constants [21]. Thus, $|H^+|$ has the chance to be measured exactly, assuming the ideal working of corresponding B_1 mapping techniques (see, e.g., [12–17]). However, the phase ϕ^+ is difficult to be determined exactly. The phase of a standard MR image is always the superposition of ϕ^+ with its counterpart of the RF reception, ϕ^- from H^- and, thus, is called “transceive phase” $\phi_0 = \phi^+ + \phi^-$. In a standard MR system with a quadrature body coil (QBC), the polarization of this coil is switched from RF transmission to RF reception for the sake of optimizing SNR. Wen observed that the resulting $\tilde{\phi}^-$ of the switched QBC closely resembles ϕ^+ [9]. Consequently, a rough approximation of ϕ^+ can be obtained by the transceive phase $\tilde{\phi}_0 = \phi^+ + \tilde{\phi}^-$ of this setup

$$\phi^+ \approx \tilde{\phi}_0/2 = (\phi^+ + \tilde{\phi}^-)/2 \quad (5)$$

sometimes called “transceive phase assumption.”

- (O2) To the leading order, the conductivity response affects the phase of the RF field, while the permittivity response affects the magnitude of the field. Thus, σ can be estimated by applying (2) only to ϕ^+ , now called “phase-based EPT”. Accordingly, ϵ can be estimated by applying (2) only to $|H^+|$, now called “magnitude-based EPT”.

In principle, these two observations pave the way to a clinically feasible EPT. Moreover, the first successful phantom and ex vivo experiments are presented in [9], which will be topic of a later section dedicated to experimental EPT results. After this publication, Wen left the topic of EPT, and again EPT was not further pursued for years.

Systematic research on EPT started in 2009 with [10]. This publication is based on the following expression which comes from a modified Helmholtz equation:

$$\kappa(\mathbf{r}) = \frac{\oint_{\partial A_r} \nabla \times \mathbf{H}(\mathbf{r}') \cdot d\mathbf{l}}{\mu_0 \omega^2 \int_{A_r} \mathbf{H}(\mathbf{r}') \cdot d\mathbf{S}}, \quad (6)$$

where A_r is an arbitrarily oriented area centered at \mathbf{r} with its boundary ∂A_r , $d\mathbf{l}$ the line element, and $d\mathbf{S}$ the surface

element. Equation (6) can be viewed as dividing Ampere’s law by Faraday’s law after suitably integrating these laws. In contrast to (2), the expression (6) requires all three components of the magnetic field \mathbf{H} . Since H^- and H_z are not measurable directly, $H^- = 0$ and $H_z = 0$ were assumed for the applied QBC [10]. Nevertheless, a couple of basic findings studied with this modified Helmholtz equation is valid for all kinds of EPT reconstructions. First of these basic findings, the violation of assumption (A1), the locally constant κ , leads to severe artifacts along boundaries between compartments of different κ . These artifacts are typically strong oscillations (under/overshooting) of the reconstructed κ as shown in Figure 3. This is predominantly a question of the numerical implementation of the calculus operations of the EPT equation applied, which always involves a number of voxels in the neighborhood of the target voxel to be reconstructed. This so-called kernel of involved voxels, regardless of the actual calculus operation, causes the mentioned oscillations as soon as it contains voxels of different κ . Thus, as shown in [10], lowering the kernel size narrows the oscillations, and a kernel of minimal size seems to be optimal. As shown in [10], lowering the kernel size also degrades the noise figure. This touches another basic finding: the second derivative, as enclosed explicitly or implicitly in all EPT equations, tends to significantly enhance the noise in the measured H^+ . For minimal kernel size, the SNR of the reconstructed κ is far below the SNR of the input H^+ [10, 22]. This initiated a bunch of activities to find the optimal tradeoff between artifacts and SNR or to find suitable workarounds, as discussed later.

Besides, for the phantom used in [10], the violation of the transceive phase assumption (O1) was proven to be far below 1° , and thus errors arising from this violation are expected to be lower than errors from other sources. Last but not least, in [10], EPT was first applied to estimate local SAR.

Another milestone of EPT reconstruction is given by [11]. In contrast to the factual, “physical” modification of (2) in [10], the modification in [11] is the result of reformatting the original equation (2) by suitably integrating its numerator and denominator:

$$\kappa(\mathbf{r}) = \frac{-\int_{\partial V_r} \nabla \left[|H^+(\mathbf{r}')| e^{i\phi^+(\mathbf{r}')} \right] \cdot d\mathbf{S}}{\mu_0 \omega^2 \int_{V_r} |H^+(\mathbf{r}')| e^{i\phi^+(\mathbf{r}')} dV}, \quad (7)$$

where V_r is a volume centered at \mathbf{r} with its boundary ∂V_r and dV is the volume element. The denominator of (7) averages the denominator of (2) over a certain volume, while the numerator integrates the normal derivative to the surface of this volume. From a numerical point of view, the minimal kernel size of (7) is larger than the minimal kernel size of (2), looking for a better solution of the above-mentioned tradeoff between boundary artifacts and noise level. A systematic comparison of the behavior of (2) and (7) is conducted

in [23]. Equation (7) can be rewritten with separate real and imaginary part

$$\kappa = \frac{-1}{\mu_0 \omega^2} \left[\left(\frac{\nabla^2 |H^+|}{|H^+|} - |\nabla \phi^+|^2 \right) + i \left(2 \nabla \ln |H^+| \cdot \nabla \phi^+ + \nabla^2 \phi^+ \right) \right]. \quad (8)$$

As already indicated in [9], observation (O2), the assumption $|\nabla^2 \phi^+| \gg 2|\nabla \ln |H^+| \cdot \nabla \phi^+|$ yields phase-based EPT for conductivity imaging

$$\sigma(\mathbf{r}) \approx \frac{\nabla^2 \phi^+(\mathbf{r})}{\mu_0 \omega}, \quad (9)$$

and the assumption $|\nabla^2 |H^+|/|H^+|| \gg |\nabla \phi^+|^2$ yields magnitude-based EPT for permittivity imaging

$$\epsilon(\mathbf{r}) \approx \frac{-\nabla^2 |H^+(\mathbf{r})|}{\mu_0 \omega^2 |H^+(\mathbf{r})|}. \quad (10)$$

Reference [11] derives analytically the related errors of these approaches and investigates systematically their feasibility. For typical κ of human tissue at 1.5 T or 3 T, the error introduced by the expressions (9)-(10) is only of the order of 10%. As can be seen directly from the corresponding error terms, phase-based EPT always yields too high conductivities, and magnitude-based EPT always yields too low permittivities. Thus, the discussed errors can be hidden by mapping not σ or ϵ , but $|\kappa|$ as shown in [24].

Phase-based EPT reveals two features invaluable for clinical applications.

- (F1) The linearity of the expression (9) supersedes the QBC transceive-phase assumption (5), allowing arbitrary combinations of RF transmit and receive coils. The resulting transceive phase, containing ϕ^+ and ϕ^- from different RF fields, still yields σ via

$$\sigma = \frac{\nabla^2 \phi_0 / 2}{\mu_0 \omega} = \frac{\nabla^2 (\phi^+ + \phi^-)}{2\mu_0 \omega} \quad (11)$$

$$= \frac{1}{2} \left(\frac{\nabla^2 \phi^+}{\mu_0 \omega} + \frac{\nabla^2 \phi^-}{\mu_0 \omega} \right) = \frac{2\sigma}{2}$$

since (9) can be based on ϕ^+ , ϕ^- , or any phase fulfilling Maxwell's equations, leading to the same σ as long as $\nabla |H^+| = 0$ and $\nabla |H^-| = 0$ are fulfilled.

- (F2) Skipping the need of mapping (the magnitude of) B_1 , which is typically a rather lengthy scan, significantly speeds up the scan time required for EPT. As discussed below, even real-time conductivity measurements seem to be possible [25]. Moreover, it opens the chance that the conductivity can be obtained via sequences which are not primarily driven for EPT, just reusing the transceive phase which usually comes for free with every MR sequence.

Shortly after [11], which was performed at $B_0 = 1.5$ T, phase-based EPT has been confirmed at $B_0 = 7$ T [26]. The impact of B_0 on EPT and the related question of B_0 optimal for EPT turned out to be a nontrivial task [27]. Obviously, higher SNR can be expected with increasing B_0 . This advantage is counterbalanced by the increasing violation of the assumption $\nabla |H^+| = 0$ for (9) or the QBC transceive phase assumption (5), respectively. Although not explicitly stated by the authors of [27], the optimal tradeoff between SNR and reconstruction accuracy seems to be given at $B_0 = 3$ T for conductivity imaging. For permittivity imaging, the violation of the assumption $\nabla \phi^+ = 0$ does not increase with B_0 , and the highest available B_0 seems to be optimal. This trend is further emphasized by the different powers of ω in (3).

Since 2009, research on EPT spread out, and more and more groups started to investigate different aspects of EPT [26–31]. Typically, the original expression (2) has been used in these studies.

The problem of separating ϕ^+ and ϕ^- from the transceive phase has been solved analytically by an approach sometimes called ‘‘Local Maxwell Tomography’’ (LMT) [32–34]. LMT is based on the insight that the reconstructed κ must not depend on the applied RF coil [31]. This is a particularly useful insight given a system with multiple, independent RF transmit channels (see, e.g., [35, 36]). Such multitransmit systems, designed primarily for RF shimming at high B_0 , offer the chance to determine κ separately by each single TX channel or any arbitrary combination of TX channels. Differences of the reconstructed κ based on different RF excitations can be related to a violated transceive phase assumption. For instance, two EPT reconstructions σ_n and σ_m can be compared based on different TX channels n and m , but same receive channel with phase ϕ^- , yielding [34]

$$\sigma_n(\mathbf{r}) - \sigma_m(\mathbf{r}) = \frac{1}{\mu_0 \omega} \nabla \phi^-(\mathbf{r}) \cdot \nabla \ln \frac{|H_n^+(\mathbf{r})|}{|H_m^+(\mathbf{r})|}. \quad (12)$$

This allows, first, first, the determination of the unknown ϕ^- and, subsequently, the straightforward determination of the unknown ϕ_n^+ and ϕ_m^+ . The central idea of comparing reconstruction results of two or more different TX channels can also be utilized to exactly distinguish $|H^-|$ from the spin magnetization M_0 , another hitherto unexplored possibility [33]. Unfortunately, the numerical effort to solve the related equations is high. It shall be clarified in future studies, if the accuracy of the obtained ϕ^+ is high enough to improve reconstruction results hitherto obtained in the framework of the discussed phase assumptions. The explicit knowledge of ϕ^+ , ϕ^- , and $|H^-|$ seems to be more urgent for the determination of local SAR [34].

Thus, at least on a theoretical basis, the issue of phase determination is figured out, and the last remaining issue for the EPT reconstruction is the treatment of nonconstant κ (see Figure 3). Equation (2) can be viewed as a simplified version of (1) using the assumption (A1) of $\nabla \kappa = 0$ so that the effect of $(\nabla \kappa / \kappa) \times [\nabla \times \mathbf{H}]$ in (1) is neglected. Here, κ might change continuously or discontinuously across boundaries of compartments with different values of κ . Both types of changing κ

and the related errors have been analyzed thoroughly in [37]. In (1), the occurring partial derivatives of κ act as additional unknowns. It was suggested that these additional unknowns can be solved using the described comparison of different RF excitations [31]. Comparing (simulations of) two different RF excitations and therefore calling the algorithm “dual excitation algorithm,” the typical boundary artifacts were significantly reduced. Alternatively, it has been proposed to multiply (1) with $\nabla \times \mathbf{H}$ yielding [38]

$$\kappa(\mathbf{r}) = -\frac{\nabla^2 \mathbf{H}(\mathbf{r}) \cdot (\nabla \times \mathbf{H}(\mathbf{r}))}{\omega^2 \mu \mathbf{H}(\mathbf{r}) \cdot (\nabla \times \mathbf{H}(\mathbf{r}))}. \quad (13)$$

This equation has the big advantage of removing the term involving $\nabla \kappa$ in (1). However, computation of (13) requires all spatial components of \mathbf{H} and $|\mathbf{H} \cdot \nabla \times \mathbf{H}| > 0$. The authors of [31, 38] propose to assume $H^- = 0$ and $H_z = 0$ as it was done in connection with (6) [10]. A challenging problem is to find an exact relation between κ and H^+ from the full equation (1) in such a way that κ can be computed robustly and efficiently using H^+ only.

From a numerical point of view, the occurring oscillations along compartment boundaries are a question of finite kernel size as explained above. Thus, instead of solving (1), boundary artifacts can be avoided by image segmentation prior to reconstruction and performing separate reconstructions on the different compartments. This was demonstrated in [39] in the framework of breast EPT, where different conductivities of highly nested fatty and ductile tissue spoil a standard EPT reconstruction completely. The image segmentation can be used for shaping the applied kernel locally to the current tissue type, as well as for locally restricting a subsequently applied smoothing filter [39]. The mentioned image segmentation can be based on standard T1/T2 weighted images, which implies that same T1/T2 coincides with same σ . This of course is not automatically fulfilled; however, violations of this assumption are expected to occur much less than discontinuous σ across T1/T2 boundaries.

This chapter ends with a brief discussion of anisotropic κ violating (A3). Anisotropic κ (a rank-2 tensor) can be characterized by its eigenvectors $\mathbf{v}_1, \mathbf{v}_2$, and \mathbf{v}_3 (unit vectors) and its corresponding eigenvalues κ_1, κ_2 , and κ_3 , respectively:

$$\kappa = (\mathbf{v}_1 \ \mathbf{v}_2 \ \mathbf{v}_3) \begin{pmatrix} \kappa_1 & 0 & 0 \\ 0 & \kappa_2 & 0 \\ 0 & 0 & \kappa_3 \end{pmatrix} \begin{pmatrix} \mathbf{v}_1 \\ \mathbf{v}_2 \\ \mathbf{v}_3 \end{pmatrix}. \quad (14)$$

Measuring anisotropy of the tissue conductivity, characterizing the underlying cell structure, might increase diagnostic information. In vivo, anisotropic conductivities can be found in tissue with preferred cell direction, for example, in muscles and nerves. However, one has to keep in mind that anisotropy of κ is expected to decrease with increasing ω , and anisotropy at Larmor frequency could be negligible. Nevertheless, it was pointed out that varying the orientation of the integration area A in (6) reflects the degree of anisotropy [40, 41]. To be precise, let $A(\mathbf{n})$ be a disk with its unit normal vector \mathbf{n} . Some

anisotropic structure of κ can be observed by displaying the following quantity on the sphere S^2 [41]:

$$\Theta(\mathbf{n}) := \frac{\oint_{\partial A(\mathbf{n})} \nabla \times \mathbf{H} \cdot d\mathbf{l}}{\mu_0 \omega^2 \int_{A(\mathbf{n})} \mathbf{H} \cdot d\mathbf{S}}, \quad \mathbf{n} \in S^2. \quad (15)$$

A perfectly isotropic κ should not depend on the direction \mathbf{n} of $A(\mathbf{n})$. On the other hand, the reconstructed κ should show a minimum for $A(\mathbf{n})$ perpendicular to the (main) direction of a (strongly) anisotropic κ . Experimental results of a straw phantom confirmed this concept [40]. However, according to corresponding simulations [41], the concept shall not work without proper knowledge of H^- .

3. EPT Sequence

3.1. Measuring B_1 Magnitude. As seen in (4), the transmit magnitude $|H^+|$, required for EPT, can be measured in a straightforward manner due to its nonlinear impact on the MR signal. In this framework, numerous techniques for $|H^+|$ mapping (B_1 mapping) are published (see, e.g., [12–17]). In principle, EPT can be based on any B_1 mapping method. The accuracy of EPT depends on the accuracy of this mapping; that is, the most accurate $|H^+|$ mapping method leads to the most accurate EPT results. Studies looking for the optimum B_1 mapping technique, independent of EPT, have been published elsewhere.

3.2. Measuring B_1 Phase. As discussed in the previous chapter, determination of the B_1 phase ϕ^+ always starts with the measurement of the transceive phase. One of the main issues of EPT, as already pointed out in [8], is the contamination of the transceive phase by unwanted phase contributions unrelated to RF penetration. The following steps from (S1) to (S4) describes how to get a transceive phase usable for EPT reconstruction.

- (S1) The transceive must not contain any contributions from B_0 , that is, any off-resonance effects. The easiest way to exclude off-resonance effects is the use of refocusing pulses, that is, sequences based on spin echoes (SE), like fast spin echo sequences, turbo spin echo sequences, and so on. In contrast, the transceive phase of field-echo based sequences includes off-resonance effects. In this case, these effects can be removed by any kind of B_0 mapping. In the easiest way, the phase can be measured at two different TE and extrapolated back to TE = 0 [26]. Also more sophisticated B_0 maps can be applied, for example, obtained in the framework of the Dixon techniques (see, e.g., [42]). On the other hand, sequences with balanced gradients (steady-state free-precession, SSFP) are known to have benign off-resonance behavior [25]. As long as B_0 inhomogeneities are too small to cause the well-known banding artifacts, which lead to phase jumps of 180° , the SSFP transceive phase fairly resembles the transceive phase of spin echo sequences [25].
- (S2) The transceive phase must not contain any contributions from eddy currents in the tissue induced

by gradient switching. This can be obtained by averaging two separate measurements with inverted gradient polarization [43]. Alternatively, the balanced gradients of SSFP sequences eliminate this unwanted phase contribution automatically [25].

- (S3) Phase contributions from flow and motion should be removed or at least suppressed as much as possible. This job can be done, for example, by double spin echo sequences [44] or, again, by SSFP [25].
- (S4) If the “full” complex EPT equation has to be solved and not the phase-based version of EPT, the transceive phase has to be unwrapped before being divided by two, (5). This unwrapping in the three spatial dimensions can be facilitated by performing it separately for each differentiation.

Thus, if applicable, SSFP sequences seem to be the sequence of choice for EPT transceive phase measurements. Due to its high efficiency, SSFP is also a good candidate for real-time phase-based EPT [25] as discussed below.

3.3. RF Shimming. More and more MR systems at $B_0 = 3$ T and above are equipped with multiple, independent RF transmit channels (see, e.g., [35, 36]). The primary goal of this technique is the compensation of B_1 inhomogeneities via RF shimming, that is, the patient-individual adjustment of the complex TX channel weights. It is important to recognize that B_1 fields obtained by this RF shimming still satisfy the Helmholtz equations (1) and (2). Thus, if $|H^+|$ and ϕ^+ of the shimmed system are measured correctly, the accuracy of EPT is not affected. However, the following topics have to be kept in mind regarding EPT in combination with RF shimming.

- (i) RF shimming allows RF excitation far from quadrature excitation. Thus, one has to be aware that the transceive phase assumption (5), derived for a QBC with switched polarization, can be significantly violated [45].
- (ii) Phase-based EPT assumes $|H^+| = \text{const}$, which can be supported by RF shimming [46]. Obviously, RF shimming impairs magnitude-based EPT. Magnitude-based EPT would benefit from RF phase shimming, as long as the resulting B_1 inhomogeneities do not cause signal voids, violating assumption (A4).
- (iii) Having the complex B_1 maps of all TX channels at hand, RF shimming can be performed a posteriori, adjusting the channel weights sequentially for certain ROIs or even voxelwise. Thus, the resulting total B_1 can be optimized locally prior to local EPT reconstructions, as was pointed out by [33].

3.4. Hybrid Sequences. Since phase-based EPT in principle just requires a standard image’s transceive phase, it is more or less straightforward to combine phase-based EPT with all kinds of other sequences. Below, two possible combinations are depicted. A lot more are expected to come up in the near future. One fruitful combination is obtained by performing EPT and MREIT simultaneously [37]. By injecting external

current in the patient for a few ms between RF pulse and signal sampling, MREIT is able to extract tissue conductivity at frequencies below 1 kHz corresponding to the duration of the current injection. Conductivity determined with EPT is related to the Larmor frequency. Thus, the EPT/MREIT hybrid sequence yields a minimal form of conductivity “spectrum.” This frequency dependence can be strikingly proved by wrapping (parts of) phantoms in insulating wrap. The EPT result is not at all affected by the wrapping. For MREIT, the apparent conductivity of the wrapped part is completely suppressed [37]. We refer to [47] that explains how high-frequency current can penetrate the thin membrane and also how this is linked to the frequency-dependent behavior of the complex potential.

Another hybrid sequence is described in [48], where EPT is combined with quantitative mapping of the susceptibility χ (QSM). This combination is driven by the idea to get a complete electromagnetic description of the tissue. EPT and QSM are based on two superposed components of the phase of a gradient echo image. QSM requires the phase component related to B_0 and off-resonance effects; EPT requires the phase component related to B_1 , that is, RF transmission and reception as described in Section 3.2. The separation of these two components, for example, by extrapolating the phase of a multiecho sequence to $TE = 0$ as described above, is the basis of both EPT and QSM. Interested only in EPT or QSM, the noninteresting phase component is just dropped. Thus, the combination of EPT and QSM is simply done by using both phase components as inputs for the respective approaches [48].

4. EPT Experiments

4.1. Phantom Studies. The principle feasibility of EPT has first been proven using phantoms with different saline concentrations covering roughly the physiologic range, showing a correlation of more than 99% between expected and obtained conductivities [9, 10]. A corresponding permittivity study was published in [49]. For low B_0 , noise in permittivity images is tremendously higher than in conductivity images, reflecting the low bending of $|H^+|$ for $B_0 < 3$ T. For increasing B_0 , the SNR gain is higher for permittivity than for conductivity, which arises from different powers of ω in (3) [24, 49].

The possibility of fast phase-based conductivity imaging has been tested with adding NaCl to a tap water phantom during scanning [25]. The applied SSFP sequence measured images of the whole phantom (size 1 liter, resolution $2.5 \times 2.5 \times 2.5$ mm³) within 4 seconds, visualizing the formation of laminar layers with different salt contents and conductivities at the bottom of the phantom.

Conductivity increases with temperature by roughly 2% per Kelvin. This feature has been confirmed with EPT by heating/cooling different phantoms with water and biologic substances (muscle sample, tomato and apple puree) [50]. For the obtained measurement accuracy, no difference in the conductivity’s temperature behavior between the different phantoms has been found. This approach might be helpful

TABLE 1: Electric properties of different compartments of the brain of a healthy volunteer, measured with EPT at 1.5T [11]. The measured values agree with values expected from the literature [51]. Phase-based EPT yields slightly increased conductivities; magnitude-based EPT yields slightly decreased permittivities.

	Conductivity [S/m]			Relative permittivity		
	Full EPT (7)	Phase-based EPT (9)	Literature [51]	Full EPT (7)	Magnitude-based EPT (10)	Literature [51]
Gray matter	0.69 ± 0.14	0.72 ± 0.15	0.51	103 ± 69	91 ± 70	97.4
White matter	0.39 ± 0.15	0.43 ± 0.15	0.29	72 ± 64	63 ± 66	67.8
Cerebrospinal fluid	1.75 ± 0.34	1.82 ± 0.37	2.07	104 ± 21	98 ± 20	97.3

in the framework of hyperthermia and thermoablative interventions.

4.2. In Vivo Studies: Brain Applications. First EPT in vivo studies have been reported by Voigt et al., investigating different volunteers' brains [11]. His results reveal several central features of in vivo EPT.

- (i) The conductivity and permittivity of healthy grey matter, white matter, and cerebrospinal fluid (CSF) measured with EPT coincide with the literature values [51].
- (ii) As expected from theory, phase-based EPT decreases obtained conductivity values by 10%, and magnitude-based EPT increases obtained permittivity values by 10% (see Table 1).
- (iii) Comparing different volunteers, results vary by roughly 15% for gray and white matter and 20% for CSF. These data comprise measurement uncertainties as well as physiologic intersubject differences.

The intersubject variability can be compared with the intra-subject variability, which has been investigated in [52]. Scanning a single volunteer 10 times over a period of three weeks, conductivity variations of roughly 10% across the gray/white matter was obtained. Since this value is close to the intersubject variability reported in [11], physiologic differences between volunteers appear to be rather small. On the other hand, intra-object conductivity variations of phantoms are far below 1%, making system instabilities an unlikely reason for the observed intra-subject variability of 10%. Alternative reasons could be subject motion, spontaneous conductivity fluctuations caused by nutrition or state of health, or others, yet unidentified subject-induced phase instabilities ("unrelated to RF penetration," see [8]).

The conductivity map of a brain of a healthy volunteer is shown in Figure 2. EPT is based on the transceive phase of an SSFP scan using a head coil at 1.5 T and a scan time of 3 minutes for an isotropic resolution of $1 \times 1 \times 1 \text{ mm}^3$. Boundary artifacts were reduced with a median filter, locally restricted by the SSFP magnitude image.

For most clinical EPT studies, the focus of interest is on oncology, particularly brain and breast tumors. Initial, single cases of brain tumors have been reported for 1.5 T [53] and 7 T [54]. All cases show a tumor conductivity increased roughly by a factor of two compared with the surrounding

white matter, as expected from [55]. In [54], the hypothesis is raised that the tumor conductivity correlates with its sodium content. Systematic studies on a larger number of brain tumor patients, trying to understand the biochemical reasons for enhanced tumor conductivity and to classify different kinds of tumors, are on the way. A single stroke patient was described by [56]. Again, a clear increase of the conductivity within the stroke area has been observed.

4.3. In Vivo Studies: Body Applications

4.3.1. Breast. The main components of breast tissue, gland and fat, differ significantly in σ . These components are typically highly nested, leading to high amount of significant conductivity discontinuities throughout the breast. These discontinuities are able to completely spoil any standard EPT reconstruction based on (2) or (9) and (10). Instead of handling conductivity discontinuities on a physical basis via (1), boundary artifacts can be avoided by image segmentation prior to reconstruction and performing separate reconstructions on the different compartments as demonstrated in [39]. Here, the image segmentation was used for shaping the applied kernel locally to the current tissue type, as well as for locally restricting the subsequently applied median filter. The image segmentation was based on the magnitude image of the 3D turbo spin echo performed to obtain the transceive phase for the EPT reconstruction. The resulting conductivity map is more or less free of boundary artifacts. The tumor clearly shows the highest conductivity throughout the breast $\sigma \sim 2.0\text{--}2.5 \text{ S/m}$. Several cysts show an intermediate conductivity $\sigma \sim 1.0\text{--}1.5 \text{ S/m}$. The conductivity of the surrounding fatty tissue is around zero $\sigma \sim \pm 0.5 \text{ S/m}$. Remaining inhomogeneities particularly in the fat compartments might arise from insufficient B_1 homogeneity or, more likely, from tissue eddy currents, since no second scan with inverted gradient polarization has been performed ([43], step (S2) in the above list). Figure 4 shows breast tumor patient study. Further breast studies are on the way (see, e.g., the breast permittivity study [57]).

4.3.2. Heart. Two isolated, perfused pig hearts where scanned with a gated SSFP sequence [58]. Conductivity values from phase-based EPT of normally perfused heart tissue were compared with the values in ischemic regions after a blockade of the left anterior descending artery. Normal conductivity values turned out to be in agreement with

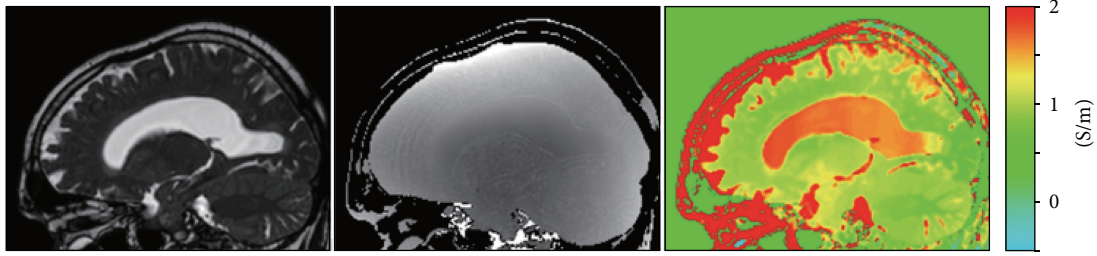


FIGURE 2: Volunteer brain study. Left: SSFP image (magnitude); center: SSFP image (phase); right: reconstructed conductivity based on the Laplacian of the SSFP phase and locally restricting the subsequent filtering using the SSFP magnitude.

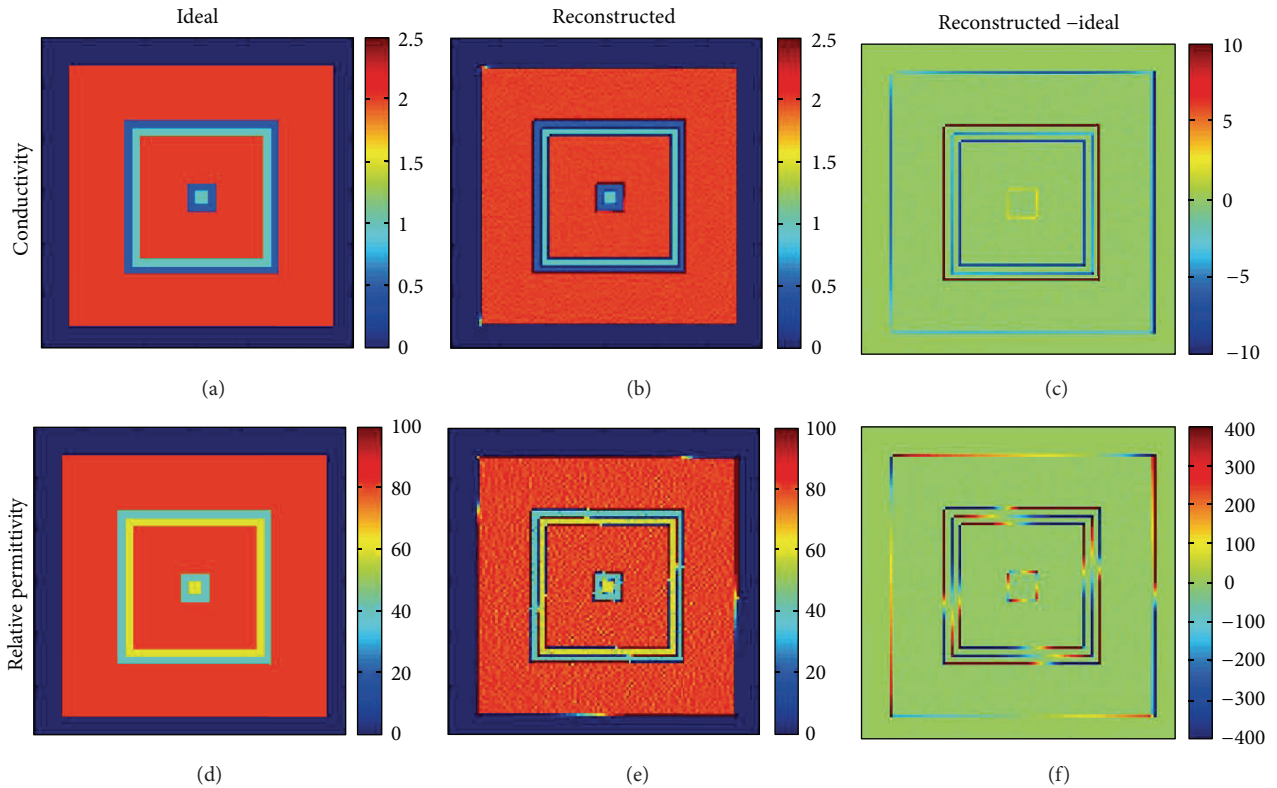


FIGURE 3: Local inhomogeneity effects using the Helmholtz equation. The reconstructed conductivity and permittivity show strong oscillations. (Simulations were done for a cylinder object of size $100 \text{ mm} \times 100 \text{ mm} \times 120 \text{ mm}$ with 3 different values of conductivity (2 S/m, 1 S/m, and 0.5 S/m) and relative permittivity (80, 60, and 40).)

the literature values, while conductivity in ischemic/infarcted areas was 60% lower than that in remote myocardium [58]. These findings are very encouraging for future, challenging *in vivo* cardiac experiments.

4.3.3. Liver. By analogy to the above-described brain studies, the intra-subject variability of the liver conductivity of healthy volunteers has been investigated [59]. The high efficiency of the applied SSFP sequence allows scanning the whole liver within a single breathhold. The obtained intra-subject and intersubject variability was of the same range as for the brain [11, 52]. A higher artifact level was observed in the liver than in the brain, presumably arising from

cardiac motion transferred to the liver and only incompletely suppressed by the applied SSFP sequence. Artifacts are more pronounced for expiration than inspiration breathhold, which can be explained by the contact of heart and liver closer in expiration than in inspiration [59].

4.3.4. Pelvis. In preparation of future pelvis tumor studies, the applicability of phase-based EPT was checked with a pelvis-sized phantom at 3 T [60]. Due to the larger dimensions of the pelvis, as compared to the head, the phase error has to be reinvestigated for this particular anatomy. According to this study, phase-based EPT seems to be sufficient when focusing only on the tumors; however,

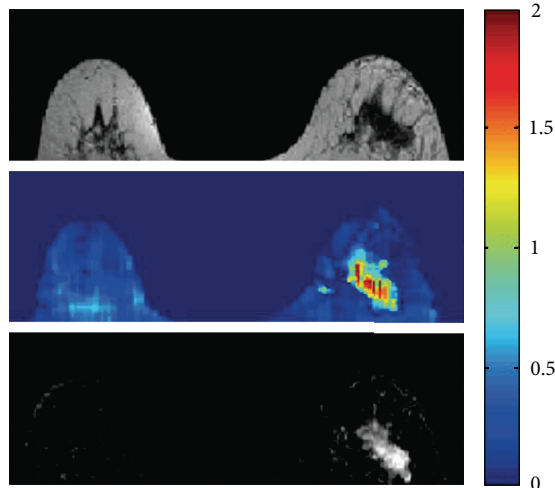


FIGURE 4: Breast tumor patient study. Top: turbo spin echo (magnitude); center: reconstructed conductivity image; bottom: contrast enhanced dynamic image. The dynamic image shows the region of the tumor.

the inclusion of $|H^+|$ could be necessary, when σ of the whole pelvis is required [60].

5. Conclusion

Tomographic imaging of the conductivity and permittivity distributions inside the human body has been an active research topic in the field of Electrical Impedance Tomography (EIT) measuring boundary current-voltage data [61]. However, wide experience in EIT for more than three decades has shown its methodological limitation in achieving robust reconstructions of static conductivity and permittivity images; EIT is insensitive to any perturbation of internal admittivity whereas it is very sensitive to forward modeling errors. It seems that boundary measurements are insufficient for robust reconstruction of the admittivity distribution inside the subject. For a robust reconstruction, we need an internal measurement that is capable of by MRI scanners as discussed in this paper.

Using standard MR systems and standard MR sequences, mapping of the electric properties seems to be clinically feasible, particularly phase-based conductivity imaging. The rapidly evolving field will certainly afford further improved measurement and reconstruction techniques in the near future. The broad spectrum of started preclinical and clinical studies raise hope that answers will soon be available concerning potential diagnostic benefits of EPT.

Acknowledgments

The first author would like to thank cordially the invaluable help of Christian Stehning and Tobias Voigt. J. K. Seo was supported by the National Research Foundation of Korea (NRF) Grant funded by the Korea government (MEST) (no. 2011-8-1782).

References

- [1] S. Grimnes and O. G. Martinsen, *Bioimpedance and Bioelectricity Basics*, Academic Press, London, UK, 2000.
- [2] M. L. Joy, G. C. Scott, and R. M. Henkelman, "In vivo detection of applied electric currents by magnetic resonance imaging," *Magnetic Resonance Imaging*, vol. 7, no. 1, pp. 89–94, 1989.
- [3] G. C. Scott, M. L. G. Joy, R. L. Armstrong, and R. M. Henkelman, "Measurement of nonuniform current density by magnetic resonance," *IEEE Transactions on Medical Imaging*, vol. 10, no. 3, pp. 362–374, 1991.
- [4] E. J. Woo, S. Y. Lee, and C. W. Mun, "Impedance tomography using internal current density distribution measured by nuclear magnetic resonance," in *3rd Mathematical Methods in Medical Imaging*, vol. 2299 of *Proceedings of SPIE*, pp. 377–385, July 1994.
- [5] J. K. Seo, J. R. Yoon, E. J. Woo, and O. Kwon, "Reconstruction of conductivity and current density images using only one component of magnetic field measurements," *IEEE Transactions on Biomedical Engineering*, vol. 50, no. 9, pp. 1121–1124, 2003.
- [6] E. J. Woo and J. K. Seo, "Magnetic resonance electrical impedance tomography (MREIT) for high-resolution conductivity imaging," *Physiological Measurement*, vol. 29, no. 10, pp. R1–R26, 2008.
- [7] J. K. Seo and E. J. Woo, "Magnetic resonance electrical impedance tomography (MREIT)," *SIAM Review*, vol. 53, no. 1, pp. 40–68, 2011.
- [8] E. M. Haacke, L. S. Pappas, E. W. Nilges, and D. H. Wu, "Extraction of conductivity and permittivity using magnetic resonance imaging," *Physics in Medicine and Biology*, vol. 36, no. 6, pp. 723–734, 1991.
- [9] H. Wen, "Non-invasive quantitative mapping of conductivity and dielectric distributions using the RF wave propagation effects in high field MRI," in *Medical Imaging: Physics of Medical Imaging*, vol. 5030 of *Proceedings of SPIE*, pp. 471–477, February 2003.
- [10] U. Katscher, T. Voigt, C. Findekklee, P. Vernickel, K. Nehrke, and O. Dossel, "Determination of electrical conductivity and local SAR via B_1 mapping," *IEEE Transactions on Medical Imaging*, vol. 28, pp. 1365–1374, 2009.
- [11] T. Voigt, U. Katscher, and O. Doessel, "Quantitative conductivity and permittivity imaging of the human brain using electric properties tomography," *Magnetic Resonance in Medicine*, vol. 66, no. 2, pp. 456–466, 2011.
- [12] S. Akoka, F. Franconi, F. Seguin, and A. Le Pape, "Radiofrequency map of an NMR coil by imaging," *Magnetic Resonance Imaging*, vol. 11, no. 3, pp. 437–441, 1993.
- [13] G. J. Barker, A. Simmons, S. R. Arridge, and P. S. Tofts, "A simple method for investigating the effects of non-uniformity of radiofrequency transmission and radiofrequency reception in MRI," *British Journal of Radiology*, vol. 71, pp. 59–67, 1998.
- [14] R. Stollberger and P. Wach, "Imaging of the active B_1 field in vivo," *Magnetic Resonance in Medicine*, vol. 36, pp. 246–251, 1996.
- [15] V. L. Yarnykh, "Actual flip-angle imaging in the pulsed steady state: a method for rapid three-dimensional mapping of the transmitted radiofrequency field," *Magnetic Resonance in Medicine*, vol. 57, no. 1, pp. 192–200, 2007.
- [16] L. I. Sacolick, F. Wiesinger, I. Hancu, and M. W. Vogel, " B_1 mapping by Bloch-Siegert shift," *Magnetic Resonance in Medicine*, vol. 63, no. 5, pp. 1315–1322, 2010.

- [17] K. Nehrke and P. Börnert, "DREAM—a novel approach for robust, ultrafast, multislice B_1 mapping," *Magnetic Resonance in Medicine*, vol. 68, pp. 1517–1526, 2012.
- [18] G. C. Scott, M. L. G. Joy, R. L. Armstrong, and R. M. Henkelman, "RF current density imaging in homogeneous media," *Magnetic Resonance in Medicine*, vol. 28, no. 2, pp. 186–201, 1992.
- [19] G. C. Scott, M. L. G. Joy, R. L. Armstrong, and R. M. Henkelman, "Rotating frame RF current density imaging," *Magnetic Resonance in Medicine*, vol. 33, no. 3, pp. 355–369, 1995.
- [20] D. Wang, T. P. DeMonte, W. Ma, M. L. G. Joy, and A. I. Nachman, "Multislice radio-frequency current density imaging," *IEEE Transactions on Medical Imaging*, vol. 28, no. 7, pp. 1083–1092, 2009.
- [21] D. I. Hoult, "The principle of reciprocity in signal strength calculations—a mathematical guide," *Concepts in Magnetic Resonance*, vol. 12, no. 4, pp. 173–187, 2000.
- [22] J. Shin, J. Lee, J. K. Seo, and D. H. Kim, "Quantification error in MREPT due to B_1 map inaccuracy," in *Proceedings of the 20th Scientific Meeting of the International Society of Magnetic Resonance in Medicine (ISMRM '12)*, vol. 2533, Melbourne, Australia, 2012.
- [23] S. B. Bulumulla, S. K. Lee, and T. B. D. Yeo, "Calculation of electrical properties from B_1^+ maps—a comparison of methods," in *Proceedings of the 20th Scientific Meeting of the International Society of Magnetic Resonance in Medicine (ISMRM '12)*, vol. 3469, 2012.
- [24] A. L. H. M. W. van Lier, U. Katscher, A. Raaijmakers, and C. A. T. van den Berg, "Wave-number imaging at 7T: increasing accuracy of EPT at high field strengths," in *Proceedings of the 20th Scientific Meeting of the International Society of Magnetic Resonance in Medicine (ISMRM '12)*, vol. 3466, Melbourne, Australia, 2012.
- [25] C. Stehning, T. R. Voigt, and U. Katscher, "Real-Time conductivity mapping using balanced SSFP and phase-based reconstruction," in *Proceedings of the 19th Scientific Meeting of the International Society of Magnetic Resonance in Medicine (ISMRM '11)*, vol. 128, 2011.
- [26] A. L. van Lier, D. O. Brunner, K. P. Pruessmann et al., " B_1^+ phase mapping at 7T and its application for in vivo electrical conductivity mapping," *Magnetic Resonance in Medicine*, vol. 67, pp. 552–561, 2012.
- [27] A. L. van Lier, A. Raaijmakers, T. Voigt, J. J. Lagendijk, U. Katscher, and C. A. van den Berg, "Electric properties tomography in the human brain at 1.5, 3, and 7 T: a comparison study," *Magnetic Resonance in Medicine*, 2013.
- [28] S. B. Bulumulla, T. B. Yeo, and Y. Zhu Y, "Direct calculation of tissue electrical parameters from B_1 maps," in *Proceedings of the 17th Scientific Meeting of the International Society of Magnetic Resonance in Medicine (ISMRM '09)*, vol. 3043, 2009.
- [29] M. A. Cloos and G. Bonmassar, "Towards direct B_1 based local SAR estimation," in *Proceedings of the 17th Scientific Meeting of the International Society of Magnetic Resonance in Medicine (ISMRM '09)*, vol. 3037, 2009.
- [30] S. Buchenau, M. Haas, J. Hennig, and M. Zaitsev, "A comparison of local SAR using individual patient data and a patient template," in *Proceedings of the 17th Scientific Meeting of the International Society of Magnetic Resonance in Medicine (ISMRM '09)*, vol. 4798, 2009.
- [31] X. Zhang, S. Zhu, and B. He, "Imaging electric properties of biological tissues by RF field mapping in MRI," *IEEE Transactions on Medical Imaging*, vol. 29, no. 2, pp. 474–481, 2010.
- [32] U. Katscher, C. Findekle, and T. Voigt, "Single element SAR measurements in a multi-transmit system," in *Proceedings of the 19th Scientific Meeting of the International Society of Magnetic Resonance in Medicine (ISMRM '11)*, vol. 494, 2011.
- [33] D. K. Sodickson, L. Alon, C. M. Deniz et al., "Local Maxwell tomography using transmit-receive coil arrays for contact-free mapping of tissue electrical properties and determination of absolute RF phase," in *Proceedings of the 20th Scientific Meeting of the International Society of Magnetic Resonance in Medicine (ISMRM '12)*, vol. 387, 2012.
- [34] U. Katscher, C. Findekle, and T. Voigt, " B_1 -based specific energy absorption rate determination for nonquadrature radiofrequency excitation," *Magnetic Resonance in Medicine*, vol. 68, pp. 1911–1918, 2012.
- [35] K. Setsompop, L. L. Wald, V. Alagappan et al., "Parallel RF transmission with eight channels at 3 Tesla," *Magnetic Resonance in Medicine*, vol. 56, no. 5, pp. 1163–1171, 2006.
- [36] P. Vernickel, P. Röschmann, C. Findekle et al., "Eight-channel transmit/receive body MRI coil at 3T," *Magnetic Resonance in Medicine*, vol. 58, no. 2, pp. 381–389, 2007.
- [37] J. K. Seo, M. O. Kim, J. Lee et al., "Error analysis of nonconstant admittance for MR-based electric property imaging," *IEEE Transactions on Medical Imaging*, vol. 31, pp. 430–437, 2012.
- [38] A. I. Nachman, D. Wang, W. Ma, and M. L. G. Joy, "A local formula for inhomogeneous complex conductivity as a function of the RF magnetic field," in *Proceedings of the 15th Scientific Meeting of the International Society of Magnetic Resonance in Medicine (ISMRM '07)*, vol. 15, 2007.
- [39] U. Katscher, K. Djamshidi, T. Voigt et al., "Estimation of breast tumor conductivity using parabolic phase fitting," in *Proceedings of the 20th Scientific Meeting of the International Society of Magnetic Resonance in Medicine (ISMRM '12)*, vol. 3482, 2012.
- [40] U. Katscher, T. Voigt, and C. Findekle, "Estimation of the anisotropy of electric conductivity via B_1 mapping," in *Proceedings of the 18th Scientific Meeting of the International Society of Magnetic Resonance in Medicine (ISMRM '10)*, vol. 2866, 2010.
- [41] J. Lee, Y. Song, N. Choi, S. Cho, J. K. Seo, and D. H. Kim, "Noninvasive measurement of conductivity anisotropy at larmor frequency using MRI," *Computational and Mathematical Methods in Medicine*. In press.
- [42] G. H. Glover and E. Schneider, "Three-point Dixon technique for true water/fat decomposition with B_0 inhomogeneity correction," *Magnetic Resonance in Medicine*, vol. 18, no. 2, pp. 371–383, 1991.
- [43] M. A. Bernstein, K. F. King, and X. J. Zhou, *Handbook of MRI Pulse Sequences*, Academic Press, 2004.
- [44] N. Choi, M. Ghim, S. Yang, S.-Y. Zho, and D.-H. Kim, "In vivo conductivity mapping using double spin echo for flow effect removal," in *Proceedings of the 19th Scientific Meeting of the International Society of Magnetic Resonance in Medicine (ISMRM '11)*, vol. 4466, 2011.
- [45] U. Katscher, C. Findekle, and T. Voigt, "Experimental estimation of local SAR in a multi-transmit system," in *Proceedings of the 17th Scientific Meeting of the International Society of Magnetic Resonance in Medicine (ISMRM '09)*, vol. 4512, 2009.
- [46] U. Katscher, A. van Lier, C. van den Berg, and J. Keupp, "RF Shimming improves phase-based conductivity imaging," in *Proceedings of the 20th Scientific Meeting of the International Society of Magnetic Resonance in Medicine (ISMRM '12)*, vol. 3487, 2012.

- [47] S. Kim, E. J. Lee, E. J. Woo, and J. K. Seo, "Asymptotic analysis of the membrane structure to sensitivity of frequency-difference electrical impedance tomography," *Inverse Problems*, vol. 28, Article ID 075004, 2012.
- [48] D. H. Kim, S. M. Gho, N. Choi, and C. Liu, "Simultaneous electromagnetic property imaging using multiecho gradient echo," in *Proceedings of the 20th Scientific Meeting of the International Society of Magnetic Resonance in Medicine (ISMRM '12)*, vol. 3464, 2012.
- [49] U. Katscher, P. Karkowski, C. Findekklee, and T. Voigt, "Permittivity determination via phantom and in vivo B_1 mapping," in *Proceedings of the 18th Scientific Meeting of the International Society of Magnetic Resonance in Medicine (ISMRM '10)*, vol. 239, 2010.
- [50] C. Leussler, P. Karkowski, and U. Katscher, "Temperature dependant conductivity change using MR based electric properties tomography," in *Proceedings of the 20th Scientific Meeting of the International Society of Magnetic Resonance in Medicine (ISMRM '12)*, vol. 3451, 2012.
- [51] S. Gabriel, R. W. Lau, and C. Gabriel, "The dielectric properties of biological tissues—II. Measurements in the frequency range 10 Hz to 20 GHz," *Physics in Medicine and Biology*, vol. 41, no. 11, pp. 2251–2269, 1996.
- [52] C. Stehning, T. R. Voigt, and U. Katscher, "Reproducibility study of 3D SSFP phase-based brain conductivity imaging," *MAGMA*, vol. 25, pp. S197–S198, 2012.
- [53] T. Voigt, O. Vaterlein, C. Stehning, U. Katscher, and J. Fiehler, "In vivo glioma characterization using MR conductivity imaging," in *Proceedings of the 19th Scientific Meeting of the International Society of Magnetic Resonance in Medicine (ISMRM '11)*, vol. 127, 2011.
- [54] A. van Lier, "Electrical conductivity imaging of brain tumours," in *Proceedings of the 19th Scientific Meeting of the International Society of Magnetic Resonance in Medicine (ISMRM '11)*, vol. 4464, 2011.
- [55] Y. Lu, B. Li, J. Xu, and J. Yu, "Dielectric properties of human glioma and surrounding tissue," *International Journal of Hyperthermia*, vol. 8, pp. 750–760, 1992.
- [56] A. van Lier, A. Kolk, M. Brundel et al., "Electrical conductivity in ischemic stroke at 7.0 Tesla: a case study," in *Proceedings of the 20th Scientific Meeting of the International Society of Magnetic Resonance in Medicine (ISMRM '12)*, vol. 3484, 2012.
- [57] S. Bulumulla and I. Hancu, "Breast permittivity imaging," in *Proceedings of the 20th Scientific Meeting of the International Society of Magnetic Resonance in Medicine (ISMRM '12)*, vol. 2532, 2012.
- [58] T. Voigt, A. Schuster, M. Ishida et al., "Conductivity imaging of an Ischemic pig heart model using electric properties tomography," in *Proceedings of the 20th Scientific Meeting of the International Society of Magnetic Resonance in Medicine (ISMRM '12)*, vol. 3483, 2012.
- [59] C. Stehning, T. Voigt, P. Karkowski, and U. Katscher, "Electric properties tomography (EPT) of the liver in a single breathhold using SSFP," in *Proceedings of the 20th Scientific Meeting of the International Society of Magnetic Resonance in Medicine (ISMRM '12)*, vol. 386, 2012.
- [60] E. Balidemaj, A. L. van Lier, A. J. Nederveen, J. Crezee, and C. A. T. van den Berg, "Feasibility of EPT in the Human Pelvis at 3T," in *Proceedings of the 20th Scientific Meeting of the International Society of Magnetic Resonance in Medicine (ISMRM '12)*, vol. 3468, 2012.
- [61] D. Holder, *Electrical Impedance Tomography: Methods, History and Applications*, IOP Publishing, Bristol, UK, 2005.

Research Article

EIT-Based Fabric Pressure Sensing

A. Yao,¹ C. L. Yang,¹ J. K. Seo,² and M. Soleimani¹

¹ *Engineering Tomography Laboratory (ETL), Department of Electronic and Electrical Engineering, University of Bath, Bath BA2 7AY, UK*

² *Department of Computational Science and Engineering, Yonsei University, Seoul 120-749, Republic of Korea*

Correspondence should be addressed to M. Soleimani; m.soleimani@bath.ac.uk

Received 9 October 2012; Revised 10 January 2013; Accepted 21 January 2013

Academic Editor: Eung Je Woo

Copyright © 2013 A. Yao et al. This is an open access article distributed under the Creative Commons Attribution License, which permits unrestricted use, distribution, and reproduction in any medium, provided the original work is properly cited.

This paper presents EIT-based fabric sensors that aim to provide a pressure mapping using the current carrying and voltage sensing electrodes attached to the boundary of the fabric patch. Pressure-induced shape change over the sensor area makes a change in the conductivity distribution which can be conveyed to the change of boundary current-voltage data. This boundary data is obtained through electrode measurements in EIT system. The corresponding inverse problem is to reconstruct the pressure and deformation map from the relationship between the applied current and the measured voltage on the fabric boundary. Taking advantage of EIT in providing dynamical images of conductivity changes due to pressure induced shape change, the pressure map can be estimated. In this paper, the EIT-based fabric sensor was presented for circular and rectangular sensor geometry. A stretch sensitive fabric was used in circular sensor with 16 electrodes and a pressure sensitive fabric was used in a rectangular sensor with 32 electrodes. A preliminary human test was carried out with the rectangular sensor for foot pressure mapping showing promising results.

1. Introduction

Electrical impedance tomography (EIT) is a fast and cost-effective technique to provide tomographic conductivity image of a subject from boundary current-voltage data. Time difference EIT technique can be used to image conductivity changes in a fabric sensor [1]. When pressure is applied to the fabric patch (the boundary is kept in a frame to maintain a fixed boundary and electrode position), the conductivity of the proposed conductive fabric changes with increasing pressure or deformation of the fabric. Pressure induced shape changes over the sensor area make changes to the conductivity distribution; the change in conductivity distribution leads to the change in current-voltage data in EIT system. EIT system displays the image of the conductivity changes from current-voltage data measured at the boundary of fabric patch. Finally, the pressure distribution could be estimated from the conductivity images.

Pressure mapping can be done with variety measurement methods: capacitive methods [2, 3], piezoelectric method [4–6], inductive method [7–9], and optoelectronic method [10–12]. Pressure mapping techniques have a wide range

of applications, including gate and pressure monitoring in biomechanics and touch sensing robotics [13–15]. A change in resistivity of a sensing region can provide an alternative method for pressure mapping and hence EIT has a potential to be used as a pressure mapping imaging tool. Industrial, geophysical, and medical applications of the EIT imaging are well understood. EIT as a pressure mapping imaging method is very new. The original idea of applying EIT-based pressure sensing for pressure ulcers was introduced by Reddy et al. [16] and Fulton and Lipczynski in 1993 [17]. However, experimental trials in [16, 17] were not very successful, partly due to the lack of suitable conductive material for EIT pressure sensor. In [18], a theoretical model was presented for a fabric-based EIT. Electrically active textiles are being developed rapidly in the past few years due to a surge in commercial interest in wearable textiles. Hassan et al. [19] proposed a fabric-based EIT sensor as an artificial robotic skin. Further image quality analyses were carried out on a polymer-based fabric EIT in [20].

In this paper, underlying mathematical framework of EIT-based fabric sensor has been explained and performs various experimental feasibility studies on the use of improved

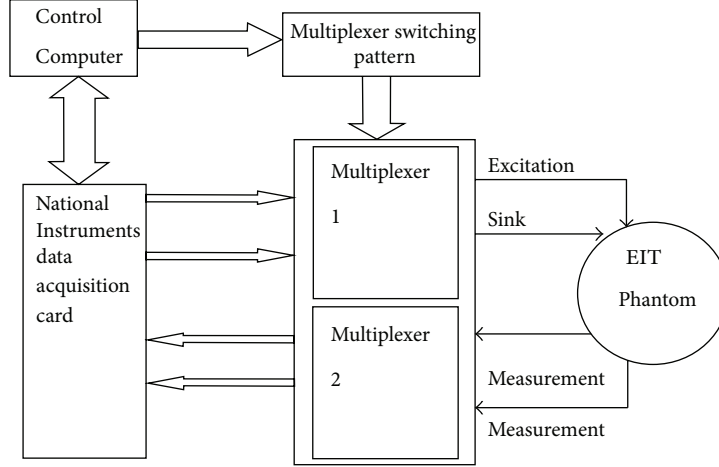


FIGURE 1: Schematic diagram of the EIT hardware.

version of EIT-based fabric sensors. The main objective of this study is to show the capability and limitation of the current generation of pressure mapping EIT system and methods. And finally the scientific challenges related to the fabric EIT have been highlighted.

2. Mathematical Model

The mathematical framework for the EIT-based pressure mapping imaging can be briefly explained. Let the fabric occupy the two-dimensional domain Ω with its boundary $\partial\Omega$. On the periphery $\partial\Omega$ of the fabric, the electrodes are attached e_l , $l = 1, 2, \dots, L$. A current of 1 mA was injected at a low frequency of 1 kHz with a chosen pair of adjacent electrodes (e_l and e_{l+1}) to generate potential over the fabric Ω . Then the resulting potential U^l satisfies

$$\nabla \cdot (\sigma \nabla U^l) = 0 \quad \text{in } \Omega \quad (1)$$

with the boundary condition [21]

$$\begin{aligned} U^l + z_k \sigma \frac{\partial U^l}{\partial n} &= V_k^l \quad \text{on } e_k, \quad k = 1, 2, \dots, L, \\ I &= \int_{e_l} \sigma \frac{\partial U^l}{\partial n} dS = - \int_{e_{l+1}} \sigma \frac{\partial U^l}{\partial n} dS, \\ \int_{e_k} \sigma \frac{\partial U^l}{\partial n} dS &= 0 \quad \text{if } k \neq l, \\ \sigma \frac{\partial U^l}{\partial n} &= 0 \quad \text{on } \frac{\partial \Omega}{U_l^l e_l}, \end{aligned} \quad (2)$$

where σ is the conductivity distribution of the fabric, z_l is the effective contact impedance at e_l , n is the unit outward normal vector, and V_k^l is the potential at e_k . The distribution of the conductivity is reflected to the measured data:

$$\mathbf{V} = (V_1^1, V_2^1, \dots, V_L^1, V_1^2, \dots, V_L^2, \dots, V_L^L) \in R^{L \times L}. \quad (3)$$

The conductivity perturbation $\Delta\sigma$ can be computed by the linearized reconstruction algorithm via

$$\Delta\sigma = (J^T J + \lambda L)^{-1} J^T \Delta\mathbf{V}, \quad (4)$$

where $\Delta\mathbf{V}$ is the perturbation of the measured data, J is the Jacobian matrix, L is the regularization matrix, and λ is the regularized parameter. To compute the Jacobian matrix a finite element method (FEM) was used: each element includes a number of cells in knitted structure and σ is assumed to be a constant on each element that is the average conductivity of these combined cells that includes air and yarn. The following flowchart summarizes how the pressure is related to the voltage change $\Delta\mathbf{V}$:

$$\text{Pressure} \Rightarrow \text{Displacement} \Rightarrow \Delta\sigma \Rightarrow \Delta\mathbf{V}. \quad (5)$$

The inverse problem is to invert this procedure.

3. Experimental Results

3.1. EIT Hardware and Fabric Sensor. A National Instruments LabVIEW Base EIT System was designed for data acquisition and a multiplexer circuit was fabricated for EIT excitation and measurement. Figure 1 shows the block diagram of the proposed EIT hardware system. The multiplexer 1 supplies excitation current to the electrodes and multiplexer 2 acquires voltage measurements. This is a simple EIT design with an SNR of 40 dB [1].

By acquiring two different sets of voltage measurement data, the reconstruction software is used to do a time difference image reconstruction. To evaluate the repeatability and reliability of the fabric-EIT system, a large number of experiments were carried out.

A number of conductive materials were used in previous studies, for example, silicone-based conductive glue with Ag fillers [18] or polymer-carbon-nanotube composites [20, 22]. In this study an off-the-shelf conductive fabric called EeonTex Conductive Fabric with the model number EeonTex LR-SL-PA-10E5 [23] was used for a circular fabric sensor. This

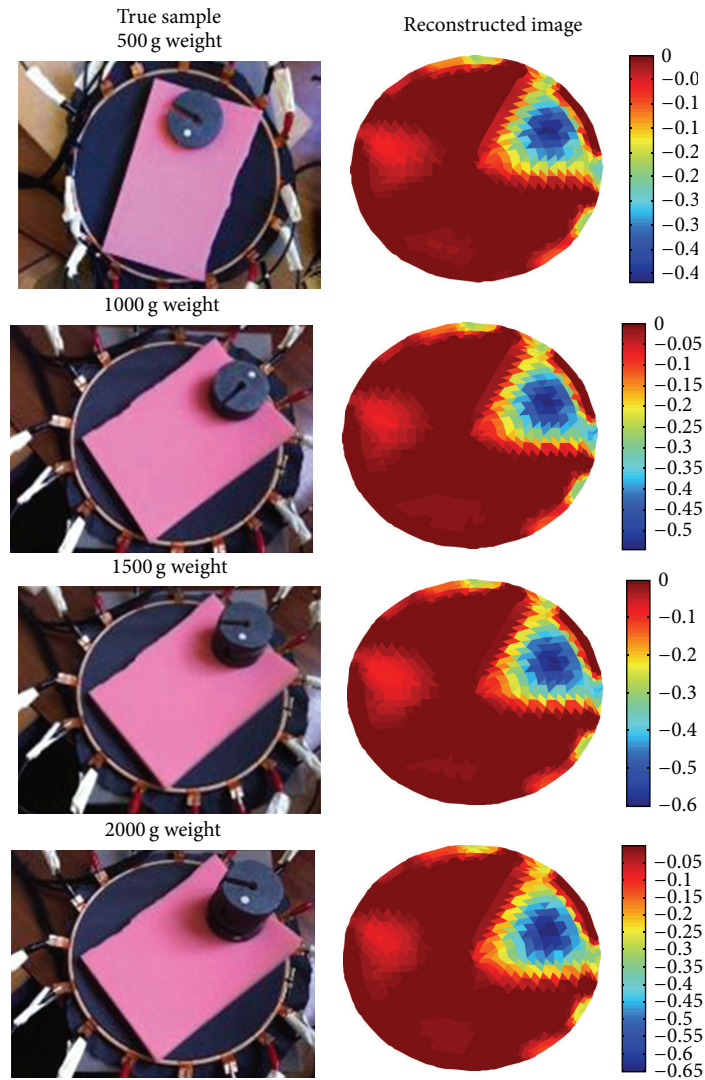


FIGURE 2: Pressure point at the boundary.

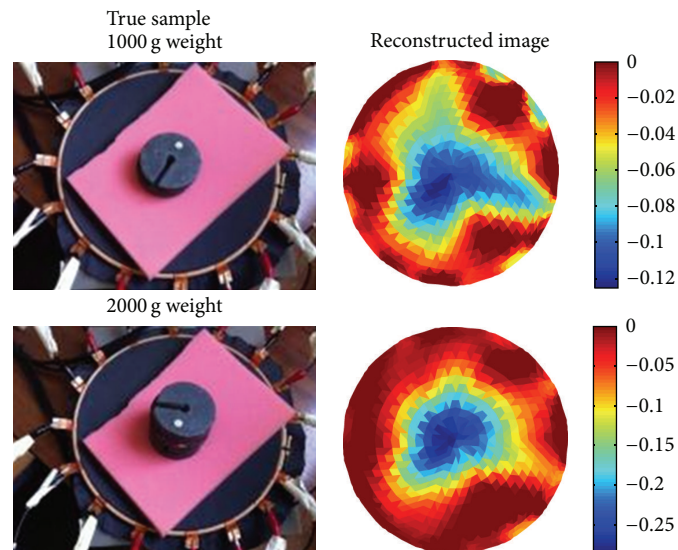


FIGURE 3: Pressure point at the centre of imaging area.

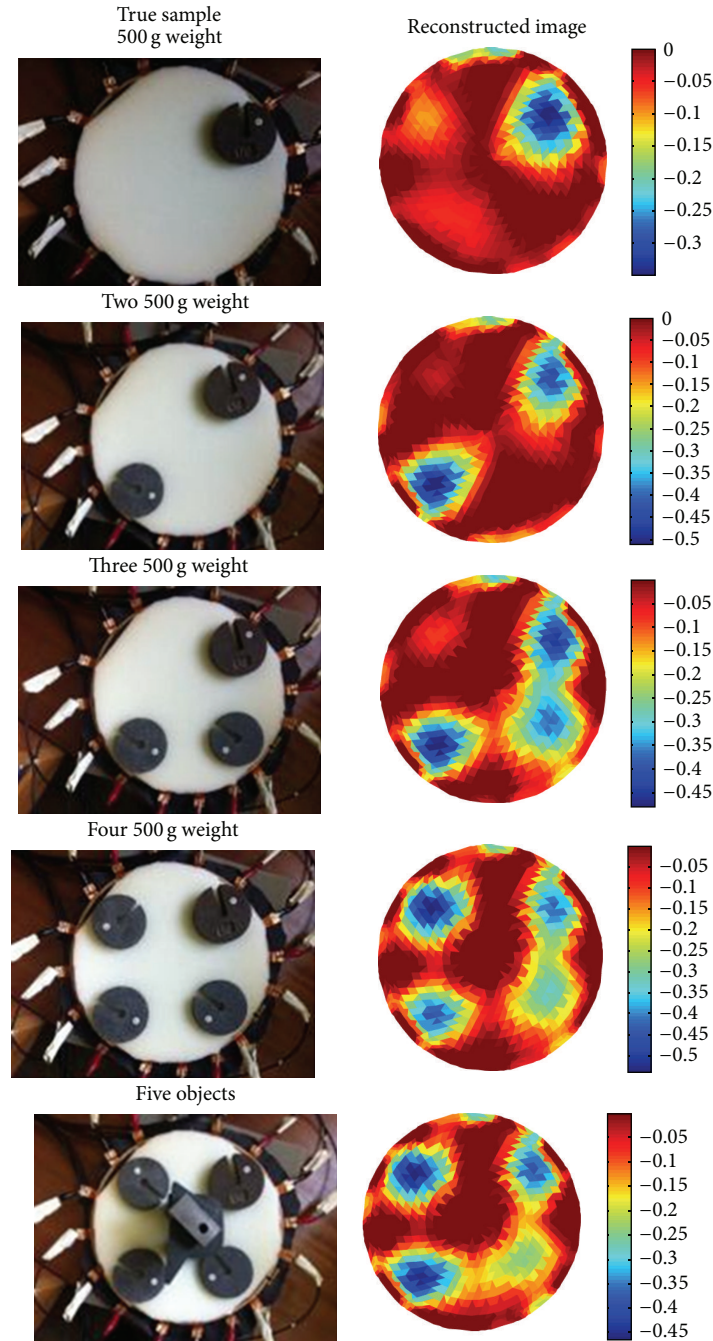


FIGURE 4: Multiple pressure reconstruction.

fabric is a knitted nylon/spandex coated with a conductive formulation. The surface resistivity of this fabric is $10^5 \Omega$ per square meter. This is a stretchable sensor showing good elastomeric and electrical properties.

The material used in the square sensor is NW170-SL-PA-1500 [24], which is also developed by the Eeonyx Corporation. It is a microfiber nonwoven material coated with conductive formulation and, by the description on the product information sheet, it is designed for application with a dynamic pressure sensing requirement. The surface

resistivity of this material is 1500Ω per square meter $\pm 15\%$.

3.2. Circular Fabric Sensor. The first experiment was designed to analyse the performance of the 16-channel circular fabric sensor. The sensor consists of 3 main parts: a wooden frame, the fabric material, and the electrodes. The frame was constructed by two wooden rings with one on the top of the fabric and the other one at the bottom, and it was used to maintain the fabric patch. Sixteen identical electrodes were placed

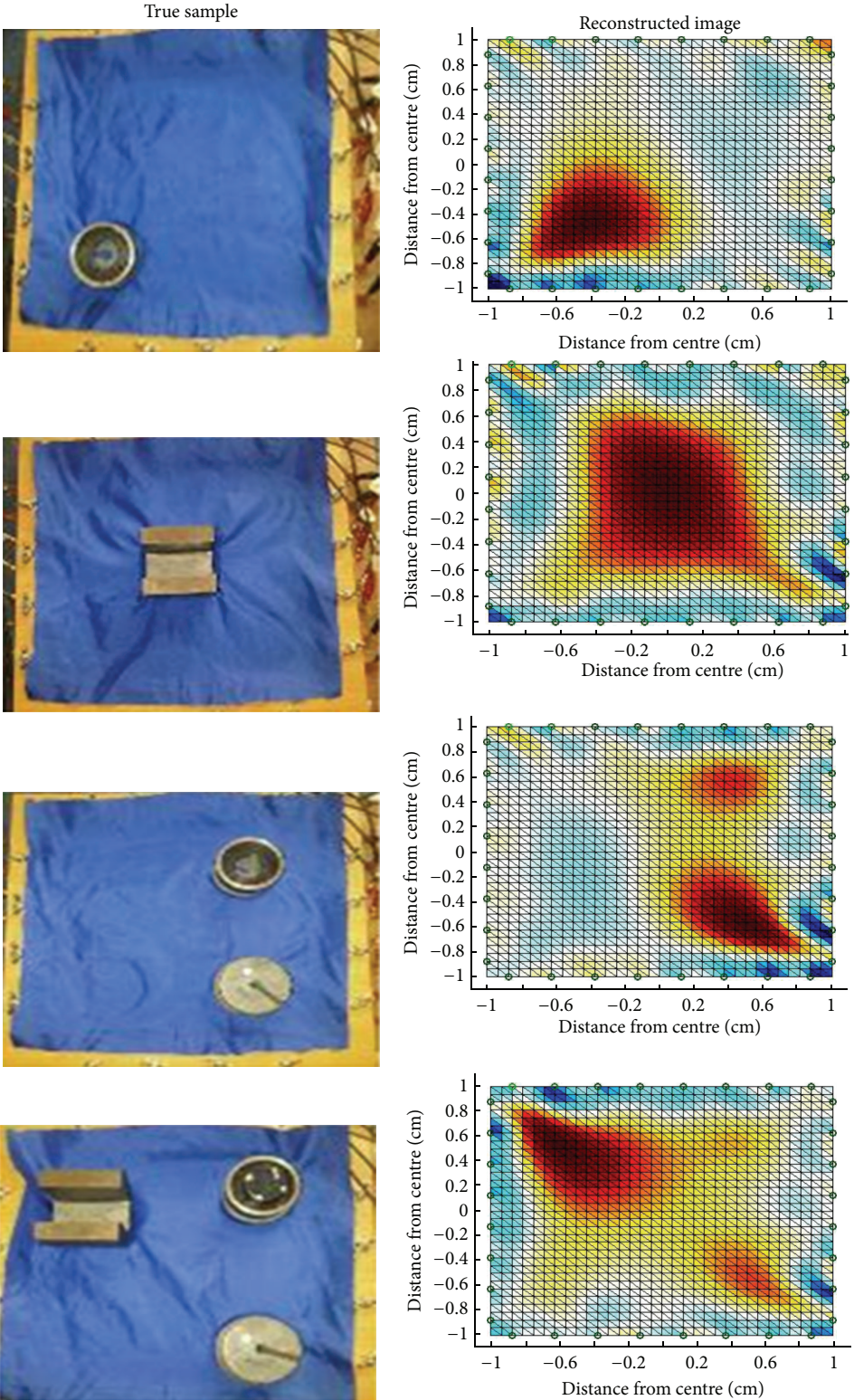


FIGURE 5: Square sensor.

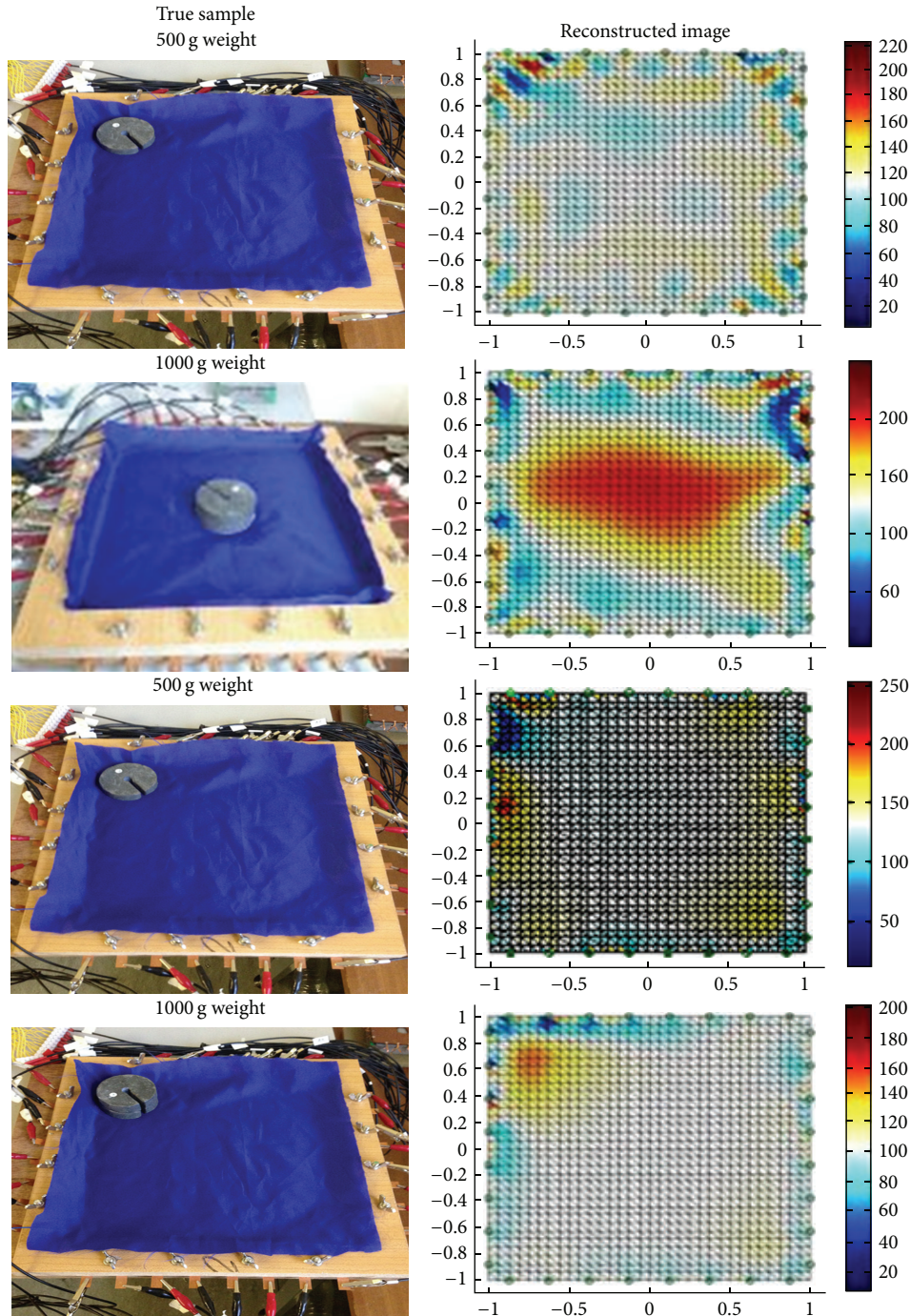


FIGURE 6: Square sensor with central and boundary pressure points.

between two wooden rings and were equally spaced in between. A foam layer was used for protecting the conductive fabric from being damaged.

Figure 2 shows the experimental results for a pressure applied close to the boundary of the imaging region. The experiments were done in four steps, starting with 500 g weight with gradually increasing the weight to 2000 g. The

reconstruction images show the location where the pressure was applied. The colour-bar scales in the image also show changes relative to the weight.

The second sets of tests were carried out in the middle of the sensor where the sensitivity is at its lowest, shown in Figure 3. Here 500 g sample did not produce a meaningful image. The result for 1000 g weight had shown the pressure

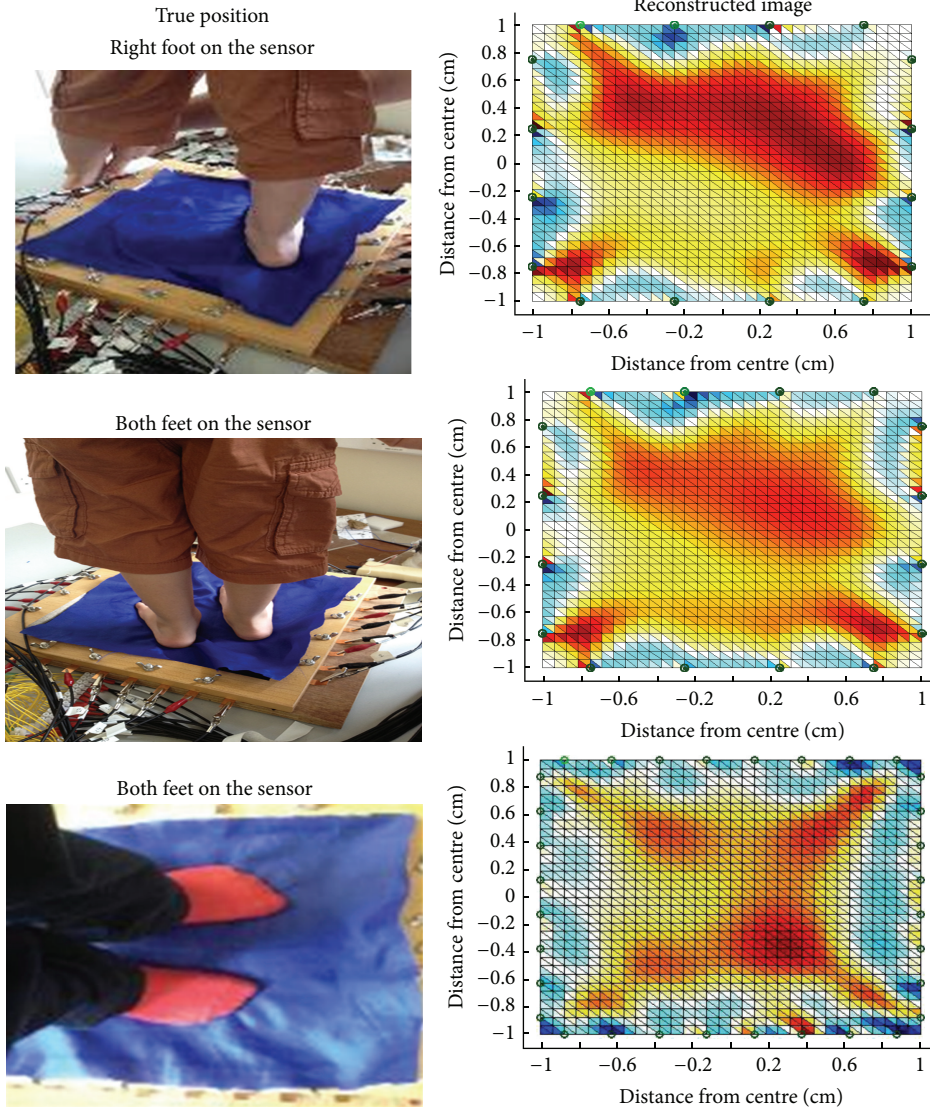


FIGURE 7: Preliminary human application.

location but with distortion due to the fact that the central position is the least sensitive area. An improvement can be observed for larger weight. The scale of colour bar in the images shows changes relative to the weight. Although it is not possible to claim proportionality between image scale and the weight changes, it is promising to see that the scale of reconstructed conductivity follows the weights.

It is useful to see how the system performs for multiple pressure locations. Figure 4 shows reconstruction of 1, 2, 3, 4, and 5 pressure points. It can be seen that the fifth object in the centre in the last experiment could not be reconstructed, which demonstrates lower sensitivity in central imaging area.

3.3. Square-Shaped Fabric Sensor. A larger area square-shaped sensor was developed for human study. A 32-channel EIT system was used for pressure mapping in a different fabric. W170-SL-PA-1500 was used as a pressure sensitive fabric in this study. The reduced stretch in this sensor reduces potential hysteresis effect since no large scaled deformation

could occur when pressure is applied. A wooden frame is used for accurate positioning of the electrodes. The first test was carried to observe the capability of the square fabric sensor of sensing various pressure points. Reconstruction results are shown in Figure 5, similar observations to that of the circular sensor. Figure 6 shows that 500 g sample could not be detected, while 1000 g sample was detected in central and boundary areas.

3.4. Preliminary Human Application Test. The first human volunteer experiments were carried out as pressure mapping imaging for foot. The sensor does not need to be in direct contact with the person's foot so it is entirely safe to test. The imaging results are shown in Figure 7. The tests were performed on single foot and on both feet of a young volunteer. The first images show the location of right foot of the volunteer. For the second experiment the left foot moved to the sensing area quickly. There is still a strong pressure in the area of right foot and this can be either a hysteresis effect

on the sensor or tendency of the volunteer to keep higher level of pressure on their right foot to keep their balance the same way as single foot experiment. The third experiment is when the volunteer moves with both feet to the fabric area. The image shows similar pressure mapping for both feet.

4. Discussion and Conclusion

In this paper, EIT-based fabric sensors were presented and tested. For an object in the central areas, the resulting image is less clear when compared to the region closer to the electrodes due to higher sensitivity. In many traditional applications of the EIT, access to central imaging area is not possible. In fabric-based EIT, it is possible to include one or more electrodes inside the imaging region, which could enhance the sensitivity in central imaging area.

The fabric conductivity changes in response to the pressure-induced shape deformation. EIT system provides a real-time imaging of the conductivity distribution change. The conductivity distribution change can be viewed as a nonlinear function of the shape change which can be expressed as a longitudinal displacement. The longitudinal displacement is determined by the pressure distribution, the boundary geometry, and the elastic property of the fabric. The displacement can be computed by solving Poisson's equation with the homogeneous Dirichlet boundary condition. These electromechanical models need to be developed in order to achieve a better understanding of fabric EIT for possible future applications. Circular-shaped fabric sensors have shown promising detectability for single and multiple objects, whereas rectangular-shaped sensors showed some artefacts near corners. The boundary data is relatively sensitive to a perturbation near the electrodes, while it is insensitive to local perturbation away from electrodes. In rectangular-shaped sensors, even if we apply a local pressure away from corners, it may produce an abrupt perturbation near the corners. This problem should be handled via a careful analysis in order to develop robust reconstruction algorithm for visualizing pressure distribution from EIT data. Our future research includes multifrequency EIT-based pressure sensing imaging. Since the modal structure of the fabric-based sensor is not entirely pure resistant, measurement of permittivity can be useful, particularly for capacitive effect in the contact nodes, and the change the deformation of the structure can provide valuable information.

Acknowledgment

The authors would like to thank the young volunteer Daniel Soleimani for taking part in the preliminary human test application. J. K. Seo is supported by the National Research Foundation of Korea (NRF) grant funded by the Korea government (MEST) no. 2011-0028868 (2012RIA2A1A03670512).

References

- [1] A. Yao and M. Soleimani, "A pressure mapping imaging device based on electrical impedance tomography of conductive fabrics," *Sensor Review*, vol. 32, no. 4, pp. 310–317, 2012.
- [2] R. Wijesiriwardana, K. Mitcham, W. Hurley, and T. Dias, "Capacitive fiber-meshed transducers for touch and proximity-sensing applications," *IEEE Sensors Journal*, vol. 5, no. 5, pp. 989–994, 2005.
- [3] A. Ueno, Y. Akabane, T. Kato, H. Hoshino, S. Kataoka, and Y. Ishiyama, "Capacitive sensing of electrocardiographic potential through cloth from the dorsal surface of the body in a supine position: a Preliminary study," *IEEE Transactions on Biomedical Engineering*, vol. 54, no. 4, 2007.
- [4] J. C. Doll, S. J. Park, and B. L. Pruitt, "Design optimization of piezoresistive cantilevers for force sensing in air and water," *Journal of Applied Physics*, vol. 106, no. 6, Article ID 064310, 2009.
- [5] H. H. Gharib and W. A. Moussa, "On the feasibility of a new approach for developing a piezoresistive 3D stress sensing rosette," *IEEE Sensors Journal*, vol. 11, no. 9, pp. 1861–1871, 2011.
- [6] M. Feneberg, K. Thonke, T. Wunderer, F. Lipski, and F. Scholz, "Piezoelectric polarization of semipolar and polar GaInN quantum wells grown on strained GaN templates," *Journal of Applied Physics*, vol. 107, no. 10, Article ID 103517, 2010.
- [7] M. Willatzen, B. Lassen, L. C. Lew Yan Voon, and R. V. N. Melnik, "Dynamic coupling of piezoelectric effects, spontaneous polarization, and strain in lattice-mismatched semiconductor quantum-well heterostructures," *Journal of Applied Physics*, vol. 100, no. 2, Article ID 024302, 2006.
- [8] D.-J. Choi, C.-T. Rim, S. Kim, and Y. K. Kwak, "High sensitivity inductive sensing system for position measurement," in *Proceedings of the 17th IEEE Instrumentation and Measurement Technology Conference (IMTC '00)*, 2000.
- [9] A. Drumea, P. Svasta, and M. Blejan, "Modelling and simulation of an inductive displacement sensor for mechatronic systems," in *Proceedings of the 33rd International Spring Seminar on Electronics Technology (ISSE '10)*, pp. 304–307, May 2010.
- [10] A. M. Lebar, G. F. Harris, J. J. Wertsch, and H. Zhu, "An optoelectric plantar "shear" sensing transducer: design, validation, and preliminary subject tests," *IEEE Transactions on Rehabilitation Engineering*, vol. 4, no. 4, pp. 310–319, 1996.
- [11] Y. H. Wen, G. Y. Yang, V. J. Bailey, G. Lin, W. C. Tang, and J. H. Keyak, "Mechanically robust micro-fabricated strain gauges for use on bones," in *Proceedings of the 3rd IEEE/EMBS Special Topic Conference on Microtechnology in Medicine and Biology*, pp. 302–304, May 2005.
- [12] Y. Kim, Y. Kim, C. Lee, and S. Kwon, "Thin polysilicon gauge for strain measurement of structural elements," *IEEE Sensors Journal*, vol. 10, no. 8, pp. 1320–1327, 2010.
- [13] K. S. Jaichandar and E. A. M. Garcia, "Intelli-sense bed patient movement sensing and anti-sweating system for bed sore prevention in a clinical environment," in *Proceedings of the 8th International Conference on Information, Communications and Signal Processing (ICICS '11)*, 2011.
- [14] H. Ruser, "Smart low-cost weather sensor as an example for "multi-component" sensors," in *Proceedings of the IEEE International Conference on Multisensor Fusion and Integration for Intelligent Systems (MFI '06)*, pp. 559–564, September 2006.
- [15] J. H. Cho, M. Kothare, and M. G. Arnold, "Reconfigurable multi-component sensors built from MEMS payloads carried by micro-robots," in *Proceedings of the IEEE Sensors Applications Symposium (SAS '10)*, pp. 15–19, February 2010.
- [16] M. Reddy, S. S. Gill, and P. A. Rochon, "Preventing pressure ulcers: a systematic review," *Journal of the American Medical Association*, vol. 296, no. 8, pp. 974–984, 2006.

- [17] W. S. Fulton and R. T. Lipczynski, "Body-support pressure measurement using electrical impedance tomography," in *Proceedings of the 15th Annual International Conference of the IEEE Engineering in Medicine and Biology Society*, pp. 98–99, October 1993.
- [18] F. Carpi and D. De Rossi, "Electroactive polymer-based devices for e-textiles in biomedicine," *IEEE Transactions on Information Technology in Biomedicine*, vol. 9, no. 3, pp. 295–318, 2005.
- [19] A. Hassan, A. Nagakubo, and Y. Kuniyoshi, "A tactile distribution sensor which enables stable measurement under high and dynamic stretch," in *Proceedings of the IEEE Symposium on 3D User Interfaces (3DUI '09)*, pp. 87–93, March 2009.
- [20] A. Elsanadedy, Y. Mamatjan, M. Ahmadi, and A. Adler, "Characterisation of conductive polymer for EIT based sensor," in *Proceedings of the International Conference on Electrical and Computer Systems (ICECS '12)*, Ottawa, Canada, August 2012.
- [21] E. Somersalo, M. Cheney, and D. Isaacson, "Existence and uniqueness for electrode models for electric current computed tomography," *SIAM Journal on Applied Mathematics*, vol. 52, no. 4, pp. 1023–1040, 1992.
- [22] Y. Tada and T. Yasunori, "A flexible and stretchable tactile sensor utilizing static electricity," in *Proceedings of the IEEE/RSJ International Conference on Intelligent Robots and Systems (IROS '07)*, pp. 684–689, November 2007.
- [23] LR-SL-PA-10E5, *Eeontex Conductive Stretchable Fabric*, Eeonyx Corporation, 2009.
- [24] NW170-SL-PA-1500, *Eeontex Conductive Nonwoven Fabric*, Eeonyx Corporation, 2009.

Research Article

CoReHA 2.0: A Software Package for *In Vivo* MREIT Experiments

Kiwan Jeon¹ and Chang-Ock Lee²

¹ National Institute for Mathematical Sciences, Daejeon 305-811, Republic of Korea

² Department of Mathematical Sciences, KAIST, Daejeon 305-701, Republic of Korea

Correspondence should be addressed to Chang-Ock Lee; colee@kaist.edu

Received 12 December 2012; Accepted 20 January 2013

Academic Editor: Jin Keun Seo

Copyright © 2013 K. Jeon and C.-O. Lee. This is an open access article distributed under the Creative Commons Attribution License, which permits unrestricted use, distribution, and reproduction in any medium, provided the original work is properly cited.

Magnetic resonance electrical impedance tomography (MREIT) is a new medical imaging modality visualizing static conductivity images of electrically conducting subjects. Recently, MREIT has rapidly progressed in its theory, algorithm, and experiment technique and now reached to the stage of *in vivo* animal experiments. In this paper, we present a software, named CoReHA 2.0 standing for the second version of conductivity reconstructor using harmonic algorithms, to facilitate *in vivo* MREIT reconstruction of conductivity image. This software offers various computational tools including preprocessing of MREIT data, identification of 2D geometry of the imaging domain and electrode positions, and reconstruction of cross-sectional scaled conductivity images from MREIT data. In particular, in the new version, we added several tools including ramp-preserving denoising, harmonic inpainting, and local harmonic B_z algorithm to deal with data from *in vivo* experiments. The presented software will be useful to researchers in the field of MREIT for simulation, validation, and further technical development.

1. Introduction

Recently, a new imaging modality called magnetic resonance electrical impedance tomography (MREIT) has been introduced, which allows high resolution imaging of tomographic electrical conductivity distributions of biological objects [1, 2]. The technique involves (i) current injection into an electrically conducting object such as animal or human body through surface electrodes, (ii) measurement of induced internal magnetic flux density using an MRI system, typically only the z -component B_z of the induced magnetic flux density $\mathbf{B} = (B_x, B_y, B_z)$, where z is the axis parallel to the main magnetic field of the MR scanner, and (iii) conductivity reconstruction by solving nonlinear boundary value problems with given injected currents and measured magnetic flux density, employing finite element methods. Although it looks straight forward to reconstruct conductivity distribution as described in the three steps, computation involves several innovative approaches including magnetic flux density estimation, data verification, segmentation, and solving forward/inverse problems. These

specific computations cannot be handled through readily available finite element packages; thus, it is required to develop a user friendly software with graphics user interface (GUI) for those who wish to reconstruct conductivity distributions. Upon these requests, we developed a software package, called CoReHA [3, 4] which stands for conductivity reconstructor using harmonic algorithms, using VC++ MFC 6.0 (Microsoft Foundation Class Library 6.0) and OpenGL under the Microsoft Windows operating system. Based on the harmonic B_z algorithm [5], CoReHA supports all procedures from the preprocessing of raw data to conductivity imaging through the intuitively apprehensible graphic user interface, more specifically, data conversion of raw k -space data, data verification, segmentation tools for numerical computation, solvers of forward/inverse problems using finite element methods, and 2D/3D data view as well as histogram. This software has been a major tool to facilitate multilateral studies for MREIT and has brought out successful reconstruction of conductivity imaging in many researches [4, 6–8].

In the stage of *in vivo* MREIT experiments, we have to address the improvement of the signal-to-noise ratio (SNR) of

measured B_z data, since B_z data has weak strength due to the low amount of injected current for the safety guide. Moreover, there may exist MR signal void regions in the animal or human body, where noise levels of B_z are excessively high, and as a result, uncertain effects are produced. For dealing with these technical problems, several methods were developed, called ramp preserving denoising [9], harmonic inpainting [10], and local harmonic B_z algorithm [11]. Incorporating these new features, we release the second version of CoReHA for *in vivo* MREIT experiments. The presented software will be useful to researchers in the field of MREIT experimental studies as well as *in vivo* animal/human experiments. CoReHA is available from the website <http://iirc.khu.ac.kr/>.

This paper is organized as follows. In Section 2, MREIT system is introduced and related works are explained. Brief explanation of the previous version of this software is given for comprehensive understanding of our works in Section 3. Details of new tools of the software for dealing with *in vivo* stage issues are provided in Section 4. Finally, we close in Section 5 with conclusions and a discussion of future works.

2. The Basic of MREIT and Related Works

We briefly explain how MR scanner is used as a tool to capture internal magnetic flux density images, and the MR scanner has its magnetic field in z -direction. Let an electrically conducting subject occupy a three-dimensional domain Ω with its boundary $\partial\Omega$ and a conductivity distribution σ . As shown in Figure 1, we attach pairs of electrodes \mathcal{E}_j^+ and \mathcal{E}_j^- along $\partial\Omega$ in order to inject a current I_j in a form of pulses whose timing is synchronized with an MR pulse sequence for $j = 1, 2$. The injection current produces current density \mathbf{J}_j satisfying the following elliptic equations:

$$\begin{aligned} \nabla \cdot (\sigma \nabla u_j [\sigma]) &= 0 \quad \text{in } \Omega, \\ I &= \int_{\mathcal{E}_j^+} \sigma \frac{\partial u_j [\sigma]}{\partial \mathbf{n}} ds = - \int_{\mathcal{E}_j^-} \sigma \frac{\partial u_j [\sigma]}{\partial \mathbf{n}} ds, \\ \nabla u_j [\sigma] \times \mathbf{n} |_{\mathcal{E}_j^+ \cup \mathcal{E}_j^-} &= 0, \\ \sigma \frac{\partial u_j [\sigma]}{\partial \mathbf{n}} &= 0 \quad \text{on } \partial\Omega \setminus \overline{\mathcal{E}_j^+ \cup \mathcal{E}_j^-}, \end{aligned} \quad (1)$$

where $\mathbf{J}_j = -\sigma \nabla u_j$. Also, magnetic flux density \mathbf{B} is given by Biot-Savart law as follows:

$$\mathbf{B}(\mathbf{x}) = \frac{\mu_0}{4\pi} \int_{\Omega} \mathbf{J}(\mathbf{x}') \times \frac{\mathbf{x} - \mathbf{x}'}{|\mathbf{x} - \mathbf{x}'|^3} d\mathbf{x}' + \mathcal{H}(\mathbf{x}), \quad (2)$$

where \mathcal{H} is magnetic flux density from electrodes, wires, and others. Note that $\nabla^2 \mathcal{H} = 0$ in Ω . Then MR spectrometer provides the complex k -space data \mathcal{S} that is influenced by B_z in the following way. Given current injection I_j , we have

$$\mathcal{S}_j(m, n, z) = \iint M(x, y, z) e^{i\delta(x, y, z)} e^{iyB_z(x, y, z)T_c} \times e^{-i(xm\Delta k_x + yn\Delta k_y)} dx dy, \quad (3)$$

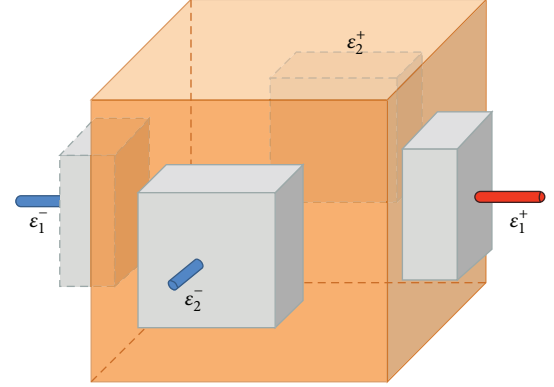


FIGURE 1: Domain Ω for MREIT.

where M is a conventional MR magnitude image, δ any systematic phase artifact, $\gamma = 26.75 \times 10^7$ rad/T-s the gyro-magnetic ratio of hydrogen, and T_c the current pulse width in seconds. By the discrete inverse Fourier transformation of the k -space data \mathcal{S} in (3), we obtain the following complex images:

$$\mathcal{M}^+(x, y, z) = M(x, y, z) e^{i\delta(x, y, z)} e^{iyB_z(x, y, z)T_c}. \quad (4)$$

To extract B_z data stably while eliminating systematic phase artifact δ , we inject the counter directional current providing the counter part of \mathcal{M}^+ in (4) so that we get

$$\mathcal{M}^-(x, y, z) = M(x, y, z) e^{i\delta(x, y, z)} e^{-iyB_z(x, y, z)T_c}. \quad (5)$$

Division of \mathcal{M}^+ by its counter part \mathcal{M}^- leads to

$$B_z(x, y, z) = \frac{1}{2\gamma T_c} \arg \left(\frac{\mathcal{M}^+(x, y, z)}{\mathcal{M}^-(x, y, z)} \right). \quad (6)$$

MRCDI [12] and early stage MREIT [13–15] use measurements of all three components of $\mathbf{B} = (B_x, B_y, B_z)$ which require subject rotations inside MR scanner. However, experiences show that these subject rotations are impractical and also cause other problems such as misalignments of pixels. Hence, in order to make the MREIT technique easily applicable to clinical situations, we should use only B_z data for the conductivity reconstruction.

In the harmonic B_z algorithm [5, 16, 17] which is the first constructive B_z -based MREIT algorithm, we inject two independent electrical currents I_1 and I_2 through two pairs of surface electrodes \mathcal{E}_1^\pm and \mathcal{E}_2^\pm , respectively, to get two raw k -space data. The amount of each injection current is determined by the product of current amplitude and time duration. A modified spin-echo pulse sequence synchronized with the current injection is typically used as described in experimental works [5, 18, 19], and $B_{z,1}$ and $B_{z,2}$ are obtained from the formula (6). Then the reconstruction algorithm is based on the following identity:

$$\begin{bmatrix} \frac{\partial \ln \sigma}{\partial x}(\mathbf{x}) \\ \frac{\partial \ln \sigma}{\partial y}(\mathbf{x}) \end{bmatrix} = \frac{1}{\mu_0} (\mathbb{A}[\sigma](\mathbf{x}))^{-1} \begin{bmatrix} \nabla^2 B_{z,1}(\mathbf{x}) \\ \nabla^2 B_{z,2}(\mathbf{x}) \end{bmatrix}, \quad \mathbf{x} \in \Omega, \quad (7)$$

where

$$\mathbb{A}[\sigma](\mathbf{x}) = \begin{bmatrix} -J_{y,1} & J_{x,1} \\ -J_{y,2} & J_{x,2} \end{bmatrix} = \begin{bmatrix} \sigma \partial_y u_1 & -\sigma \partial_x u_1 \\ \sigma \partial_y u_2 & -\sigma \partial_x u_2 \end{bmatrix}, \quad \mathbf{x} \in \Omega \quad (8)$$

and $J_{x,j}$ and $J_{y,j}$ are the x and y components of induced current density \mathbf{J}_j , respectively. We now present the conductivity reconstruction procedure using the harmonic B_z algorithm in CoReHA, which consists of six steps.

Step 1. We impress electrical currents I_1 and I_2 through pairs of surface electrodes \mathcal{E}_1^\pm and \mathcal{E}_2^\pm , respectively, and get the k -space data \mathcal{S}_j for $j = 1, 2$ using an MR scanner.

Step 2. We produce an MR magnitude image M and induced magnetic flux densities $B_{z,j}$ from the k -space data \mathcal{S}_j for $j = 1, 2$ given by (6).

Step 3. Using the MR magnitude image M , we perform segmentation of $\partial\Omega$ and \mathcal{E}_j^\pm . Here, we use level-set-based segmentations.

Step 4. We set the initial guess $\sigma^0(\mathbf{x}, z) = 1$ in Ω .

Step 5. We solve the problem (1) with $\sigma = \sigma^0$.

Step 6. We solve

$$\nabla_{xy}^2 \ln \sigma^1 = \nabla_{xy} \cdot \left(\mathbb{A}[\sigma^0]^{-1} \begin{bmatrix} \nabla^2 B_{z,1} \\ \nabla^2 B_{z,2} \end{bmatrix} \right) \quad \text{in } \Omega_z \quad (9)$$

with the boundary condition

$$\nabla_{xy} \ln \sigma^1 \cdot \mathbf{v} = \left(\mathbb{A}[\sigma^0]^{-1} \begin{bmatrix} \nabla^2 B_{z,1} \\ \nabla^2 B_{z,2} \end{bmatrix} \right) \cdot \mathbf{v} \quad \text{on } \partial\Omega_z, \quad (10)$$

where ∇_{xy}^2 and ∇_{xy} are two-dimensional Laplacian and gradient operators on the xy -plane, respectively, Ω_z a two-dimensional slice of Ω , which is perpendicular to the z -axis, and \mathbf{v} the two-dimensional outward normal vector to $\partial\Omega_z$.

Note that in the harmonic B_z algorithm in [5, 16], Steps 5 and 6 are repeated to get σ^n from σ^{n-1} until it converges. In order to ensure the convergence of the harmonic B_z algorithm, the conductivity values of the subject's boundary should be homogeneous and the contrast of the conductivity distribution is assumed small enough [16, 17]. But, in general, the conductivity distribution of animal and human is quite inhomogeneous [11]. Also, for the completion of the iterative procedure, we have to resolve heavy cost computational issues for 3D forward problem (1), related to, for example, 3D segmentation, 3D mesh generation, and 3D forward problem solver. Fortunately, for the clinical purpose, it is enough to find the scaled conductivity images instead of the true ones because the reconstructed scaled ones reflect the fine details of the true conductivity contrast when the conductivity contrast is low [11]. Hence, in CoReHA, we

iterate Steps 5 and 6 only once. Due to the same reason, in Step 5, we solve a simplified problem

$$\begin{aligned} \nabla_{xy} \cdot (\sigma \nabla_{xy} u_j[\sigma]) &= 0 \quad \text{in } \Omega_z \\ u_j &= 1 \quad \text{on } \mathcal{E}_j^+ \cap \Omega_z \\ u_j &= -1 \quad \text{on } \mathcal{E}_j^- \cap \Omega_z \\ \sigma \frac{\partial u_j[\sigma]}{\partial \mathbf{v}} &= 0 \quad \text{on } \partial\Omega_z \setminus \overline{\mathcal{E}_j^+ \cup \mathcal{E}_j^-}, \end{aligned} \quad (11)$$

instead of (1). In addition, in Step 6, we adopt the boundary condition

$$\sigma^1 = 1 \quad \text{on } \partial\Omega_z, \quad (12)$$

to replace (10). Note that three-dimensional Laplacian of B_z may not be invalid due to the circumstance of the experiments. Hence, CoReHA supports for both 2D and 3D Laplacian of B_z .

3. CoReHA 1.0: For Multilateral Studies

CoReHA implements Step 2 through 6 of the harmonic B_z algorithm since Step 1 is about the experiment using an MR scanner and EIT equipment. In this section, we briefly describe each step of CoReHA 1.0 for understanding the software package on the whole.

After an MREIT experiment, one can perform the phase extraction process by applying fast Fourier transform in Section 2 as well as obtain the MR imaging by taking magnitude of \mathcal{M}^\pm . For this computation, we use FFTW [20], one of the well-known fast Fourier transform libraries, for obtaining (4) from (3). Since B_z in (6) is wrapped due to the branch cut of argument operator, we apply the Goldstein's algorithm [21] for two-dimensional phase unwrapping. Note that even if B_z data is continuous in the xy -plane given by phase unwrapping, we do not guarantee the continuity along the z -direction. In order to verify the continuity of B_z along the z -direction, CoReHA supports a verification tool. Hence, if the verification fails, one should drop $(\partial^2/\partial z^2)B_z$ in $\nabla^2 B_z$ for preventing the artifact coming from wrong Laplacian calculation.

In order to get the imaging domain, we have employed statistically reinstating method (SRM) [22] on MR image, which is a level-set-based segmentation method. After the boundary of the object including electrodes is segmented by SRM, one can operate additional manual work to configure the object without electrodes or to modify the local geometry. After segmentation, one can generate the triangle mesh for the numerical computation. For the triangulation, we adopt the Triangle [23] which is a well-known open source software for the two-dimensional triangulation.

For the computation of (11) and (9), we implement the standard \mathcal{P}_1 finite element method and apply the conjugate gradient (CG) method for matrix inversion. The size of generated triangulation is automatically determined by given geometrical information and its size is small enough to

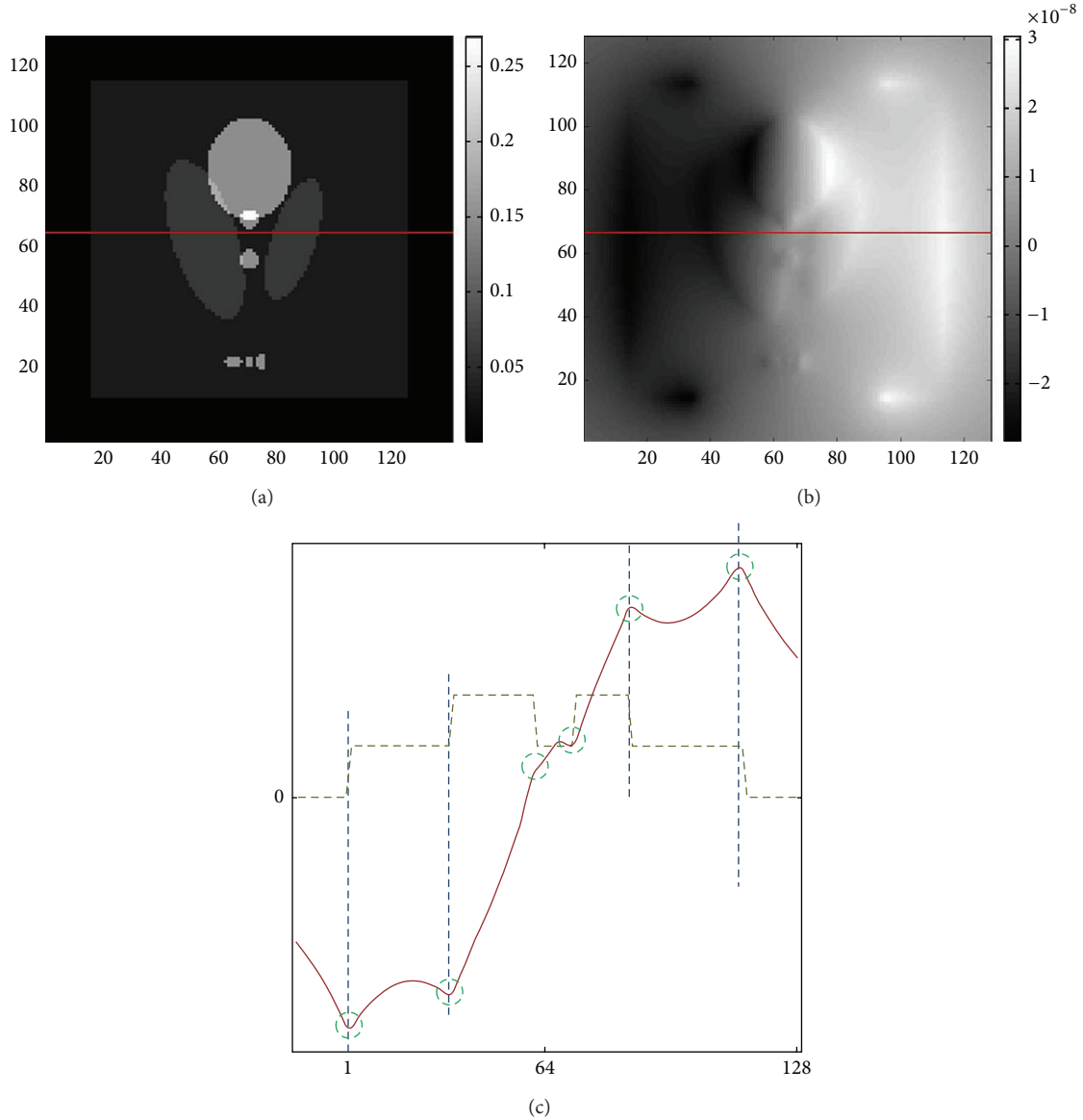


FIGURE 2: Explanation of ramp structure. (a) Conductivity distribution. (b) Corresponding B_z data generated by the current injection along vertical direction. (c) 1D profiles along the line $y = 64$ which is indicated by the red line in (a) and (b). Green dotted line is the conductivity distribution and the red one is the B_z data. Locations of conductivity change match the ramp structure which is characterised by changes of slopes of the B_z data.

cover the pixel size. Of course, one can adjust the size of triangulation for one's own purpose.

For the details of CoReHA 1.0, see [3].

4. CoReHA 2.0: For Better Imaging Quality

In this section, we describe in detail new features in the second version of CoReHA for dealing with *in vivo* MREIT experiments.

4.1. Preprocessing: Ramp Preserving Denoising. For the safety of the subject in *in vivo* experiments, the amount of injected current I should be reduced less than a few milliamperes.

The SNR of B_z data is also directly affected by the noise of \mathcal{M} . Therefore, a proper denoising method is required for obtaining the reconstructed image with reduced noise artifact. Let us consider the reconstruction identity (7) for the derivation of denoising algorithm. Apparently, the change of the conductivity distribution $\nabla_{xy} \ln \sigma$ is directly proportional to the Laplacian of B_z data if the matrix $\mathbb{A}[\sigma](\mathbf{x})$ is invertible. When we apply a denoising algorithm, the structure of ramp should be preserved in order to prevent the change of shape or wrong alignment of anomaly location. For our better understanding, we illustrate a simple example using a modified Shepp-Logan phantom. We compute the current density using (11) with the vertically identical conductivity

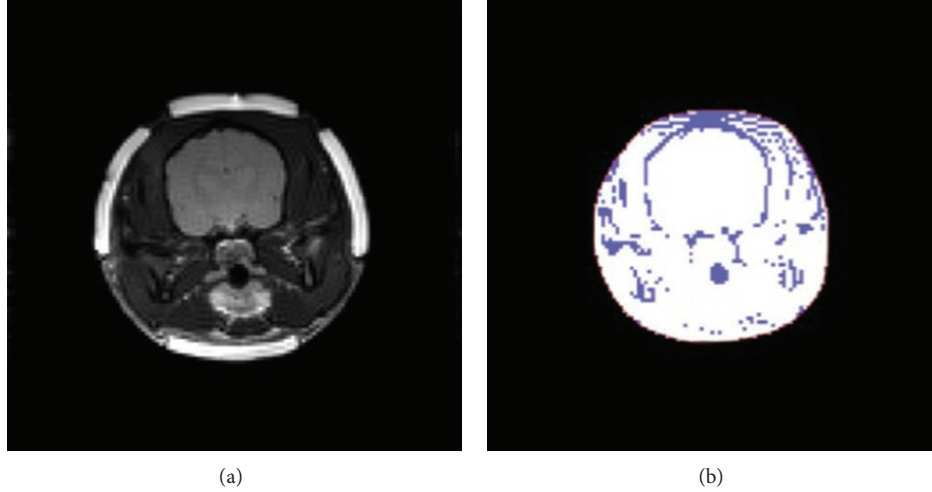


FIGURE 3: Defected region select using threshold (a) MR image and (b) defected region by the thresholding (purple color).

distribution given in Figure 2(a). Applying the Biot-Savart law (2), we obtain the B_z data as shown in Figure 2(b). We can see that the ramp structure of B_z reflects the change of the conductivity distribution as shown in Figure 2(c). In order to keep the ramp structure during the denoising, we adopt a nonlinear diffusion equation method based on structure tensor [9, 24].

For the sake of completeness, we summarise the results in [9, 24]. Let us consider the structure tensor U defined by

$$U := \sum_{i=1}^2 \nabla_{xy} w_i \nabla_{xy} w_i^T, \quad (13)$$

where

$$\begin{pmatrix} w_1 \\ w_2 \end{pmatrix} := \nabla_{xy} B_z = \begin{pmatrix} \partial_x B_z \\ \partial_y B_z \end{pmatrix}. \quad (14)$$

To reduce the noise, we solve the following nonlinear PDE cooperating with the structure tensor U :

$$\begin{aligned} \partial_t B_z(\mathbf{x}, t) &= \nabla_{xy} \cdot \left(g(U(\mathbf{x}, T_2)) \nabla_{xy} B_z(\mathbf{x}, t) \right) \\ &\quad \text{in } R \times (0, T_1], \\ \left(g(U(\mathbf{x}, T_2)) \nabla_{xy} B_z(\mathbf{x}, t) \right) \cdot \mathbf{n} &= 0 \quad \text{on } \partial R \times (0, T_1], \\ B_z(\mathbf{x}, 0) &= B_z(\mathbf{x}) \quad \text{on } R, \end{aligned} \quad (15)$$

with

$$\begin{aligned} \partial_t u_{ij}(\mathbf{x}, \tau) &= \nabla_{xy} \cdot \left(g(U_s) \nabla_{xy} u_{ij}(\mathbf{x}, \tau) \right) \quad \text{in } R \times (0, T_2], \\ \left(g(U_s) \nabla_{xy} u_{ij}(\mathbf{x}, \tau) \right) \cdot \mathbf{n} &= 0 \quad \text{on } \partial R \times (0, T_2], \end{aligned}$$

$$\begin{aligned} u_{ij}(\mathbf{x}, 0) &= \left(\sum_{k=1}^2 \nabla_{xy} w_k(\mathbf{x}, t) \nabla_{xy} w_k(\mathbf{x}, t)^T \right)_{ij} \quad \text{on } R, \\ g(U) &= \frac{1}{\sqrt{1+\Lambda}} v_\Lambda v_\Lambda^T + \frac{1}{\sqrt{1+\lambda}} v_\lambda v_\lambda^T, \end{aligned} \quad (16)$$

where R is a two-dimensional region for the slice of B_z data, u_{ij} is the (i, j) element of U , Λ and λ are maximum and minimum eigenvalues of U , respectively, v_Λ and v_λ are corresponding normalized eigenvectors, and $U_s \equiv G_s * U$ is the (element by element) convolution of U with the two-dimensional Gaussian kernel G_s with a standard deviation s . In the new version of CoReHA, the user only considers the parameter T_1 , the total diffusion time of the denoising algorithm. Through extensive numerical studies [9, 24], we figured out that the denoising results are robust to the tensor regularization time T_2 . The noise level of B_z affects only T_1 . Consequently, we fix $T_2 = 2$ in this version, which seems to be enough time to regularize the diffusion tensor. Note that the denoising algorithm is only valid when the user considers two-dimensional Laplacian of B_z since the diffusion process is on the xy -plane. For more details, see [9].

4.2. Preprocessing: Harmonic Inpainting Using MR Data.

Let us revisit (6). In a local region of Ω , where $|\mathcal{M}^\pm| \approx 0$, B_z is defected severely by the amplification of noise due to the division procedure. In the previous version of CoReHA to overcome this trouble, a manual segmentation tool was provided for the extraction of the problematic region with the harmonic inpainting algorithm [10] to solve the Poisson equation. However, the manual segmentation causes user-dependent reconstruction results. For dealing with this situation, we assume that the defected region has low MR magnitude and its conductivity distribution is homogenous so that $\nabla^2 B_z = 0$. Then, we automatically select the defected region by taking a threshold for the MR data. Figure 3 shows an example for the selection of the defected

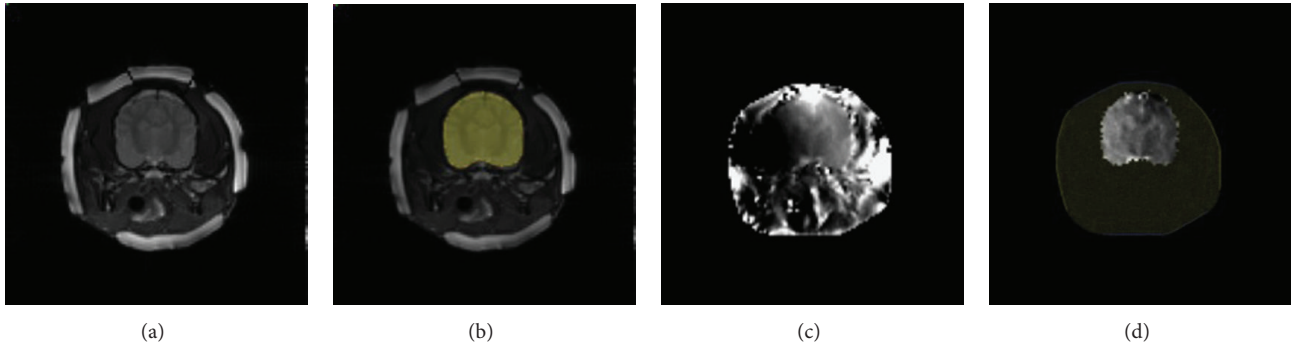


FIGURE 4: Local harmonic B_z algorithm: (a) MR image, (b) selected interested region, (c) conductivity reconstruction on the whole domain, and (d) conductivity reconstruction using the local harmonic B_z algorithm.

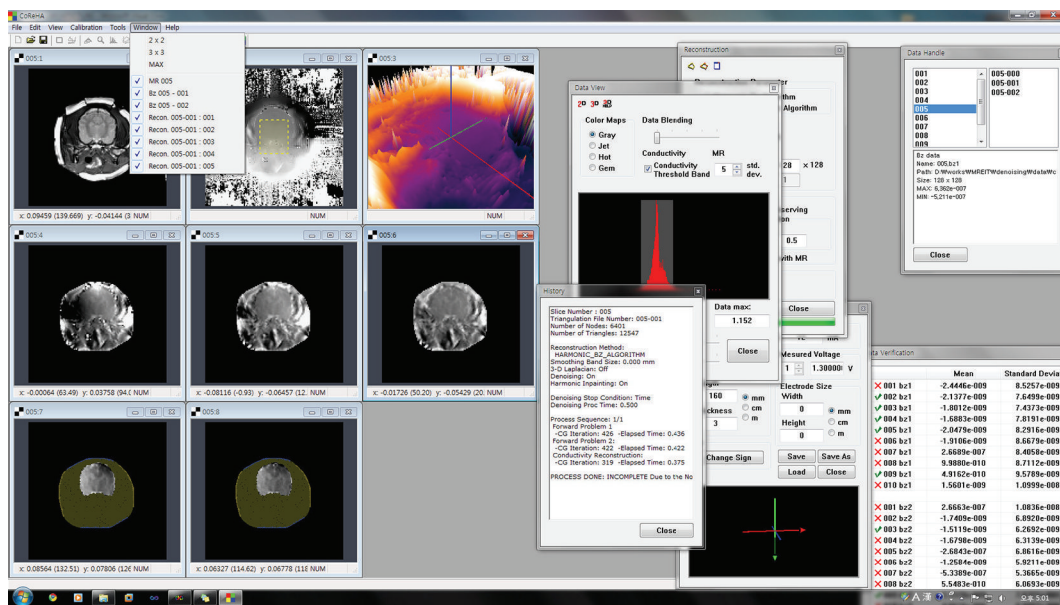


FIGURE 5: Snapshot of CoReHA 2.0.

region by thresholding. In the new version of CoReHA, we consider the 10% of maximum magnitude of MR data as a threshold. Incorporating the ramp-preserving denoising, we additionally apply isotropic diffusion on the defected region within enough duration. The user does not need to consider how well the defected region is segmented; therefore, it guarantees the robustness of the conductivity reconstruction without user dependency.

4.3. Reconstruction: Local Harmonic B_z Algorithm. We support a modified local harmonic B_z algorithm [11] for the successful reconstruction by excluding the defected region directly. Let D be a local region without defection which attracts our interests. Then, we locally reconstruct the conductivity by solving (9) and (10) on the local region D instead of the whole domain Ω . In order to solve (9) with (10), we use a \mathcal{P}_1 finite element method on a selected triangle mesh and apply conjugate gradient (CG) method for matrix inversion. CoReHA 2.0 supports a user interface to draw and

manipulate a polygonal local region by adding or removing points. It is useful when the user wants to see a small local change of conductivity on the local region such as brain or pelvis. In Figure 4(c), we see that the reconstructed conductivity is severely contaminated by locally magnified noise. But, Figure 4(d) shows the successful reconstruction of local brain region by the local harmonic B_z algorithm.

4.4. Additional Tools. Due to the different physical properties between water and fat, the measured MR signal can be shifted in the fat region, since the MR scanner assumes that spin isochromats precess at the Larmor frequency of water. Therefore, the MR signal may become void, and overlapped images are produced in the animal/human experiments. To overcome this difficulty, new version of CoReHA contains the chemical shift correction using 3-points Dixon method [25]. In the k -space data conversion, one can manipulate the MR signal using the user interface which provides separated water and fat images of MR. For more details, see [25].

Furthermore, we implemented many useful features to help our understanding of MR, B_z , and conductivity images, for example, magnification windows and advanced alignment and resizing of windows. Figure 5 is a snapshot of CoReHA 2.0, that shows newly introduced features.

5. Conclusions and Future Works

In this paper, we presented new features in a software package, called CoReHA 2.0, to deal with the data from the *in vivo* stage of MREIT. In this version, we enhanced the preprocessing procedure based on the ramp preserving denoising and harmonic inpainting with MR data to increase SNR of B_z data in the *in vivo* experiment. Also, we provided a user interface for the local harmonic B_z algorithm for the reconstruction on the locally interested region. The performance results of suggested algorithms and methods are given in [26]. Note that CoReHA reconstructs the contrast image of conductivity. For the medical diagnosis, the contrast image is enough. However, recently the necessity for the true conductivity came to the fore. For the true conductivity image reconstruction, we need a subject-dependent 3D segmentation and modeling tools, 3D denoising algorithm, and 3D finite element solver and higher order methods for more accurate computation.

Conflict of Interests

The authors declare that this paper has no conflict of interests with CoReHA 2.0 software.

Acknowledgment

This work was supported by NRF-2011-0015399.

References

- [1] J. K. Seo and E. J. Woo, "Magnetic resonance electrical impedance tomography (MREIT)," *SIAM Review*, vol. 53, no. 1, pp. 40–68, 2011.
- [2] E. J. Woo and J. K. Seo, "Magnetic resonance electrical impedance tomography (MREIT) for high-resolution conductivity imaging," *Physiological Measurement*, vol. 29, no. 10, pp. R1–R26, 2008.
- [3] K. Jeon, C.-O. Lee, H. J. Kim, E. J. Woo, and J. K. Seo, "CoReHA: conductivity reconstructor using harmonic algorithms for magnetic resonance electrical impedance tomography (MREIT)," *Journal of Biomedical Engineering*, vol. 30, no. 5, pp. 279–287, 2009.
- [4] K. Jeon, A. S. Minhas, Y. T. Kim et al., "MREIT conductivity imaging of the postmortem canine abdomen using CoReHA," *Physiological Measurement*, vol. 30, no. 9, pp. 957–966, 2009.
- [5] J. K. Seo, J. R. Yoon, E. J. Woo, and O. Kwon, "Reconstruction of conductivity and current density images using only one component of magnetic field measurements," *IEEE Transactions on Biomedical Engineering*, vol. 50, no. 9, pp. 1121–1124, 2003.
- [6] W. C. Jeong, Y. T. Kim, A. S. Minhas et al., "In vivo conductivity imaging of human knee using 3 mA injection current in MREIT," *Journal of Physics*, vol. 224, no. 1, Article ID 012148, 2010.
- [7] H. J. Kim, W. C. Jeong, A. S. Minhas et al., "In vivo conductivity imaging of canine male pelvis using a 3T MREIT system," *Journal of Physics*, vol. 224, no. 1, Article ID 012020, 2010.
- [8] A. S. Minhas, Y. T. Kim, Y. Han, W. C. Jeong, H. J. Kim, and E. J. Woo, "Experiment performance evaluation of multi-echo ICNE pulse sequence in magnetic resonance electrical impedance tomography," *Magnetic Resonance in Medicine*, vol. 66, no. 4, pp. 957–956, 2011.
- [9] C.-O. Lee, K. Jeon, S. Ahn, H. J. Kim, and E. J. Woo, "Ramp-preserving denoising for conductivity image reconstruction in magnetic resonance electrical impedance tomography," *IEEE Transactions on Biomedical Engineering*, vol. 58, no. 7, pp. 2038–2050, 2011.
- [10] B. I. Lee, S. H. Lee, T. S. Kim, O. Kwon, E. J. Woo, and J. K. Seo, "Harmonic decomposition in PDE-based denoising technique for magnetic resonance electrical impedance tomography," *IEEE Transactions on Biomedical Engineering*, vol. 52, no. 11, pp. 1912–1920, 2005.
- [11] J. K. Seo, S. W. Kim, S. Kim et al., "Local harmonic B_z algorithm with domain decomposition in MREIT: computer simulation study," *IEEE Transactions on Medical Imaging*, vol. 27, no. 12, pp. 1754–1761, 2008.
- [12] Y. Z. Ider and O. Birgul, "Use of magnetic field generated by the internal distribution of injected currents of electrical impedance tomography," *Elektrik*, vol. 6, pp. 215–225, 1998.
- [13] O. Kwon, E. J. Woo, J. R. Yoon, and J. K. Seo, "Magnetic resonance electrical impedance tomography (MREIT): simulation study of J-substitution algorithm," *IEEE Transactions on Biomedical Engineering*, vol. 49, no. 2, pp. 160–167, 2002.
- [14] E. J. Woo, S. Y. Lee, and C. W. Mun, "Impedance tomography using internal current density distribution measured by nuclear magnetic resonance," in *Proceedings of SPIE Mathematical Methods in Medical Imaging III*, vol. 2299, pp. 377–385, July 1994.
- [15] N. Zhang, *Electrical impedance tomography based on current density imaging [M.S. thesis]*, University of Toronto, Toronto, Canada, 1992.
- [16] J. J. Liu, J. K. Seo, M. Sinl, and E. J. Woo, "On the convergence of the harmonic B_z algorithm in magnetic resonance electrical impedance tomography," *SIAM Journal on Applied Mathematics*, vol. 67, no. 5, pp. 1259–1282, 2007.
- [17] J. J. Liu, J. K. Seo, and E. J. Woo, "A posteriori error estimate and convergence analysis for conductivity image reconstruction in MREIT," *SIAM Journal on Applied Mathematics*, vol. 70, no. 8, pp. 2883–2903, 2010.
- [18] C. Park, O. Kwon, E. J. Woo, and J. K. Seo, "Electrical conductivity imaging using gradient B_z decomposition algorithm in magnetic resonance electrical impedance tomography (MREIT)," *IEEE Transactions on Medical Imaging*, vol. 23, no. 3, pp. 388–394, 2004.
- [19] E. J. Woo, S. Y. Lee, J. K. Seo, O. Kwon, S. H. Oh, and B. I. Lee, "Conductivity images of biological tissue phantoms using a 3.0 Tesla MREIT system," in *Proceedings of the 26th Annual International Conference of the IEEE Engineering in Medicine and Biology Society (EMBC '04)*, pp. 1287–1289, San Francisco, NC, USA, September 2004.
- [20] M. Frigo and S. G. Johnson, 2008, <http://www.fftw.org/>.
- [21] D. C. Ghiglia and M. D. Pritt, *Two-Dimensional Phase Unwrapping: Theory, Algorithm and Software*, Wiley Interscience, New York, NY, USA, 1998.
- [22] S. H. Park, C.-O. Lee, and J. Hahn, "Image segmentation based on the statistical variational formulation using the local region

- information,” Research Report 08-03, The Korea Advanced Institute of Science and Technology (KAIST), Daejeon, Republic of Korea, 2008.
- [23] J. R. Shewchuk, “Triangle: a two-dimensional quality mesh generator and Delaunay triangulator,” 2005, <http://www.cs.cmu.edu/~quake/triangle.html>.
- [24] J. Hahn and C. O. Lee, “A nonlinear structure tensor with the diffusivity matrix composed of the image gradient,” *Journal of Mathematical Imaging and Vision*, vol. 34, no. 2, pp. 137–151, 2009.
- [25] A. S. Minhas, Y. T. Kim, W. C. Jeong, H. J. Kim, S. Y. Lee, and E. J. Woo, “Chemical shift artifact correction in MREIT,” *Journal of Biomedical Engineering*, vol. 30, pp. 461–468, 2009.
- [26] K. Jeon, H. J. Kim, C. O. Lee, J. K. Seo, and E. J. Woo, “Integration of the denoising, inpainting and local harmonic B_z algorithm for MREIT imaging of intact animals,” *Physics in Medicine and Biology*, vol. 55, no. 24, pp. 7541–7556, 2010.

Research Article

An Iterative Method for Problems with Multiscale Conductivity

Hyea Hyun Kim,¹ Atul S. Minhas,^{2,3} and Eung Je Woo³

¹Department of Applied Mathematics, Kyung Hee University, P.O. Box 446-701, Yongin, Republic of Korea

²Samsung Electronics Co. Ltd., Suwon, Republic of Korea

³Department of Biomedical Engineering, Kyung Hee University, P.O. Box 446-701, Yongin, Republic of Korea

Correspondence should be addressed to Hyea Hyun Kim, hyeahyun@gmail.com

Received 5 June 2012; Accepted 16 October 2012

Academic Editor: Bill Lionheart

Copyright © 2012 Hyea Hyun Kim et al. This is an open access article distributed under the Creative Commons Attribution License, which permits unrestricted use, distribution, and reproduction in any medium, provided the original work is properly cited.

A model with its conductivity varying highly across a very thin layer will be considered. It is related to a stable phantom model, which is invented to generate a certain apparent conductivity inside a region surrounded by a thin cylinder with holes. The thin cylinder is an insulator and both inside and outside the thin cylinder are filled with the same saline. The injected current can enter only through the holes adopted to the thin cylinder. The model has a high contrast of conductivity discontinuity across the thin cylinder and the thickness of the layer and the size of holes are very small compared to the domain of the model problem. Numerical methods for such a model require a very fine mesh near the thin layer to resolve the conductivity discontinuity. In this work, an efficient numerical method for such a model problem is proposed by employing a uniform mesh, which need not resolve the conductivity discontinuity. The discrete problem is then solved by an iterative method, where the solution is improved by solving a simple discrete problem with a uniform conductivity. At each iteration, the right-hand side is updated by integrating the previous iterate over the thin cylinder. This process results in a certain smoothing effect on microscopic structures and our discrete model can provide a more practical tool for simulating the apparent conductivity. The convergence of the iterative method is analyzed regarding the contrast in the conductivity and the relative thickness of the layer. In numerical experiments, solutions of our method are compared to reference solutions obtained from COMSOL, where very fine meshes are used to resolve the conductivity discontinuity in the model. Errors of the voltage in L^2 norm follow $O(h)$ asymptotically and the current density matches quite well those from the reference solution for a sufficiently small mesh size h . The experimental results present a promising feature of our approach for simulating the apparent conductivity related to changes in microscopic cellular structures.

1. Introduction

Electrical conductivity of a material is a measure of its ability to allow the movement of electric charge. Based on the material's atomic or molecular composition, electric charge may be either in the form of free electrons or ions. In a homogeneous saline solution, for example, there is ionic electric charge and its conductivity is determined by the total sum of the multiplication of concentration and the mobility of various ions presents in the solution [1]. The mobility of ions depends on the structural composition of the environment in which they are moving. A typical example is the movement of ions across the membrane of a cell in biological materials. The membrane itself is an insulator but it has pores which allow the flow of ions [2].

To better understand this bioelectric phenomenon a simple yet robust modeling method would be highly beneficial.

When a material is homogeneous, a simple way to measure its conductivity is to take the ratio of absolute value of the current density and electric field inside the material [1]. This is not so simple in biological tissues which are heterogeneous, consisting of cells, extracellular structures and fluids. To measure conductivity in a controlled way, we have to probe the material by injecting current and measure induced voltage or vice versa [1, 3, 4]. Other measurement methods include injecting the current or RF/acoustic magnetic field and measuring the induced magnetic field/flux density [5–10]. In this work, we consider the conductivity measurements using a technique called magnetic resonance electrical impedance tomography (MREIT). In MREIT, tissues are probed by externally injected currents and induced

magnetic flux densities are measured using MRI scanner. An image reconstruction algorithm uses these measurements to reconstruct conductivity image of tissues [3].

The microscopic cellular structure affects the current flow pattern in biological tissues. The macroscopic conductivity measured by a current injection based probing method can be, therefore, understood as the apparent conductivity [11]. The apparent conductivity at a fixed macroscopic scale is determined as a congregation of microscopic effects within the tissue. Especially at low frequency, the membrane greatly affects a measured apparent conductivity value of the tissue at a macroscopic scale since the cellular membrane can be modeled as an insulating sphere with holes where ions can migrate [11]. An ability to model the microscopic effects within the tissue would be highly beneficial to better understand the nature of conductivity of biological materials.

Since we are interested in a macroscopic conductivity value, we need to understand how the microscopic structure influences the macroscopic conductivity measurement. To understand the meaning of a measured conductivity in relation with microscopic changes at the cellular membranes, we need quantitatively relate the apparent conductivity at the macroscopic scale with microscopic structural changes. Due to the scale difference, a numerical study may require a highly nonuniform mesh with a tremendously large number of elements resulting in a huge amount of computations and memory requirement, which may not be practically feasible.

There have been previous studies to address practical numerical methods for treating such a model heterogeneity [12–14]. In [13], finite difference methods were developed by correcting the finite difference stencils according to the conductivity discontinuity. Calculation of the correction term becomes quite complicated when a model with microscopic structure is considered. In [12], coarse finite element basis is built by solving the model problem in each coarse mesh with an appropriate boundary condition regarding the conductivity discontinuity. A discrete model is then built by using the coarse basis functions. This process can be understood as smoothing on the conductivity discontinuity. This approach still gives less accurate approximations than the work [13] and results in a ill-conditioned linear system depending on the heterogeneity of the conductivity. In [14], a practical discrete method was developed for simulating fluid-structure interaction by using two independent variables: Eulerian variable for the fluid on the background and Lagrangian variable for the immersed moving elastic body. After the separation, the interaction between the fluid and the elastic body is calculated by using a smoothed approximation to the Dirac delta function, where the Dirac delta function is used to model the location of the moving elastic body. The smoothed approximation is the force imposed by the elastic body on the fluid. After solving fluid equations with the exerting force, the location of the elastic body is updated by the fluid velocity. We refer the references therein for many successful applications of the immersed boundary methods; it is known to be the most practical discrete model for simulating a very thin elastic body.

A discrete model with certain smoothing on the microscopic structures will be more appropriate for our purpose than a very accurate discrete model. In this work, for a more practical method we propose an iterative method which employs a uniform mesh rather than a highly nonuniform mesh. We consider a model with a single cell and propose a new numerical method based on uniform meshes without much concern on the microscopic structures in the single cell. We first solve a simple model with a uniform conductivity and we then iteratively improve the numerical accuracy by updating the right-hand side of the simple model. The right-hand side is calculated by integrating the current solution over the single cell membrane, which could provide a certain smoothing effect similarly to that in [14] when a model with many of them is considered to study macroscopic properties related to changes in microscopic cellular structures. We note that at each iteration a simple model with the uniform conductivity is solved, thus any available fast solvers, that is, FFT (Fast Fourier Transform) [15] or multigrid methods [16], can be utilized to speed up the computing time. We analyze the convergence of the iterative method with respect to the contrast of the conductivity difference and the relative thickness of the cell membrane.

Our method is tested for a simple model with a single cell and then more complex models with many of small cells. These results are compared to reference solutions from COMSOL (COMSOL Inc., USA), where very refined nonuniform meshes are used to address high contrast of conductivity jump across the thin cellular membrane. The errors of voltage in L^2 norm asymptotically follow the first-order $O(h)$ accuracy for the given mesh size h and the current density agrees quite well to that of reference solutions. To address capability of our method for capturing anisotropic cellular structures, we test a model with many cells, where holes are adopted to each cell membrane at various locations. Those results present a promising feature of our method for approximating macroscopic properties related to microscopic structural changes.

This paper is organized as follows. In Section 2, a model problem with multiscale structures, FE (finite element) discretization of the model problem, and an iterative method for solutions of the discrete model are described. In Section 2.5, convergence of the iterative method is analyzed related to the thickness of the cell membrane and the contrast of conductivity jump across the cell membrane. Numerical results are presented in Section 3. Discussion and conclusion are provided in Sections 4 and 5.

2. Methods

2.1. Model Problem. We consider a model elliptic problem with highly varying conductivity across a thin layer A inside Ω ,

$$\begin{aligned} -\nabla \cdot (\sigma(x)\nabla u(x)) &= 0, \quad \forall x \in \Omega, \\ u(x) &= g_D(x), \quad \forall x \in \partial\Omega_D, \\ \frac{\partial u}{\partial n}(x) &= g_N(x), \quad \forall x \in \partial\Omega_N, \end{aligned} \tag{1}$$

where the conductivity is given by

$$\sigma(x) = \begin{cases} \sigma_0, & x \in \Omega \setminus A, \\ \sigma_A, & x \in A, \end{cases} \quad (2)$$

with the two positive constants σ_0 and σ_A , such that $\sigma_0 \gg \sigma_A$. Here, $\partial\Omega_D$ and $\partial\Omega_N$ denote the parts of the boundary of Ω with the Dirichlet and the Neumann boundary conditions, respectively. Figure 2(a) illustrates the model problem at microscopic scale. In the model, a thin layer A with four holes is introduced to simulate a semipermeable membrane of a single cell lying inside an extracellular space Ω . Similar model appears in the phantom model invented in [17] based on the experimental phantom adopted by Oh et al.

2.2. Multiscalability of Model Problem. The description of our model inherits two types of multiscales: the conductivity difference between the cell membrane and the extracellular region and the size difference between the thickness of the cell membrane and the diameter of the extracellular region. In order to build a discrete model for such a problem, a very elaborated unstructured mesh is unavoidable to resolve the conductivity discontinuity; see Figure 3. Finite element methods on the given unstructured mesh result in a very ill-conditioned linear system due to highly heterogeneous conductivity, aspect ratio of anisotropic element, and inhomogeneous mesh size [18–21]. In [13], to deal with conductivity discontinuity finite difference methods were developed by correcting the finite difference stencils according to the conductivity discontinuity. Calculation of the correction term is quite complicated and becomes even impossible for such a thin anomaly region A with many adopted holes. Therefore both approaches become impractical for our model problem. We emphasize that our purpose is to simulate an apparent conductivity influenced by microscopic structural changes in the cellular membrane. For our purpose, a discrete model with a certain smoothing on the microscopic structures will be more desirable than a very accurate discrete model. In the following subsection, our numerical method will be developed to address this respect.

2.3. Model Discretization. We discretize the model problem in (1) using finite element methods [22] with a uniform mesh. Let \mathcal{T}_h be a uniform mesh. We then introduce a piecewise-linear conforming finite element space X_h obtained from the uniform mesh. Here we emphasize that the mesh need not resolve the conductivity discontinuity.

We obtain a weak form of (1) using test functions $v \in H_D^1(\Omega)$,

$$\int_{\Omega} \sigma(x) \nabla u(x) \cdot \nabla v(x) dx = \int_{\partial\Omega_N} g_N(x(s)) v(x(s)) dx(s), \quad (3)$$

where $H_D^1(\Omega)$ is the space of functions which are square integrable up to first derivatives and have zero values on $\partial\Omega_D$, the part of boundary where the Dirichlet boundary

condition is given. We then approximate $u(x)$ with the finite element basis in X_h ,

$$u(x) \simeq \sum_{j \in \mathcal{N}_{I,N}} U_j \phi_j(x) + \sum_{j \in \mathcal{N}_D} U_j \phi_j(x). \quad (4)$$

Here $\phi_j(x)$ are nodal basis functions to nodes x_j , $\mathcal{N}_{I,N}$ is the set with indices of nodes from the uniform mesh, which are located interior to Ω and on $\partial\Omega_N$, the part of boundary where the Neumann boundary condition is provided, and \mathcal{N}_D is the set with indices of nodes on $\partial\Omega_D$, the other part of the boundary where the Dirichlet boundary condition is imposed. For nodes x_j on $\partial\Omega_D$, the corresponding nodal values U_j are determined by the Dirichlet boundary condition, that is, $U_j = g_D(x_j)$ for all j in \mathcal{N}_D .

By approximating $u(x)$ and using test functions $\phi_i(x)$, for all i in $\mathcal{N}_{I,N}$, we obtain finite element discretization of the model problem in (3),

$$\int_{\Omega} \sigma(x) \nabla \phi_i(x) \cdot \nabla \left(\sum_{j \in \mathcal{N}_{I,N}} \phi_j(x) U_j \right) dx = g_i \quad \forall i \in \mathcal{N}_{I,N}, \quad (5)$$

where

$$g_i = \int_{\partial\Omega_N} g_N(x(s)) \phi_i(x(s)) dx(s) - \int_{\Omega} \sigma(x) \nabla \phi_i(x) \cdot \nabla \left(\sum_{j \in \mathcal{N}_D} g_D(x_j) \phi_j(x) \right) dx. \quad (6)$$

The resulting linear system from the above Galerkin approximation depends on $\sigma(x)$. The uniform mesh in our discretization admits the discontinuous conductivity inside a single grid; hence finite element approximation from such uniform mesh results in certain smoothing in our discrete model; see Figure 1. Such a smoothing could provide a more practical tool for calculating the apparent conductivity regarding changes in microscopic cellular structures, while the order of accuracy in our discrete model becomes lower than that in the discrete model from very refined meshes. The size of linear system in our case becomes smaller than the case using a very fine unstructured mesh. However, the conductivity discontinuity across the thin layer still makes the resulting linear system ill conditioned. In order to get faster solutions for the discrete model in (5), we will develop an iterative method for solving the discrete model.

2.4. Iterative Method. Our iterative method will be based on a fixed-point iteration. We decompose the conductivity into

$$\sigma(x) = \sigma_0 - \tilde{\sigma}_A(x), \quad (7)$$

where $\tilde{\sigma}_A(x)$ is defined as

$$\tilde{\sigma}_A(x) = \begin{cases} 0, & x \in \Omega \setminus A, \\ \sigma_0 - \sigma_A, & x \in A. \end{cases} \quad (8)$$

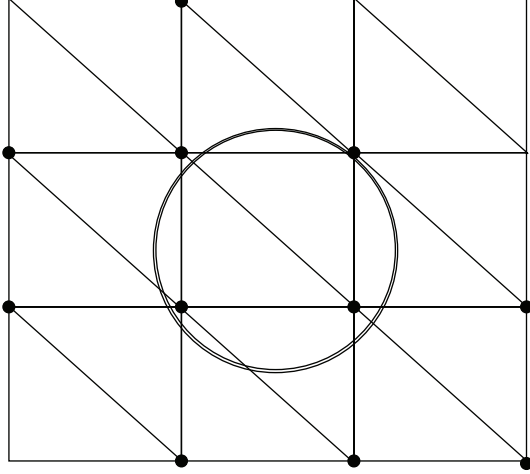


FIGURE 1: An illustration of uniform mesh and anomaly region: anomaly region A is the ring surrounded by the two circles; the microscopic structure of A is smoothed out by the nodal basis functions (to the black dots) of which support intersects the anomaly region A .

Using (7) we rewrite (5) into

$$\begin{aligned} \sigma_0 \int_{\Omega} \nabla \phi_i(x) \cdot \nabla \left(\sum_{j \in \mathcal{N}_{I,N}} \phi_j(x) U_j \right) dx \\ - \int_{\Omega} \tilde{\sigma}_A(x) \nabla \phi_i(x) \cdot \nabla \left(\sum_{j \in \mathcal{N}_{I,N}} \phi_j(x) U_j \right) dx = g_i, \end{aligned} \quad (9)$$

and we obtain

$$\sigma_0 K U = g + K_{\tilde{\sigma}_A} U, \quad (10)$$

where

$$\begin{aligned} (K)_{ij} &= \int_{\Omega} \nabla \phi_i(x) \cdot \nabla \phi_j(x) dx, \quad i, j \in \mathcal{N}_{I,N}, \\ (K_{\tilde{\sigma}_A})_{ij} \\ &= \int_{\Omega} (\sigma_0 - \sigma_A) \chi_A(x) \nabla \phi_i(x) \cdot \nabla \phi_j(x) dx, \quad i, j \in \mathcal{N}_{I,N}. \end{aligned} \quad (11)$$

Here U and g denote the vector of components U_i and g_i for i in $\mathcal{N}_{I,N}$, respectively, and $\chi_A(x)$ is the characteristic function regarding the set A , that is,

$$\chi_A(x) = \begin{cases} 1, & x \in A, \\ 0, & x \in \Omega \setminus A. \end{cases} \quad (12)$$

We now propose an iterative method for (10).

Algorithm 1 (iterative method).

- (i) Step 1: let $U^{(0)}$ be an initial.
- (ii) Step 2: iterate until $U^{(n)}$ converges.

Given $U^{(n)}$, update $U^{(n+1)}$ from

$$\sigma_0 K U^{(n+1)} = g + K_{\tilde{\sigma}_A} U^{(n)}. \quad (13)$$

Before we discuss the convergence of the above iterative method, we define the following concept. For a $m \times m$ matrix K_1 , we define a norm by

$$\|K_1\| := \max_{v \in \mathbb{R}^m, v \neq 0} \sqrt{\frac{(K_1 v)^T K_1 v}{v^T v}}. \quad (14)$$

We say a matrix K_1 is *symmetric* when $K_1^T = K_1$. For symmetric matrices K_1 and K_2 , we define the relation

$$K_1 \leq K_2, \quad (15)$$

when the two matrices satisfy

$$v^T K_1 v \leq v^T K_2 v, \quad \forall v \in \mathbb{R}^m. \quad (16)$$

The relation means that all the eigenvalues of K_1 are bounded by the maximum eigenvalue of K_2 . We say that a symmetric matrix K_1 is *positive definite* when

$$v^T K_1 v > 0, \quad \forall v (\neq 0) \in \mathbb{R}^m. \quad (17)$$

For a symmetric and positive definite matrix K_1 , the norm $\|K_1\|$ is identical to the maximum eigenvalue of the matrix K_1 . We note that the two matrices K and $K_{\tilde{\sigma}_A}$ in the above algorithm are symmetric and positive definite. For any given symmetric and positive definite matrix S , we obtain that

$$K_1 \leq K_2 \quad \text{implies} \quad \|S^{-1} K_1\| \leq \|S^{-1} K_2\|. \quad (18)$$

Since $\sigma_0 > \sigma_A$, the matrix $K_{\tilde{\sigma}_A}$ satisfies that

$$0 < K_{\tilde{\sigma}_A} < \sigma_0 K. \quad (19)$$

Let $E^{(n+1)} = U^{(n+1)} - U^{(n)}$ and then

$$E^{(n+1)} = (\sigma_0 K)^{-1} K_{\tilde{\sigma}_A} E^{(n)}. \quad (20)$$

From (19) combined with (18), we obtain that

$$\left\| (\sigma_0 K)^{-1} K_{\tilde{\sigma}_A} \right\| < 1, \quad (21)$$

and $\|E^{(n+1)}\|$ then converge to zero; in other words, the iterates $U^{(n)}$ converge,

$$U^{(n+1)} = (\sigma_0 K)^{-1} g + (\sigma_0 K)^{-1} K_{\tilde{\sigma}_A} U^{(n)}. \quad (22)$$

Therefore, our iterative method is a form of a fixed-point iteration.

We also observe fast convergence when the area of A is relatively small part of Ω , which is the case in our model. At each iteration, we solve the system with the stiffness matrix $\sigma_0 K$ and the right-hand side computed from the previous iterate $U^{(n)}$. Since K is obtained from the uniform mesh, we can employ any available fast solver to find the update $U^{(n+1)}$, such as a multigrid preconditioner or fast Fourier transform. The conductivity discontinuity is treated in the term $K_{\tilde{\sigma}_A} U^{(n)}$, which amounts to evaluate integration over the anomaly region A . For an accurate integration, we apply the composite Gaussian quadrature.

Our resulting method becomes similar to the immersed boundary methods [14] in the respect that the conductivity discontinuity in the model is treated as the source term of the simple model problem with a uniform conductivity, of which problem is well approximated by using a uniform mesh.

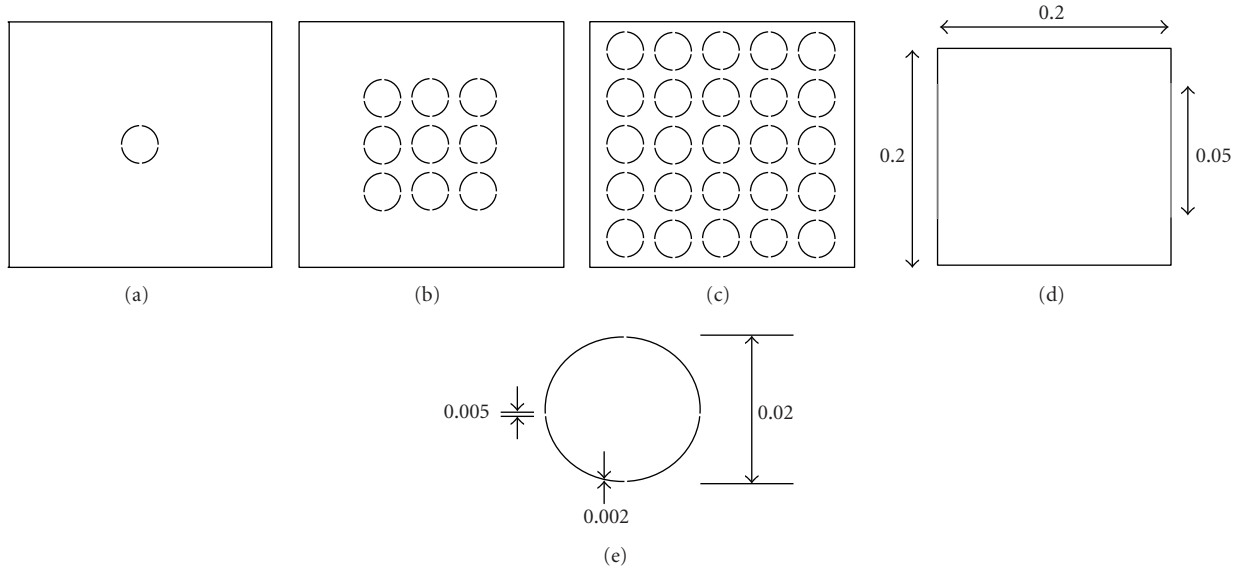


FIGURE 2: Model geometry with (a) 1, (b) 9, and (c) 25 anomalies with four holes orthogonal to each other. (d) Outer domain dimensions and (e) anomaly dimensions.

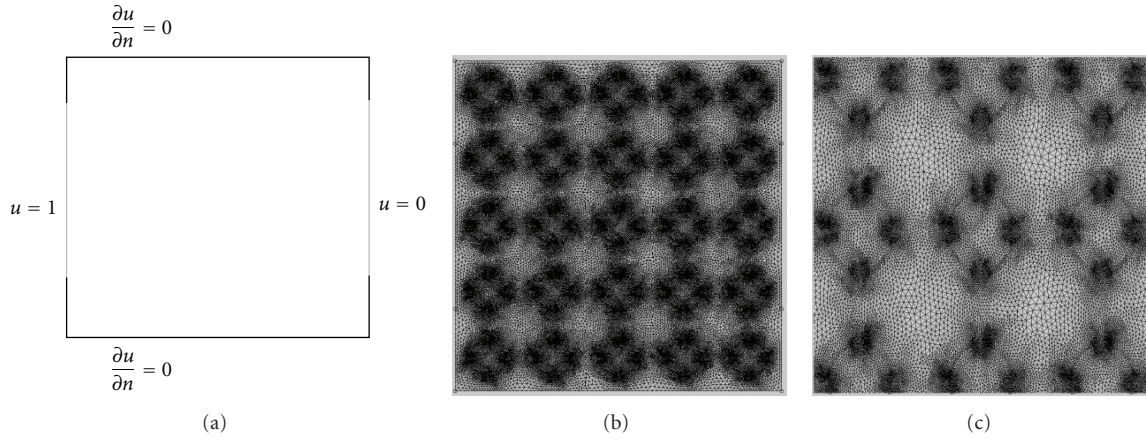


FIGURE 3: Numerical modeling of problem in COMSOL. (a) Boundary conditions, (b) mesh, and (c) magnified domain.

2.5. Convergence of Iterative Method. In this subsection, we will provide a more precise contraction modulus for $(\sigma_0 K)^{-1} K_{\tilde{\sigma}_A}$ depending on the relative ratio of the thickness of the anomaly to the mesh size and the relative ratio of σ_A to σ_0 . We define

$$\gamma := \max_{\tau \in \mathcal{T}_h} \frac{|A \cap \tau|}{|\tau|}, \quad \epsilon := \frac{\sigma_A}{\sigma_0}, \quad (23)$$

where $|\tau|$ is the area of the set τ .

For each triangle τ in \mathcal{T}_h , such that $\tau \cap A \neq \emptyset$, we can extend A to B so that $|B \cap \tau| = \gamma |\tau|$ and then we define $\tilde{\sigma}_B$ by

$$\tilde{\sigma}_B(x) = \begin{cases} \sigma_0 - \sigma_A, & x \in B, \\ 0, & x \in \Omega \setminus B. \end{cases} \quad (24)$$

Since

$$\tilde{\sigma}_A(x) \leq \tilde{\sigma}_B(x) < \sigma_0, \quad (25)$$

we obtain that

$$K_{\tilde{\sigma}_A} \leq K_{\tilde{\sigma}_B} < \sigma_0 K, \quad (26)$$

where matrices $K_{\tilde{\sigma}_A}$, $K_{\tilde{\sigma}_B}$, and $\sigma_0 K$ correspond to conductivity functions $\tilde{\sigma}_A(x)$, $\tilde{\sigma}_B(x)$, and σ_0 , respectively.

By using that $|B \cap \tau|$ is the same value $\gamma |\tau|$ for all triangles τ , which intersect A , and $(\nabla \phi_i(x) \cdot \nabla \phi_j(x))|_{\tau}$ are constant for each τ , we have

$$K_{\tilde{\sigma}_B} \leq \gamma(\sigma_0 - \sigma_A)K \quad (27)$$

and thus

$$K_{\tilde{\sigma}_A} \leq \gamma(\sigma_0 - \sigma_A)K. \quad (28)$$

By applying $(\sigma_0 K)^{-1}$ on both sides of the above inequality, see (18), we finally obtain that

$$\left\| (\sigma_0 K)^{-1} K_{\tilde{\sigma}_A} \right\| \leq \gamma(1 - \epsilon). \quad (29)$$

The error reduction in the iterative method is bounded by γ and ϵ . When A intersects only a small number of triangles in \mathcal{T}_h , we obtain a better reduction factor since most entries in K_{σ_A} are zero.

Theorem 2. *The error reduction factor in the iterative method is at least determined by*

$$(\sigma_0 K)^{-1} K_{\sigma_A} \leq \gamma(1 - \epsilon), \quad (30)$$

where γ and ϵ are parameters defined by

$$\gamma := \max_{\tau \in \mathcal{T}_h} \frac{|A \cap \tau|}{|\tau|}, \quad \epsilon := \frac{\sigma_A}{\sigma_0}. \quad (31)$$

Remark 3. When the thickness of A is δ , $\gamma \simeq (\delta/h)$. Therefore the error reduction factor is determined by the relative ratio of the thickness of the anomaly to the mesh size. As the anomaly region A becomes thinner and occupies a smaller part of Ω , the error reduction factor becomes smaller for a given mesh size h and a given relative ratio of conductivity ϵ .

Remark 4. For a faster convergence of our iterative method, the suggested mesh size h for a given thickness δ is to satisfy

$$h > \frac{1}{c} \delta, \quad (32)$$

for some positive number $c < 1$. With such an h , the error reduction factor is then bounded by the constant c . From the following numerical experiments, the L^2 errors of solutions in our discrete model are observed to follow $O(h)$. The mesh size h should be determined considering the required accuracy as well as the convergence of the iterative method.

3. Numerical Results

We present numerical experiments on the proposed method. We will consider models in Figure 2. The problem domain $\Omega = (-0.1, 0.1)^2$ is a rectangular region and the anomaly region A consists of thin circles with small adopted holes. The thickness δ of the circle is 0.002 and the diameter of the each circle is 0.02. The diameter of holes introduced in each circle is 0.005. The conductivity in the anomaly region is given by 0.001 and the conductivity is given by 1 elsewhere, that is, $\sigma_A = 0.001$ and $\sigma_0 = 1$. For all the models in the following experiments, $\epsilon = 0.001$, $\delta = 0.002$, and $\gamma (= \delta/h)$ will be determined once the mesh size h is chosen.

We study the behavior of errors by approximating the model problem with finite element methods on uniform grids, which do not resolve conductivity discontinuity across the anomaly region A . We first study the single cell model shown in Figure 2(a). We then consider more complex models with multiple cells as shown in Figures 2(b) and 2(c). In order to compute errors, we obtain a reference solution from COMSOL by solving the same model problems using a very refined unstructured mesh which can resolve the conductivity discontinuity; see Figure 3. We considered the stationary solver of COMSOL to obtain the reference solution for various models in this work. The stationary solver

TABLE 1: The L^2 errors for the model (a). Ω : the whole domain, Ω_I : the region inside the circle, $\|u - U_h\|_D$: errors of voltage (solution) in the region D , $\|J - J_h\|_D$: errors of current density (computed from voltage) in the region D , and Iter.: number of iterations.

N	$\ u - U_h\ _\Omega$	$\ u - U_h\ _{\Omega_I}$	$\ J - J_h\ _\Omega$	$\ J - J_h\ _{\Omega_I}$	Iter.
16	0.0081	0.0000	0.0692	0.0157	4
32	0.0046	0.0145	0.0692	0.5800	6
64	0.0033	0.0070	0.0548	0.5347	10
128	0.0017	0.0038	0.0340	0.2208	38
256	0.0007	0.0001	0.0324	0.0061	164

works on linear and nonlinear stationary PDE problems. Internally, a function called femstatic works as a stationary solver for both linear and nonlinear problems. The default value is ‘‘auto,’’ which means that femstatic automatically selects a solver depending on the problem’s linearity. A linear solver is selected by femstatic for the model problems in this work. COMSOL uses either direct or iterative linear system solvers to solve the system matrix. Various preconditioner algorithms are used to deal with the ill conditioning of the system matrix. Those include incomplete LU, geometric multigrid, incomplete Cholesky, and few others (COMSOL Inc., USA).

In Table 1, we report relative L^2 errors of the solution (voltage) and the current density for decreasing the mesh size h . Here N denotes the number of grid in each direction and Ω_I denotes that the error is computed over the region inside the circle. For example, the relative L^2 error for $u - U_h$ in Ω_I is calculated by

$$\|u - U_h\|_{\Omega_I} := \sqrt{\frac{\sum_{x_i \in \Omega_I} (u(x_i) - U_h(x_i))^2}{\sum_{x_i \in \Omega_I} u^2(x_i)}}, \quad (33)$$

where u is the reference solution from COMSOL, U_h is the solution from our method with mesh size h , and x_i are grid points located in Ω_I . In the iterative method, the iteration is stopped when the relative error in two consecutive iterates is reduced by a factor of 10^6 , that is,

$$\frac{\|U^{(n+1)} - U^{(n)}\|_\Omega}{\|U^{(n)}\|_\Omega} \leq 10^{-6}. \quad (34)$$

and the number of iteration counts is also reported in Table 1 for each grid level.

We observe that the errors in voltage follow $O(h)$ over the whole domain Ω and the errors inside the circle show better accuracy. The current density $J = \|(J_1, J_2)\|$ is calculated at each grid point (x_i, y_j) by using the voltage solution u . The current density J_h from our method is calculated as the same way using U_h . As we can see from the results, the errors in the current density become much smaller as the mesh size is getting smaller, since the derivative of voltage is well approximated using the smaller mesh size. To obtain more accurate approximation for the current density, we can formulate a first-order system of (1) by introducing a new variable, $\mathbf{J} = \sigma(x) \nabla u(x)$. A similar idea to the current work can be used for the first-order system. This problem will be addressed in our forthcoming research.

TABLE 2: The L^2 errors for the models (b) and (c). $\|u - U_h\|_\Omega$: errors in the solution (voltage), $\|J - J_h\|_\Omega$: errors in current density (computed from voltage), and Iter.: number of iterations.

N	Model (b)			Model (c)		
	$\ u - U_h\ _\Omega$	$\ J - J_h\ _\Omega$	Iter.	$\ u - U_h\ _\Omega$	$\ J - J_h\ _\Omega$	Iter.
32	0.0121	0.1828	7	0.0096	0.3220	7
64	0.0120	0.1800	13	0.0091	0.3070	14
128	0.0067	0.1413	47	0.0053	0.2449	50
256	0.0022	0.0462	397	0.0035	0.0640	739

About the iteration counts, the error reduction rate in the iterative method depends on γ and ϵ . For a given N , $h = 0.4/N$ and then the ratio between h and $\delta = 0.002$ becomes

$$\gamma \simeq \frac{\delta}{h} = 0.005 \times N. \quad (35)$$

As we can observe from the numerical experiments when $N < 100$, we have faster convergence in the iterative method.

In Table 2, we report errors for models with a more complicated anomaly A , which consists of many circles with holes. The behavior of errors is similar to this observed in Table 1. For the same grid level N , the iteration count gets larger as more circles are introduced in the anomaly region A , that is, from model (a) to model (c). When $N \leq 128$, even for a very complicated anomaly case of model (c) we observe quite good iteration counts. In Figures 4 and 5, we also plot solutions and current densities obtained from COMSOL and our method and we can observe good agreement for all the three models.

In order to show that our method is capable of capturing macroscopic properties, we apply our method to a model with anisotropic conductivity. Here we consider a circle with two horizontally adopted holes; the center of each hole is located at the left and right end points of the circle. To study anisotropic models, we inject a current in the horizontal direction or in the vertical direction, and we also consider a circle without any adopted hole.

In Figures 6 and 7, the voltage and current density are presented for models with each anomaly consisting of circles with two horizontally adopted holes. Here on the boundary of the domain the current is injected in the horizontal direction. We compare the results from our method with $N = 256$ and from COMSOL with a very fine mesh. We observe that these two results match well and they are also in a good agreement with those in the previous two Figures 4 and 5, when the anomaly consists of circles with two horizontal and two vertical holes, and the current is horizontally injected on the boundary.

In Figures 8 and 9, the voltage and current density are presented for models with each anomaly consisting of circles with two horizontally adopted holes. Here on the boundary of the domain the current is injected in the vertical direction. We compare the results from our model with $N = 256$ and from COMSOL with a very fine mesh. We observe that the vertically injected current cannot detect the horizontally adopted holes in each circle.

In Figures 10 and 11, the voltage and current density are presented for models with each anomaly consisting of circles without any adopted holes. We compare the results from our model with $N = 256$ and from COMSOL with a very fine mesh. We observe that the results here are quite similar to those in Figures 8 and 9.

The numerical study on anisotropic conductivity models presents that our method is capable of capturing the macroscopic conductivity with respect to changes in microscopic cellular membranes.

4. Discussion

We developed a practical numerical method for simulating the macroscopic conductivity related to microscopic changes in cellular membranes. Finite element discretization with a uniform mesh is applied to the multiscale model without much concern on the microscopic structures. We refer to previous studies as those in [12, 14] where similar ideas were developed for multiscale problems or for multiple structures.

For a more practical method, we used a standard linear finite element basis of the uniform mesh rather than using the coarse basis in [12]. Similarly to [14], smoothed approximation of microscopic cellular structures is imbedded in the right-hand side of the iterative method, where a simple discrete model with uniform conductivity is solved to improve the accuracy. Convergence of the iterative method was analyzed regarding the contrast in the conductivity difference and the relative ratio of the cell membrane to the mesh size.

Since the uniform mesh does not resolve the conductivity discontinuity, our method results in a less accurate approximation as in [14]. In the current work, we report numerical results which present $O(h)$ convergence in L^2 errors in the whole domain Ω . Such property of the approximation was already reported in [14] when a very thin elastic body is considered.

From numerical experiments, we can see that our method is capable of capturing the apparent conductivity with respect to changes in microscopic cellular structures. To obtain a more accurate current approximation, our method can be further applied to the first-order system of two unknowns, $\mathbf{J} = \sigma(x)\nabla u$ and u , and this will be addressed in our forthcoming research.

5. Conclusion

This kind of multiscale approach is needed to properly interpret reconstructed conductivity images in MREIT in relation with microscopic structural changes in cellular membranes. We will use the proposed method to construct an inhomogeneous tissue model including many cells with different membrane structures of holes. We will compute magnetic flux density as well as voltage and current density for MREIT simulation. Using the computed magnetic flux density, we will reconstruct images of apparent conductivity. We will see how apparent conductivity changes as we change the microscopic cellular membrane structures. We will

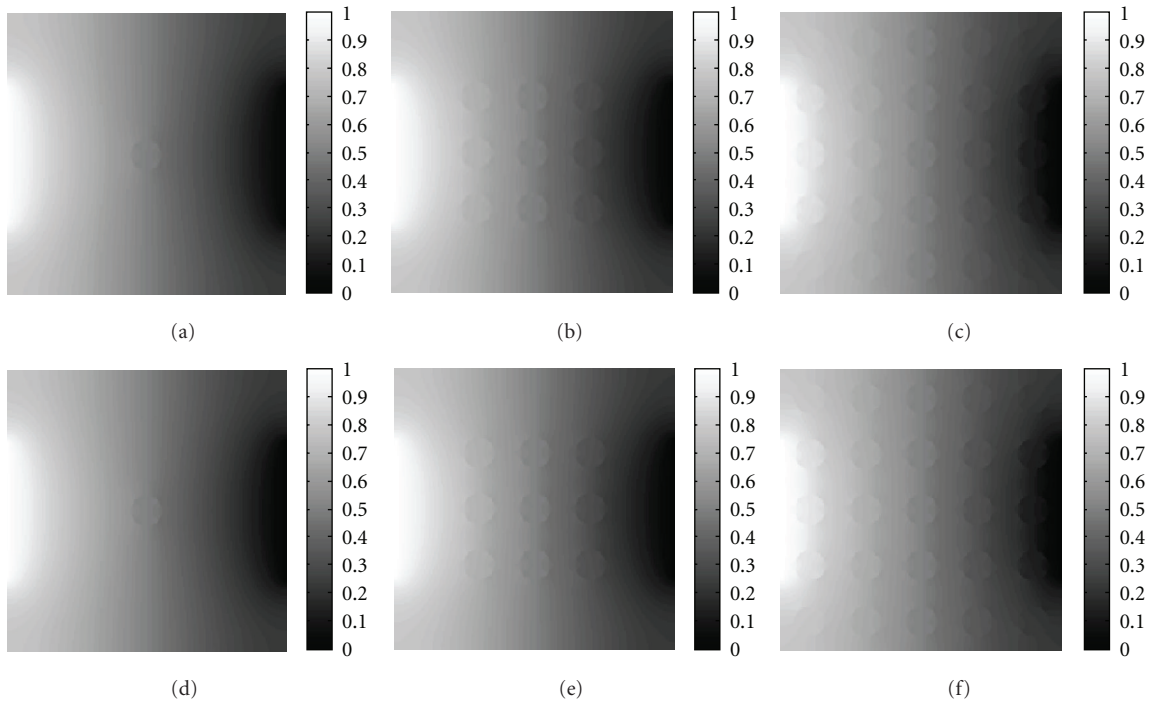


FIGURE 4: (a)–(c) are reference solutions from the model with 1, 9, and 25 anomalies with 4 holes. (d)–(f) are the corresponding solutions using the iterative method. The resolution is 256×256 .

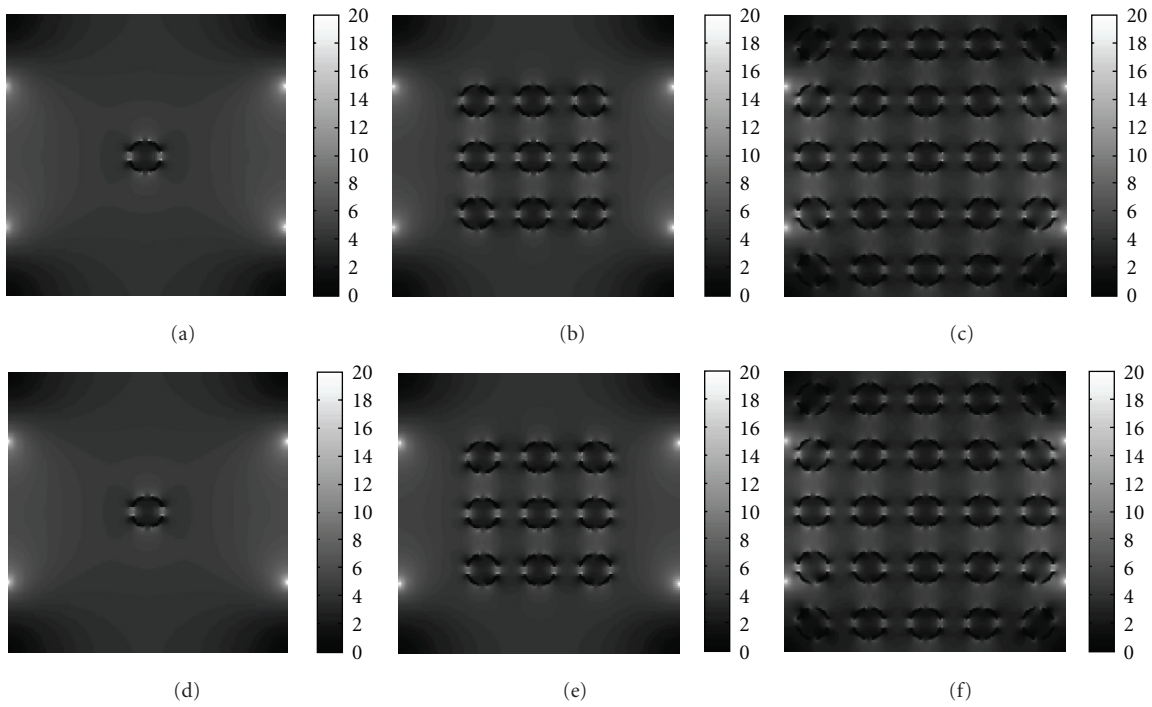


FIGURE 5: (a)–(c) are reference current densities from the model with 1, 9, and 25 anomalies with 4 holes. (d)–(f) are the corresponding current densities using the iterative method. The resolution is 256×256 .

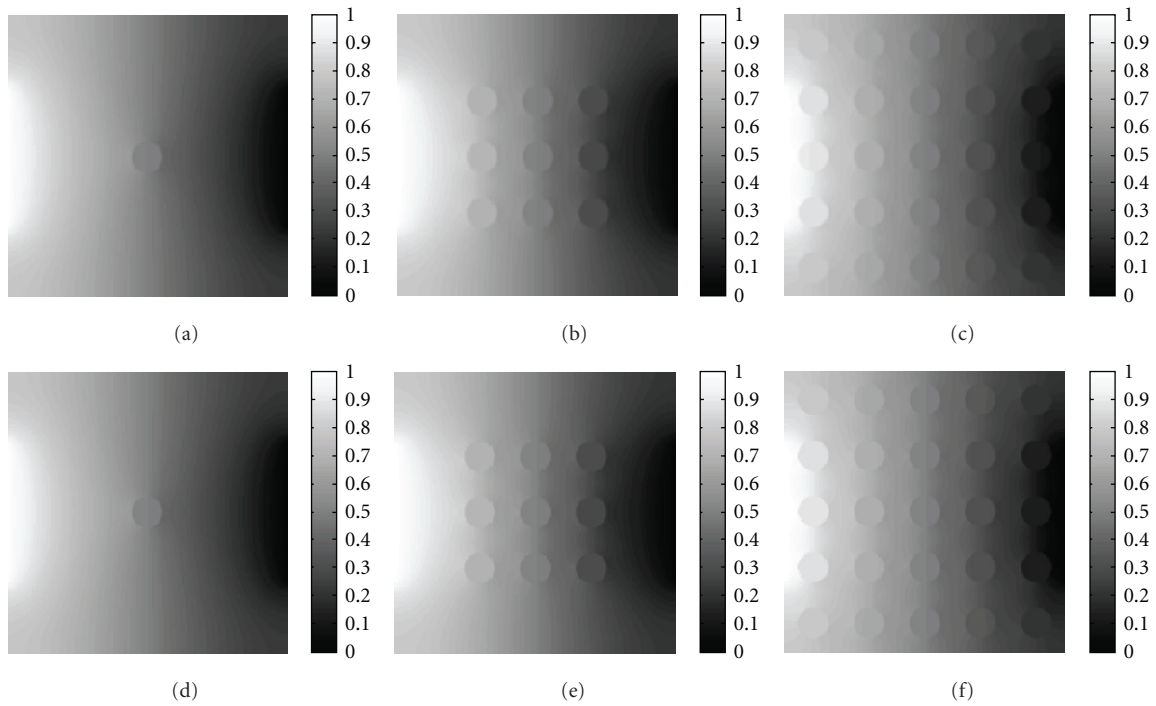


FIGURE 6: Horizontal current injection for horizontally adopted holes: (a)–(c) are reference solutions from the model with 1, 9, and 25 anomalies with 2 holes. (d)–(f) are the corresponding solutions using the iterative method. The resolution is 256×256 .

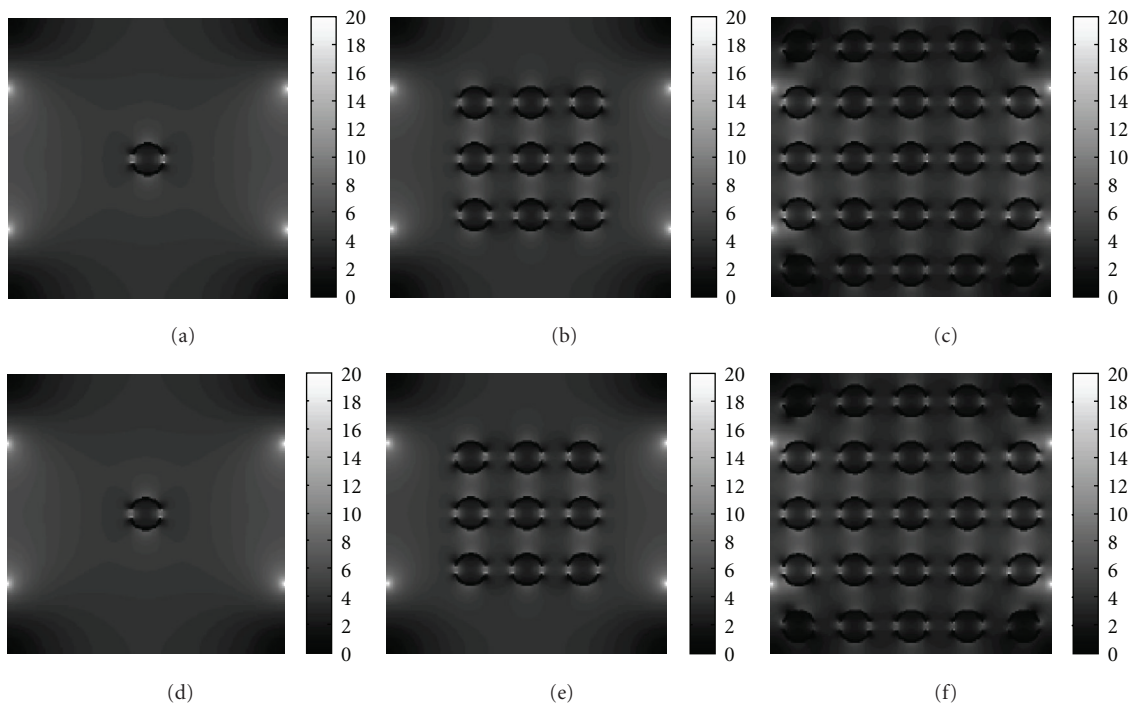


FIGURE 7: Horizontal current injection for horizontally adopted holes: (a)–(c) are reference current densities from the model with 1, 9, and 25 anomalies with 2 holes. (d)–(f) are the corresponding current densities using the iterative method. The resolution is 256×256 .

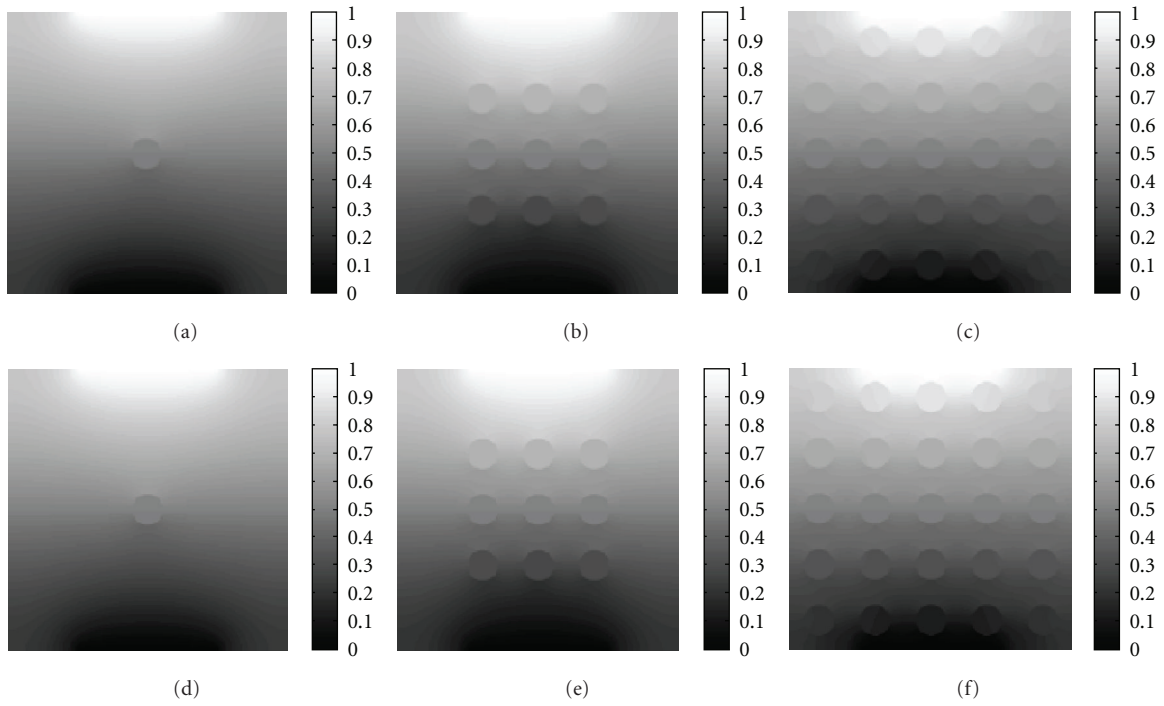


FIGURE 8: Vertical current injection for horizontally adopted holes: (a)–(c) are reference solutions from the model with 1, 9, and 25 anomalies with 2 holes. (d)–(f) are the corresponding solutions using the iterative method. The resolution is 256×256 .

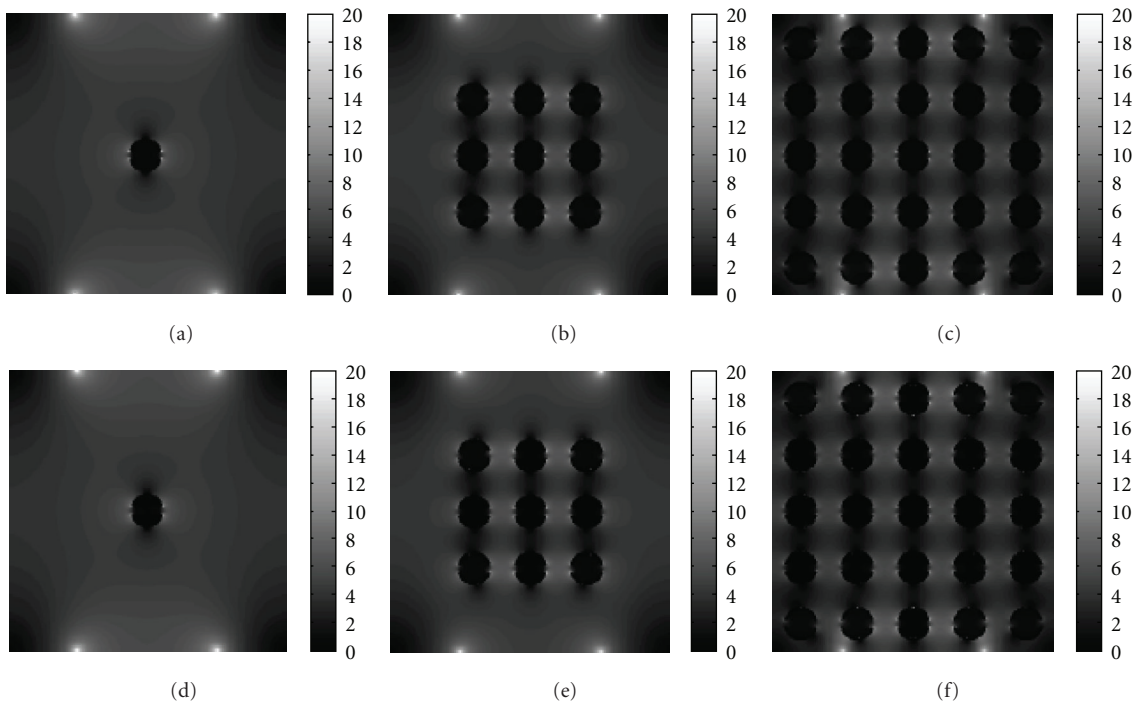


FIGURE 9: Vertical current injection for horizontally adopted holes: (a)–(c) are reference current densities from the model with 1, 9, and 25 anomalies with 2 holes. (d)–(f) are the corresponding current densities using the iterative method. The resolution is 256×256 .

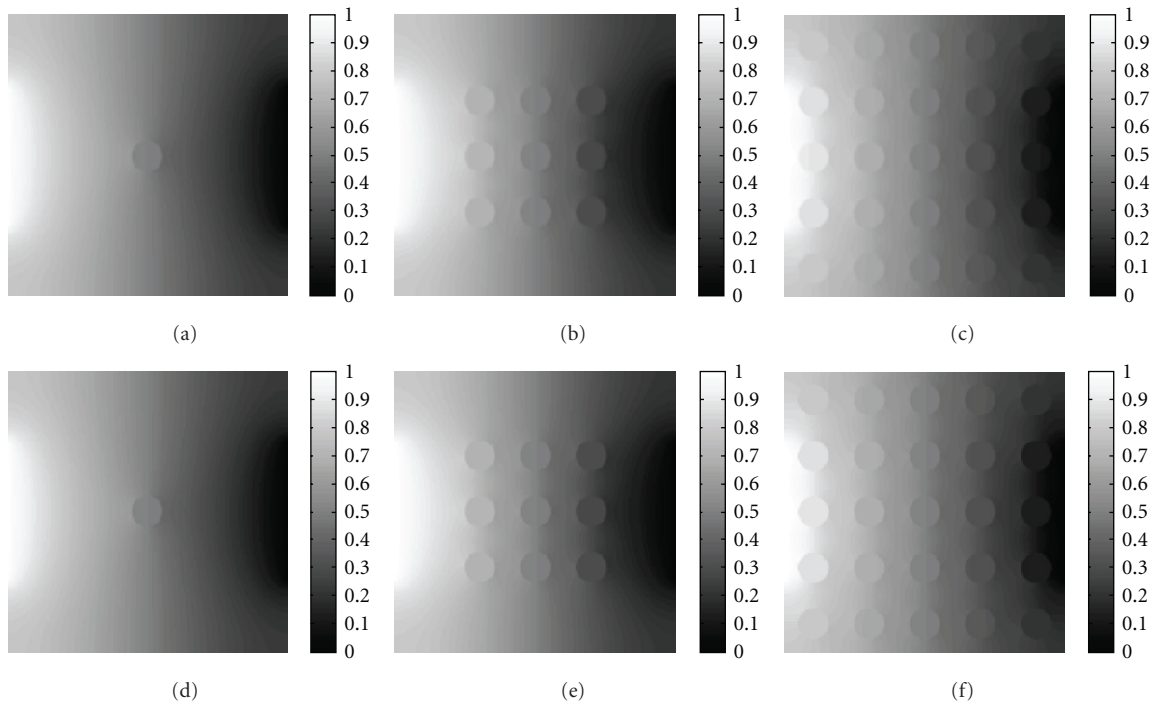


FIGURE 10: Horizontal current injection for no adopted holes: (a)–(c) are reference solutions from the model with 1, 9, and 25 anomalies with no holes. (d)–(f) are the corresponding solutions using the iterative method. The resolution is 256×256 .

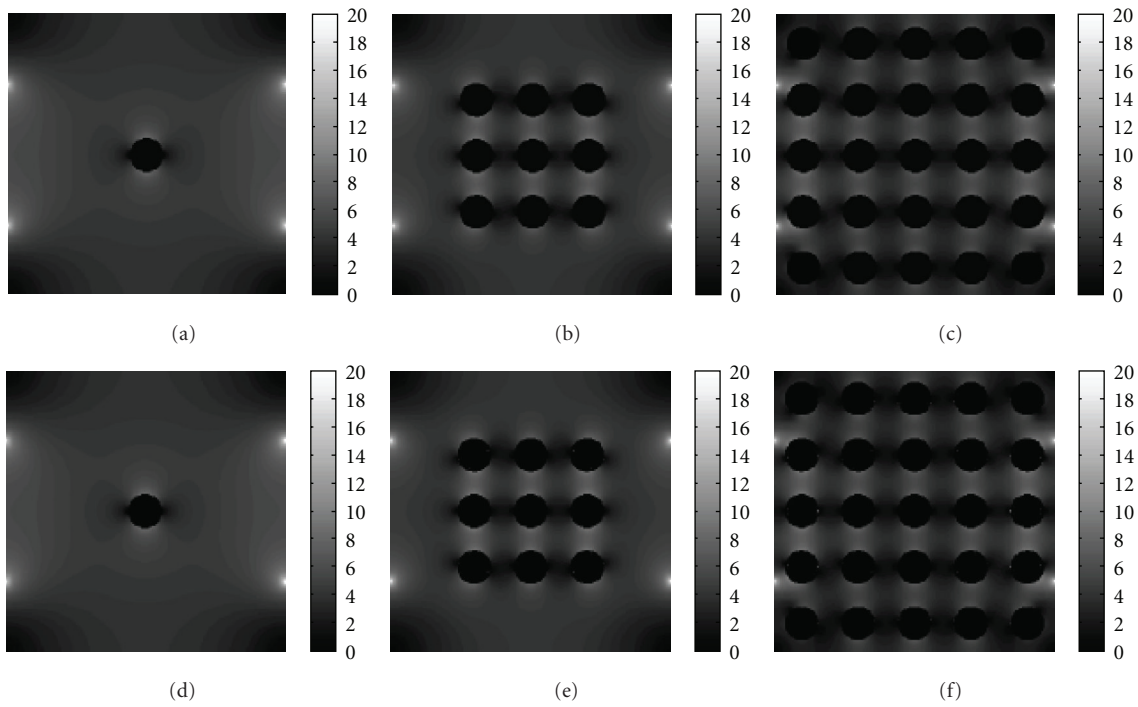


FIGURE 11: Horizontal current injection for no adopted holes: (a)–(c) are reference current densities from the model with 1, 9, and 25 anomalies with no holes. (d)–(f) are the corresponding current densities using the iterative method. The resolution is 256×256 .

combine the proposed method with MREIT simulation so that we can interpret an apparent conductivity reconstructed by using an MREIT algorithm.

Acknowledgment

The third author was supported by the National Research Foundation of Korea (NRF) Grant funded by the Korea government (MEST) (no. 20100018275).

References

- [1] S. Grimnes and O. G. Martinsen, *Bioimpedance and Bioelectricity Basics*, Academic press, 2008.
- [2] J. McMurry, M. E. Castellion, D. S. Ballantine, C. A. Hoeger, and A. N. D. V. E. Peterson, *Fundamentals of General, Organic, and Biological Chemistry*, Prentice Hall, 2009.
- [3] J. K. Seo and E. J. Woo, "Magnetic resonance electrical impedance tomography (MREIT)," *SIAM Review*, vol. 52, pp. 40–68, 2011.
- [4] J. Z. Tsai, J. A. Will, S. H. V. Stelle et al., "In-vivo measurement of swine myocardial resistivity," *IEEE Transactions on Biomedical Engineering*, vol. 49, no. 5, pp. 472–483, 2002.
- [5] H. Griffiths, "Magnetic induction tomography," *Measurement Science and Technology*, vol. 12, no. 8, pp. 1126–1131, 2001.
- [6] U. Katscher, M. Hanft, P. Vernickel, and C. Findekle, "Experimental verification of electric properties tomography (ept)," in *Proceedings of 14th Conference of International Society of Magnetic Resonance in Medicine*, pp. 30–35, 2006.
- [7] X. Li and B. He, "Multi-excitation magnetoacoustic tomography with magnetic induction (mat-mi)," *Journal of Physics*, vol. 224, no. 1, Article ID 012035, 2010.
- [8] B. C. Towe and M. R. Islam, "A magneto-acoustic method for the noninvasive measurement of bioelectric currents," *IEEE Transactions on Biomedical Engineering*, vol. 35, no. 10, pp. 892–894, 1988.
- [9] R. Xia, X. Li, and B. He, "Magnetoacoustic tomographic imaging of electrical impedance with magnetic induction," *Applied Physics Letters*, vol. 91, no. 8, Article ID 083903, 2007.
- [10] Y. Xu and B. He, "Magnetoacoustic tomography with magnetic induction (MAT-MI)," *Physics in Medicine and Biology*, vol. 50, pp. 5175–5187, 2005.
- [11] Y. T. Kim, T. I. Oh, and E. J. Woo, "Experimental verification of contrast mechanism in magnetic resonance electrical impedance tomography (MREIT)," in *Proceedings of the 32nd Annual International Conference of the IEEE Engineering in Medicine and Biology Society (EMBC '10)*, pp. 4987–4990, September 2010.
- [12] T. Y. Hou and X. H. Wu, "A multiscale finite element method for elliptic problems in composite materials and porous media," *Journal of Computational Physics*, vol. 134, no. 1, pp. 169–189, 1997.
- [13] R. J. Leveque and Z. Li, "Immersed interface method for elliptic equations with discontinuous coefficients and singular sources," *SIAM Journal on Numerical Analysis*, vol. 31, no. 4, pp. 1019–1044, 1994.
- [14] C. S. Peskin, "The immersed boundary method," *Acta Numerica*, vol. 11, pp. 479–517, 2002.
- [15] C. Van Loan, *Computational Frameworks for the Fast Fourier Transform*, vol. 10 of *Frontiers in Applied Mathematics*, SIAM, Philadelphia, Pa, USA, 1992.
- [16] W. L. Briggs, V. E. Henson, and S. F. McCormick, *A Multigrid Tutorial*, *Society for Industrial and Applied Mathematics*, SIAM, Philadelphia, Pa, USA, 2nd edition, 2000.
- [17] T. I. Oh, Y. T. Kim, A. Minhas, J. K. Seo, O. I. Kwon, and E. J. Woo, "Ion mobility imaging and contrast mechanism of apparent conductivity in MREIT," *Physics in Medicine and Biology*, vol. 47, pp. 4142–4162, 2011.
- [18] R. E. Bank and L. R. Scott, "On the conditioning of finite element equations with highly refined meshes," *SIAM Journal on Numerical Analysis*, vol. 26, pp. 1383–1394, 1989.
- [19] L. Branets and G. F. Carey, "Condition number bounds and mesh quality," *Numerical Linear Algebra with Applications*, vol. 17, no. 5, pp. 855–869, 2010.
- [20] S. C. Brenner and L. R. Scott, *The Mathematical Theory of Finite Element Methods*, vol. 15 of *Texts in Applied Mathematics*, Springer, New York, NY, USA, 3rd edition, 2008.
- [21] G. Strang and G. Fix, *An Analysis of the Finite Element Method*, Wellesley-Cambridge Press, Wellesley, Mass, USA, 2nd edition, 2008.
- [22] P. G. Ciarlet, *The Finite Element Method for Elliptic Problems*, vol. 40 of *Classics in Applied Mathematics*, SIAM, Philadelphia, Pa, USA, 2002, Reprint of the 1978 original.